Muk Chen Ong

Applications of a Standard High Reynolds Number k-ε Model and a Stochastic Scour Prediction Model for Marine Structures

Muk Chen Ong

Doctoral Thesis

NTNU
Norwegian University of
Science and Technology
Thesis for the degree of
philosophiae doctor
Faculty of Engineering Science and Technology
Department of Marine Technology

NTNU
Norwegian University of
Science and Technology

NTNU
Norwegian University of
Science and Technology

NTNU

Muk Chen Ong

Applications of a Standard High Reynolds Number k-ε Model and a Stochastic Scour Prediction Model for Marine Structures

Thesis for the degree of philosophiae doctor

Trondheim, April 2009

Norwegian University of
Science and Technology
Faculty of Engineering Science and Technology
Department of Marine Technology

NTNU
Norwegian University of
Science and Technology

Muk Chen Ong

Applications of a Standard High Reynolds Number k-ε Model and a Stochastic Scour Prediction Model for Marine Structures

Thesis for the degree of philosophiae doctor

Trondheim, April 2009

Abstract

The present thesis is concerned with applications of a standard high Reynolds number k-ε model in coastal, marine and offshore engineering and a stochastic scour prediction model on marine structures.

Part I – Computational Fluid Dynamic Work

The rough turbulent oscillatory boundary layer flows with suspended sediments are studied by using a standard high Reynolds number k-ε model with a sediment suspension model. The boundary layer flow under sinusoidal waves over a rough bed is considered. For intermediate and shallow water depths, the trajectories of the wave orbital velocities are ellipses that flatten as the bottom is approached. Hence, a boundary layer approximation applies, and the sea bed boundary layer flow is assumed horizontally uniform. The predicted mean velocity, turbulent kinetic energy, shear stress and bed friction velocity yield good agreements with the published experimental data. The magnitude of the mean sediment concentration profile is overall under-predicted by a factor of 2.5 as compared with the published experimental data. This is considered to be a good result within the modeling of sediment transport.

Numerical simulations of high Reynolds number flows (covering the supercritical to upper-transition flow regimes) around a two-dimensional (2D) smooth circular cylinder have been performed by using 2D Unsteady Reynolds-Averaged Navier-Stokes (URANS) equations with the standard high Reynolds number k-ε model. The objective of this study is to evaluate the applicability of the model for engineering design within these flow regimes. The results are compared with published experimental data and numerical results. Satisfactory results for engineering design purposes are obtained in these flow regimes (i.e. $Re > 10^6$) as compared with the published experimental data and numerical results, although the model is known to yield less accurate predictions of flow with strong anisotropic turbulence.

Flows around a 2D circular cylinder close to a non-movable flat seabed at Reynolds number ranging from 1×10^4 to 4.8×10^4 (in the subcritical flow regime) and at 3.6×10^6 (in the upper-transition flow regime) are investigated. This study is useful for the engineering design of marine pipelines and risers which are often subject to very high Reynolds number flows in

the open sea environment. The flows are investigated numerically using 2D URANS equations with the standard high Reynolds number k-ε model. The results are compared with published experimental data and numerical results by considering effects of gap ratios, incident boundary layer thicknesses, Reynolds numbers and bed roughness. The suppression and development of the vortex shedding are studied. Under-predictions of the essential hydrodynamic quantities of the cylinder are observed in the subcritical flow regime due to the limitation of the turbulence model. However, satisfactory results are obtained for the flows at $Re = 3.6 \times 10^6$ (in the upper-transition flow regime). The mean pressure distribution and the friction velocity distribution along the bed are predicted reasonably well as compared with the published experimental and numerical results in the subcritical flow regime. Reasonable results are also obtained in the upper-transition flow regime although experimental data are required for validation. An example of bedload transport estimation is included in this study for demonstrating the influence of bed friction velocity on the sediment transport along the movable seabed.

Overall it appears that the standard high Reynolds number k-ε model is able to predict near-bed high Reynolds number flows in open sea environment reasonably well for engineering design purposes. However, more relevant experimental data are required in order to perform more detailed validation for very high Reynolds number flows. In the meantime the model should be useful as an engineering assessment tool for design work.

Part II – Stochastic Approach for Predictions of Random Wave-Induced Scour

Two analytical studies have been carried out for scour predictions around marine pipelines in shoaling conditions and at the trunk section of breakwaters under the effect of random waves by using a stochastic approach.

So far, no studies are available in the open literature dealing with the random wave-induced scour below pipelines in shoaling conditions. In this study, the random wave-induced scour depth is estimated by using the proposed stochastic model. It appears that the model gives reasonable scour predictions.

In the case of random wave-induced scour at the trunk section of breakwaters, scarce experimental data and scour prediction formulas are available in the open literature. A similar stochastic approach to that mentioned above is also used to quantify the random wave-induced scour depth at the trunk section of vertical-wall and rubble-mound breakwaters. Satisfactory predictions are obtained by comparing the results with two sets of published experimental data.

Generally the stochastic method gives reasonable random wave-induced scour predictions for these marine structures. However, more experimental data are required before a conclusion regarding the validity of this approach can be given. In the meantime, the method should be useful as an engineering tool for design purpose beneath random waves.

Acknowledgements

List of Publications

This thesis is written as a collection of five papers which are published or in press, and one manuscript which will be submitted for journal publication. They are listed as follows:

1) Ong, M.C., Utnes, T., Holmedal, L.E., Myrhaug, D. and Pettersen, B. (2007). Validation of a dynamic turbulence-closure model for rough turbulent oscillatory flows with suspended sediments. *Proceedings of MekIT'07, 4th National Conference on Computational Mechanics*, Trondheim, Norway, pp. 285-293.

2) Ong, M.C., Utnes, T., Holmedal, L.E., Myrhaug, D. and Pettersen, B. (2009). Numerical simulation of flow around a smooth circular cylinder at very high Reynolds numbers. *Marine Structures*, 22, 142-153.

3) Ong, M.C., Utnes, T. Holmedal, L.E., Myrhaug, D. and Pettersen, B. (2008). Numerical simulation of flow around a marine pipeline close to the seabed. *Proceedings of 31st International Conference on Coastal Engineering*, Hamburg, Germany (In press).

4) Ong, M.C., Utnes, T., Holmedal, L.E., Myrhaug, D. and Pettersen, B. (2009). Numerical simulation of flow around a circular cylinder close to a flat seabed at high Reynolds numbers (Submitted to *Coastal Engineering*).

5) Myrhaug, D., Ong, M.C. and Gjengedal, C. (2008). Scour below marine pipelines in shoaling conditions for random waves. *Coastal Engineering*, 55(12), 1219-1223.

6) Myrhaug, D. and Ong, M.C. (2009). Random wave-induced scour at the trunk section of a breakwater. *Coastal Engineering*, 56(5-6), 688-692.

Regarding the authorship and my contributions in these papers, I am the first author of *Papers 1, 2, 3* and *4* and I was responsible for performing the numerical simulations, providing the results and discussions, and writing the papers under the supervision of Prof. Dag Myrhaug, Dr. Lars Erik Holmedal and Prof. Bjørnar Pettersen. Dr. Torbjørn Utnes is the second author of these papers and he is the original developer of the CFD codes.

As the second author of *Papers 5* and *6*, I was responsible for performing the numerical calculations, providing the results (figures) and commenting the papers. Prof. Dag Myrhaug (the first author) initiated the studies, wrote the papers and is the originator of the stochastic method used in these two papers. The content in *Paper 5* is related to Cecilie Gjengedal's (third author in *Paper* 5) master thesis under the supervision of Prof. Dag Myrhaug.

Table of Contents

Chapter 1

Introduction

1.1. Background and Motivation

The rapid developments of offshore oil and gas industry for drilling, well intervention, production and storage at sea, aquaculture industry and the exploitation of renewable energy from wind, waves and current have increased the importance of flow-structure interactions and sediment transport around marine structures such as platform legs/columns, pipelines and risers. These marine structures are often subject to very high Reynolds number flows, especially in the open sea environment. The flow mechanisms and the near-bed sediment transport around these structures are complex. Hence, more research of the high Reynolds number flows in the ocean is necessary in order to gain a better understanding of the flow characteristics and dynamic responses of these structures. Furthermore, very high Reynolds number flows related to marine structures are hard and expensive to measure. Therefore an attractive alternative is to use Computational Fluid Dynamics (CFD) to obtain the essential hydrodynamic quantities needed for engineering design.

One interesting and complicated dynamic process in the ocean is the seabed boundary layer flow. This topic has gained intense international attention from different research areas during the past decades. Coastal engineers, offshore engineers and naval architects use the knowledge in studying near-shore sediment transport, coastal contaminant transport, scour around marine structures, and interaction between ships and the seabed. Physical understanding of the seabed boundary layer flow is therefore required.

The seabed boundary layers are generally in the rough turbulent flow regime, and this provides a challenge both in mathematical and physical modelling. Moreover, the non-linear wave-current interaction near the seabed further complicates the flow mechanism. A variety of mathematical models have been developed for this engineering challenge, ranging from simple parametric models via dynamic eddy viscosity models and Reynolds-Averaged Navier-Stokes (RANS) models, to Large Eddy Simulation (LES) and Direct Numerical

Simulation (DNS). These models have many corresponding applications ranging from engineering modelling to pure physics. In this thesis, dynamic rough turbulent oscillatory flows with suspended sediments have been studied using unsteady RANS (URANS) equations with a standard high Reynolds number k-ε model. Details of the research work are presented in Chapter 5.

Many marine structures have circular cylindrical shapes, such as marine pipelines, marine risers and offshore platform legs. With their typical diameter ranging from 0.2m to 4m, they are often subject to flow conditions corresponding to very high Reynolds number ($Re = U_\infty D/v$) flows with typical values of O(10^5) - O(10^7). This covers the supercritical ($3.5\times10^5 < Re < 1.5\times10^6$) to transcritical ($Re > 4\times10^6$) flow regimes. Here U_∞ is the free stream velocity; D is the cylinder diameter; and v is the kinematic viscosity. Zdravkovich (1997) and Sumer and Fredsøe (1997) have provided a detailed summary on the flows around circular cylinders; these flows have different characteristics in different Reynolds number flow regimes. So far, not many numerical studies have been carried out to predict the flows around an isolated circular cylinder at such very high Reynolds numbers. In this thesis two-dimensional (2D) URANS equations with the standard high Reynolds number k-ε model have been used to evaluate its applicability in engineering design within the high Reynolds number flow regimes ($Re > 10^6$). Details of the study are presented in Chapter 6.

Some circular marine structures are located near the seabed, for example marine pipelines and marine risers. They are subject to seabed boundary layer flows, which affect the flow around the cylinders. For example, a marine pipeline is normally laid on the seabed or buried in the seabed. Free span may occur due to scour, leading to a gap (G) between the pipeline and the seabed usually in the range $0.1D$ to $1D$. The seabed boundary layer flow and the gap complicate the flow around the pipelines. The hydrodynamic characteristics of steady flow around a horizontal smooth circular cylinder near a non-movable flat bed represent an idealized situation of a pipeline near the seabed. Hence, it is essential to understand the flow mechanisms around the pipeline and along the flat seabed. In the present study, high Reynolds number flows, ranging from $Re = $ O(10^4) to O(10^6), around a circular cylinder close to the seabed has been investigated using the 2D URANS with the standard high Reynolds number k-ε model. Effects of gap ratio, incident boundary layer flow thickness, Reynolds number and roughness of the bed have been considered. Chapters 7 and 8 give the details of the study.

The present research work referred to above is related to CFD work. In addition, two analytical studies have been carried out for scour predictions around marine pipelines under shoaling conditions and at the trunk section of breakwaters under the effect of random waves. These analytical studies will provide useful validation information for CFD simulations.

Scour hole around marine structures often affects the safety and the stability of the structures. Sumer and Fredsøe (2002) have summarized the scour mechanisms around various marine structures in great details. Useful semi-empirical models for predictions of the scour depth under current and regular/random waves have been proposed by various researchers. However, only a few studies have been performed for the random wave-induced scour.

Marine pipelines on sandy seabed in the coastal zone are exposed to random waves under shoaling and breaking conditions, and consequently it leads to scour around the pipelines. So far, no studies are available in the open literature dealing with the random wave-induced scour below pipelines under shoaling conditions. In this thesis, the random wave-induced scour depth is estimated by using a stochastic approach described in Section 9.5. Chapter 10 shows the details of the study.

Wave-induced scour is one of the major failure modes of breakwaters. In the case of random wave-induced scour at the trunk section of breakwaters, scarce experimental data and scour prediction formulas are available in the open literature. Hughes and Fowler (1991) presented the scour depth data and formula for vertical breakwater; and Sumer and Fredsøe (2000) presented the scour depth data for rubble-mound breakwater. In the present study, a similar stochastic approach to that mentioned above is used to quantify the random wave-induced scour depth at the trunk section of vertical-wall and rubble-mound breakwaters. Details of the study are presented in Chapter 11.

1.2. Objectives and Outline of the Thesis

The objectives of the present study are:

(i) To assess the applicability of a standard high Reynolds number k-ε model in flows around circular marine structures in very high Reynolds number flow regimes.

(ii) To predict the random wave-induced scour at marine structures by using a stochastic approach

Basically the thesis comprises two main parts: The first part shows the CFD work for the 1st objective; and the second part shows the analytical work for the 2nd objective.

Outline of the thesis is stated as follows:

4

Chapter 1 gives the introduction of this thesis which gives the overall background and motivation, the objectives of the study and the content of the thesis.

<u>Part I – CFD Work</u>

Chapter 2 gives a brief review of turbulent oscillatory boundary layer flows with suspension of sand at high Reynolds numbers

Chapter 3 gives a brief review of flows around a circular cylinder and the development of vortex shedding.

Chapter 4 describes the governing equations – URANS, the standard high Reynolds number k-ε model and the algorithm of Segregated Implicit Projection Method.

Chapter 5 gives the results of a validation study of a standard high Reynolds number k-ε model for rough turbulent oscillatory flows with suspended sediment. The numerical results are compared with published experimental data.

Chapter 6 presents the numerical simulation of flows around a smooth circular cylinder at very high Reynolds numbers (Re > 10^6), covering supercritical to upper-transition flow regimes. The objective of this study is to evaluate whether the 2D URANS equations with a standard high Reynolds number k-ε model is applicable for marine engineering design at Reynolds numbers ranging from 1×10^6 to 3.6×10^6.

Chapter 7 presents the numerical simulation of flow around a marine pipeline close to the seabed. The Reynolds number ranges from 1×10^4 to 4.8×10^4. The 2D URANS equations with a standard high Reynolds number k-ε model are solved to study the flow mechanisms. Effects of gap ratios, incident boundary layer thickness and Reynolds numbers are considered. Suppression and development of vortex-shedding are investigated numerically. Note that detailed convergence studies are given in Chapter 8.

Chapter 8 presents the numerical simulation of flows around a circular cylinder close to the flat seabed at high Reynolds numbers, i.e. $Re = 3.6\times10^6$ and $Re = 1\times10^4$- 4.8×10^4. The 2D URANS equations with a standard high Reynolds number k-ε model are solved to study the flow mechanisms by considering effects of gap ratios, Reynolds numbers and roughness of the seabed. Development of vortex-shedding are investigated numerically. Bedload sediment transport along the bed for small gap ratios is discussed together with the pressure and friction velocity along the bed.

Part II – Stochastic Approach for Predictions of Random Wave-Induced Scour

Chapter 9 gives a literature review of scour around marine pipelines and breakwaters. The theoretical basis of a stochastic approach is also given.

Chapter 10 presents the stochastic approach by which the scour depth below pipelines in shoaling conditions beneath non-breaking and breaking random waves can be derived. An example of calculation is also presented.

Chapter 11 presents the prediction of random wave-induced scour depth at the trunk section of vertical-wall and rubble-mound breakwaters by using the stochastic approach. Comparisons are made between the present predictions, published empirical formulas and published experimental data.

Recommendations for future work are given at the end of the thesis.

References

Hughes, S.A. and Fowler, J.A. (1991). Wave-induced scour predictions at vertical walls. *ASCE Proc. Conf. Coastal Sediments 91*, pp. 1886-1899.

Sumer, B.M. and Fredsøe, J. (1997). *Hydrodynamics around Cylindrical Structures: Advanced series on ocean engineering- Vol. 12*, World Scientific, Singapore.

Sumer, B.M. and Fredsøe, J. (2000). Experimental study of 2D scour and its protection at a rubble-mound breakwater. *Coast. Eng.*, 40, 59-87.

Sumer, B.M. and Fredsøe, J. (2002). *The Mechanics of Scour in the Marine Environment: Advanced series on ocean engineering- Vol. 17*, World Scientific, Singapore.

Zdravkovich, M.M. (1997). *Flow around Circular Cylinders, Vol. 1: Fundamentals*, Oxford University Press, New York.

Chapter 2

Turbulent Oscillatory Boundary Layer Flows with Suspension of Sand at High Reynolds Numbers

2.1. Introduction

High Reynolds number flows in the open sea environment are often a challenge for coastal, offshore and marine engineers. In order to design coastal protections and marine/offshore structures safely, the knowledge of both near-bed hydraulics and hydrodynamics is essential. The textbooks by Fredsøe and Deigaard (1992) and Nielsen (1992) provide an overview over the seabed boundary layers as well as sediment-transport and bedforms induced by the near-bed flow.

 In this chapter, turbulent oscillatory boundary layer flows induced by ocean surface waves with suspension of sands at high Reynolds numbers will be discussed in the following three sections. These sections will also give a brief literature review for the present CFD work in Chapter 5.

2.2. Laboratory Experiments of Turbulent Oscillatory Boundary Layer Flows

Beneath a progressive linear wave, the amplitudes of the particle orbits vary hyperbolically with the distance from the seabed (Fig. 2.1). For intermediate and shallow water depths, the trajectories of the wave orbital velocities are ellipses that flatten as the seabed is approached. Therefore, measurements in an oscillating water tunnel can represent the seabed boundary layer flow fairly well.

Bagnold (1946) studied the mechanisms of the formation of sand ripples and water vortices on a sandy bed by oscillating a section of bed with sand in still water. Wave friction factors

for small values of A/K_N in the rough turbulent regime were obtained. Here A is the near-bed wave excursion amplitude and K_N is the Nikuradse equivalent roughness. The same approach was also used by Kalkanis (1957, 1964) who measured the velocity profiles. Jonsson (1963) carried out the first extensive experimental measurements in the turbulent wave boundary layer. He measured the velocity distributions over a hydraulically rough boundary and computed the shear stress distributions from the velocity profiles using the momentum-integral equation. Jonsson and Carlsen (1976) carried out supplementary tests to Jonsson (1963). Tanaka et al. (1983) measured the smooth turbulent wave boundary layer in a wind tunnel using a hot wire anemometer. Hino et al. (1983), Sleath (1987) and Jensen et al. (1989) provided comprehensive experimental measurements consisting of the mean and the turbulence properties of smooth-bed and rough-bed oscillatory boundary layer flows using a laser-Doppler anemometer. Dohmen-Janssen (1999) investigated experimentally the phase lag between the Reynolds stress and velocity in rough turbulent oscillatory flows.
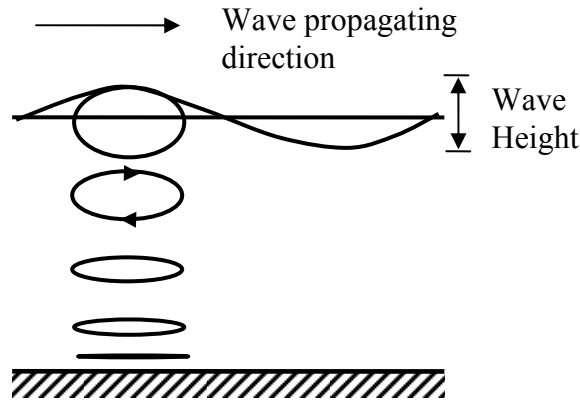
Figure 2.1. Wave particle motion at different depths between water surface and seabed.

2.2.1. Smooth bed

Hino et al. (1983) and Jensen et al. (1989) carried out their experiments in the Reynolds number Re_A ($=U_mA/v$) range of 7.5×10^3 to 6×10^6, covering laminar to fully turbulent flow regimes. Here U_m is the near-bed velocity amplitude. Figure 2.2 shows a chart given by Jensen et al. (1989) to determine the corresponding flow regimes at different phases within a wave cycle. In the figure, the normalized friction coefficient is defined by

$$f_w^* = \frac{2\dfrac{\overline{\tau}_o}{\rho}\Big/U_m^2}{\cos\left(\omega t - \pi/4\right)} \qquad (2.1)$$

where $\bar{\tau}_o$ is the mean bed shear stress; ω is the frequency of the wave motion; ρ is the density of the fluid and t is the time. The friction coefficient is normalized with the factor $\cos(\omega t - \pi/4)$ so that the laminar flow data will fall onto one common line. This is because the laminar flow solution is known to satisfy the relation (Batchelor, 1967):

$$\tau_o = \frac{\rho U_m^2}{Re_A^{1/2}} \cos\left(\omega t - \pi/4\right) \tag{2.2}$$

Figure 2.2 shows that three distinct flow regimes, i.e. the laminar, the transitional and the turbulent regimes, are experienced by every individual phase of flows as Re_A increases. The figure also indicates that the transitional regime occurs over a range of Re_A, from 1.5×10^5 to 1×10^6. The flow becomes fully turbulent when $Re_A > 1\times10^6$.
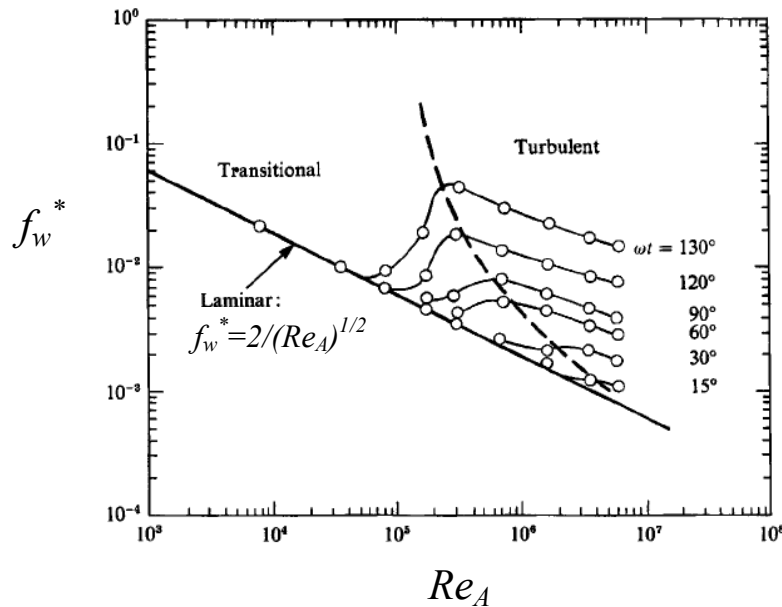
Figure 2.2. Normalized friction coefficient versus Re_A at different phase values for the smooth bed (reproduced from Jensen et al. (1989)).

Figure 2.3 gives the velocity profiles for four different Reynolds numbers ($Re_A = 2.8\times10^5$, 5×10^5, 1.6×10^6 and 6×10^6) reported by Jensen et al. (1989) (experiments), Hino et al. (1983) (experiments) and Spalart and Baldwin (1987) (Direct Numerical Simulation (DNS)). The characteristic features of the flows are described by Jensen et al. (1989) as follows:

(i)   The velocity profile eventually reaches a state where the logarithmic layer exists.
(ii) The logarithmic layer grows in thickness, as the flow proceeds further in the phase space.
(iii) The phenomenon continues until the point of flow reversal near the bed is reached.
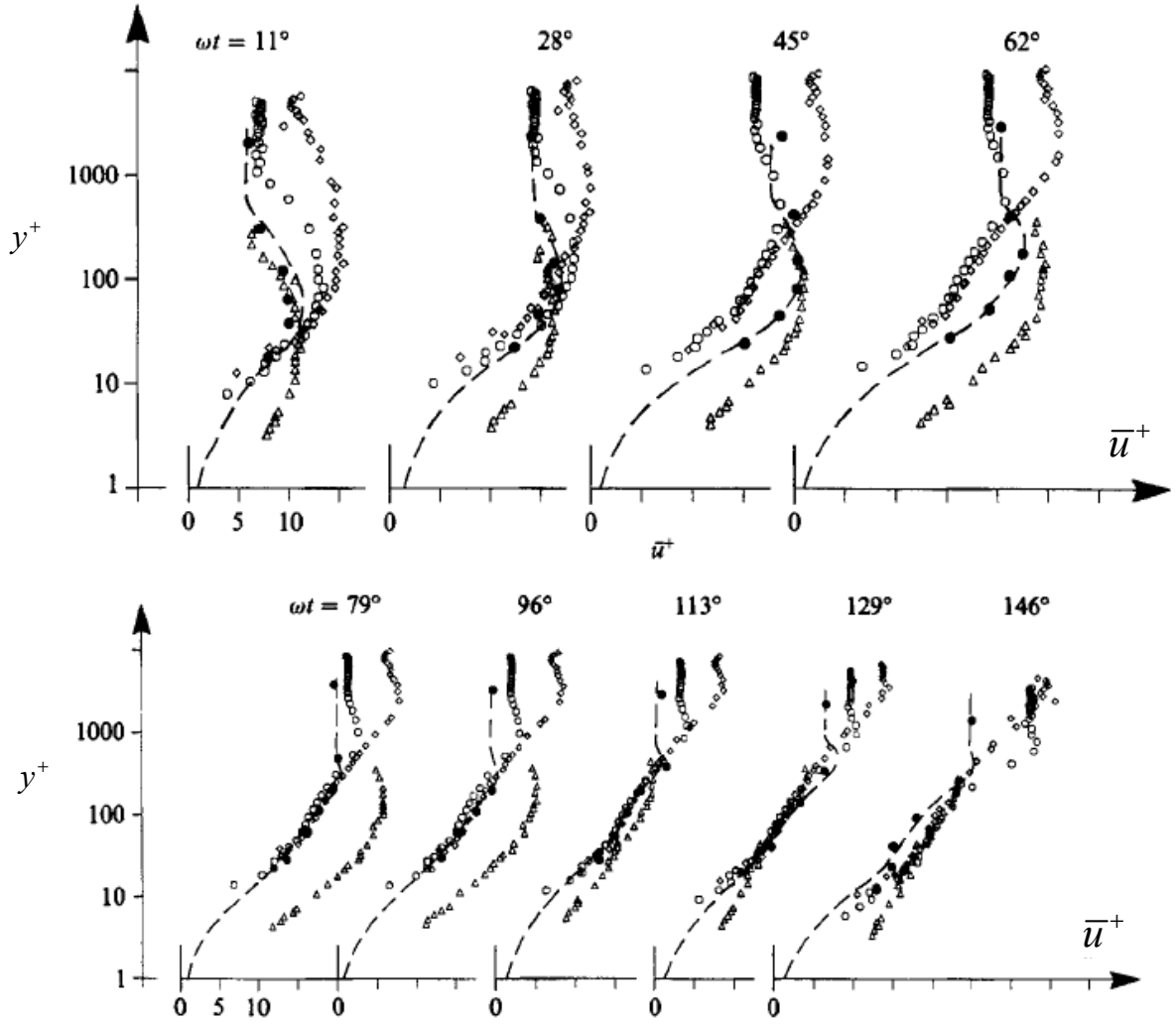
Figure 2.3. Mean velocity distributions in semi-log plot for various Re_A for the smooth bed. ($\diamondsuit$, Re_A= 6×10⁶, Test 10; $\bigcirc$, Re_A= 1.6×10⁶, Test 8; $\bullet$, Re_A= 5×10⁵, Test 6) by Jensen et al. (1989); Dashed lines, Re_A= 5×10⁵ by Spalart and Baldwin's (1987) DNS; $\triangle$, Re_A= 2.8×10⁵ by Hino et al. (1983). $\overline{u}^+ = \overline{u} / u_*$ where $\overline{u}$ is the mean velocity and u_* is the bed friction velocity . $y^+ = yu_* / \nu$ where y is the normal direction away from the bed (from Jensen et al. (1989)).

Furthermore, it is observed that the logarithmic layer exists earlier at the higher Reynolds numbers. This behaviour can also be explained by Fig. 2.2 which shows that the flow has to reach the fully developed turbulent state for the establishment of the logarithmic layer. More details of discussions are given in Jensen et al. (1989) and Hino et al. (1983).

2.2.2. Rough bed

Under storm conditions the boundary layer flow near the seabed covered by sand is usually in the rough turbulent flow regime. At large values of the Shields parameter (i.e. the non-

dimensional bed shear stress), the moving bed is flat, and A/K_N is in the range 10^3-10^4 (Jensen et al., 1989). K_N^+ is the roughness Reynolds number defined by

$$K_N^+ = \frac{K_N u_{*m}}{\nu} \qquad (2.3)$$

where u_{*m} is the maximum value of bed friction velocity within a wave cycle. The flow is rough if $K_N^+ > 70$, transitional smooth-to-rough turbulent if $5 < K_N^+ < 70$, and smooth turbulent if $K_N^+ < 5$ (Schlichting, 1979). The bed roughness is due to the individual sand grains. By considering this, the rough bed oscillatory boundary layer flow experiments with large A/K_N, i.e. A/K_N =1114 reported by Sleath (1987) and A/K_N = 3700 reported by Jensen et al.(1989), are more realistic representations of the wave boundary layer flows which occur near the seabed under storm conditions. They found that the flow quantities for fully developed turbulent flows over a completely rough boundary are dependent on A/K_N only.

Figure 2.4 shows the velocity profiles at various phases for three different values of A/K_N (124, 730 and 3700) reported by Jensen et al. (1989) and Jonsson and Carlsen (1976). It is seen that the logarithmic layer is established very early in the acceleration stage (at $\omega t = 30^o$) in all the three cases. The thickness of the logarithmic layer is the largest for A/K_N =3700, and thus larger A/K_N corresponds to thicker boundary layers.

Sleath (1987) and Jensen et al. (1989) reported that the turbulence quantities are also dependent on A/K_N in fully rough turbulent flow. The effect of A/K_N is strong near the bed and slowly diminishes at locations away from the bed.
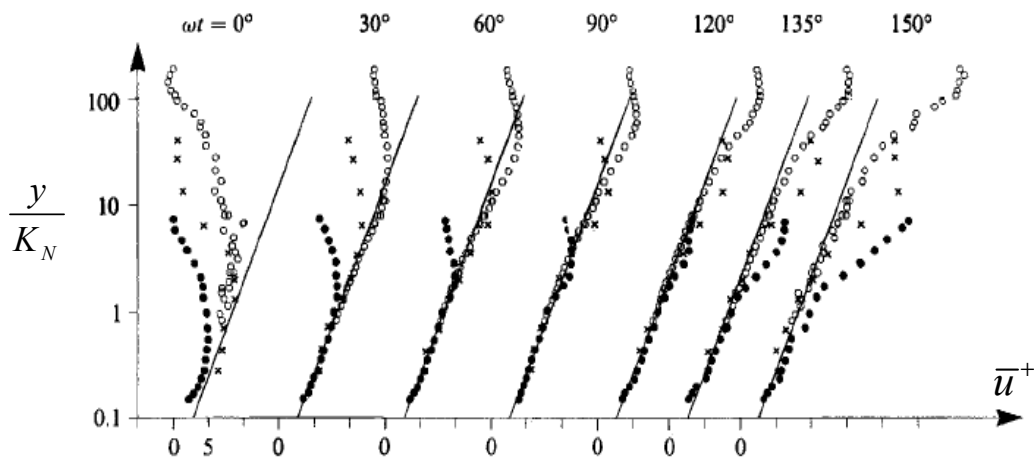
Figure 2.4. Mean velocity distributions in semi-log plot for various A/K_N. Rough bed. ($\bigcirc$, A/K_N = 3700, Test 13; $\times$, A/K_N = 730, Test 15) by Jensen et al. (1989); $\bullet$, A/K_N = 124, Jonsson and Carlsen (1976) (from Jensen et al. (1989)).

2.3. Computational Models for Turbulent Oscillatory Boundary Layer Flows

The earliest computational approaches on turbulent oscillatory boundary layer flows applied zero-equation models, mainly eddy viscosity models, Prandtl's mixing length models and the von Kármán momentum integral method.

Kaijura (1968) applied an eddy viscosity model by assuming the eddy viscosity (v_T) to be independent of time and dividing the oscillatory boundary layer flow into three layers, which are the inner layer with constant v_T, the overlap layer with v_T varying linearly with depth, and the outer layer with constant v_T. Brevik (1981) obtained an analytical solution of the pure oscillatory boundary layer specifying the eddy viscosity to be linear in the inner layer and constant in the outer layer. Myrhaug (1982) used a parabolic distribution of the eddy viscosity in the inner layer and a constant eddy viscosity in the outer layer, and obtained an analytical solution for the oscillatory boundary layer. Trowbridge and Madsen (1984) used a time and depth dependent eddy viscosity of the form

$$v_T = v_{T0} \, \mathrm{Re} \left\{ 1 + a\left(z\right) e^{i2\omega t} \right\} \qquad\qquad (2.4)$$

where z is the elevation from the bed; v_{T0} is linear in z in the inner layer and constant in the outer layer; $\mathrm{Re}\{\}$ denotes the real part; and $a(z)$ is a function of z. An analytical solution of the velocity profile within the boundary layer was obtained. However, the comparisons with the experimental data by Jonsson and Carlsen (1976) revealed that the results did not differ significantly from those using time invariant eddy viscosity. Davies (1986a) developed a similar model as Trowbridge and Madsen (1984), but with their v_{T0} being constant.

Bakker (1974) applied the Prandtl's mixing length model for wave boundary layer with the application of the finite difference method. Bakker and van Doorn (1978, 1981) further improved this method and provided experimental results. Their predictions yielded a reasonable agreement with their experimental results. Their model was then extended to predict three-dimensional boundary layers by van Kesteren and Bakker (1984).

von Kármán (1930) found that the wall shear stress could be obtained by assuming a reasonable velocity profile within the boundary layer and integrating the boundary layer equations vertically over the boundary layer. This approach is generally known as von Kármán momentum integral method. Fredsøe (1984) based his model on this method. He realized that the instantaneous velocities within the wave boundary layer and current boundary layer could be modelled with separate time dependent logarithmic velocity profiles, respectively. The time-averaged velocity profile was also assumed to be logarithmic with

respect to z. This model has proved to predict shear stresses in good agreement with the experimental data by Jensen et al. (1989) for both smooth and rough oscillatory boundary layer flows.

Davies (1986b) and Justesen (1988) investigated the pure oscillatory boundary layer using a one-equation model. Their comparisons with the measurements by Jonsson and Carlsen (1976) showed that not all the details of the flow were captured. Justesen (1991) and Holmedal (2002) used a standard high Reynolds number k-ε model to predict the rough turbulent oscillatory flow. Their predictions were compared with the experimental data by Jensen et al. (1989, Test No. 13). Mean velocity profiles and bed shear stress variation predicted by the model show good agreement with the experimental data. Brørs and Eidsvik (1994) predicted the experimental results by Jensen et al. (1989) to a great detail using a Reynolds stress model. Thais et al. (1999) applied the low Reynolds number k-ε model of Chien (1982) to study the Reynolds number variation in oscillatory boundary layers. Their model was able to capture the variation of the main flow variables (time-average velocity, shear stress and turbulent kinetic energy) through the wave cycle compared with the experimental data by Sleath (1987) and Jensen et al. (1989). Puleo et al. (2004) and Foti and Scandura (2004) used the k-ω model and compared its predictions with the Jensen et al. (1989, Test No.13) data. They found that the k-ω model yielded good predictions of the turbulent kinetic energy and the bed shear stress. Sana et al. (2009) applied a blended k-ω/k-ε model proposed by Menter (1994) to a rough oscillatory boundary layer. The model generally showed a reasonable agreement with the Jensen et al. (1989, Test No. 12) data. However, a few discrepancies in velocity and turbulent kinetic energy were observed during the deceleration phase.

It is difficult to apply Large Eddy Simulation (LES) on the seabed boundary layer, especially for the case of rough seabed, although wall laws can be applied in simulations using e.g. a Smagorisky model (Holmedal, 2002). For DNS it is not possible to resolve the geometry of e.g. sand grains on a rough bed (Holmedal, 2002). Spalart and Baldwin (1987) carried out DNS simulation of smooth oscillatory boundary layer flows. Their numerical results are in good agreement with the experimental data of Jensen et al. (1989) (see Fig. 2.3). Vittori and Verzicco (1998) performed a DNS of oscillatory boundary layer flow over a smooth plate with infinitesimal 3D imperfections. These imperfections were found to influence the turbulent flow structure for a sufficiently large Reynolds number. Lu (1999) and Hsu et al. (2000) used LES with a dynamic Smagorisky model of Germano et al. (1991) to study the oscillatory flow over a smooth flat plate. Their numerical results were in reasonable agreement with the experimental data of Hino et al. (1983), but no detailed description of the turbulence was provided. Lohman et al. (2006) investigated the smooth turbulent wave boundary layer by applying LES with the classical Smagorinsky model. Their results are in satisfactory agreement with the Jensen et al. (1989, Test No. 10) data. They also commented

that Hsu et al.'s (2000) dynamic Smagorinsky model showed no improvement compared to their results.

The main objective of the present CFD work is to assess the applicability of the standard high Reynolds number k-ε model for engineering design at high Reynolds numbers. Hence, similar to Justesen (1991) and Holmedal et al. (2003), the standard high Reynolds number k-ε model is used to investigate rough turbulent oscillatory flows. The predictions of mean velocity, turbulent kinetic energy, shear stress and bed friction velocity are compared with the Jensen et al. (1989, Test no. 13) data. Details of this numerical work are given in Chapter 5.

2.4. Suspension of Sand in Turbulent Oscillatory Flows

The understanding of the physical processes of the near-bed sediment dynamics under the influence of waves and currents is of great importance for predictions of seabed and coast-line changes. Near the seabed, the wave-induced water motion (horizontal oscillatory flow) is forcing the bottom boundary layer which results from the friction at the seabed. Due to the roughness of the seabed, the boundary layer is often rough turbulent. Inside this boundary layer, the turbulent oscillatory flow is responsible for the inception of seabed sediment motions, for bringing the sediments into suspension, and for the transport of the sediments. In more extreme wave conditions or more shallow water, the seabed becomes plane and sheet flow becomes the dominant transport mode.

Horikawa et al. (1982), Staub et al. (1983) and Ribberink and Al-Salem (1995) measured instantaneous sediment concentrations and velocities under sinusoidal waves (regular waves) with sheet flow conditions in oscillating water tunnels. Dohmen-Janssen and Hanes (2002) conducted their experiments in a large scale wave flume. They found that the mean suspended sediment concentration under gravity waves is much higher than those found in oscillating water tunnels under similar conditions. O'Donoghue and Wright (2004) presented detailed suspended sediment concentration measurements under oscillatory sheet flow conditions. Their experiments covered a wide range of sand beds and included study of graded sands systematically linked to the study of well-sorted sands.

A number of numerical investigations, on predicting the concentration of suspended sediments under sheet flow conditions for regular waves, have been carried out. The sediment diffusivity has been typically taken equal to, or proportional to, the eddy viscosity. Bakker (1974) applied a mixing length model to predict the time and space variations of suspended sediments during a wave cycle. Ribberink and Al-Salem (1991) further developed the approach by using a reference concentration obtained from the instantaneous bottom shear stress by the Engelund and Fredsøe (1976) formula. Hagatun and Eidsvik (1986) used a

standard high Reynolds number k-ε model with a sediment diffusion equation to investigate the seabed boundary layer as well as the time-dependent vertical distribution of sediment concentrations below large sinusoidal waves, as well as waves plus current. The sediment diffusivity was set equal to the eddy viscosity obtained from the k-ε model. A simplified version of the Engelund and Fredsøe (1976) formula was used together with the instantaneous bottom shear stress to obtain the reference sediment concentration near the bed. They predicted the experimental data by Staub et al. (1983) and the field measurements by Madsen and Grant (1977) reasonably well. Davies and Li (1997) used a one-equation model combined with the diffusion equation for suspended sediments to investigate the sediment transport beneath large symmetric and asymmetric regular waves, as well as beneath co-directional waves plus current. Their predictions yielded a fair agreement with the experimental data reported by Ribberink and Al-Salem (1995) for both regular symmetric and asymmetric waves. Holmedal et al. (2004) investigated the suspended sediment concentration under sheet flow conditions beneath random waves alone as well as under random waves plus current by using the standard high Reynolds number k-ε model based on linearized boundary layer equations with horizontal forcing. The sediment diffusivity was set equal to the eddy viscosity plus the laminar viscosity obtained from the k-ε model. The reference sediment concentration is obtained from the instantaneous bottom shear stress by using Zyserman and Fredsøe (1994) formula. Their model was also validated by comparing their predicted suspended sediment concentration with the experimental data by Staub et al. (1983), Ribberink and Al-Salem (1995) and Katopodi et al. (1994) beneath regular waves alone and regular waves plus current. Their comparisons between the predicted and measured suspended sediment concentrations show that the sediment diffusion model gives a fair prediction within the inner suspension layer. Numerical results of Holmedal et al. (2004) and the experimental results of Ribberink and Al-Salem (1994) also indicate that the irregularity of the flow does not severely affect the time-averaged suspended concentration profiles. This finding is useful for complicated coastal sediment transport problems under random waves.

It appears that the standard high Reynolds number k-ε model performs reasonably well in predicting the suspended sediment concentration under turbulent oscillatory flow conditions. A similar approach to that by Holmedal et al. (2004) is used in the present study. The predictions are compared with the experimental data reported by Ribberink and Al-Salem (1995). Details of the numerical work are given in Chapter 5.

References

Bagnold, R.A. (1946). Motion of waves in shallow water. Interactions between waves and sand bottom. *Proc. R. Soc. London Ser. A*, 187, 1-15.

Bakker, W.T. (1974). Sand concentration in an oscillatory flow. *Proc. 14th Int. Conf. Coast. Eng.*, Copenhagen, Denmark, pp. 1129-1148.

Bakker, W.T. and van Doorn, T. (1978). Near bottom velocities in waves with a current. *Proc. 16th Int. Conf. on Coast. Eng.*, Hamburg, Germany, ASCE, pp. 1394-1413.

Bakker, W.T. and van Doorn, T. (1981). Experimental investigation of near-bottom velocities in water waves without and with a current. Report of investigations M 1423 Part 1., Toegepast Onderzoek Waterstaat, The Netherlands.

Batchelor, G.K. (1967). *An Introduction to Fluid Dynamics*, Cambridge University Press.

Brevik, I. (1981). Oscillatory rough turbulent boundary layers. *J. Waterways, Harbors and Coastal Eng. Div.*, ASCE, 107(WW3), 175-188.

Brørs, B. and Eidsvik, K.J. (1994). Oscillatory boundary layer flows modelled with dynamic Reynolds stress turbulence closure. *Cont. Shelf Res.*, vol.14 (13/14), 1455–4752.

Chien, K.Y. (1982). Predictions of channel and boundary layer flows with a low-Reynolds-number turbulence model. *AIAA J.*, 20, 33–38.

Davies, A.G. (1986a). A model of oscillatory rough turbulent boundary layer flow, *Est Coast. Shelf Sci.*, 23(3), 353-374.

Davies A.G. (1986b). A numerical model of the wave boundary layer. *Cont. Shelf Res.*, 6(6), 715-739.

Davies, A.G. and Li, Z. (1997). Modelling sediment transport beneath regular symmetrical and asymmetrical wave above a plane bed. *Cont. Shelf Res.*, 17(5), 555-582.

Dohmen-Janssen, C.M. (1999). *Grain Size Influence on Sediment Transport in Oscillatory Sheet Flow. Phase-Lags and Mobile-Bed Effects*. Ph.D. Thesis, Delft University of Technology, The Netherlands.

Dohmen-Janssen, C.M. and Hanes, D.M. (2002). Sheet flow dynamics under monochromatic nonbreaking waves. *J. Geophys. Res.*, 107(C10), 3149. doi:10.1029/2001JC001045.

Engelund, F. and Fredsøe, J. (1976). A sediment transport model for straight alluvial channels. *Nordic Hydrology 7*, 293-306.

Fredsøe, J. (1984). Turbulent boundary layer in wave-current motion. *J. Hydr. Eng.*, ASCE, 110, 1103-1120.

Fredsøe, J. and Deigaard, R. (1992). *Mechanics of Coastal Sediment Transport*. World Scientific, Singapore.

Foti, E. and Scandura, P. (2004). A low Reynolds number k-ε model validated for oscillatory flows over smooth and rough wall. *Coast. Eng.*, 51, 173-184.

Germano, M., Piomelli, U., Moin, P. and Cabot, W.H. (1991). A dynamic subgrid-scale eddy viscosity model. *Phys. Fluids*, A 3, 1760-1765.

Hagatun, K. and Eidsvik, K.J. (1986). Oscillating turbulent boundary layers with suspended sediment. *J. Geophys. Res.*, 91(C11), 13045-13055.

Hino, M., Kashiwayanagi, M., Nakayama, A. and Hara, T. (1983). Experiments on the turbulence statistics and the structure of a reciprocating oscillatory flow. *J. Fluid Mech.*, 131, 363-400.

Holmedal, L. E. (2002). *Wave-Current Interactions in the Vicinity of the Sea Bed*. Ph.D. Thesis, NTNU, Norway.

Holmedal, L.E., Myrhaug, D., Rue, H. (2003). The sea bed boundary layer under random waves plus current. *Cont. Shelf Res.*, 23(7), 717-750.

Holmedal, L.E., Myrhaug, D., Eidsvik, K.J. (2004). Sediment suspension under sheet flow conditions beneath random waves plus current. *Cont. Shelf Res.*, 24, 2065-2091.

Horikawa, H., Watanabe, A. and Katori, S. (1982). Sediment transport under sheet flow condition. *Proc. 18th Int. Conf. Coast. Eng.,* Cape Town, pp. 1335–1352.

Hsu, C.T., Lu, X. and Kwan, M.K. (2000). LES and RANS studies of oscillating flows over flat plate. J. Eng. Mech., 126(2), 186-193.

Jensen, B.L., Sumer, B.M. and Fredsøe, J. (1989). Turbulent oscillatory boundary layers at high Reynolds numbers. *J. Fluid Mech.*, 206, 265-297.

Jonsson, I.G. (1963). Measurements in the turbulent wave boundary layer. *10th Congress IAHR*, Vol. 1, London, UK, pp. 85-92.

Jonsson, I.G. and Carlsen, N.A. (1976). Experimental and theoretical investigations in an oscillatory turbulent boundary layer. *J. Hydr. Res.*, 14(1), 45-60.

Justesen, P. (1988). A note on turbulence calculations in the wave boundary layer. *J. Hydr. Res.*, 29, 699-711.

Justesen, P. (1991). *Turbulent Wave Boundary Layers. Series Paper 43*, Ph.D. Thesis, Technical University of Denmark, Institute of Hydrodynamics and Hydraulic Engineering.

18

Kaijura, K. (1968). A model for the bottom boundary layer in water waves. *Bull. Earthquake Res. Inst.*, 45, 75-173.

Kalkanis, G. (1957). Turbulent flow near an oscillating wall. Series No. 72, Issue No. 3, University of California, Inst. Eng. Res.

Kalkanis, G. (1964). Transportation of bed material due to wave action. Technical Memo. No. 2, U.S. Army, Coast. Eng. Res. Center.

Katopodi, I., Ribberink, J.S., Ruol, P., Lodahl, C. (1994). Sediment transport measurements in combined wave-current flows. *Proc. Coast. Dynamics ASCE*, pp. 837-851.

Lohmann, I.P., Fredsøe, J., Sumer, B.M. and Christensen, E.D. (2006). Large eddy simulation of the ventilated wave boundary layer. *J. Geophys. Res.*, 111, C06036, doi: 10.1029/ 2005JC002946.

Lu, X. (1999). Numerical study of an oscillatory turbulent flow over a flat plate. *Acta Mechanica Sinica (English Series)*, 15(1), 8-14.

Madsen, O.S. and Grant, W.D. (1977). Quantitative description of sediment transport by waves. *Proc. 15th Coast. Eng. Conf. ASCE*, New York, pp. 1093-1112.

Menter, F.R. (1994). Two-equation eddy-viscosity turbulence models for engineering applications. *AIAA J.*, 32(8), 1598-1605.

Myrhaug, D. (1982). On a theoretical model of combined wave and current boundary layers. *Ocean Eng.*, 9(6), 547-565.

Nielsen, P. (1992). *Coastal Bottom Boundary Layers and Sediment Transport*. World Scientific, Singapore.

O'Donoghue, T. and Wright, S. (2004). Concentrations in oscillatory sheet flow for well sorted and graded sands. *Coast. Eng.*, 50(3), 117-138.

Puleo, J.A., Mouraenko, O. and Hanes, D.M. (2004). One-dimensional wave bottom boundary layer model comparison: specific eddy viscosity and turbulence closure models. *J. Waterway, Port, Coastal and Ocean Eng.*, ASCE, 130(6), 322-325.

Ribberink, J.S. and Al-Salem, A.A. (1991). Near-bed sediment transport and suspended sediment concentrations under waves. *Proc. Int. Symposium Transport of Suspended Sediments and its Mathematical Modelling*, Florence, pp. 375-388.

Ribberink, J.S. and Al-Salem, A.A. (1994). Sediment transport in oscillatory boundary layers in cases of rippled beds and sheet flow. *J. Geophys. Res.*, 99 (C6), 12707-12727.

Ribberink, J.S. and Al-Salem, A.A. (1995). Sheet flow and suspension of sand in oscillatory boundary layers. *Coast. Eng.*, 25, 205–225.

Sana, A., Ghumman, A. and Tanaka, H. (2009). Modelling of a rough-wall oscillatory boundary layer using two-equation turbulence models. *J. Hydr. Eng.*, 135(1), 60-65.

Schlichting, H. (1979). *Boundary Layer Theory*, 7th edition, McGraw-Hill, New York.

Sleath, J.F.A. (1987). Turbulent oscillatory flow over rough beds. *J. Fluid Mech.*, 182, 369-409.

Spalart, P.R. and Baldwin, B.S. (1987). Direct simulation of a turbulent oscillating boundary layer. NASA Technical memorandum 89640, Ames Research Center, Mofett Field, California.

Staub, C., Svendsen, I.A. and Jonsson, I. G. (1983). Variation of sediment suspension in oscillatory flow. Prog. Rep., ISVA, Tech Univ. Denmark, Vol.58, 41–49.

Tanaka, H., Chian, C.S. and Shuto, N. (1983). Experiments on an oscillatory flow accompanied with a unidirectional motion, *Coast. Eng. Jap.*, 26, 19-37.

Thais, L., Chapalain, G. and Smaoui, H. (1999). Reynolds number variation in oscillatory boundary layers. Part 1. Purely oscillatory motion. *Coast. Eng.*, 36, 111-146.

Trowbridge, J. and Madsen, O.S. (1984). Turbulent wave boundary layers 1. model formulation and first order solution. *J. Geophy. Res.*, 89(C5), 7989-7997.

van Kesteren, W.G.M. and Bakker, W.T, (1984). Near bottom velocities in waves with a current; analytical and numerical computations. *Proc. 19th Int. Conf. Coast. Eng.*, Houston, Texas, pp. 1161-1177.

von Kármán, T. (1930). Mechanische ähnlichkeit und Turbulenz. *Math-Phys. Klasse*, Vol. 58, p.6.

Vittori, G. and Verzicco, R. (1998). Direct simulation of transition in an oscillatory boundary layer. *J. Fluid Mech.*, 371, 207-232.

Zyserman, J.A. and Fredsøe, J. (1994). Data analysis of bed concentration of suspended sediment. *J. Hydr. Eng.*, 120(9), 1021-1042.

Chapter 3

Flow around a Circular Cylinder at High Reynolds Numbers

3.1. Introduction

Flow around a circular cylinder represents an idealized bluff body flow which is of great interest for a wide range of engineering applications. This thesis focuses on the coastal and marine applications. Marine pipelines, risers, offshore platform support legs, etc, are typically circular cylinders. In open sea environments, they are often subject to high Reynolds number flows (i.e. higher than 10^6). In this chapter, a brief review of flow around a circular cylinder is given.

3.2. Regimes of Flow around a Smooth Circular Cylinder

The Reynolds number is a governing parameter for the flow around a two-dimensional smooth circular cylinder.

$$Re = \frac{U_\infty D}{\nu} \tag{3.1}$$

As *Re* increases from zero, the flow mechanism undergoes large changes. Figure 3.1 shows the regimes of flow around a smooth circular cylinder in steady current. The definition sketch of the regions of wake and boundary layer is shown in Fig. 3.2. In the case of laminar boundary layer, the boundary layer thickness *δ* is (Schlichting,1979)

$$\frac{\delta}{D} = O\left(\frac{1}{\sqrt{Re}}\right) \tag{3.2}$$

It is observed that *δ/D* << 1 for *Re* larger than O(10^2).
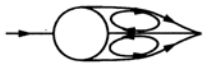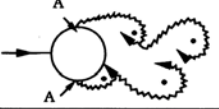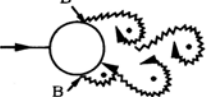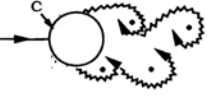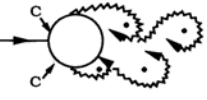
a)		No separation. Creeping flow	Re < 5
b)		A fixed pair of symmetric vortices	5 < Re < 40
c)		Laminar vortex street	40 < Re < 200
d)		Transition to turbulence in the wake	200 < Re < 300
e)		Wake completely turbulent. A:Laminar boundary layer separation	$300 < Re < 3 \times 10^5$ Subcritical
f)		A:Laminar boundary layer separation B:Turbulent boundary layer separation;but boundary layer laminar	$3 \times 10^5 < Re < 3.5 \times 10^5$ Critical (Lower transition)
g)		B: Turbulent boundary layer separation;the boundary layer partly laminar partly turbulent	$3.5 \times 10^5 < Re < 1.5 \times 10^6$ Supercritical
h)		C: Boundary layer completely turbulent at one side	$1.5 \times 10^6 < Re < 4 \times 10^6$ Upper transition
i)		C: Boundary layer completely turbulent at two sides	$4 \times 10^6 < Re$ Transcritical

Figure 3.1. Regimes of flow around a smooth circular cylinder in steady current (from Sumer and Fredsøe (1997)).

Wake region

Boundary layer

Separation

Incoming flow
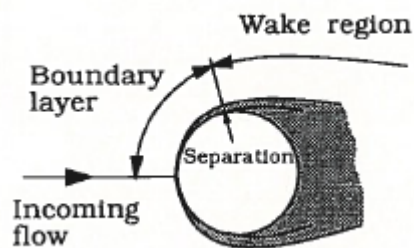
Figure 3.2. Definition sketch of the regions of wake and boundary layer (from Sumer and Fredsøe (1997)).

For *Re* < 5 (Fig. 3.1a), creeping flow is firmly attached to the surface of the cylinder. The steady and symmetric laminar shear layers do not form any visible wake, and no separation occurs. Separation of flow begins to happen at *Re*~5 when a distinct, steady, symmetric, and closed near-wake is formed behind the cylinder, as seen in Figs. 3.1b and 3.3. The free shear layers meet at the end of the near-wake at the confluence point. For 5< *Re* <40, the length of this vortex formation increases with *Re* (Batchelor, 1967).
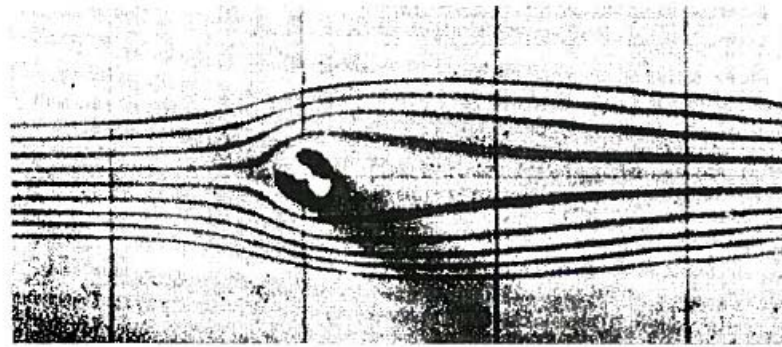
Figure 3.3. Steady closed near wake, *Re* = 23 (from Thom (1933)).

The elongated closed near-wake becomes unstable for *Re* > 30-48 and a sinusoidal oscillation of shear layers starts at the confluence point, as observed in Fig. 3.4b. This is considered as the initiation of vortex shedding, in which vortices are shed alternately at either side of the cylinder at a certain frequency. The amplitude of the oscillation increases with the increase of *Re* (see Fig. 3.4). Consequently, an appearance of a vortex street is formed downstream of the cylinder. For the range of the Reynolds number 40< *Re* <200 (Fig. 3.1c), the vortex street is laminar (Sumer and Fredsøe, 1997). Williamson (1989) found that the shedding is essentially two-dimensional and does not vary in spanwise direction.

Transition to turbulence occurs in the wake region (Fig. 3.1d) and the region of transition to turbulence moves towards the back of the cylinder as *Re* increases in the range 200 < *Re* < 300 (Bloor, 1964). Bloor (1964) found that the vortices formed in the near wake of the cylinder are turbulent at *Re* = 400. The vortex shedding mechanism in this range of *Re* becomes three-dimensional, and the vortices are shed in cells in the spanwise direction (Williamson, 1988). Although the wake is completely turbulent for *Re* > 300, the boundary layer over the cylinder surface remains laminar for a wide range of *Re*, i.e. $300 < Re < 3 \times 10^5$. This regime is known as subcritical flow regime (Fig. 3.1e).

Transition to turbulence occurs in the boundary layer for $Re > 3 \times 10^5$. Figs. 3.1f-3.1i show that the region of transition to turbulence first happens at the separation point, and then it moves upstream towards the stagnation point as *Re* increases (Sumer and Fredsøe, 1997). For $3 \times 10^5 < Re < 3.5 \times 10^5$ (Fig. 3.1f) the boundary layer becomes turbulent at the separation point; however, it occurs only at one side of the cylinder. The boundary layer at the separation

point is turbulent at one side of the cylinder and laminar at the other side. The turbulent boundary layer switches from one side to the other occasionally. This flow asymmetry causes a non-zero mean lift on the cylinder (Schewe, 1983). This flow regime is known as the critical flow regime.
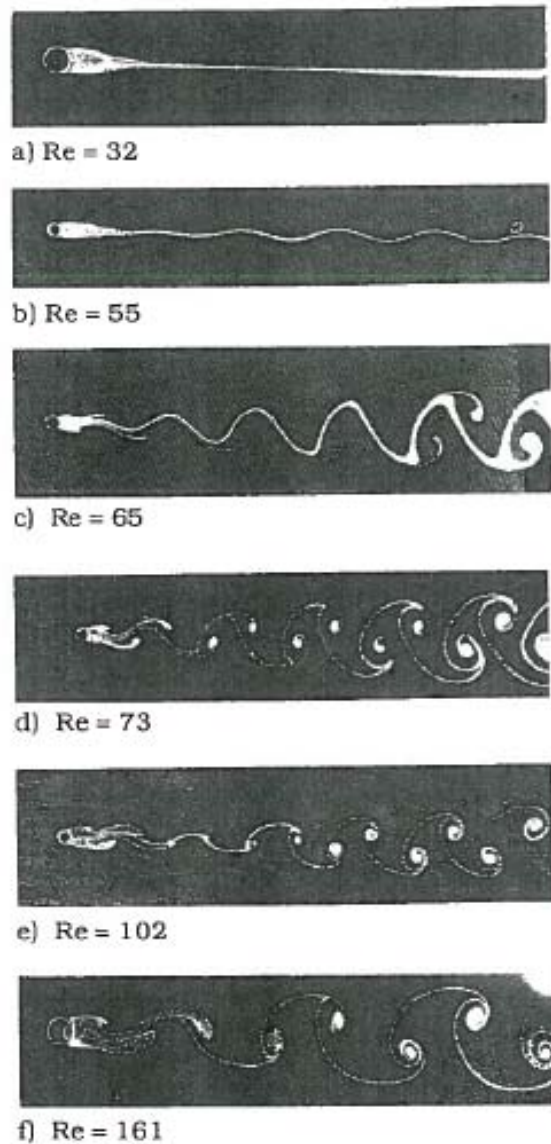
Figure 3.4. Development of vortex shedding behind a circular cylinder in a stream of oil with increasing *Re*. 32 ≤ *Re* ≤161 (from Homann (1936)).

The boundary layer at the separation point is turbulent on both sides of the cylinder for $3.5\times10^5 < Re < 1.5\times10^6$. The region of transition to turbulence is located between the stagnation point and the separation point. This flow regime is called supercritical flow regime. The boundary layer on one side becomes fully turbulent and partly laminar and partly

turbulent on the other side when $Re > 1.5 \times 10^6$. This flow regime, known as the upper-transition flow regime, is in the range of Re, $1.5 \times 10^6 < Re < 4.5 \times 10^6$.

For $Re > 4.5 \times 10^6$, the boundary layer around the cylinder surface is completely turbulent, and is referred to as the transcritical regime.

In the present study, applications of flow around a circular cylinder in marine and offshore engineering are investigated numerically in Chapter 6. These engineering applications are often subject to flow conditions corresponding to very high Reynolds number, $Re \sim O(10^6)$ to $O(10^7)$, covering the supercritical to the transcritical flow regimes. This is because the diameters of circular marine structures are large (i.e. 0.3m to 1m for marine pipelines, 0.2m to 1m for marine risers, and 1m to 3.5m for offshore platform legs) and the flow velocity are often high in the ocean.

3.3. Vortex Shedding

Vortex shedding is the dominating flow feature for $Re > 40$. The boundary layer around the cylinder surface separates due to the adverse pressure gradient which reduces the skin friction to zero. As a result of this, a shear layer is formed, as shown in Fig. 3.5. The boundary layer around the cylinder contains a significant amount of vorticity, and this vorticity is fed into the shear layer formed downstream of the separation point. The shear layer rolls up into a vortex with a sign identical to that of fed-in vorticity (Vortex A, Fig. 3.5a). Similarly, Vortex B which rotates in the opposite direction is formed on the other side of the cylinder. The pair formed by these two vortices is unstable when exposed to small disturbances. Consequently, one vortex grows larger than the other and it leads to vortex shedding (Sumer and Fredsøe, 1997).

According to Gerrard (1966) and Sumer and Fredsøe (1997), the development of vortex shedding (Fig. 3.6) is described in the following way. In the present context, the vorticity in Vortex A is in the clockwise direction whereas Vortex B is in counter-clockwise direction. The larger vortex (Vortex A) becomes strong enough to draw the other vortex (Vortex B) across the wake as observed in Fig. 3.6a. The Vortex B with the opposite sign of vorticity approaches Vortex A and then cuts off the supply of vorticity to Vortex A from its shear layer. Vortex A is then shed as a free vortex which is convected downstream by the flow. After the shedding of Vortex A, a new vortex (Vortex C) is formed at the same side of the cylinder. Now, Vortex B will play the same role as Vortex A. It will grow in size and strength to draw Vortex C across the wake and then be shed (Fig. 3.6b). The shedding will continue to occur in an alternate manner between the two sides of the cylinder.

a)

Stagnation point

A

B

b)

y

U_c

Shear layer

Vorticity

δ

$\bar{u}$

Boundary layer

Detailed picture of flow near separation
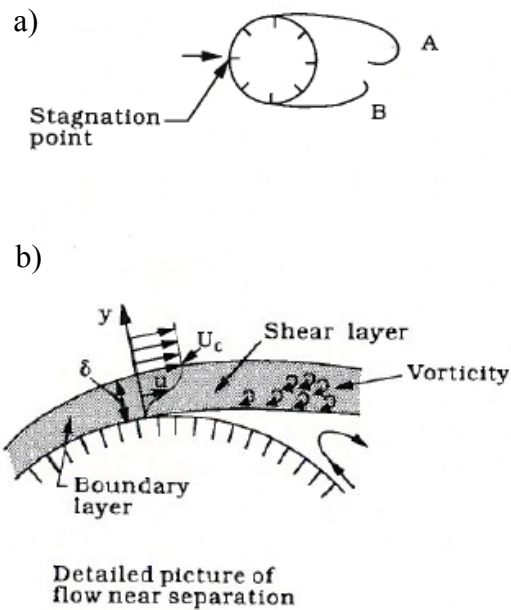
Figure 3.5. The shear layer. The shear layers roll up to form lee-wake vortices, A and B (from Sumer and Fredsøe (1997)).

a)

A

B

b)

C

A

B
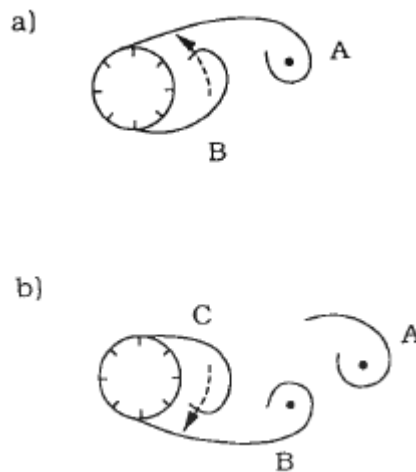
Figure 3.6. Development of vortex shedding (from Sumer and Fredsøe (1997)).

Hence, vortex shedding occurs due to the interaction of the two shear layers. No vortex shedding will occur if this interaction is prevented. For example, when the cylinder is placed close to a flat bed, the wall reduces the strength of the shear layer at the side of the cylinder close to the bed; this will lead to a weak interaction between the two shear layers at both sides of the cylinder. In this case, the vortex shedding will be suppressed. The understanding of this

flow feature is important for marine applications, e.g. for horizontal marine pipelines or risers close to the seabed. The significant variation of hydrodynamic data, such as drag force, lift force, vortex shedding frequency, etc, are observed by varying the gap size between the cylinder and the bed, especially in high Reynolds number flow regimes, i.e. $Re > 10^6$. Therefore, numerical studies of flow around a circular cylinder close to a flat bed at high Reynolds numbers, covering Reynolds number ranging from 1×10^4 to 4.8×10^4 (in the subcritical flow regime) and 3.6×10^6 (in the upper-transition regime) are presented in Chapters 7 and 8, respectively.

References

Batchelor, G.K. (1967). *An Introduction to Fluid Dynamics*, Cambridge University Press.

Bloor, M.S. (1964). The transition to turbulence in the wake of a circular cylinder. *J. Fluid Mech.*, 19, 290-304.

Gerrard, J.H. (1966). The mechanics of the formation region of vortices behind bluff bodies. *J. Fluid Mech.*, 25, 401-413.

Homann, F. (1936). Einfluss grosser zähigkeit bei strömung um zylinder. *Forschung auf dem Gebiete des Ingenieurwesen*, 7(1), 1-10.

Schewe, G. (1983). On the force fluctuations acting on a circular cylinder in cross flow from subcritical up to transcritical Reynolds numbers. *J. Fluid Mech.*, 133, 265-285.

Schlichting, H. (1979). *Boundary Layer Theory*, 7th edition, McGraw-Hill, New York.

Sumer, B.M. and Fredsøe, J. (1997). *Hydrodynamics around Cylindrical Structures: Advanced series on ocean engineering- Vol. 12*, World Scientific, Singapore.

Thom, A. (1933). The flow past circular cylinders at low speeds. *Proc. Royal Society*, A141, pp. 651-659.

Williamson, C.H.K. (1988). The existence of two stages in the transition to three-dimensionality of a cylinder wake. *Phys. Fluids*, 31(11), 3165-3168.

Williamson, C.H.K. (1989). Oblique and parallel modes of vortex shedding in the wake of a circular cylinder at low Reynolds number. *J. Fluid Mech.*, 206, 579-627.

Chapter 4

Computational Method

4.1. Introduction

Computational Fluid Dynamics (CFD) is an increasingly important tool for analyzing flows around marine structures. In operating conditions, marine structures are often subject to high Reynolds number flow conditions. At high Reynolds numbers, flows are turbulent. Turbulent flows are highly irregular; however, they are governed by the exact Navier-Stokes equations. Efficient numerical algorithms solving the Navier-Stokes equations and the turbulence models for high Reynolds number flows are still considered as a major challenge although many numerical methods (e.g. SIMPLE-like class of algorithms and projection methods) have been developed. Furthermore, the appropriateness of turbulence models for the targeted engineering applications should be considered carefully. The computer and cost efficiency of the computational method is also important, especially for engineering applications.

There are numerous approaches available for simulating turbulent flows, such as Direct Numerical Simulation (DNS), turbulent-viscosity models (e.g. the k-ε model, the k-ω model, etc), Reynolds-stress models and Large Eddy Simulation (LES). However, the standard high Reynolds number k-ε model has been incorporated into most commercial CFD codes. When used in conjunction with wall functions, it is generally taken as being computationally less expensive than DNS and LES. In this thesis, the applicability of this turbulence model in simulating the high Reynolds number flows for marine applications is investigated.

By taking high Reynolds turbulent flows as a motivating factor, Utnes (2008) proposed a segregated implicit projection numerical algorithm for solving the incompressible Unsteady Reynolds-Averaged Navier-Stokes (URANS) equations and the standard high Reynolds number k-ε model by using a Galerkin finite element method. This numerical method is $1^{st}/2^{nd}$ order in time and 2nd order in spatial discretization. This method has proved to be robust and stable in applications of high Reynolds number flows (Ong et al. (2007), Utnes (2008), Ong et al. (2008, 2009)).

By using this computational method (Utnes, 2008), numerical studies on rough turbulent oscillatory flows with suspended sediments (e.g. wave boundary layer flows with suspended sediments), flows around an isolated smooth circular cylinder at very high Reynolds numbers (e.g. flows around marine pipelines and risers), flows around a circular cylinder close to the seabed at very high Reynolds number (e.g. flows around marine pipelines and risers close to the seabed) are presented in Chapter 5, 6, 7 and 8, respectively.

The governing equations (URANS), the standard high Reynolds number k-ε model and the segregated implicit projection numerical algorithm will be described briefly in the following sections.

4.2. Governing Equations and the Standard High Reynolds Number k-ε Model

The Reynolds-averaged equations for conservation of mass and momentum are given by

$$\frac{\partial u_i}{\partial x_i} = 0 \tag{4.1}$$

$$\frac{\partial u_i}{\partial t} + u_j \frac{\partial u_i}{\partial x_j} = -\frac{1}{\rho}\left(\frac{\partial P}{\partial x_i}\right) + v\frac{\partial^2 u_i}{\partial x_j^2} - \frac{\partial \overline{u_i' u_j'}}{\partial x_j} \tag{4.2}$$

where i, j = 1, 2. Here x_1 and x_2 denote the horizontal and vertical directions, respectively; u_1 and u_2 are the corresponding mean velocity components; $\overline{u_i' u_j'}$ is the Reynolds stress component where u_i' denotes the fluctuating part of the velocity; v is the kinematic viscosity; and P is the dynamic pressure.

The Reynolds stress component, $\overline{u_i' u_j'}$, is expressed in terms of a turbulent viscosity v_T and the mean flow gradients using the Boussinesq approximation,

$$-\overline{u_i' u_j'} = v_T\left(\frac{\partial u_i}{\partial x_j} + \frac{\partial u_j}{\partial x_i}\right) - \frac{2}{3}k\delta_{ij} \tag{4.3}$$

where k is the turbulent kinetic energy and δ_{ij} is the kronecker delta function.

A standard high Reynolds number k-ε turbulence model (see e.g. Launder and Spalding (1972); Rodi (1993)) is used in the present study. This model has been applied previously on vortex shedding flow by Majumdar and Rodi (1985). The k and ε equations are given by:

$$\frac{\partial k}{\partial t} + u_j \frac{\partial k}{\partial x_j} = \frac{\partial}{\partial x_j}\left(\frac{v_T}{\sigma_k}\frac{\partial k}{\partial x_j}\right) + v_T\left(\frac{\partial u_i}{\partial x_j} + \frac{\partial u_j}{\partial x_i}\right)\frac{\partial u_i}{\partial x_j} - \varepsilon \tag{4.4}$$

$$\frac{\partial \varepsilon}{\partial t} + u_j \frac{\partial \varepsilon}{\partial x_j} = \frac{\partial}{\partial x_j}\left(\frac{v_T}{\sigma_\varepsilon}\frac{\partial \varepsilon}{\partial x_j}\right) + C_1 \frac{\varepsilon}{k} v_T\left(\frac{\partial u_i}{\partial x_j} + \frac{\partial u_j}{\partial x_i}\right)\frac{\partial u_i}{\partial x_j} - C_2 \frac{\varepsilon^2}{k} \tag{4.5}$$

where ε is the rate of viscous dissipation and $v_T = C_\mu \dfrac{k^2}{\varepsilon}$. The following standard model coefficients have been adopted: ($C_1 = 1.44$, $C_2 = 1.92$, $C_\mu = 0.09$, $\sigma_k = 1.0$, $\sigma_\varepsilon = 1.3$).

The governing equations (4.1) to (4.5) are discretized in space by use of a mixed finite element method, and these semi-discretized equations may be written in compressed form as

$$M\dot{u} + A\left(u\right)u + Gp = f \tag{4.6}$$

$$G^T u = 0 \tag{4.7}$$

$$M_\theta \dot{\theta} + A_\theta\left(u\right)\theta = s \tag{4.8}$$

Here M represents the mass matrix, $A(u) = K + N(u)$ is the sum of diffusion and advection matrices, G is the gradient matrix, and (f, s) represent source terms. u and p are defined here as nodal vectors for velocity and pressure, θ represents the nodal vector for scalar variables (e.g. kinetic energy (k), rate of viscous dissipation (ε), suspended sediment concentration (C), etc) and M_θ represents the mass matrix for scalar variables. The matrices involved in the equations are given below as an element by element integration, as follows:

$$M^e = \int_{\Omega^e} \phi\phi^T d\Omega \ \ ; \ \ K^e = v\int_{\Omega^e} \nabla\phi\cdot\nabla\phi^T d\Omega \ \ ;$$
$$G^e = -\int_{\Omega^e} \nabla\phi\psi^T d\Omega \ \ ; \ \ N\left(u\right)^e = \int_{\Omega^e} \phi\, u\cdot\nabla\phi^T d\Omega \tag{4.9}$$

where Ω is the computational domain. Subscript e denotes that the integration is performed over each element. The global interactions are obtained by summing (assembling) the element contributions into the system matrix. Test/basic functions (ϕ, ψ) are associated with velocity and pressure, respectively.

The time integration is performed using a semi-implicit two-level formulation (Utnes, 2008), and the discretized equation system may then be written in the following form:

$$\left[\tilde{M} + \alpha A_{n+\alpha} \right] u_{n+1} = \left[\tilde{M} - \left(1-\alpha\right) A_{n+\alpha} \right] u_n - Gp_{n+1} + f_{n+\alpha} \tag{4.10}$$

$$G^T u_{n+1} = 0 \tag{4.11}$$

$$\left[\tilde{M}_\theta + \alpha A_{\theta,n+\alpha} \right] \theta_{n+1} = \left[\tilde{M}_\theta - \left(1-\alpha\right) A_{\theta,n+\alpha} \right] \theta_n + s_{n+\alpha} \tag{4.12}$$

where $\tilde{M} = M /\Delta t$ and $\tilde{M}_\theta = M_\theta / \Delta t$. Subscripts n, $n+1$ and $n+\alpha$ indicate time levels. The implicit parameter α is chosen in the interval $1/2 \le \alpha \le 1$. The fully implicit case, $\alpha = 1$, is suitable for steady state computation, and the time-centered case, $\alpha = 1/2$ is suitable for time-accurate computations. The notation $f_{n+\alpha} = \alpha f_{n+\alpha} + (1-\alpha) f_n$ is used, and same for s.

4.3. Segregated Implicit Projection Algorithm

A segregated implicit projection method proposed by Utnes (2008) is adopted for all the numerical simulations in this thesis. This numerical algorithm is non-iterative, with corrections within each time-step.

The proposed algorithm is given by the following steps:

1) Predict the pressure and advection velocity via a pseudo-velocity prediction from the system

$$\tilde{M} \Delta u_* = A_n u_n + f_n \; ; \; Lp_* = G^T u_* \tag{4.13}$$

where $\Delta u_* = u_* - u_n$, and Laplacian operator $L = \Delta t\, G^T M_L^{-1} G$, where M_L is the lumped mass matrix.

2) Compute the velocity field from the (semi) implicit momentum equation

$$\left[\tilde{M} + \alpha A_{n+\alpha} \right] \Delta \tilde{u}_{n+1} = -A_{n+\alpha} u_n - Gp_* + f_{n+\alpha} \tag{4.14}$$

where $\Delta \tilde{u}_{n+1} = \tilde{u}_{n+1} - u_n$, and the advection velocity is given by extrapolation as $\hat{u}_{n+\alpha} = (1+\alpha) u_n - \alpha u_{n-1}$.

3) Correct the velocity and pressure fields by use of the projection step

$$L\Delta p_{n+1} = G^T \tilde{u}_{n+1} \; ; \; \tilde{M}\left(u_{n+1} - \tilde{u}_{n+1}\right) = -G\Delta p_{n+1} \tag{4.15}$$

where the updated pressure is $p_{n+1} = p_* + \Delta p_{n+1}$.

4) Compute (semi) implicit equations for other scalar quantities:

$$\left[\tilde{M}_\theta + \alpha A_{\theta,n+\alpha}\right]\Delta\theta_{n+1} = -A_{\theta,n+\alpha}\theta_n + s_{n+\alpha} \tag{4.16}$$

where $\Delta\theta_{n+1} = \theta_{n+1} - \theta_n$.

The implementation is used based on Q_1Q_0 mixed elements, i.e. multilinear velocity and constant pressure on the element niveau. The analyses of consistency and time accuracy are given in Utnes (2008).

References

Launder, B.E. and Spalding, D.B. (1972). *Mathematical models of turbulence,* Academic Press, London.

Majumdar, S. and Rodi, W. (1985). Numerical calculation of turbulent flow past circular cylinder. *Proc. 7th Turbulent Shear Flow Symposium*, Stanford, USA, 3.13-3.25.

Ong, M.C., Utnes, T., Holmedal, L.E., Myrhaug, D. and Pettersen, B. (2007). Validation of a dynamic turbulence-closure model for rough turbulent oscillatory flows with suspended sediments. *Comp. Mech.*, MekIT'07, Trondheim, Norway, pp. 285-293.

Ong, M.C., Utnes, T., Holmedal, L.E., Myrhaug, D. and Pettersen, B. (2008). Numerical simulation of flow around a marine pipeline close to the seabed. *Proc. 31st Int. Conf. Coast. Eng.*, Hamburg, Germany (In Press).

Ong, M.C., Utnes, T., Holmedal, L.E., Myrhaug, D. and Pettersen, B. (2009). Numerical simulation of flow around a smooth circular cylinder at very high Reynolds numbers. *Marine Struc.*, 22, 142-153.

Rodi, W. (1993). *Turbulence models and their application in hydraulics. A state-of-the-art review. IAHR Monograph Series, 3rd Ed.,* A.A. Balkema, Rotterdam, Netherlands.

Utnes, T. (2008). A segregated implicit pressure projection method for incompressible flows. *J. Comp. Physics*, 227, 2198-2211.

Chapter 5

Validation of a Dynamic Turbulence-Closure Model for Rough Turbulent Oscillatory Flows with Suspended Sediments

Muk Chen Ong[*], Torbjørn Utnes[†], Lars Erik Holmedal[*], Dag Myrhaug[*] and Bjørnar Pettersen[*]

* Department of Marine Technology
Norwegian University of Science and Technology
e–mail: ong@ntnu.no

[†] SINTEF IKT Applied Mathematics

Summary[#] This paper presents a validation study of a standard high Reynolds number k-ε model for rough turbulent oscillatory flows with suspended sediments. The predicted mean velocity, turbulent kinetic energy, shear stress and bed friction velocity yield good agreements with experimental results. The magnitude of the mean sediment concentration profile is overall under-predicted by an averaged factor of 2.5 as compared to the experimental results; this is considered to be a good result within the modelling of sediment transport.

Introduction

The rapid development of offshore oil fields has increased the importance of submarine pipelines for transport of oil and gas. Interactions between the pipelines and erodible seabed under wave-current conditions tend to cause scouring around the pipelines, which might lead

---

to structural failure of the pipelines due to vortex-induced vibrations. Our long-term goal is to develop a robust numerical scour predictive model to assist designing the pipelines.

The understanding of the near-bed sediment dynamics under the influence of waves is of great importance for predictions of seabed changes. In order to simulate the sediment suspension in the bottom wave boundary layer, the near-bed flows outside the bottom boundary is specified from potential theory. Sleath [10] and Jensen et al. [6] presented detailed experimental investigations on the wave boundary layer, including measurements of mean velocity profiles, profiles of turbulence quantities and bottom shear stresses. The sea bed boundary layer has been investigated by a number of researchers ([1], [3], [7], [8]), using turbulence models. Justesen [7], [8] used a standard high Reynolds number k-ε model; the predicted velocities and turbulence quantities were in good agreement with the experimental results by Jensen et al. [6] and Sleath [10]. Brørs and Eidsvik [1] predicted the experimental results by Jensen et al. [6] to a great detail using a Reynolds stress model.

Horikawa et al. [5], Staub et al. [11] and Ribberink and Al-Salem [9] measured instantaneous sediment concentrations and velocities under sinusoidal waves in an oscillating water tunnel. Davies and Li [2] and Holmedal et al. [4] applied one-equation and two-equation models, respectively, in conjunction with a diffusion equation for suspended sediments, to investigate the sediment transport beneath regular waves. The predicted sediment concentration profiles were in good agreement with the experimental measurements by Ribberink and Al-Salem [9]. This paper presents a validation study of a standard high Reynolds number k-ε model for rough turbulent oscillatory flows with suspended sediments. Predictions of the turbulent mean velocity profiles, turbulent kinetic energy profiles, Reynolds stress profiles and bed friction velocities are compared with the experimental results (Test no. 13) reported by Jensen et al. [6]. Moreover, the sediment diffusion model is verified against the experimental results by Ribberink and Al-Salem [9].

Mathematical Formulation

(i) Flow model

The boundary layer flow under sinusoidal waves over a rough flat bed is considered. The horizontal coordinate at the bed and the vertical coordinate away from the bed are given as x and y, respectively.

The near-bed velocity outside the boundary layer is

$$U_\infty(t) = U_m \sin(\omega t) \tag{1}$$

where U_m is the near-bed velocity amplitude, and ω is the angular frequency of the oscillation.

For intermediate and shallow water depths, the trajectories of the wave orbital velocities are ellipses that flatten as the bottom is approached. Hence, a boundary layer approximation applies, and the sea bed boundary layer flow is assumed horizontally uniform (consequently the convective terms disappear). The Reynolds-averaged equation for fluid momentum is simplified as

$$\frac{\partial u}{\partial t} = -\frac{1}{\rho}\frac{\partial p}{\partial x} + \frac{\partial}{\partial y}\left(\nu_T \frac{\partial u}{\partial y}\right) \tag{2}$$

where u is the horizontal velocity component, p is the pressure, ρ is the density of water, and ν_T is the turbulent viscosity. A turbulence model is required throughout the flow field; in the present study, a standard high Reynolds number k-ε model has been applied. Since the flow is considered horizontally uniform, the convective terms are neglected in the transport equations for the turbulent quantities, i.e.

$$\frac{\partial k}{\partial t} = \frac{\partial}{\partial y}\left(\frac{\nu_T}{\sigma_k}\frac{\partial k}{\partial y}\right) + \nu_T\left(\frac{\partial u}{\partial y}\right)^2 - \varepsilon \tag{3}$$

$$\frac{\partial \varepsilon}{\partial t} = \frac{\partial}{\partial y}\left(\frac{\nu_T}{\sigma_\varepsilon}\frac{\partial \varepsilon}{\partial y}\right) + C_1 \frac{\varepsilon}{k}\nu_T\left(\frac{\partial u}{\partial y}\right)^2 - C_2 \frac{\varepsilon^2}{k} \tag{4}$$

The turbulent viscosity is given by $\nu_T = C_\mu k^2/\varepsilon$. The following standard model coefficients have been adopted: ($C_1 = 1.44$, $C_2 = 1.92$, $C_\mu = 0.09$, $\sigma_k = 1.0$, $\sigma_\varepsilon = 1.3$).

The equation for the sediment concentration, C, is given as:

$$\frac{\partial C}{\partial t} = w_s \frac{\partial C}{\partial y} + \frac{\partial}{\partial y}\left(\nu_T \frac{\partial C}{\partial y}\right) \tag{5}$$

where w_s is the constant settling velocity of sediment in still water.

(ii) Boundary conditions

(a)Bottom boundary conditions

The sea bed is assumed to be hydraulically rough. No-slip condition is applied at the theoretical bed level, $y_o = K_N/30$, i.e.

$$u = 0 \tag{6}$$

K_N is the Nikuradse roughness ($= 2.5d_{50}$) and d_{50} is the median grain size diameter.

The bottom boundary conditions for k and ε are given in a standard manner, i.e.

$$k = \frac{u_*^2}{\sqrt{C_\mu}} \quad , \quad \varepsilon = C_\mu^{\frac{3}{4}} \frac{k^{\frac{3}{2}}}{\kappa y_p} \tag{7}$$

where y_p is the distance of the first node away from wall; $\kappa = 0{:}41$ is the von Karman constant and u_* is the bed friction velocity.

The reference sediment concentration C_a near the sea bed is obtained from the Zyserman and Fredsøe [13] formula:

$$C_a = \frac{0.331 \left(|\theta| - \theta_c \right)^{1.75}}{1 + 0.720 \left(|\theta| - \theta_c \right)^{1.75}} \quad \text{at} \quad y = y_a = 2d_{50} \tag{8}$$

where θ is the instantaneous Shields parameter given by

$$\theta = \frac{\tau_w}{\rho g \left(S - 1 \right) d_{50}} \tag{9}$$

Here θ_c is the critical Shields parameter which must be exceeded for sediment movements to take place, taken as 0.045. Moreover, τ_w is the instantaneous wall shear stress, g is the acceleration of gravity and $S = 2.65$ is the density ratio between the sediments and the water.

(b)Top boundary conditions

At the upper boundary (in the free stream), the Neumann condition is applied on the velocity (implying no shear stress), i.e.,

$$\frac{\partial u}{\partial y} = 0 \tag{10}$$

Zero flux conditions are imposed for k and ε, expressed as

$$\frac{\partial k}{\partial y} = \frac{\partial \varepsilon}{\partial y} = 0 \tag{11}$$

A no-flux condition is imposed for the sediment concentration,

$$\nu_T \frac{\partial C}{\partial y} + w_s C = 0 \tag{12}$$

(iii) Forcing function

Since the boundary layer approximation applies, the horizontal pressure gradient is constant throughout the boundary layer. The horizontal pressure gradient, $\partial p/\partial x$ is given from the free stream velocity as

$$-\frac{1}{\rho} \frac{\partial p}{\partial x} = \frac{\partial U_\infty}{\partial t} \tag{13}$$

(iv) Numerical solution procedure and initial conditions

Equations 2 to 5 are solved using a Galerkin finite element method using a Segregated Implicit Projection (SIP) solution algorithm proposed by Utnes [12]. This method is 1st order in time and 2nd order in spatial discretization. Stretching of the mesh is performed to achieve a fine resolution close to the bed. Small positive values of the mean turbulence, sediment and flow quantities are initially introduced, and the equations are integrated in time until a steady state is achieved.

Results and Discussions

(i) Rough turbulent oscillatory flow

One of the most detailed measurements of the rough turbulent wave boundary layer flow is

Test no.13 from Jensen et al. [6] measured in a U-shaped oscillatory flow water tunnel. In the following, a comparison between prediction and these measurements is presented. Such comparisons have been published earlier by, among others, Justesen [8] and Holmedal [3]; the purpose of reproducing these results is to show the capability of the present model to predict the wave boundary layer over a rough bed.

The test conditions are given by $U_m = 2$m/s, a wave period of $T = 9.72$s, and a ratio between the near-bed wave excursion amplitude and the Nikuradse roughness, $A/K_N = 3700$, where $A = U_m/\omega$. The computation has been carried out with a total of 136 elements and a time step of $\Delta t = T/720$. Both grid and time-step convergence studies have been performed to ensure a sufficient numerical accuracy.

Figure 1 shows the characteristics of the mean velocity profiles in the wave boundary layer; Figure 1(a) shows three profiles in the acceleration phase, whereas Figure 1(b) shows three profiles in the deceleration phase. Both figures indicate that the present model is capable of predicting the overshoot at zero free stream velocity as well as the distinct differences of the shape in the acceleration and decelerating phases. The predicted velocity follows the logarithmic wall law close to the bed.

Figure 2 presents the predicted and measured turbulent kinetic energy profiles at four different phases during a half wave cycle. The turbulent kinetic energy profiles are overall slightly under-predicted as compared to the experimental results.

The shear stress, τ, in the boundary layer is related to the turbulent viscosity and the velocity gradient, i.e.

$$\frac{\tau}{\rho} = v_T \frac{\partial u}{\partial y} \qquad (14)$$

The prediction of shear stress profiles at four different phases over a half wave cycle is in good agreement with the measurements as shown in Figure 3.

The bed shear stress, τ_b, is the key quantity that drives the sediment transport. The friction velocity, u_*, is defined by

$$u_* = \sqrt{\frac{\tau_b}{\rho}} \qquad (15)$$

Figure 4 shows the predicted and measured friction velocity during one wave cycle. It is observed that the friction velocity is slightly under-predicted compared to the experimental results.
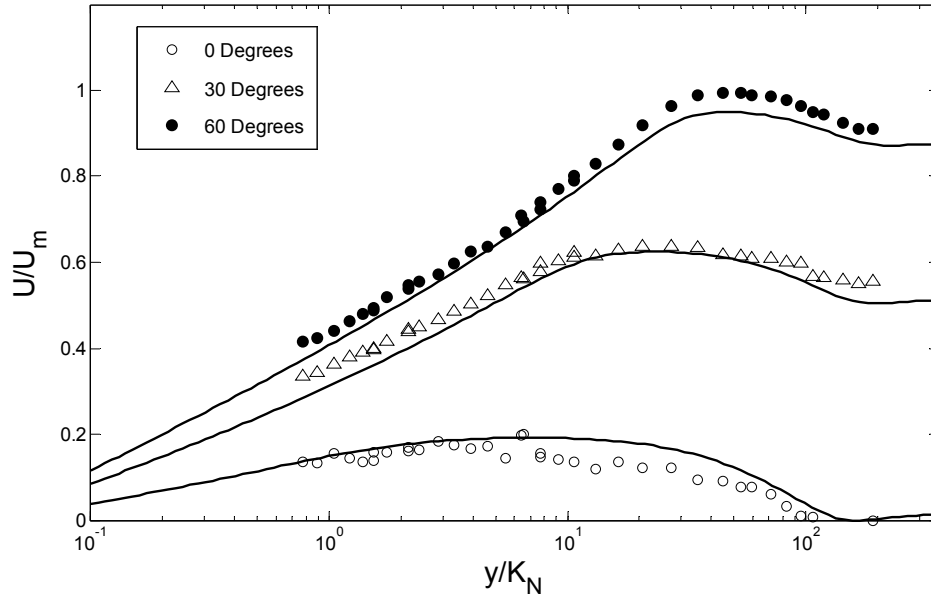
(a)
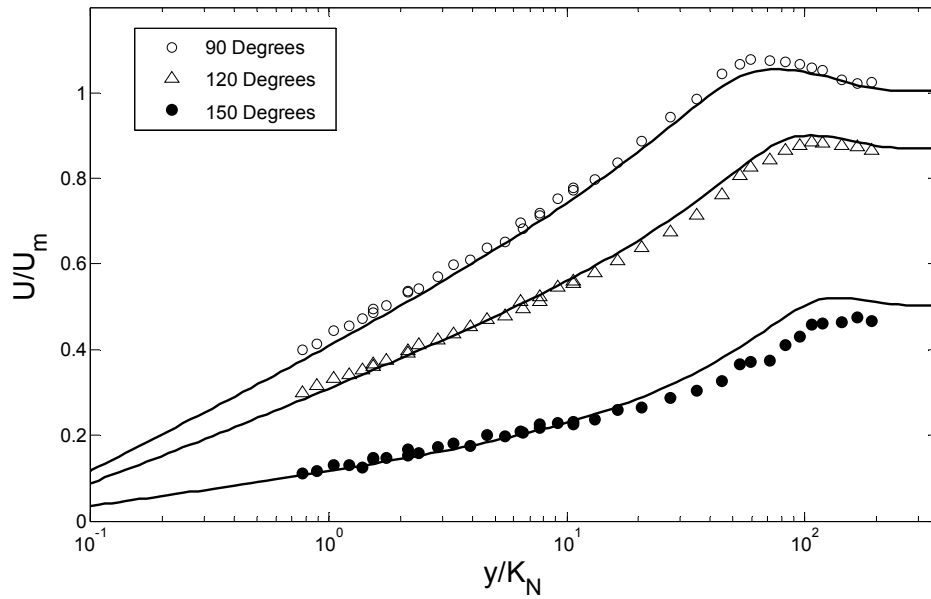
(b)

Figure 1: Comparisons of predicted and measured velocity profiles from Jensen et al. [6], Test No. 13 at different phases in a wave cycle. (a) Three profiles in the acceleration phase; (b) three profiles in the deceleration phase.
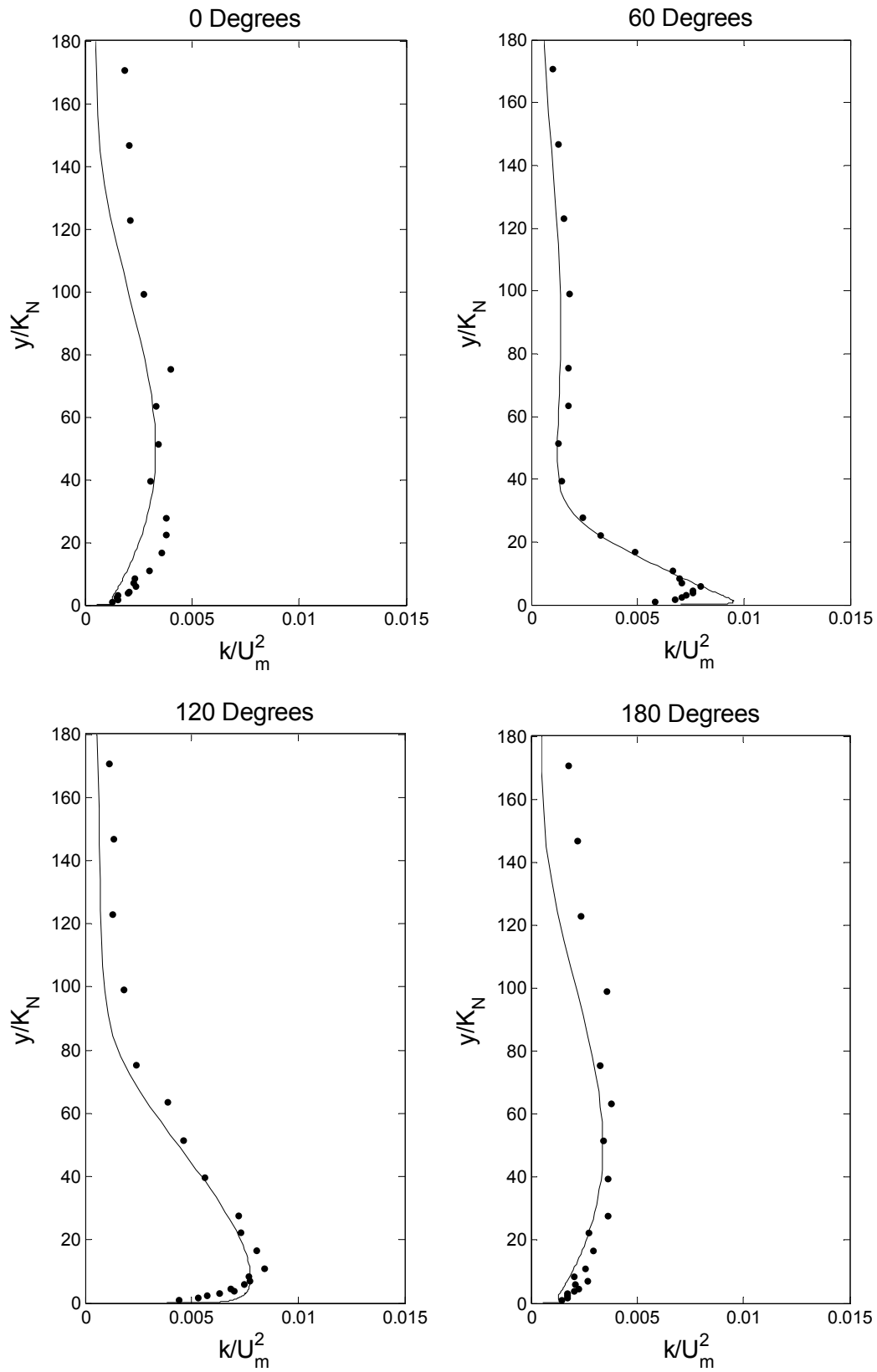
Figure 2: Comparisons of predicted and measured turbulence kinetic energy profiles from Jensen et al. [6], Test No. 13 at different phases in a wave cycle.
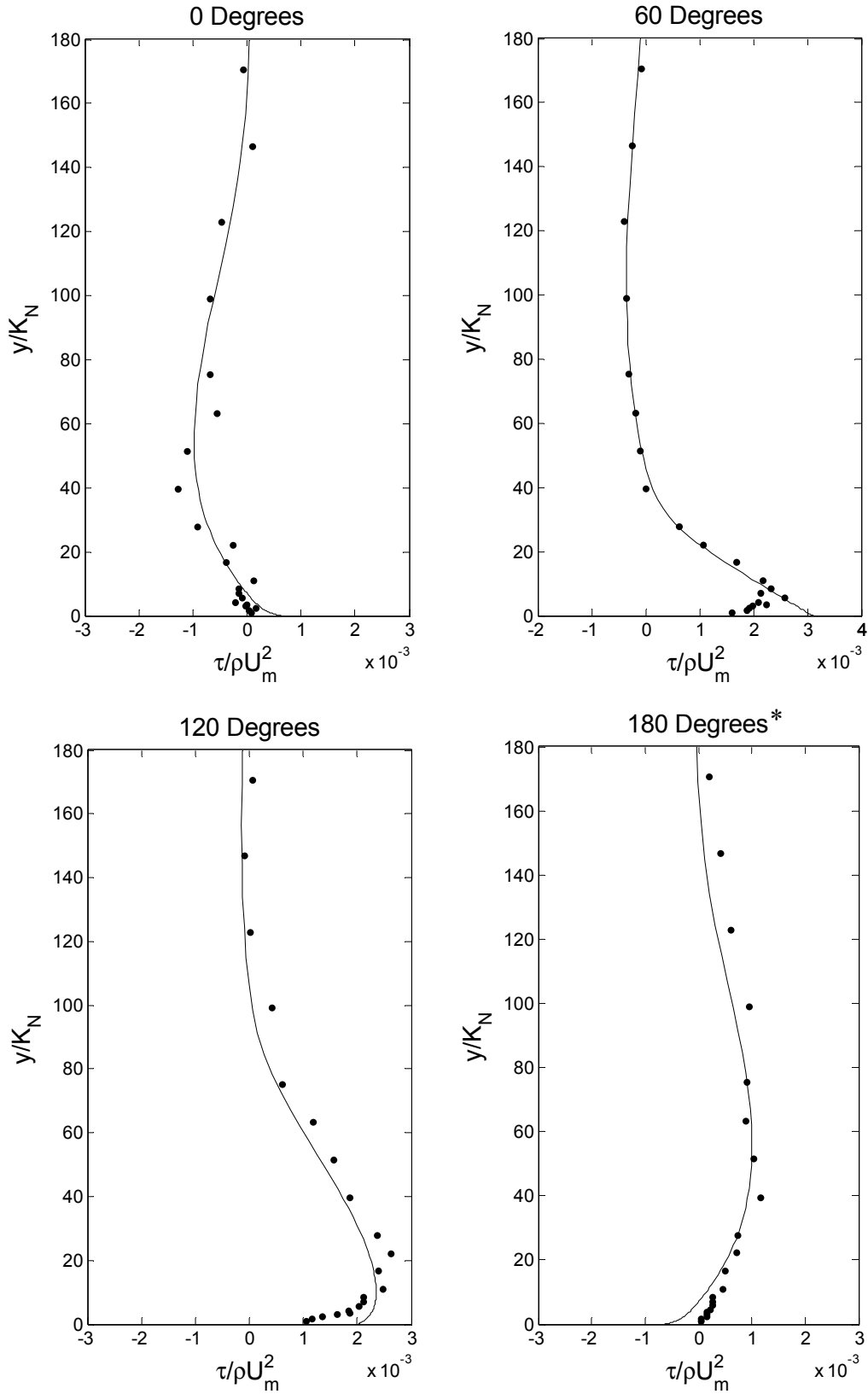
Figure 3: Comparisons of predicted and measured shear stress profiles from Jensen et al. [6], Test No. 13 at different phases in a wave cycle.

---

[*] The figure (180 Degrees) in the conference paper was misprinted. The correct version is updated here.

44
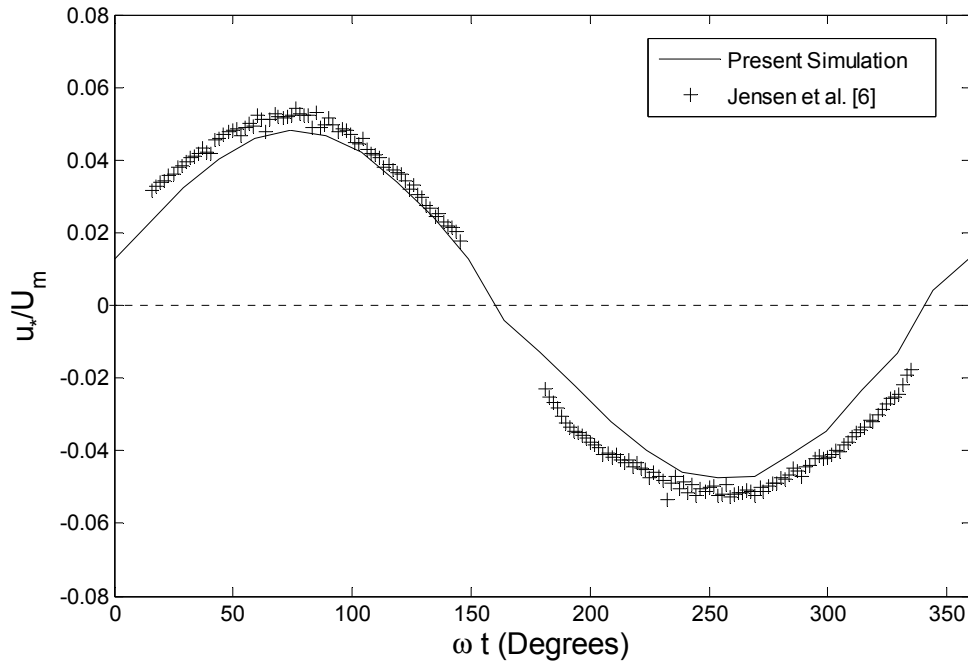
Figure 4: Comparisons of predicted and measured bed friction velocity from Jensen et al. [6], Test No. 13 within a wave cycle.

(ii) Rough turbulent oscillatory flow with suspended sediments

The suspended sediment concentration measured in an oscillating water tunnel (sheet flow condition) by Ribberink and Al-Salem [9], is used for comparison. The sinusoidal wave used in the experiment has a velocity amplitude of $U_m = 1.7$m/s and a wave period of $T = 7.2$s. The median grain diameter of the sediments is 0.21mm, and the settling velocity is 0.026m/s. The computation has been carried out with a total of 110 elements and a time step of $\Delta t = T/2880$. Both grid and time-step convergence studies have been performed to ensure a sufficient numerical accuracy.

As shown in Figure 5, the mean sediment concentration profile, $C_{average}$ (averaged over a wave period), is in reasonable agreement with the experimental results, although it is overall under-predicted by a factor of 2.5. For sediment transport, a prediction of the measured sediment concentration within a factor of 2-3 is considered as a good result.
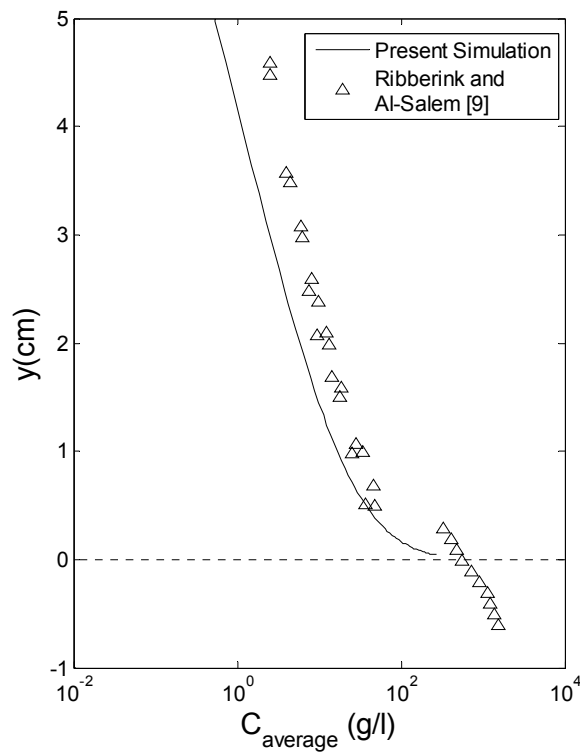
Figure 5: Comparisons of the predicted and measured mean sediment concentration profile; measurements by Ribberink and Al-Salem [9].

Conclusions

A standard high Reynolds number k-ε model with a sediment suspension model has been validated for rough turbulent oscillatory boundary layer flow. The predicted mean velocity, turbulent kinetic energy, shear stress and bed friction velocity yield an overall good agreement with experimental results; although the mean sediment concentration profile is under-predicted by an averaged factor of 2.5.

References

[1] B. Brørs and K. J. Eidsvik Oscillatory boundary layer flows modelled with dynamic Reynolds stress turbulence closure. *Cont. Shelf Res.*, vol.14(13/14), 1455–4752, 1994.

[2] A. G. Davies and Z. Li Modelling sediment transport beneath regular symmetrical and asymmetrical wave above a plane bed. *Cont. Shelf Res.*, vol.17(5), 555–582, 1997.

[3] L. E. Holmedal Wave-current interactions in the vicinity of sea bed. *PhD. Thesis, NTNU, Norway.*, 2002.

[4] L. E. Holmedal, D. Myrhaug and K. J. Eidsvik Sediment suspension under sheet flow conditions beneath random waves plus current. *Cont. Shelf Res.*, vol.24, 2065–2091, 2004.

[5] H. Horikawa, A. Watanabe and S. Katori Sediment transport under sheet flow condition. *Proc. 18th Int. Conf. Coast. Eng., Cape Town*, pages 1335–1352, 1982.

[6] B. L. Jensen, B. M. Sumer and J. Fredsøe Turbulent oscillatory boundary layers at high Reynolds numbers. *J. Fluid. Mech.*, vol.206, 265–297, 1989.

[7] P. Justesen Prediction of turbulent oscillatory flow over rough beds. *Coast. Eng.*, vol.12, 257–284, 1988.

[8] P. Justesen A note on turbulence calculations in the wave boundary layer. *J. Hydr. Res.*, vol.29, 257–284, 1991.

[9] J. S. Ribberink and A. A. Al-Salem Sheet flow and suspension of sand in oscillatory boundary layers. *Coast. Eng.*, vol.25, 205–225, 1995.

[10] J. F. A. Sleath Turbulence flow over rough beds. *J. Fluid. Mech.*, vol.182, 369–409, 1987.

[11] C. Staub, I. A. Svendsen and I. G. Jonsson Variation of sediment suspension in oscillatory flow. *Prog. Rep., ISVA, Tech Univ. Denmark.*, vol.58, 41–49, 1983.

[12] T. Utnes A segregated implicit pressure projection method for turbulent flows. *Submitted to J. Comp. Physics.*, 2007.

[13] J. A. Zyserman and J. Fredsøe Data analysis of bed concentration of suspended sediment. *J. Hydr. Eng.*, vol.120(9), 1021–1042, 1994.

Chapter 6

Numerical Simulation of Flow around a Smooth Circular Cylinder at Very High Reynolds Numbers

Muk Chen Ong[a], Torbjørn Utnes[b], Lars Erik Holmedal[a], Dag Myrhaug[a] and Bjørnar Pettersen[a]

[a] Department of Marine Technology,
  Norwegian University of Science and Technology, NO-7491 Trondheim, Norway.

[b] SINTEF IKT Applied Mathematics, NO-7465 Trondheim, Norway.

Abstract[#]

High Reynolds number flows ($Re = 1\times10^6$, 2×10^6 and 3.6×10^6, based on the free stream velocity and cylinder diameter) covering the supercritical to upper-transition flow regimes around a two-dimensional (2D) smooth circular cylinder, have been investigated numerically using 2D Unsteady Reynolds-Averaged Navier-Stokes (URANS) equations with a standard high Reynolds number k-ε turbulence model. The objective of the present study is to evaluate whether the model is applicable for engineering design within these flow regimes. The results are compared with published experimental data and numerical results. Although the k-ε model is known to yield less accurate predictions of flows with strong anisotropic turbulence, satisfactory results for engineering design purposes are obtained for high Reynolds number flows around a smooth circular cylinder in the supercritical and upper-transition flow regimes, i.e. $Re > 10^6$. This is based on the comparison with published experimental data and numerical results.

Keywords: Numerical models; Cylinder; Turbulent flow; High Reynolds number.

---

1. Introduction

One of the classical problems in fluid mechanics is the flow around a circular cylinder. This represents an idealized bluff body flow which is of great interest for a wide range of engineering applications, such as hydrodynamic loading on marine pipelines, risers, offshore platform support legs, etc. Many of these engineering applications are often subject to flow conditions corresponding to very high Reynolds number ($Re = U_\infty D/v$) flows with typical values of $O(10^6)$ - $O(10^7)$. This covers the supercritical ($3.5\times10^5 < Re < 1.5\times10^6$) to transcritical ($Re > 4\times10^6$) flow regimes. A detailed definition of the flow regimes is given in by Sumer and Fredsøe (1997). Here U_∞ is the free stream velocity; D is the cylinder diameter; and v is the kinematic viscosity. These very high Reynolds number flow conditions are hard and expensive to achieve in an experimental setup requiring appropriate experimental facilities, minimizing human and instrument errors during measuring hydrodynamic quantities etc. Therefore an attractive alternative is to use Computational Fluid Dynamics (CFD) to obtain the essential hydrodynamic quantities needed for engineering design. For example, Schulz and Meling (2004) used a multi-strip method to analyze the flow-structure interaction of long flexible risers. This was achieved by solving the two-dimensional (2D) Unsteady Reynolds-Averaged Navier-Stokes (URANS) equations (using a Spalart-Allmaras turbulence model) in conjunction with a finite element structural dynamic response model. A number of individual 2D CFD simulations of cross sections along the riser were combined with a full 3D structural analysis to predict overall vortex-induced vibration (VIV) loads and displacement of the riser. They showed that a relatively modest number of sections could be used to capture multi-modal VIV responses in long risers. Chaplin et al. (2005) compared laboratory measurements of the VIV of a vertical model riser in a stepped current with predictions obtained with 11 different numerical models. It was shown that empirical-based models were better in predicting cross-flow displacements than the CFD-based models. This might be due to uncertainties in CFD turbulence modeling and the modeling technique of the vortex-shedding interacting with dynamic response of the structure (see Chaplin et al. (2005)). Thus, more computational and experimental research on high Reynolds number flows over a rigid cylinder section is necessary in order to gain better understanding on dynamic responses of slender marine structures.

To date, not many numerical simulations have been performed to predict very high Reynolds number flows ($Re > 10^6$) around a smooth circular cylinder due to the complexity of the flow. Direct Numerical Simulation (DNS) of flows at such very high Reynolds numbers is not presently possible because of the high demand on the computational resources. Among the few numerical results reported in the open literature (for $Re > 10^6$) are those of Catalano et al. (2003) and Singh and Mittal (2005). Catalano et al. (2003) applied 3D Large Eddy Simulation (LES) with wall modeling as well as URANS using the standard high Reynolds number k-ε model of Launder and Spalding (1972) with wall functions, for $0.5\times10^6 < Re <$

4×10^6. Singh and Mittal (2005) performed their studies for $100 < Re < 1\times10^7$ using a 2D LES method. Catalano et al. (2003) mainly focused on the cases of $Re = 0.5\times10^6$ and 1×10^6 when the drag coefficient is recovering from the drag crisis (sudden loss of drag at $Re \sim 2\times10^5$). Their numerical results captured the delayed boundary layer separation and reduced drag coefficients correctly right after the drag crisis. They concluded that the LES results were considerably more accurate than the URANS results at $Re = 1\times10^6$. However, they also commented that the LES results became less accurate compared with the experimental data at higher Reynolds numbers due to their insufficient grid resolution. Singh and Mittal's (2005) main objective was to investigate a possible relationship between the drag crisis and the instability of the separated shear layer. Their computations were able to capture the sudden reduction in drag coefficient close to the critical Re. Even though their study primarily focuses on the flow in the subcritical regime ($300 < Re < 3\times10^5$), they also presented some results for the flow beyond the supercritical flow regime, i.e. $Re > 10^6$.

The standard high Reynolds number k-ε model has been incorporated into most commercial CFD codes. When used in conjunction with wall functions, it is generally taken as being computationally less expensive than LES and DNS. Nevertheless, the model has been well-documented for several shortcomings, especially in the subcritical flow regime where the drag crisis occurs. Franke et al. (1989) and Tutar and Holdø (2001) evaluated numerically the detailed experiments of Cantwell and Coles (1983) at $Re = 1.4\times10^5$. Franke et al. (1989) applied URANS with the standard high Reynolds number k-ε model of Launder and Spalding (1972); Tutar and Holdø (2001) used both the standard high Reynolds number k-ε model and non-linear k-ε models. Their results were mainly obtained for the flow in the subcritical flow regime at the start of the drag crisis. Both studies concluded that the k-ε models give an inaccurate prediction of flows with strong anisotropic turbulence. Catalano et al. (2003) presented time-averaged drag coefficients for $Re = 1\times10^6$, 2×10^6 and 4×10^6, Strouhal number for $Re = 1\times10^6$ and mean pressure distribution for $Re = 1\times10^6$ using URANS with a standard high Reynolds number k-ε model. Most of their results were given for $Re = 1\times10^6$, but for $Re = 2\times10^6$ and 4×10^6 (in the upper-transition regime) they only presented the time-averaged drag coefficients without discussing the applicability of the model in this upper-transition flow regime. Their results appear to yield satisfactory agreements with experimental data.

The main objective of the present study is to evaluate whether the standard high Reynolds number k-ε model is applicable for engineering applications in the supercritical and upper-transition flow regimes (after the drag crisis). The flows around a 2D smooth circular cylinder at $Re = 1\times10^6$, 2×10^6 and 3.6×10^6 are investigated numerically, and these results are compared with available experimental data and the numerical results reported by Catalano et al. (2003) and Singh and Mittal (2005).

2. Mathematical Formulation

2.1. Flow model

The Reynolds-averaged equations for conservation of mass and momentum are given by

$$\frac{\partial u_i}{\partial x_i} = 0 \tag{1}$$

$$\frac{\partial u_i}{\partial t} + u_j \frac{\partial u_i}{\partial x_j} = -\frac{1}{\rho}\left(\frac{\partial P}{\partial x_i}\right) + v\frac{\partial^2 u_i}{\partial x_j^2} - \frac{\partial \overline{u_i' u_j'}}{\partial x_j} \tag{2}$$

where i, j = 1, 2. Here x_1 and x_2 denote the horizontal and vertical directions, respectively; u_1 and u_2 are the corresponding mean velocity components; $\overline{u_i' u_j'}$ is the Reynolds stress component where u_i' denotes the fluctuating part of the velocity; P is the dynamic pressure; and ρ is the density of the fluid.

The Reynolds stress component, $\overline{u_i' u_j'}$, is expressed in terms of a turbulent viscosity v_T and the mean flow gradients using the Boussinesq approximation,

$$-\overline{u_i' u_j'} = v_T\left(\frac{\partial u_i}{\partial x_j} + \frac{\partial u_j}{\partial x_i}\right) - \frac{2}{3}k\delta_{ij} \tag{3}$$

where k is the turbulent kinetic energy and δ_{ij} is the kronecker delta function.

A standard high Reynolds number k-ε turbulence model (see e.g. Launder and Spalding (1972); Rodi (1993)) is used in the present study. This model has been applied previously on vortex-shedding flow by Majumdar and Rodi (1985). The k and ε equations are given by:

$$\frac{\partial k}{\partial t} + u_j \frac{\partial k}{\partial x_j} = \frac{\partial}{\partial x_j}\left(\frac{v_T}{\sigma_k}\frac{\partial k}{\partial x_j}\right) + v_T\left(\frac{\partial u_i}{\partial x_j} + \frac{\partial u_j}{\partial x_i}\right)\frac{\partial u_i}{\partial x_j} - \varepsilon \tag{4}$$

$$\frac{\partial \varepsilon}{\partial t} + u_j \frac{\partial \varepsilon}{\partial x_j} = \frac{\partial}{\partial x_j}\left(\frac{v_T}{\sigma_\varepsilon}\frac{\partial \varepsilon}{\partial x_j}\right) + C_1\frac{\varepsilon}{k}v_T\left(\frac{\partial u_i}{\partial x_j} + \frac{\partial u_j}{\partial x_i}\right)\frac{\partial u_i}{\partial x_j} - C_2\frac{\varepsilon^2}{k} \tag{5}$$

where $v_T = C_\mu \frac{k^2}{\varepsilon}$. The following standard model coefficients have been adopted: ($C_1 = 1.44$, $C_2 = 1.92$, $C_\mu = 0.09$, $\sigma_k = 1.0$, $\sigma_\varepsilon = 1.3$).

2.2. *Numerical solution procedure, computational domain and boundary conditions*

The Reynolds-averaged equations for conservation of mass and momentum, in conjunction with a standard high Reynolds number k-ε model, are solved by using a Galerkin finite element method. A Segregated Implicit Projection (SIP) solution algorithm proposed by Utnes (2008) is used for the time-step solution. Here this numerical method is 1$^{\text{st}}$ order in time and 2$^{\text{nd}}$ order in spatial discretization. A detailed description of the method is given by Utnes (2008).

The geometric size of the rectangular computational domain and the boundary conditions imposed for all simulations are shown in Fig. 1. The size of the whole computational domain is 27D × 14D with the cylinder in the centre of the vertical plane. The upper and lower boundaries are located at a distance 7D from the centre of the cylinder; this ensures that these boundaries have no effect on the flow around the cylinder. The flow inlet is located 7D upstream from the centre of the cylinder, and the flow outlet is located 20D downstream from the centre of the cylinder. These distances are sufficient to eliminate the far field effects on the flow upstream and downstream of the cylinder. The boundary conditions used for the numerical simulations are as follows:

(i) Uniform flow is specified at the inlet with $u_1 = U_\infty$, $u_2 = 0$. The free stream inlet turbulence values for kinetic energy ($k = (3/2)(I_u U_\infty)^2$) and turbulent dissipation ($\varepsilon = (C_\mu k^{3/2})/(0.1L)$), proposed by Tutar and Holdø (2001), have been imposed based on a turbulent intensity ($I_u = u_1'/U_\infty$) of 0.8% and a non-dimensional turbulent length scale (L/D) of 0.0045.

(ii) Along the outflow boundary, u_1, u_2, k and ε are specified as free boundary conditions in a finite element context. This means that a traction-free velocity-pressure boundary condition is applied for u_1, u_2 and P (see Gresho and Sani (1999) and Utnes (1988) for details), while the flux is set equal to zero for k and ε. Along the upper and lower boundaries, u_1, k and ε are free, while u_2 is set equal to zero.

52
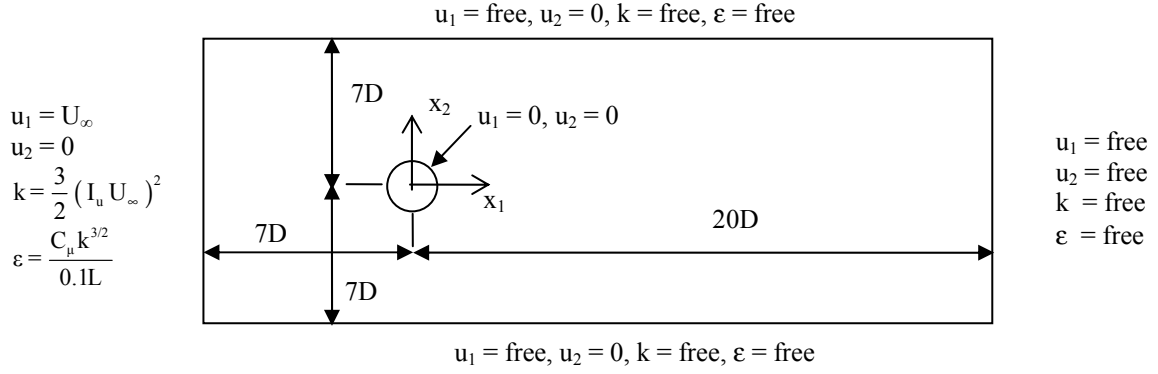
Fig. 1. The size of the computational domain and the imposed boundary conditions.

(iii)   No-slip condition is applied on the cylinder surface with $u_1 = u_2 = 0$.

(iv)   Standard near-wall conditions are applied for k and ε near the cylinder wall (see e.g. Rodi (1993)) as

$$k = \frac{u_*^2}{\sqrt{C_\mu}} \quad , \quad \varepsilon = C_\mu^{\frac{3}{4}} \frac{k^{\frac{3}{2}}}{\kappa h_p} \tag{6}$$

where h_p is the radial distance between the first node and the wall, $\kappa = 0.41$ is the von Karman constant, and u_* is the wall friction velocity obtained from the logarithmic (log) law. It is well known that the log law

$$u^+ = \frac{1}{\kappa} \ln \left(9 \cdot \delta^+ \right) \tag{7}$$

is applicable for $\delta^+ \geq 30$, where $\delta^+ = h_p u_* / \nu$, $u^+ = u_{tan}/u_*$, and u_{tan} = tangential velocity to the wall. In the viscous sublayer

$$u^+ = \delta^+ \qquad \text{for} \qquad \delta^+ \leq 5 \tag{8}$$

It is not possible to know δ^+ at the first node normal to the cylinder wall a priori. Therefore the wall law is given by the log law for $\delta^+ \geq 30$, by $u^+ = \delta^+$ for $\delta^+ \leq 5$, and by a weighted average (linear interpolation) of these two wall laws in the buffer zone, i.e. $5 < \delta^+ < 30$ (see e.g. Davies (1972)):

$$u^+ = \cfrac{1}{\left(\cfrac{\kappa w}{\ln\left(9 \cdot \delta^+\right)}\right) + \left(\cfrac{1-w}{\delta^+}\right)} \quad \text{for} \quad 5 < \delta^+ < 30 \qquad (9)$$

where $w = (\delta^+ - 5)/25$. One should note that this blending method is sometimes sensitive to the grid resolution; hence, trial and error of grid adjustment is required in order to avoid non-realistic results.

Stretching of the mesh is performed to achieve a fine resolution of the region close to the cylinder surface. A grid convergence study has been performed for the flow at Re $= 3.6 \times 10^6$ with 4 sets of meshes as shown in Table 1. Fig. 2 shows that the computations with the meshes M3 (48706 nodes) and M4 (67034 nodes) yield insignificant changes of results in terms of time-averaged drag coefficient (C_D) and root-mean-square value of fluctuating lift coefficient (C_{Lrms}), i.e. the same result for C_D up to the fourth decimal and 0.13% difference in C_{Lrms}. Therefore, mesh M3 is considered to give sufficient grid resolution. Fig. 3 shows the computational mesh M3. For mesh M3, the radial distance to the first node from the cylinder surface is 0.044% of the cylinder diameter. A non-dimensional time step (Δt) of $0.001D/U_\infty$ is used; and the simulation is run for 250 non-dimensional time units (D/U_∞). δ^+ varies from 0 to 87 depending on the local skin friction, as shown in Fig. 4. Furthermore, in order to ensure the time step convergence, the flow has also been computed with a reduced Δt of $0.0005D/U_\infty$ using mesh M3. The deviation of C_D and C_{Lrms} from the simulation with $\Delta t = 0.001D/U_\infty$, which are 0.04% for C_D and 0.39% for C_{Lrms}. Hence it is concluded that Mesh M3 with $\Delta t = 0.001D/U_\infty$ gives a sufficient numerical accuracy. This is also used for the present computations at $Re = 1 \times 10^6$ and 2×10^6.

Table 1. Details of the finite element mesh used and the results of grid convergence study.

Mesh	Nodes	Elements	Nc	Nt	C_D	C_{Lrms}	St
M1	27874	27512	304	76	0.4594	0.0806	0.2823
M2	38766	38340	360	90	0.4586	0.0767	0.2899
M3	48706	47600	400	100	0.4573	0.0766	0.3052
M4	67034	66480	480	120	0.4573	0.0765	0.3052

Note: Nc = Number of nodes in the cylinder circumferential direction; and Nt = Number of nodes in cylinder wall normal direction.
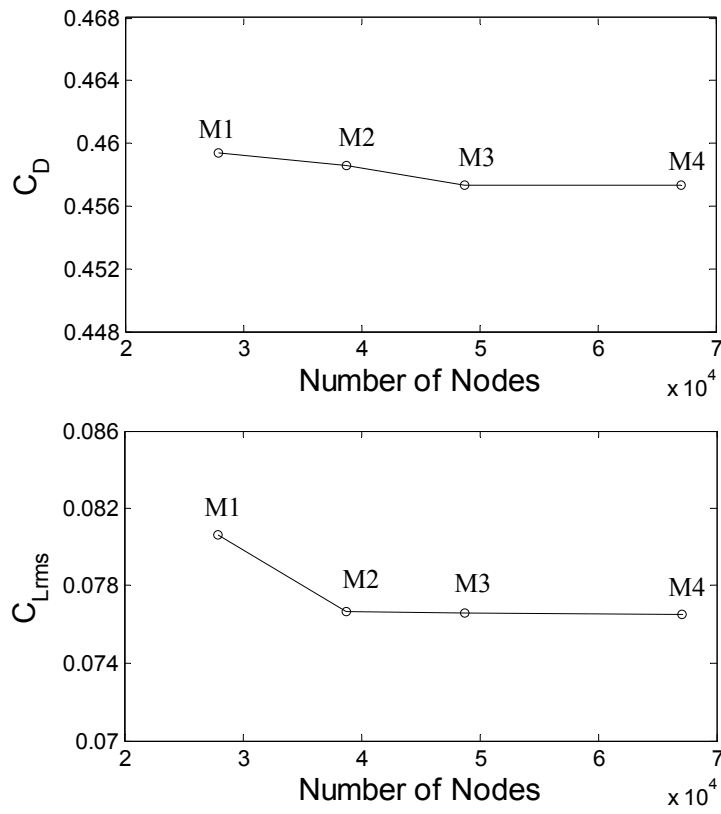
Fig. 2. Grid convergence study for C_D and C_{Lrms} with respect to the number of nodes in the computational domain, see also Table 1.
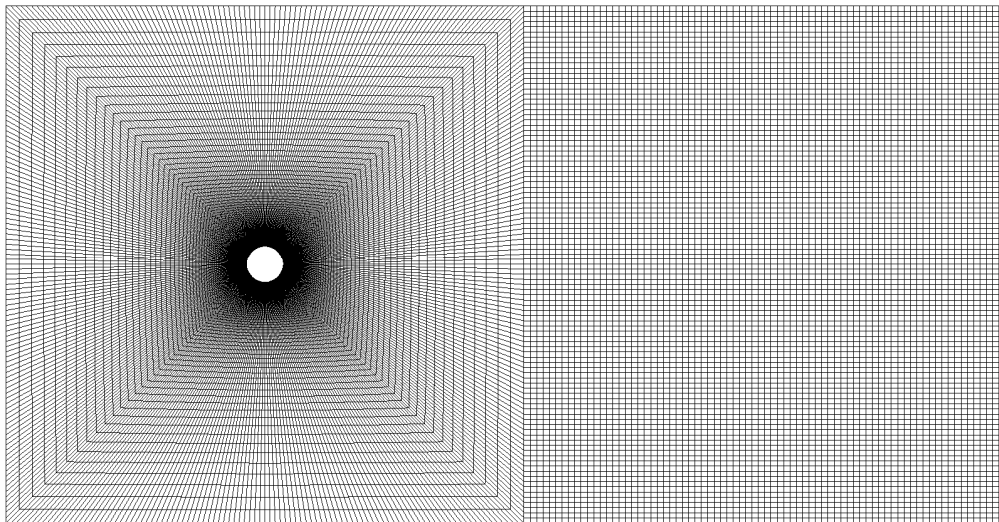
(a)

Fig. 3. The computational mesh M3 with 48706 nodes and 47600 elements.
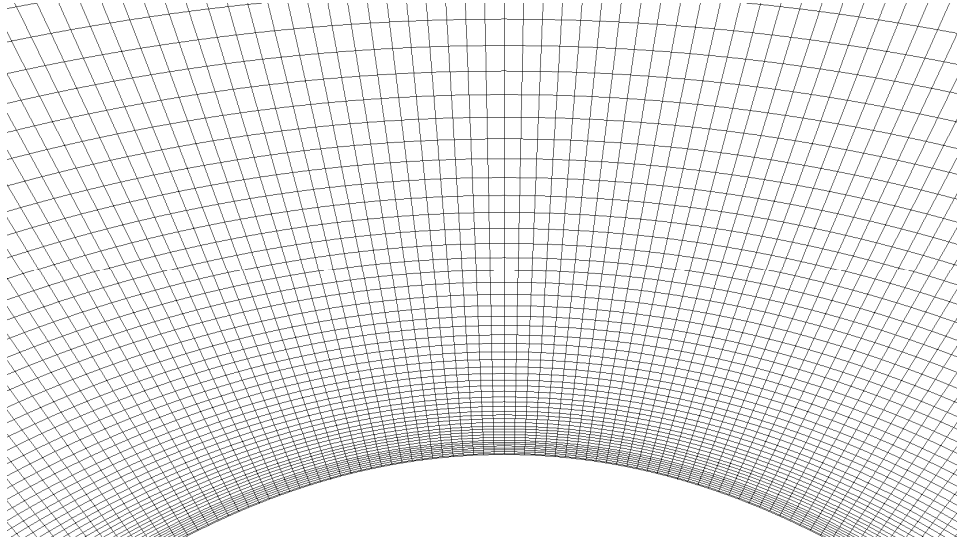
(b)

Fig. 3. The computational mesh M3 with 48706 nodes and 47600 elements.
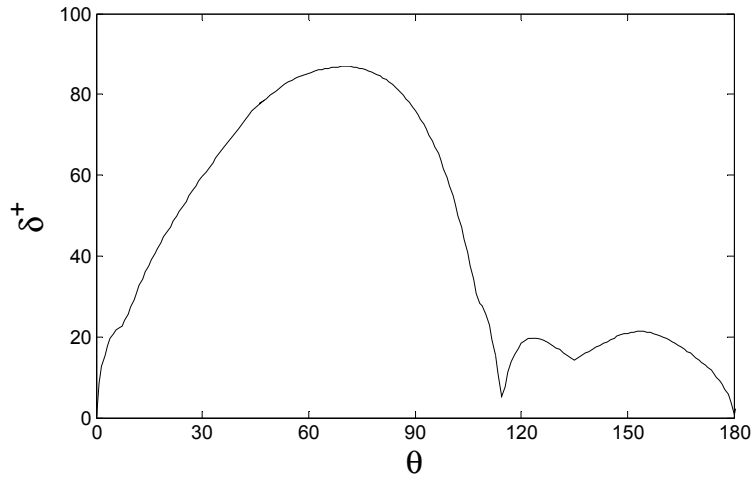
Fig. 4. The variation of δ^+ around the cylinder. θ is the peripheral angle of the cylinder measured clockwise from the stagnation point.

3.   Results and Discussion

The computations have been performed at $Re = 1 \times 10^6$, 2×10^6 and 3.6×10^6, covering the supercritical to upper-transition flow regimes. The objective is to evaluate the applicability of using a standard high Reynolds number $k\text{-}\varepsilon$ model for engineering computations of flow

around a smooth circular cylinder in the supercritical and the upper-transition flow regimes. Therefore, essential hydrodynamic quantities, such as C_D, C_{Lrms} and St, have been predicted and compared with published experimental data (Fung (1960); Roshko (1961); Achenbach (1968); Jones (1968); James et al. (1980), Schewe (1983); Zdravkovich (1997)) and numerical results (Catalano et al. (2003); Singh and Mittal (2005)). Here $St = fD/U_\infty$ is the Strouhal number, where f is the vortex-shedding frequency. The comparisons are shown in Table 2 for $Re = 1\times10^6$ and 3.6×10^6. Generally the present predictions are within the range of the experimental data and in reasonable agreement with the published numerical results. For $Re = 1\times10^6$, the predicted C_D is 0.5174; and it lies between those predicted by 3D LES: $C_D = 0.31$ (Catalano et al. 2003) and 2D LES: $C_D = 0.591$ (Singh and Mittal 2005). Fig. 5 shows the values of C_D as a function of Reynolds number. Small discrepancies between the present results and the URANS results reported by Catalano et al. (2003) are seen. The present computed C_D decreases slightly as the Reynolds number increases, whereas the URANS results reported by Catalano et al. (2003) exhibit a slight increase of C_D. This might be caused by different implementations of the wall function. The numerical results (except those by Singh and Mittal (2005)) exhibit a smaller variation with Reynolds number for $Re > 10^6$ than the experimental data that generally shows an obvious increase of C_D in the supercritical flow regime. However, it appears that URANS with the standard high Reynolds number k-ε model is able to give satisfactory predictions of commonly-used hydrodynamic quantities in engineering design (i.e. C_D, C_{Lrms} and St) in the supercritical and the upper-transition flow regimes, i.e. $Re > 10^6$.

Table 2. Numerical and experimental results at $Re = 1\times10^6$ and 3.6×10^6.

Re		C_D	C_{Lrms}	St
1×10^6 (supercritical regime)	Present simulation	0.5174	0.0901	0.2823
	Catalano et al. (2003) 3D LES	0.31	-	0.35
	Catalano et al. (2003) URANS	0.41	-	-
	Singh and Mittal (2005) 2D LES	0.591	-	-
	Published experimental data	0.21-0.63	0.03-0.15	0.18-0.50
3.6×10^6 (Upper-transition regime)	Present simulation	0.4573	0.0766	0.3052
	Catalano et al.(2003) URANS $Re = 4\times10^6$	0.46	-	-
	Published experimental data	0.36-0.75	0.06-0.14	0.17-0.29
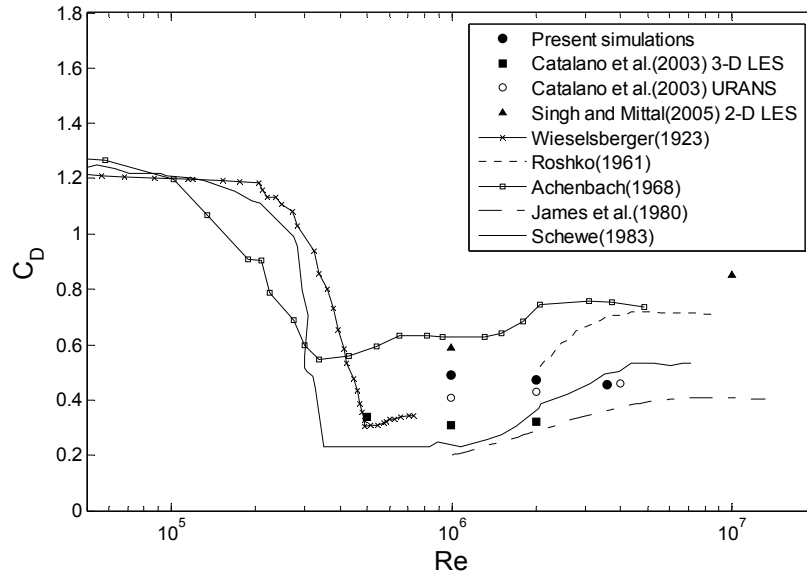
Fig. 5. Time-averaged drag coefficient as a function of Reynolds number.

Relf (1921) and Wieselsberger (1923) inferred that the periodic vortex shedding should cease due to the chaotic state of free shear layers when the flow becomes turbulent upstream of the separation. This was indeed noted by Cincotta et al. (1966), Loiseau and Szechenyi (1972) and Schewe (1983) in the supercritical regime. Roshko (1961), Cincotta et al. (1966) and Schewe (1983) measured the frequency of vortex-shedding beyond the supercritical regime, i.e. $Re = 3.5 \times 10^6$ to 6×10^6. In this range of Reynolds number, they discovered a narrow spectral peak of vortex-shedding frequency, showing that the periodic vortex-shedding motion reappeared. Fig. 6 shows an example of contours of the non-dimensional vorticity magnitude ($\omega D/U_\infty$) for $Re = 3.6 \times 10^6$ at the non-dimensional time of 250 D/U_∞, predicted by the present numerical model. It appears that the present model is able to produce the vortex-shedding motion with a periodic vortex street qualitatively.
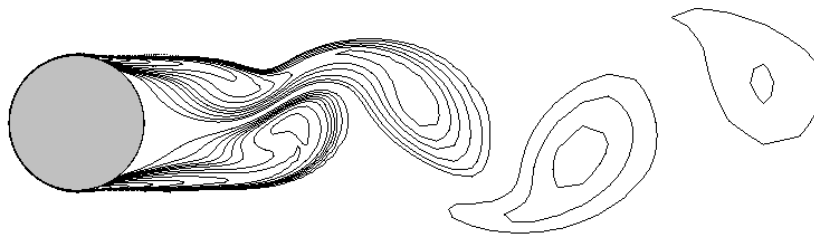
Fig. 6. Instantaneous non-dimensional vorticity contour of flow around a smooth circular cylinder for $Re = 3.6 \times 10^6$ at the non-dimensional time of 250 D/U_∞. 40 contour levels from $\omega D/U_\infty = -520$ to $\omega D/U_\infty = 520$ are plotted.

Fig. 7 shows the predicted mean pressure distribution ($C_p = [p_c-p_{c\infty}]/[0.5\rho U_\infty^2]$) at $Re = 1\times10^6$ compared with the experimental data ($Re = 1.2\times10^6$) from Warschauer and Leene (1971), the 3D LES results and the URANS results by Catalano et al. (2003), and the 2D LES results by Singh and Mittal (2005) . Here p_c is the static pressure at the peripherical angle of the cylinder, θ, measured clockwise from the stagnation point; and $p_{c\infty}$ is the static pressure of the flow at infinity. The present URANS results qualitatively capture the trend of the experimental data and the LES results reported by both Catalano et al. (2003) and Singh and Mittal (2005), but the discrepancy with the experimental data is larger. The discrepancy between the present URANS results and the URANS results by Catalano et al. (2003) might be due to the different implementations of the wall function. The present URANS results, the URANS results by Catalano et al. (2003) and the 2D LES results by Singh and Mittal (2005) show a moderate over-prediction of the negative C_p at the back half of the cylinder. It is well known that the flow in the separation point region has strong pressure gradients, and that it is very difficult to model accurately. Fig. 7 also shows that the 3D LES results by Catalano et al. (2003) agree well with the measurements around the entire cylinder surface. This may show the limitation of using 2D URANS models for turbulent flow, as effects from the spanwise secondary flow are not considered in the 2D simulation (see e.g. Mittal and Balachandar (1995)). It is interesting to observe that for the higher Reynolds number flow at $Re = 3.6\times10^6$, the predicted C_p in Fig. 8 shows a better agreement with the experimental data from Achenbach (1968) than for $Re = 1\times10^6$ shown in Fig. 7. The reason might be that at $Re = 3.6\times10^6$ the boundary layer ahead of the separation point at one side of the cylinder is completely turbulent, while at $Re = 1\times10^6$ the boundary layers at both sides of the cylinder are partly laminar and partly turbulent; see e.g. Sumer and Fredsøe (1997, Fig. 1.1) for a detailed description of the flow around a circular cylinder in steady flow. Hence the URANS with the standard high Reynolds number k-ε model, for which a fully developed turbulent flow is assumed, is expected to be more capable of predicting the flow at $Re = 3.6\times10^6$ (upper-transition flow regime) than at $Re = 1\times10^6$ (supercritical flow regime). From Fig. 8 an approximate 30% under-prediction of the negative C_p is observed at the back half of the cylinder due to the difficulty in modeling the strong pressure gradient accurately.

The predictions of the skin friction coefficient ($C_f = \tau/[0.5\rho U_\infty^2]$, where τ is the tangential wall shear stress) are shown in Fig. 9 for $Re = 1\times10^6$, 2×10^6 and 3.6×10^6. In the same figure, the 3D LES results by Catalano et al. (2003), obtained at $Re = 0.5\times10^6$, 1×10^6 and 2×10^6, are plotted for comparison. The present predictions show a similar shape of the C_f distribution around the cylinder surface as the 3D LES results; the maximum magnitude of C_f decreases as the Reynolds number increases, which agrees qualitatively with the 3D LES results by Catalano et al. (2003). It is observed that the present predictions yield a lower maximum magnitude of C_f than the 3D LES results for the same Reynolds number. Further discussion of this discrepancy of results is given in the next paragraph.
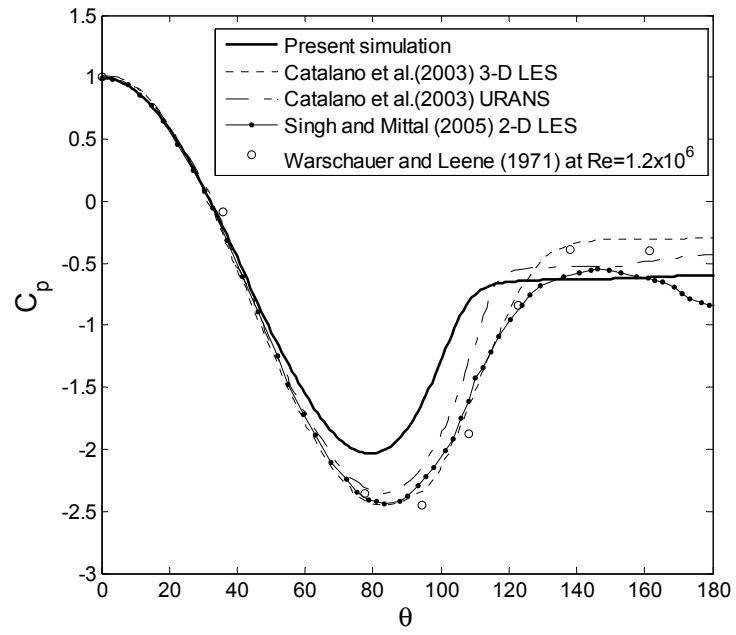
Fig. 7. Mean pressure distribution on the cylinder at $Re = 1 \times 10^6$.
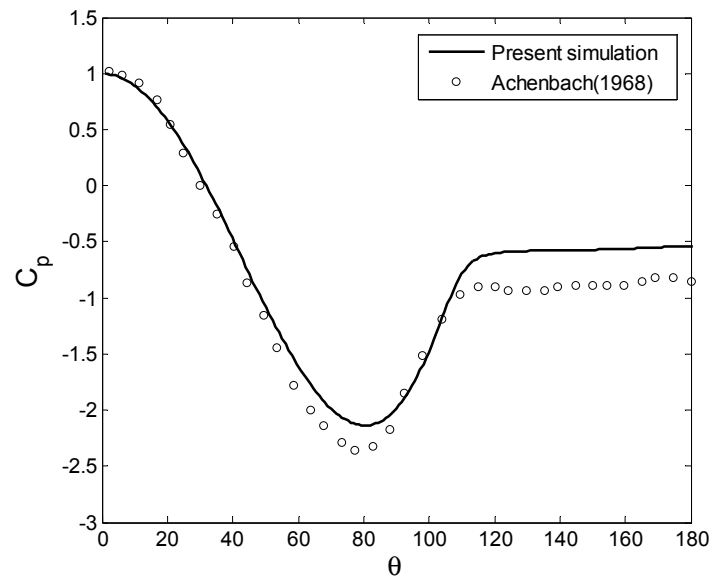
Fig. 8. Mean pressure distribution on the cylinder at $Re = 3.6 \times 10^6$.
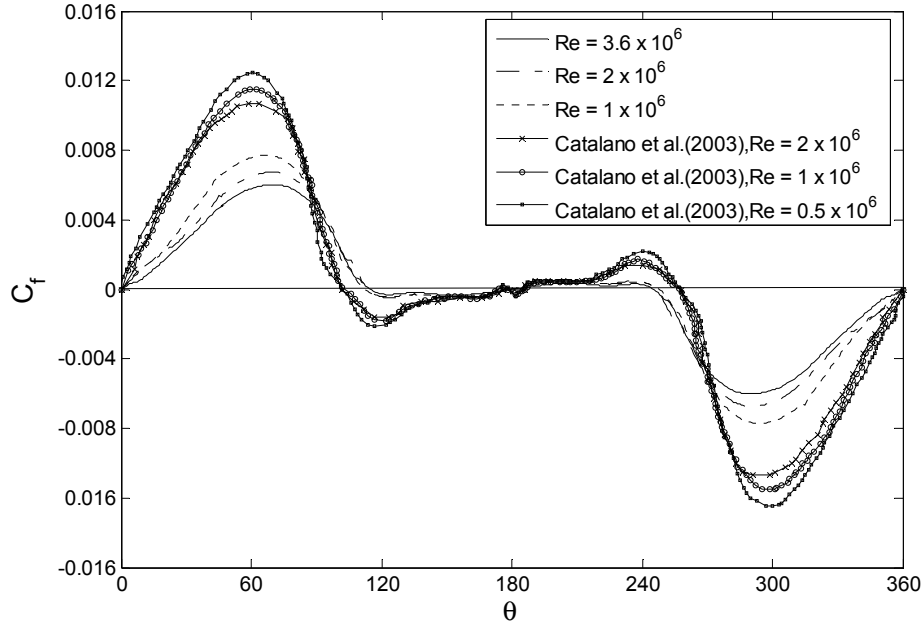
Fig. 9. Comparison of skin friction distribution around the cylinder between the present computations and the 3D LES simulations by Catalano et al. (2003).

Fig. 10 shows the predicted C_f at $Re = 2\times10^6$ and 3.6×10^6 together with the 3D LES results at $Re = 2\times10^6$ and the experimental data by Achenbach (1968) at $Re = 3.6\times10^6$. Even though the 3D LES results are not for the same Reynolds number as the experimental data, Fig. 9 shows that the predicted C_f distributions do not change significantly with Reynolds number neither for the present simulations nor for the 3D LES simulations by Catalano et al. (2003). Therefore, the comparison shown in Fig. 10 seems reasonable. Based on these observations, it appears that the C_f distribution obtained from the present simulations agrees better with the experimental data than those by Catalano et al. (2003). However, Catalano et al. (2003) commented that their grid resolution was not sufficient in their work when they compared their results with the experimental data in the high Reynolds number regimes. This might explain that the present predictions show a better agreement with the experimental data. It is also noted that both the present model and the 3D LES model by Catalano et al. (2003) over-predict C_f on the front half of the cylinder (i.e. before the separation) compared with the experimental data. The C_f distribution on the back half of the cylinder is generally under-predicted by the present model compared with the experimental data. Furthermore, it is also observed that the predicted time-averaged separation angle (θ_s) at $Re = 3.6\times10^6$ is 114°, which is in good agreement with the measured of 115° reported by Achenbach (1968).

Overall, the URANS with the standard high Reynolds number k-ε model appears to give satisfactory predictions of the flow around a 2D smooth circular cylinder in the range $Re = 1\times10^6$ to 3.6×10^6. This is based on comparing the results with the published experimental

data and numerical results. The results of the present study are encouraging for CFD-based engineering applications, e.g. modeling of vortex-induced vibration responses of marine pipelines and risers together with a strip theory approach to obtain 3D hydrodynamic loads, because the URANS with the standard high Reynolds number $k\text{-}\varepsilon$ model requires less computational effort compared with LES and DNS for $Re > 1\times10^6$ (beyond the supercritical flow regime). Furthermore, its accessibility is high as it is available in most of the commercial CFD software packages.
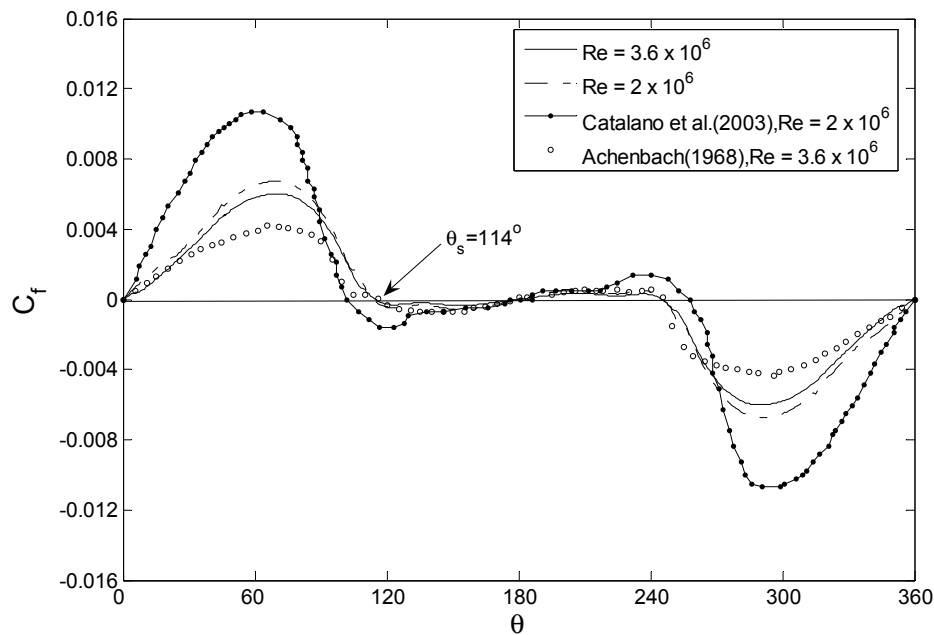
Fig. 10. Distribution of the skin friction coefficient on the cylinder in the upper-transition regime.

4.   Conclusions

The flow around a 2D smooth circular cylinder has been computed for very high Reynolds numbers, covering the supercritical to upper-transition flow regime, using the 2D URANS in conjunction with a standard high Reynolds number $k\text{-}\varepsilon$ model. Although it has been shown earlier that this model gives less accurate predictions of flow with strong anisotropic turbulence, the present study shows that for engineering design purposes it gives satisfactory qualitative agreements with the published experimental data and numerical results in the supercritical and upper-transition flow regimes, i.e. $Re > 10^6$. However, more experimental data are required beyond the supercritical flow regime, especially velocity and Reynolds stress profile measurements, in order to perform a more detailed validation study of the

model. In the meantime the present study should be reliable and useful as an engineering assessment tool for design work.

Acknowledgements

References

Achenbach, E. (1968). Distribution of local pressure and skin friction around a circular cylinder in cross-flow up to Re $=5\times10^6$. *J. Fluid Mech.,* 34 (4), 625-639.

Cantwell, B. and Coles, D. (1983). An experimental study of entrainment and transport in the turbulent near wake of a circular cylinder. *J. Fluid Mech*., 139, 321-374.

Catalano, P., Wang, M., Iaccarino, G. and Moin, P. (2003). Numerical simulation of the flow around a circular cylinder at high Reynolds numbers. *Int. J. Heat Fluid Flow*, 24, 463-469.

Chaplin, J.R., Bearman, P.W., Cheng, Y., Fontaine, E., Graham, J.M.R., Herfjord, K., Huera Huarte, F.J., Isherwood, M., Lambrakos, K., Larsen, C.M., Meneghini, J.R., Moe, G., Pattenden, R.J., Triantafyllou, M.S. and Willden, R.H.J. (2005). Blind predictions of laboratory measurements of vortex-induced vibrations of a tension riser. *J. Fluids and Structures*, 21, 25-40.

Cincotta, T.T., Jones, G.W. and Walker, W.W. (1966). Experimental investigation of wind induced oscillation effects on cylinders in two dimensional flow at high Reynolds numbers. National Aeronautics and Space Administration, NASA TMX 57779, paper 20.1-20.35.

Davies, J.T. (1972). *Turbulence Phenomena*, Academic Press, London.

Franke, R., Rodi, W. and Schönung, B. (1989). Analysis of experimental vortex shedding data with respect to turbulence modeling. *Proc. 7th Turbulent Shear Flow Symposium*, Stanford, USA, 24.4.1-24.4.5.

Fung, Y.C. (1960). Fluctuating lift and drag acting on a cylinder in a flow at supercritical Reynolds numbers. *J. Aeronautical Sciences*, 27, 801-814.

Gresho, P.M. and Sani, R.L. (1999). *Incompressible flow and the finite element method,* John Wiley & Sons Ltd, West Sussex, England.

James, W.D., Paris, S.W. and Malcolm, G.V. (1980). Study of viscous cross flow effects on circular cylinders at high Reynolds numbers. *AIAA Journal*, 18, 1066-1072.

Jones, G.W. (1968). Unsteady lift forces generated by vortex shedding about large stationary and oscillating cylinders at high Reynolds numbers. *ASME Proc. Sym. on Unsteady Flow,* Philadelphia, 68-FE-36.

Launder, B.E. and Spalding, D.B. (1972). *Mathematical models of turbulence,* Academic Press, London.

Loiseau, H. and Szechenyi, E. (1972). Experimental analysis of lift on a fixed cylinder subjected to cross flow at high Reynolds numbers. *La Recherche Aerospatiale,* No 5, 279-291.

Majumdar, S. and Rodi, W. (1985). Numerical calculation of turbulent flow past circular cylinder. *Proc. 7th Turbulent Shear Flow Symposium*, Stanford, USA, 3.13-3.25.

Mittal, R. and Balachandar, S. (1995). Effect of three-dimensionality on the lift and drag of nominally two-dimesional cylinders. *Phys. Fluids*, 7, 1841-1865.

Relf, E.F. (1921). On the sound emitted by wires of circular cross section when exposed to an air current. *Philosophical Magazine*, 6th series, 42, 173-176.

Rodi, W. (1993). *Turbulence Models and Their Application in Hydraulics. A state-of-the-art review.* IAHR Monograph Series*, 3rd Ed.,* A.A. Balkema, Rotterdam, Netherlands.

Roshko, A. (1961). Experiments of the flow past a circular cylinder at very high Reynolds number. *J. Fluid Mech.*, 10, 345-356.

Schewe, G. (1983). On the force fluctuations acting on a circular cylinder in cross flow from subcritical up to transcritical Reynolds numbers. *J. Fluid Mech.*, 133, 265-285.

Schulz, K.W. and Meling, T.S. (2004). Multi-strip numerical analysis for flexible riser response. *Proc. 23rd Int. Conf. on Offshore Mech. and Arctic Engineering*, OMAE2004-51186, Vancouver, Canada,

Singh, S.P. and Mittal, S. (2005). Flow past a cylinder: shear layer instability and drag crisis. *Int. J. Numer. Meth. Fluids*, 47, 75-98.

Sumer, B.M. and Fredsøe, J. (1997). *Hydrodynamics around Cylindrical Structures: Advanced series on ocean engineering- Vol. 12*, World Scientific, Singapore.

Tutar, M. and Holdø, A.E. (2001). Computational modeling of flow around a circular cylinder in sub-critical flow regime with various turbulence models. *Int. J. Numer. Meth. Fluids*, 35, 763-784.

Utnes, T. (1988). Two-equation (k, ε) turbulence computations by the use of a finite element model. *Int. J. Numer. Meth. Fluids*, 8, 965-975.

Utnes, T. (2008). A segregated implicit pressure projection method for incompressible flows. *J. Comp. Physics*, 227, 2198-2211.

Warschauer, K.A. and Leene, J.A. (1971). Experiments on mean and fluctuating pressures of

circular cylinders at cross flow at very high Reynolds numbers. *Proc. Int. Conf. on Wind Effects on Buildings and Structures*, Tokyo, Japan, 305-315.

Wieselsberger, C. (1923). Results of aerodynamic research at Göttingen(in German). *II Lieferung*.

Zdravkovich, M.M. (1997). *Flow around Circular Cylinders, Vol. 1: Fundamentals*, Oxford University Press, New York.

Chapter 7

Numerical Simulation of Flow around a Marine Pipeline Close to the Seabed

Muk Chen Ong[1], Torbjørn Utnes[2], Lars Erik Holmedal[1], Dag Myrhaug[1] and Bjørnar Pettersen[1]

[1] Department of Marine Technology,
  Norwegian University of Science and Technology, NO-7491 Trondheim, Norway.

[2] SINTEF IKT Applied Mathematics, NO-7465 Trondheim, Norway.

Abstract[#]

The flows, at Reynolds number (*Re,* based on the free stream velocity and cylinder diameter) ranging from 1×10^4 to 4.8×10^4 in the subcritical flow regime, around a two-dimensional (2D) circular cylinder close to a non-movable flat bed have been investigated numerically using 2D Unsteady Reynolds-Averaged Navier Stokes (URANS) equations with a standard high Reynolds number k-ε model. The results are compared with published experimental data and numerical results by considering effects of gap ratios, incident boundary layer thicknesses, Reynolds numbers and roughness of the flat bed. Studies on the suppression and the development of the vortex shedding are performed and reasonable flow mechanisms are observed. Under-predictions of the essential hydrodynamic quantities of the cylinder are seen due to the limitation of the turbulence model. The mean pressure distribution along the flat bed is predicted reasonably well as compared with the published experimental and numerical results.

Keywords: Numerical models; Marine pipeline; Flat bed; High Reynolds number; Circular cylinder.

Chapter 8

Numerical Simulation of Flow around a Circular Cylinder Close to a Flat Seabed at High Reynolds Numbers

Muk Chen Ong[a], Torbjørn Utnes[b], Lars Erik Holmedal[a], Dag Myrhaug[a] and Bjørnar Pettersen[a]

[a] Department of Marine Technology,
 Norwegian University of Science and Technology, NO-7491 Trondheim, Norway.

[b] SINTEF IKT Applied Mathematics, NO-7465 Trondheim, Norway.

Abstract[#]

High Reynolds number flows around a circular cylinder close to a flat seabed have been computed using a two-dimensional standard high Reynolds number k-ε turbulence model. The effects of gap to diameter ratio, Reynolds number and flat seabed roughness for a given boundary layer thickness of the inlet flow upstream of the cylinder have been investigated. Hydrodynamic quantities and the resulting bedload transport have been predicted, and the vortex shedding mechanisms have been investigated. Predictions of hydrodynamic quantities around a cylinder located far away from the bed (so that the effect of the bed is negligible) are in satisfactory agreement with published experimental data and numerical results obtained for the flow around an isolated cylinder. Results for lower Reynolds number flows have also been computed for comparison with the high Reynolds number flow results. Overall it appears that the present approach is suitable for design purposes at high Reynolds numbers which are present near the seabed in the real ocean.

Keywords: Numerical models; Flat bed; High Reynolds number; Circular cylinder; Turbulent flow.

---

1.   Introduction

Marine pipelines and risers are widely used for transporting oil and gas from offshore fields. They are often subject to high Reynolds numbers flow with typical values of $O(10^4) - O(10^7)$, covering subcritical ($300 < Re < 3 \times 10^5$) to trancritical ($Re > 4 \times 10^6$) flow regimes. Here $Re = U_\infty D / v$ where D is the cylinder diameter; U_∞ is the free stream velocity; and v is the kinematic viscosity. Detailed information on the flow around these cylindrical marine structures is essential for engineering applications, e.g. predictions of scour and structural response. The hydrodynamic characteristics of steady flow around a horizontal smooth circular cylinder near a fixed flat bed represent an idealized situation of a pipeline or a riser near the seabed. The proximity of the cylinder to the seabed affects the flows around the cylinder and along the bed. Consequently it alters the magnitude and direction of forces exerted on the cylinder. The flow mechanism is complex and depends on governing parameters such as the Reynolds number (Re), the gap to diameter ratio (G/D) and the incident boundary layer thickness to diameter ratio (δ/D). Here G is the minimum distance between the bottom of the cylinder and the seabed, and δ is the boundary layer thickness of the inlet flow upstream of the cylinder (see Fig. 1 for definitions).

Several experimental studies have been carried out to investigate flow cases at high Reynolds numbers which ranges from $O(10^4)$ to $O(10^5)$ in the subcritical flow regime (see e.g. Bearman and Zdravkovich (1978), Zdravkovich (1985), Jensen et al. (1990), Taniguchi and Miyakoshi (1990), Lei et al. (1999), Wang and Tan (2008)). Bearman and Zdravkovich (1978) investigated the influence of G/D on the vortex shedding and its spectral behaviour with an upstream flow of $\delta/D = 0.8$ at Re ranging from 2.5×10^4 to 4.8×10^4. They measured the distribution of mean pressure around the cylinder and along the bed at $Re = 4.8 \times 10^4$, and showed that the vortex shedding motion behind a circular cylinder close to a wall is suppressed at $G/D < 0.3$. Here the G/D corresponding to the onset of vortex shedding is defined as the critical ratio, G/D_c. Zdravkovich (1985) measured the drag and lift force on circular cylinders near a bed for $4.8 \times 10^4 \leq Re \leq 3 \times 10^5$ and $0.12 < \delta/D < 0.97$. He found that the lift coefficient is governed by G/D, while the drag coefficient is dominated by G/δ. Lei et al. (1999) studied the flow around a smooth circular cylinder immersed in different boundary layer thicknesses ($\delta/D = 0.14 - 2.89$) at Re ranging from 1.31×10^4 to 1.45×10^4. Their experimental results showed that both drag and lift coefficients strongly depend on G/D, and are affected by δ/D. They found that the variation of the root-mean-square (rms) fluctuating lift coefficient (C_{Lrms}) can be used to determine the suppression and onset of the vortex shedding. Their observations also showed that the vortex shedding is suppressed at G/D of 0.2-0.3, depending on different δ/D. Taniguchi and Miyakoshi (1990) studied fluctuations of lift and drag forces on the cylinder and the bed interference effects in terms of G/D and δ/D at $Re = 9.4 \times 10^4$. They found that the fluctuating lift force increases sharply and that the regular vortex shedding starts to form beyond G/D_c. Jensen et al. (1990) carried out experiments in

an open water flume to study the flow around and forces on a pipeline near a fixed scoured bed in steady current. They presented the time-averaged drag coefficient (C_D), the time-averaged lift coefficient (C_L), C_{Lrms} and the Strouhal number ($St = fD/U_\infty$) for the case of a cylinder over a flat bed at $Re = 1 \times 10^4$ with $\delta/D = 2$; here f is the vortex shedding frequency. Wang and Tan (2008) studied the near-wake flow characteristics of a circular cylinder close to a flat bed for $Re = 1.2 \times 10^4$ and $\delta/D = 0.4$. Their results showed that instantaneous flow fields depend strongly on G/D, and that the flow is characterized by a periodic vortex shedding for $G/D \geq 0.3$.

Few numerical studies have been performed for flows around a circular cylinder near a flat bed at $Re > 10^4$. Brørs (1999) and Zhao et al. (2007) applied a standard high Reynolds number k-ε model at $Re = 1.5 \times 10^4$ and a k-ω model at $Re = 2 \times 10^4$, respectively. Their results yielded a good qualitative agreement with published experimental data. However, detailed comparisons with experimental results for $G/D < 0.4$ are not made. Recently Ong et al. (2008) applied the standard high Reynolds number k-ε model at $Re = 1 \times 10^4$ - 4.8×10^4 with $\delta/D = 0.14$ - 2. Comparisons of numerical results with published experimental data were provided for $G/D < 0.4$. They found that under-predictions of the essential hydrodynamic quantities (such as C_D, C_L, St, C_{Lrms} and C_p) were observed in the subcritical flow regime due to the well-known limited capacity of the k-ε model (and similar two-equation turbulence closures) to capture the vortex shedding correctly. Here C_p is the mean pressure coefficient around the cylinder. There is also a limitation of using two-dimensional (2D) models for three-dimensional (3D) flow, as effects from the spanwise secondary flow are not considered in the 2D simulation (see e.g. Mittal and Balachandar (1995)). However, the mean pressure and the friction velocity along the bed were predicted reasonably well as compared with published experimental and numerical results in the subcritical flow regime. For lower Reynolds number flows, Lei et al. (2000) investigated the suppression of the vortex shedding by solving Navier-Stokes equations for 2D viscous flows (without using any turbulence model) in the Re range 80 - 1000. They showed that G/D_c, at which the vortex shedding is suppressed, depends on Re.

Ong et al. (2009) and Catalano et al. (2003) presented numerical results on flow around an isolated smooth circular cylinder subject to a steady current at Re ranging from 0.5×10^6 to 4×10^6 by using the standard high Reynolds number k-ε model. Overall, their results are in satisfactory agreement with published experimental data. To our knowledge, neither numerical nor experimental studies are available in the open literature for flows around a circular cylinder close to a flat bed beyond the supercritical flow regime ($Re > 1 \times 10^6$).

In the present study, flows at $Re = 3.6 \times 10^6$ and $\delta/D = 0.48$ with two different bed roughnesses ($z_w = 1 \times 10^{-6}$m and 2×10^{-5}m) are investigated numerically by using the 2D Unsteady Reynolds-Averaged Navier-Stokes (URANS) equations with a standard high Reynolds

number k-ε model. Here $z_w = d_{50}/12$ where d_{50} is the median grain size diameter. Furthermore, flows at lower Reynolds numbers, $Re = 1\times10^4$ - 4.8×10^4 and $\delta/D = 0.14 - 2$, have been predicted (see also Ong et al. (2008)). These predictions are included for comparison with the high Reynolds number results. Effects of gap to diameter ratio, Reynolds number, flat seabed roughness for a given boundary layer thickness of the inlet flow upstream of the cylinder are investigated. Hydrodynamic quantities and the resulting bedload sediment transport are predicted. Mechanisms of vortex shedding are also investigated.

2.   Mathematical Formulation

2.1.   Flow model

The equations to be solved are the Reynolds-averaged equations for conservation of mass and momentum, given by

$$\frac{\partial u_i}{\partial x_i} = 0 \tag{1}$$

$$\frac{\partial u_i}{\partial t} + u_j \frac{\partial u_i}{\partial x_j} = -\frac{1}{\rho}\left(\frac{\partial P}{\partial x_i}\right) + v\frac{\partial^2 u_i}{\partial x_j^2} - \frac{\partial \overline{u_i' u_j'}}{\partial x_j} \tag{2}$$

where i, j = 1, 2. Here x_1 and x_2 denote the streamwise and wall-normal directions; u_1 and u_2 are the corresponding mean velocity components; $\overline{u_i' u_j'}$ is the Reynolds stress component; P is the dynamic pressure; and ρ is the density of the fluid.

The Reynolds stress component, $\overline{u_i' u_j'}$, which appears in Eq.(2), is expressed in terms of a turbulent viscosity, v_T, and the mean flow gradients using the Boussinesq approximation,

$$-\overline{u_i' u_j'} = v_T\left(\frac{\partial u_i}{\partial x_j} + \frac{\partial u_j}{\partial x_i}\right) - \frac{2}{3}k\delta_{ij} \tag{3}$$

where k is the turbulent kinetic energy and δ_{ij} is the kronecker delta.

A standard high Reynolds number k-ε turbulence model (see e.g. Launder and Spalding (1972); Rodi (1993)) is used in the present study; the model has been applied previously on vortex shedding flow by Majumdar and Rodi (1985). The k and ε equations are given by:

$$\frac{\partial k}{\partial t} + u_j \frac{\partial k}{\partial x_j} = \frac{\partial}{\partial x_j}\left(\frac{v_T}{\sigma_k}\frac{\partial k}{\partial x_j}\right) + v_T \left(\frac{\partial u_i}{\partial x_j} + \frac{\partial u_j}{\partial x_i}\right)\frac{\partial u_i}{\partial x_j} - \varepsilon \tag{4}$$

$$\frac{\partial \varepsilon}{\partial t} + u_j \frac{\partial \varepsilon}{\partial x_j} = \frac{\partial}{\partial x_j}\left(\frac{v_T}{\sigma_\varepsilon}\frac{\partial \varepsilon}{\partial x_j}\right) + C_1 \frac{\varepsilon}{k} v_T \left(\frac{\partial u_i}{\partial x_j} + \frac{\partial u_j}{\partial x_i}\right)\frac{\partial u_i}{\partial x_j} - C_2 \frac{\varepsilon^2}{k} \tag{5}$$

where ε is the rate of viscous dissipation and $v_T = C_\mu \dfrac{k^2}{\varepsilon}$. The following standard model coefficients have been adopted: ($C_1 = 1.44$, $C_2 = 1.92$, $C_\mu = 0.09$, $\sigma_k = 1.0$, $\sigma_\varepsilon = 1.3$).

2.2. *Numerical solution procedure, computational domain and boundary conditions*

The Reynolds-averaged equations for conservation of mass and momentum, in conjunction with a standard high Reynolds number k-ε model, are solved by using a Galerkin finite element method. A segregated implicit projection solution algorithm proposed by Utnes (2008) is used for the time-step solution. This numerical method is 2nd order both in time and spatial discretization. A detailed description of the method is given in Utnes (2008).

The size of the rectangular computational domain and the boundary conditions imposed for the present simulations are shown in Fig. 1. The size of the whole computational domain is 30D by 10D. The upper boundary is located at a distance varying from 8.5D to 9.4D from the center of the cylinder depending on the corresponding gap to diameter ratio; this ensures that the boundary have no effect on the flow around the cylinder and the flat bed. The flow inlet is located 10D upstream from the center of the cylinder, and the flow outlet is located 20D downstream from the center of the cylinder. These distances are sufficient to eliminate far field effects from the flow upstream and downstream of the cylinder. The boundary conditions used for the numerical simulations are as follows:

(i)   A boundary layer flow is specified at the inlet (see Fig. 1)

$$u_1(Y) = \min\left\{\frac{u_*}{\kappa}\ln\left(\frac{Y}{z_w}\right), U_\infty\right\} \tag{6}$$

$$u_2(Y) = 0 \tag{7}$$

$$k(Y) = \max\left\{C_\mu^{-1/2}\left(1-\frac{Y}{\delta}\right)^2 u_*^2, 0.0001U_\infty^2\right\} \tag{8}$$

$$\varepsilon(Y) = \frac{C_\mu^{3/4} k(Y)^{3/2}}{\ell} \tag{9}$$

$$\ell = \min\left\{ \kappa Y\left(1 + 3.5\frac{Y}{\delta}\right)^{-1}, C_\mu \delta \right\} \tag{10}$$

Here Y denotes the wall normal direction starting from the flat bed (see Fig. 1). The friction velocity is evaluated as $u_* = \kappa U_\infty / \ln(\delta/z_w)$, and $\kappa = 0.41$ is the von Kármán constant. ℓ is an estimate of the turbulent length scale (see e.g. Brørs(1999)).

(ii) Along the outlet boundary, u_1, u_2, k and ε are specified as free boundary conditions in a finite element context. This means that a traction-free velocity-pressure boundary condition is applied for u_1, u_2 and P (see Gresho and Sani (1999) and Utnes (1988) for details), while the flux is set equal to zero for k and ε. Along the upper and lower boundaries, u_1, k and ε are free, while u_2 is set equal to zero.

(iii) No-slip condition is applied on the cylinder surface and the flat bed with $u_1 = u_2 = 0$.

(iv) Standard near-wall conditions are applied for k and ε near the cylinder wall and the flat bed (see e.g. Rodi (1993)) as

$$k = \frac{u_*^2}{\sqrt{C_\mu}} \quad , \quad \varepsilon = C_\mu^{\frac{3}{4}} \frac{k^{\frac{3}{2}}}{\kappa h_p} \tag{11}$$

where h_p is the radial distance from the wall to the first node away from the wall, and u_* is the wall friction velocity obtained from the logarithmic (log) law.

$$\frac{u_{tan}}{u_*} = \frac{1}{\kappa} \ln\left(\frac{h_p}{z_*}\right) \qquad \text{where} \quad z_* = (z_0, z_w) \tag{12}$$

Here u_{tan} is the tangential velocity to the wall, z_0 is the roughness parameter of the cylinder surface and z_* is a switch parameter for the wall roughness. A small roughness with $z_0 = 1 \times 10^{-6}$m (i.e. $d_{50} = 12 z_0 = 0.012$mm) is used for the cylinder for all the present simulations. This small roughness leads to almost the same results as a smooth logarithmic wall function, but is preferred because of enhanced numerical stability of the simulations.

Figure 1. Definition sketch for flow around a circular cylinder close to a flat bed. The origin of (x_1, x_2) is at the center of the cylinder.

Stretching of the mesh is performed to achieve a fine resolution of the region close to the cylinder surface and the bed. When the grid is refined, the symmetrical grid elements nearest to the cylinder surface are kept constant. The beds with small roughness $z_w = 1 \times 10^{-6}$m and higher roughness $z_w = 2 \times 10^{-5}$m (i.e. $d_{50} = 12 z_w = 0.24$mm) are used for the simulations at $Re = 3.6 \times 10^6$, whereas the bed with small roughness $z_w = 1 \times 10^{-6}$m is used for the simulations at $Re \sim O(10^4)$.

2.3. Convergence studies

Both grid and time-step convergence studies have been performed for flows at $Re = 1.31 \times 10^4$ (the subcritical flow regime) and $Re = 3.6 \times 10^6$ (the upper-transition flow regime) for cases of $\delta/D = 0.48$ and $G/D = (0.1, 0.2, 0.3, 0.4, 0.6, 0.8, 1)$. The variations of C_D and C_L are considered in both grid and time-step convergence studies. Here C_D and C_L are calculated based on the definitions $F_D = 0.5 \, \rho D C_D \, U_\infty^2$ and $F_L = 0.5 \, \rho D C_L \, U_\infty^2$, where F_D and F_L are the time-averaged integrated horizontal and vertical forces per unit length, respectively, acting on the cylinder. The variation of C_D and C_L between two consecutive meshes should be kept within 5%. The results are shown in Fig. 2 for $Re = 1.31 \times 10^4$ and $\delta/D = 0.48$ with $z_w = 1 \times 10^{-6}$m, Fig. 3 for $Re = 3.6 \times 10^6$ and $\delta/D = 0.48$ with $z_w = 1 \times 10^{-6}$m, and Fig. 4 for $Re = 3.6 \times 10^6$ and $\delta/D = 0.48$ with $z_w = 2 \times 10^{-5}$m.

For the case of $Re = 1.31 \times 10^4$ and $\delta/D = 0.48$ with $z_w = 1 \times 10^{-6}$m, three meshes with approximately 10000, 15000 and 20000 elements are used to perform the grid convergence studies. By comparing the results of the meshes with approximately 15000 and 20000 elements, C_D varies from 0.08% to 0.49% and C_L varies from 0.90% and 4.28% for $G/D =$

(0.1, 0.2, 0.3, 0.4, 0.6, 0.8, 1) (see Fig. 2). Therefore, the meshes with approximately 20000 elements are considered to give a sufficient grid resolution. An example of the mesh with 20480 elements for $G/D = 0.4$ is shown in Fig. 5. The radial distance to the first node from the cylinder surface is $0.0005D$. A non-dimensional time step (Δt) of $0.001D/U_\infty$ is used; and the simulations are run for 200 non-dimensional time units (D/U_∞) to obtain a developed flow. These cases have also been computed with a reduced Δt of $0.0005D/U_\infty$ using the corresponding mesh for the cases of different G/D. The maximum deviations of C_D and C_L from the simulations with $\Delta t = 0.001D/U_\infty$ are 0.04% and 3.86%, respectively. Hence, meshes with $\Delta t = 0.001D/U_\infty$ are considered to give a sufficient numerical accuracy. These meshes are also used for the present computations at $Re = 1.36 \times 10^4$ with $\delta/D = 0.14$, $Re = 1 \times 10^4$ with $\delta/D = 2$ and $Re = 4.8 \times 10^4$ with $\delta/D = 0.8$.

Similarly, for the cases of $Re = 3.6 \times 10^6$ and $\delta/D = 0.48$ with $z_w = 1 \times 10^{-6}$m, grid and time-step convergence studies have been performed for the cases of $G/D = $ (0.1, 0.2, 0.3, 0.4, 0.6, 0.8, 1). Denser meshes with approximately 20000, 31000 and 40000 elements have been used for the grid convergence studies. Here C_D varies from 0.091% to 1.22% and C_L varies from 1.31% and 3.50% for $G/D = $ (0.1, 0.2, 0.3, 0.4, 0.6, 0.8, 1) (see Fig. 3) by comparing the results of the meshes with approximately 31000 and 40000 elements. Therefore, the meshes with approximately 40000 elements are considered to give a sufficient grid resolution. The radial distance to the first node from the cylinder surface is $0.0005D$. A non-dimensional time step (Δt) of $0.001D/U_\infty$ is used; and the simulations are run for 200 non-dimensional time units (D/U_∞). Also, these cases have been computed with a reduced Δt of $0.0005D/U_\infty$ using the meshes from the grid convergence studies. The maximum deviations of C_D and C_L from the simulations with $\Delta t = 0.001D/U_\infty$ are 0.054% for C_D and 2.75% for C_L. Hence, meshes with $\Delta t = 0.001D/U_\infty$ are considered to give a sufficient numerical accuracy.

The same sets of meshes are used to check the grid and time-step convergence for the flow cases of $Re = 3.6 \times 10^6$ and $\delta/D = 0.48$ with $z_w = 2 \times 10^{-5}$m. Figure 4 shows that the maximum deviations of C_D and C_L between the meshes with approximately 31000 and 40000 elements are 0.94% and 2.87%, respectively. Thus, they fall within the convergence criteria in the present study, i.e. within 5%. Hence, meshes with approximately 40000 elements are considered to give sufficient grid resolution. Also here the flows have been computed with a reduced Δt of $0.0005D/U_\infty$. The maximum deviations of C_D and C_L from the simulations with $\Delta t = 0.001D/U_\infty$ are 0.022% for C_D and 2.95% for C_L.

One should note that C_L is the crucial parameter for the convergence studies because it is observed to be more sensitive to the variations of mesh and time-step than C_D.
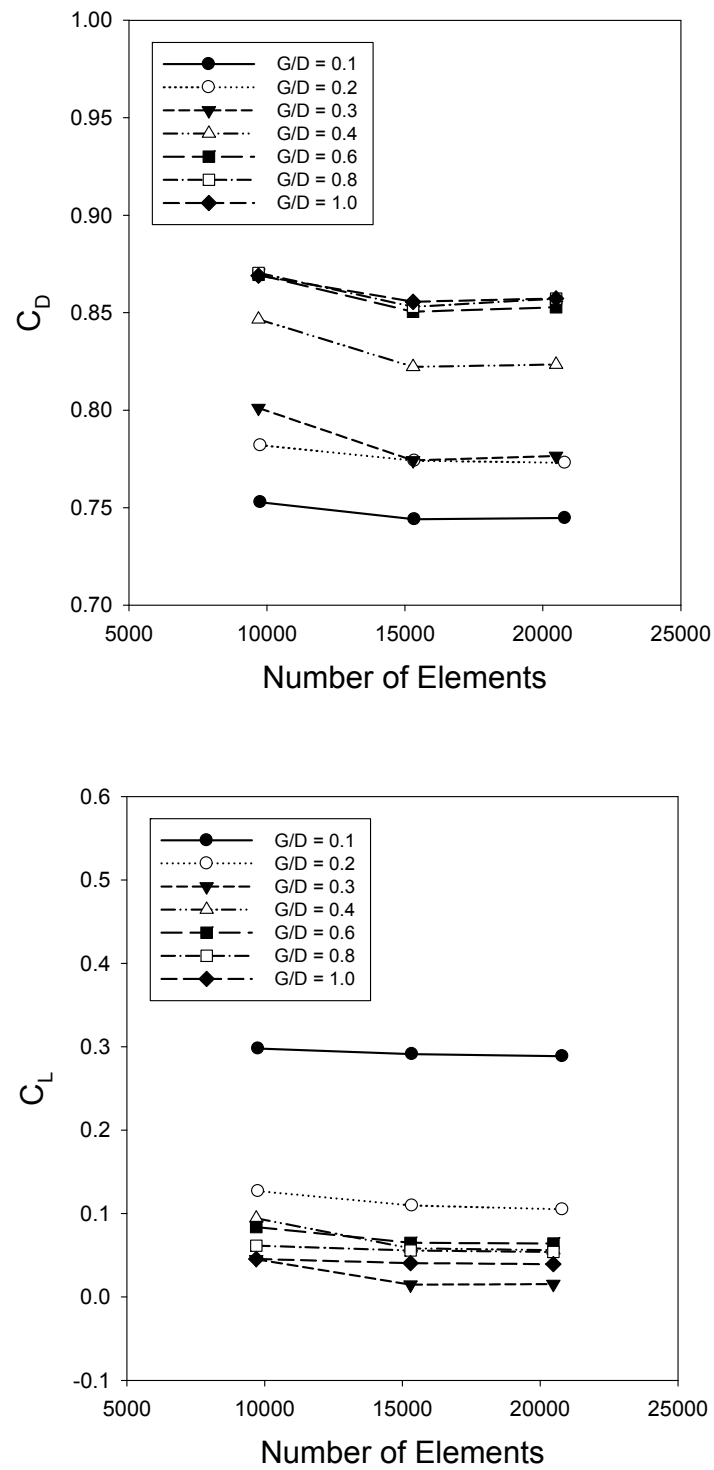
Figure 2. Grid convergence study for C_D and C_L with respect to the number of elements in the computational domain at $Re = 1.31 \times 10^4$ with $\delta/D = 0.48$ and $z_w = 1 \times 10^{-6}$ m.
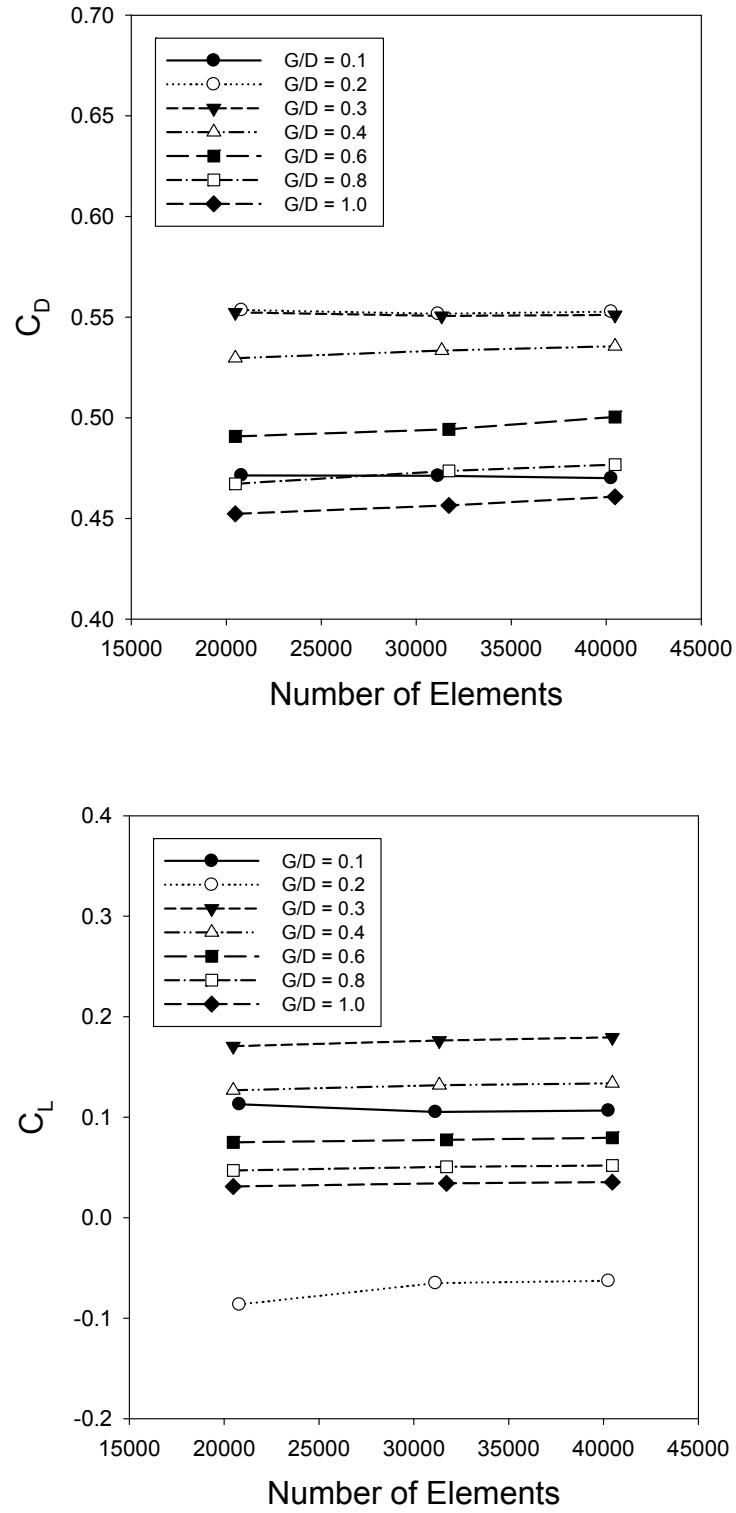
Figure 3. Grid convergence study for C_D and C_L with respect to the number of elements in the computational domain for $Re = 3.6 \times 10^6$ with $\delta/D = 0.48$ and $z_w = 1 \times 10^{-6}$m.
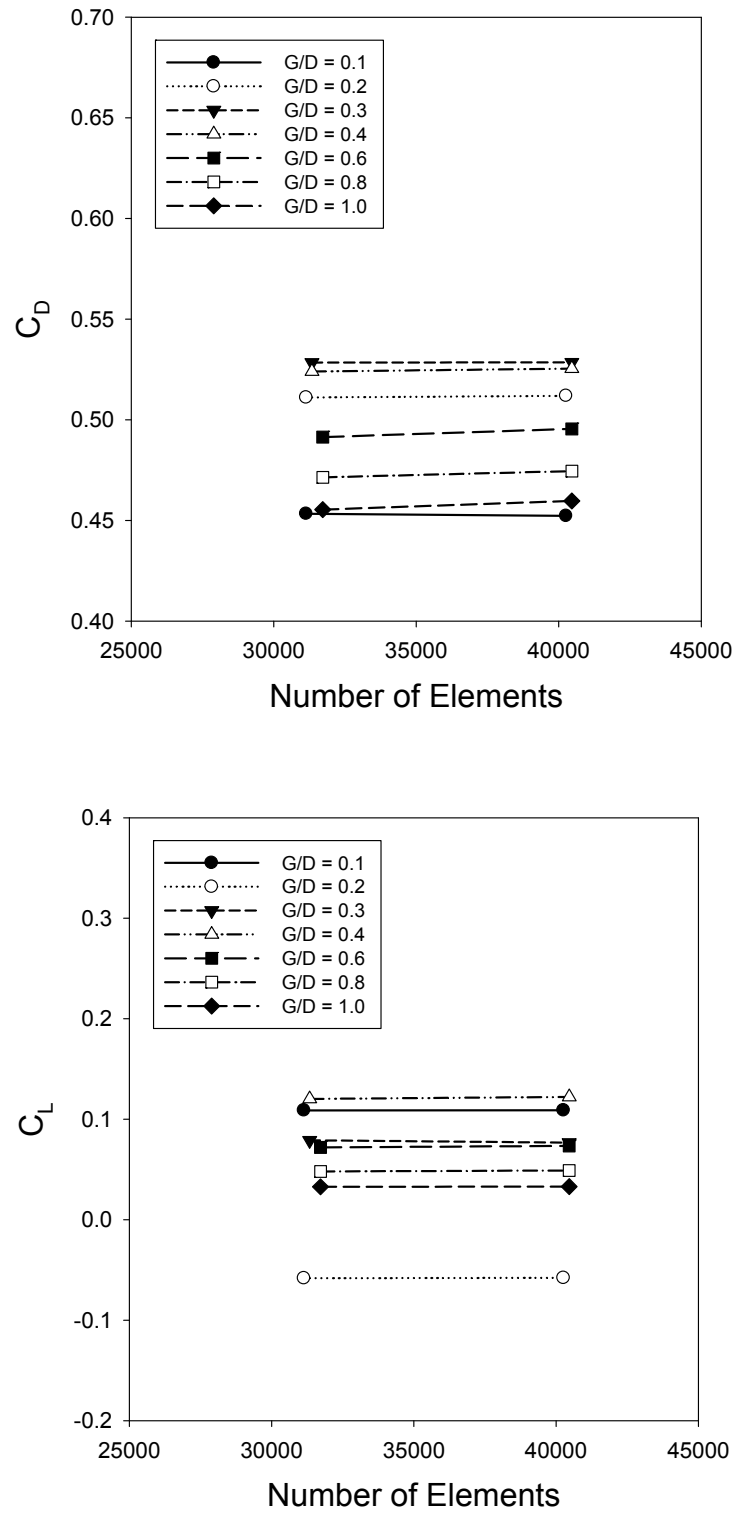
Figure 4. Grid convergence study for C_D and C_L with respect to the number of elements in the computational domain for $Re = 3.6 \times 10^6$ with $\delta/D = 0.48$ and $z_w = 2 \times 10^{-5}$m.
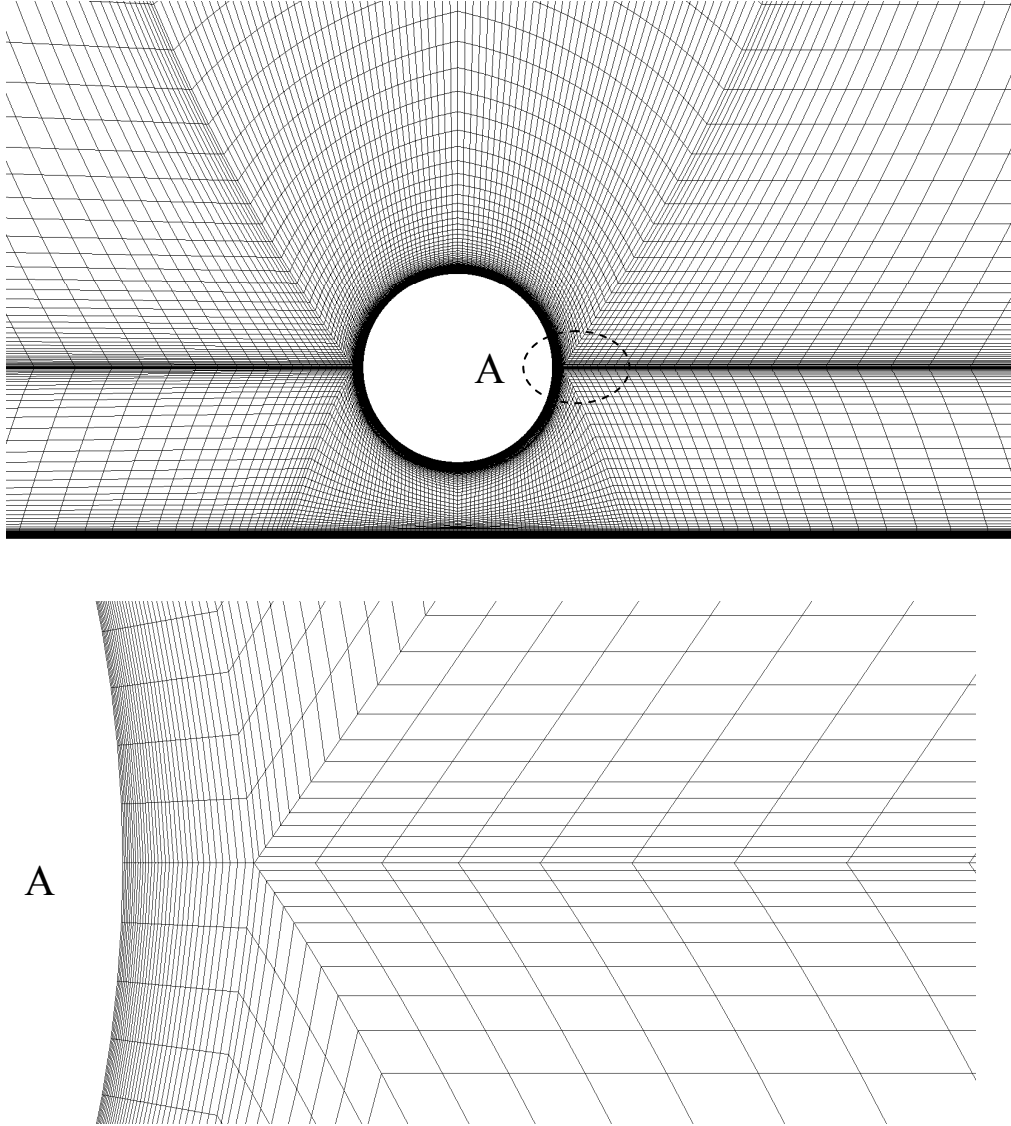
Figure 5. An example of the mesh (*G/D* = 0.4) with 20480 elements and 20816 nodes for the simulations at *Re* ~ O(10^4).

3.   Results and Discussion

The discussion will be focused on high Reynolds number flows at $Re = 3.6 \times 10^6$ with $\delta/D =$ 0.48 and $z_w = (1 \times 10^{-6}\text{m}, 2 \times 10^{-5}\text{m})$. In this flow regime, there are neither experimental nor numerical results available in the open literature. However, the present results will be validated by comparing the present numerical results for *G/D* = 1 with both published experimental data and numerical results for an isolated cylinder subject to a steady current in the same flow regime, since the effect of the bed on the flow around the cylinder is

insignificant for $G/D = 1$. Results for lower Reynolds number flows ($Re = 1\times10^4$ - 4.8×10^4 and $\delta/D = 0.14$ - 2) will also be computed and compared with published numerical results and experimental data. These results are compared with the high Reynolds number flow results. Further discussions of the lower Reynolds number flows are given in Ong et al. (2008). The present results also include discussion of the observed flow features related to the development of vortex-shedding and the estimation of bedload sediment transport.

3.1 Hydrodynamic quantities of the cylinder for engineering design

Figure 6 shows the values of C_D versus G/D at $Re = 3.6\times10^6$ with $\delta/D = 0.48$ for $z_w = 1\times10^{-6}$m and 2×10^{-5}m. It appears that C_D increases as G/D increases for $G/D \leq 0.3$. This is because the cylinder is subject to higher inflow velocity in the boundary layer when it is farther away from the bed. The feature is similar to that observed for $Re \sim O(10^4)$ (including Jensen et al.'s (1990) experimental data, Lei et al.'s (1999) experimental data and Zhao et al.'s (2007) k-ω results), as shown in Fig. 7. For $G/D > 0.3$, C_D decreases as G/D increases, approaching a constant, which means that the influence of the bed becomes negligible. The C_D value for $G/D = 1$ and $z_w = 1\times10^{-6}$m is within the range of the published experimental data and numerical results for steady flow around an isolated circular cylinder, see Table 1. For $G/D \leq 0.4$, Fig. 6 shows that the higher bed roughness reduces the drag force on the cylinder. This is because, for the same δ/D and Re, an increased bed roughness reduces the velocity within the boundary layer; see e.g. Eq. (12).
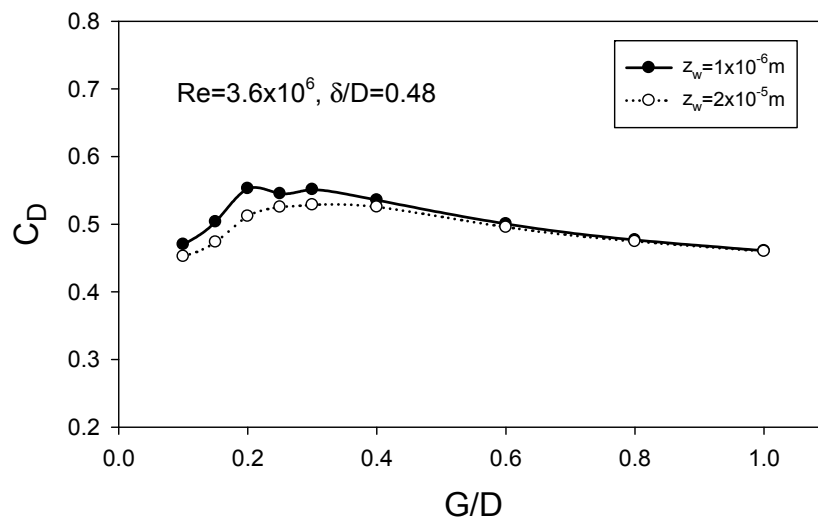

Figure 6. Time-averaged drag coefficient versus gap to diameter ratio for the given values of *Re*, *δ/D* and *z_w*.
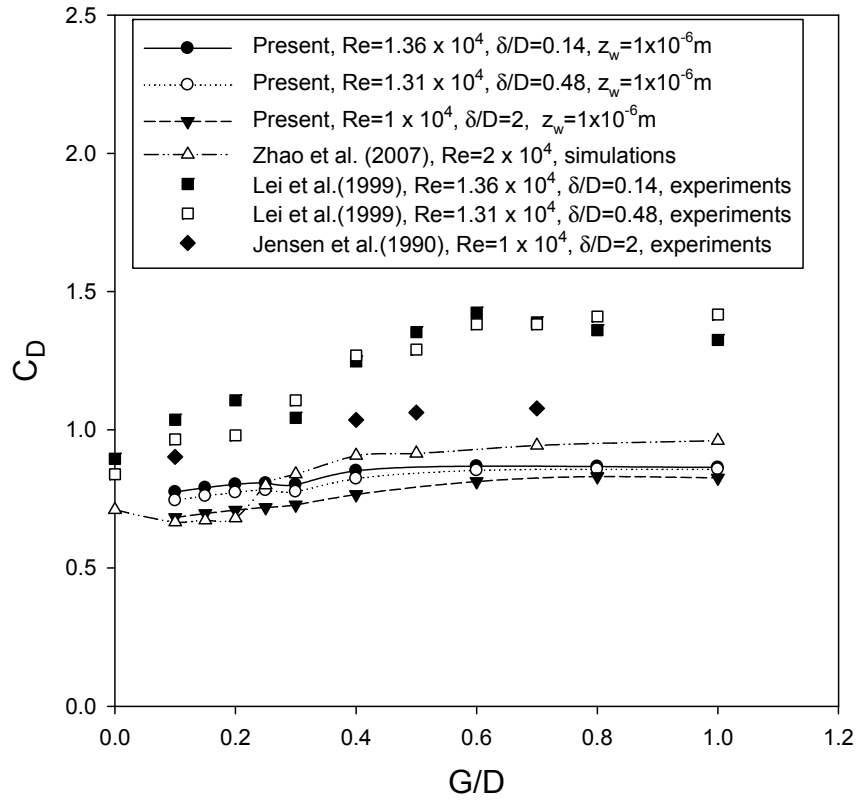
Figure 7. Time-averaged drag coefficient versus gap to diameter ratio for $Re \sim O(10^4)$.

Table 1. Numerical results and experimental data at $Re = 3.6 \times 10^6$.

Re	**Description**		C_D	C_{Lrms}	*St*
3.6×10^6 (Upper-transition regime)	$G/D = 1$	Present simulation with $z_w = 1 \times 10^{-6}$m	0.4608	0.0857	0.3052
	Flow around an isolated cylinder	Ong et al. (2009)	0.4573	0.0766	0.3052
		Catalano et al.(2003) URANS $Re = 4 \times 10^6$	0.46	-	-
		Published experimental data (summarized by Zdravkovich (1997))	0.36-0.75	0.06-0.14	0.17-0.29

Figure 8 shows C_L versus G/D at $Re = 3.6 \times 10^6$ with $\delta/D = 0.48$ for $z_w = 1 \times 10^{-6}$m and 2×10^{-5}m. It appears that C_L becomes negative for $0.15 < G/D < 0.3$ for both roughnesses. Moreover, C_L is more negative for the roughest bed. The negative C_L will be discussed later in conjunction with the mean pressure around the cylinder shown in Fig. 12.
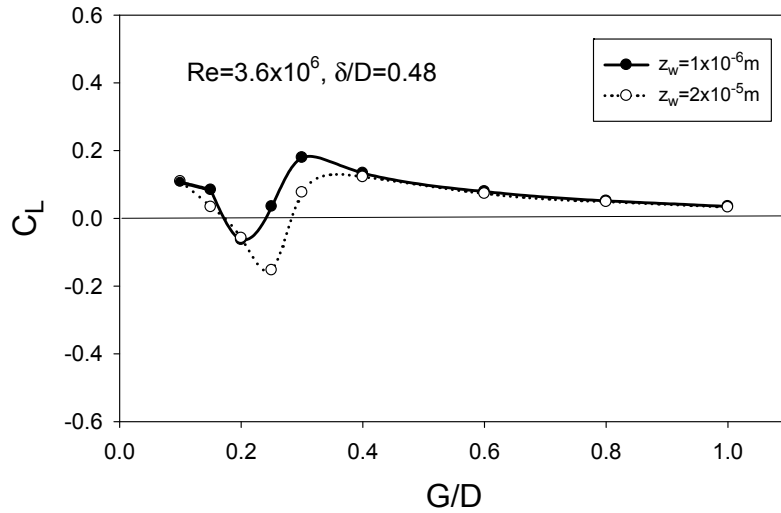
Figure 8. Time-averaged lift coefficient versus gap to diameter ratio for the given values of *Re*, *δ/D* and *z_w*.

Figure 9 shows *St* versus *G/D* at *Re* = 3.6×10⁶ with *δ/D* = 0.48 for z_w = 1×10⁻⁶m and 2×10⁻⁵m. It appears that the bed roughness does not affect *St*; higher bed roughness might be needed in order to see any effect on *St*. For *G/D* < 0.6, *St* increases slightly as *G/D* increases, suggesting that the vortex shedding is developing from a suppressed stage to a fully-developed stage as the influence of the bed is diminishing. This feature is similar to the present numerical results and the Jensen et al. (1990) experimental data for *Re* ~ O(10⁴) as shown in Fig. 10. However, this is not the case neither for Lei et al. (1999) nor for Wang and Tan (2008). The value *St* = 0.3052 at *G/D* = 1.0 for z_w = 1×10⁻⁶m agrees fairly well with the published experimental and numerical results for the flow around an isolated smooth circular cylinder in the same flow regime as shown in Table 1.
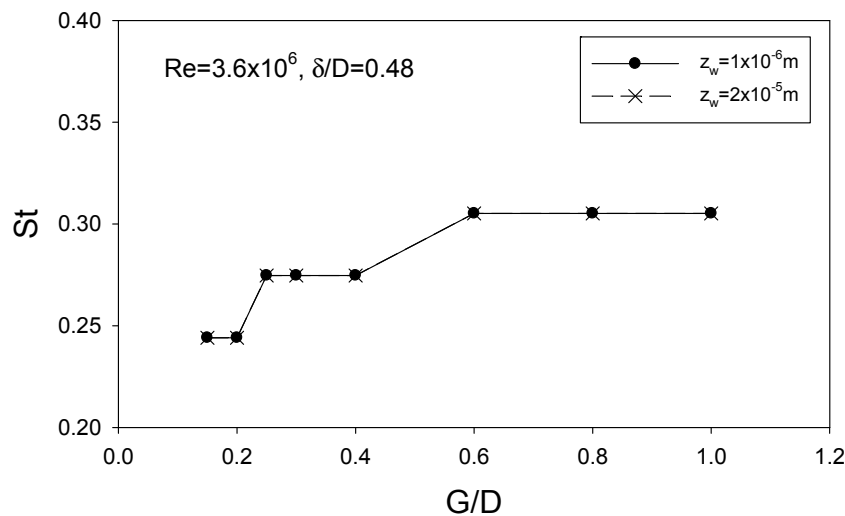

Figure 9. Strouhal number versus gap to diameter ratio for the given values of *Re*, *δ/D* and *z_w*.
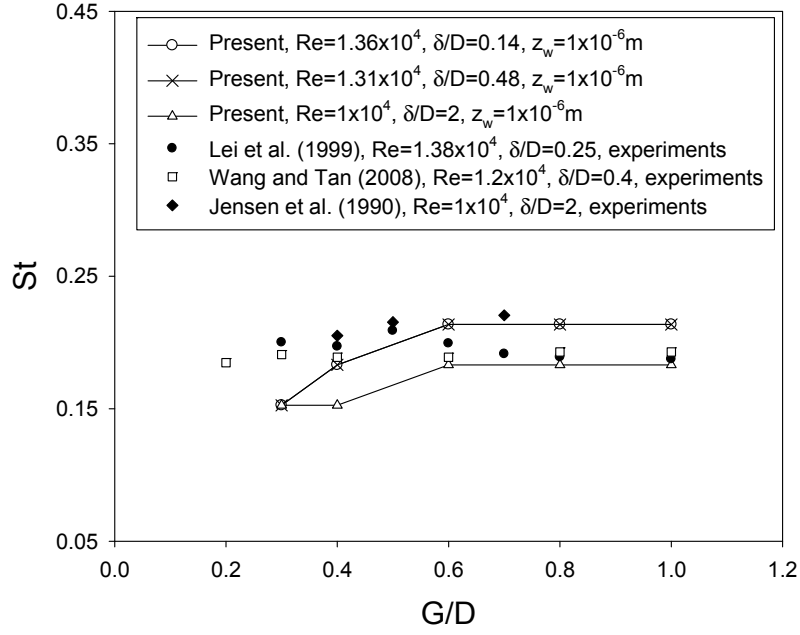
Figure 10. Strouhal number versus gap to diameter ratio for $Re \sim O(10^4)$.

Figure 11 shows the predicted mean pressure distribution ($C_p = [p_c\text{-}p_\infty]/[0.5\rho U_\infty^2]$) around the cylinder close to a bed with $z_w = 1\times10^{-6}$m for $Re = 3.6\times10^6$, $\delta/D = 0.48$ and $G/D = 1$. Here p_c is the pressure at the peripheral angle of the cylinder, θ, measured clockwise from the front point on the horizontal axis of the cylinder (see Fig. 1); and p_∞ is the pressure of the flow at infinity. Comparisons are made with Ong et al.'s (2009) numerical results and Achenbach's (1968) experimental data; both are for an isolated smooth cylinder. It appears that C_p around the cylinder is symmetric about the horizontal centerline of the cylinder. The present results agree well with the results by Ong et al. (2009) and Achenbach (1968), although there is an under-prediction of the negative C_p observed at the back half of the cylinder. This might be due to that it is difficult to model the strong pressure gradient accurately as mentioned by Ong et al. (2009).

Figure 12 shows C_p around the cylinder for $Re = 3.6\times10^6$, $\delta/D = 0.48$ and $G/D = (0.1, 0.25, 0.8)$ close to the bed with $z_w = 1\times10^{-6}$m. For $G/D = 0.1$, C_p is asymmetric about the horizontal centerline of the cylinder; the positive zone of C_p is skewed and located in the area upstream near the gap. This skewed C_p gives a net upward lift force on the cylinder, making C_L positive as shown in Fig. 8. The negative lift force is observed for $0.15 < G/D < 0.3$ (Fig. 8), and the existence of the downward lift force can be explained by looking at the variation of C_p for different G/D. Figure 12 shows that for $G/D = 0.25$, the positive pressure zone moves clockwise towards $\theta = 0°$. This means that the strength of the upward force is reduced when G/D becomes larger. However, the negative C_p (suction) at the gap ($\theta = 270°$) remains large, and eventually causes a net downward force exerted on the cylinder. When the gap becomes

larger, the velocity at the gap slows down and the suction at the gap becomes less negative. This changes the net downward force to a net upward lift force as shown in Fig. 8. As *G/D* increases, the influence of the bed decreases, and consequently C_p becomes symmetric as shown in Fig. 12 for *G/D* = 0.8. The strength of the net upward lift force is reduced and approaches zero as *G/D* approaches infinity.
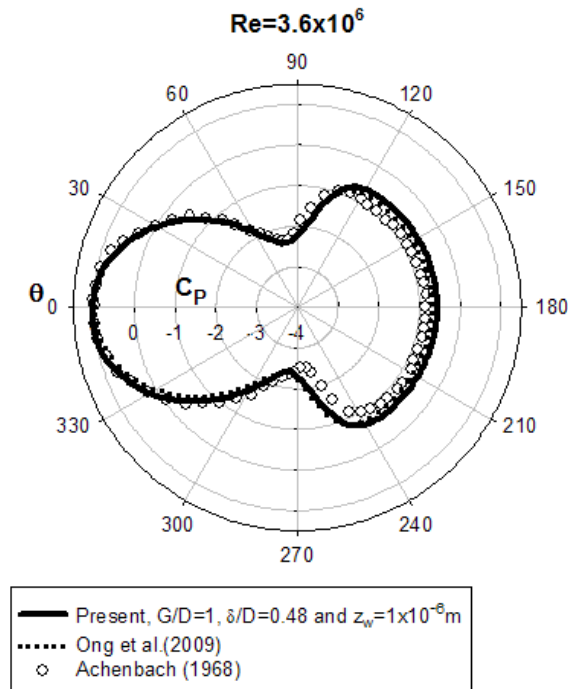

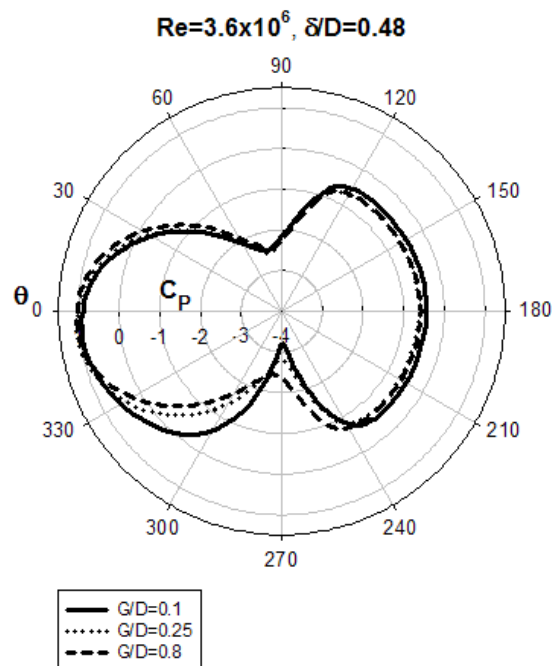Figure 11. Mean pressure coefficient around the cylinder at *Re* = 3.6×10^6.

Figure 12. Mean pressure coefficient around the cylinder for *Re* = 3.6×10^6, *δ/D* = 0.48, z_w = 1×10^{-6}m and *G/D* = (0.1, 0.25, 0.8).

Figure 13 shows C_p around the cylinder for $G/D = 0.1$, 0.25 and 0.8 near a flat rough bed with $z_w = 2\times10^{-5}$m, including comparisons with the results for $z_w = 1\times10^{-6}$m. It appears that the effect of the roughness is small for $G/D = 0.1$ and 0.8, corresponding to the results for C_D in Fig. 6 and C_L in Fig. 8. However, for $G/D = 0.25$, the magnitude of negative C_p at $\theta = 270^\circ$ is higher for the case of the rougher bed ($z_w = 2\times10^{-5}$m) than for the case of $z_w = 1\times10^{-6}$m. This causes C_L to become more negative at $G/D = 0.25$ for $z_w = 2\times10^{-5}$m than for $z_w = 1\times10^{-6}$m, as shown in Fig. 8.
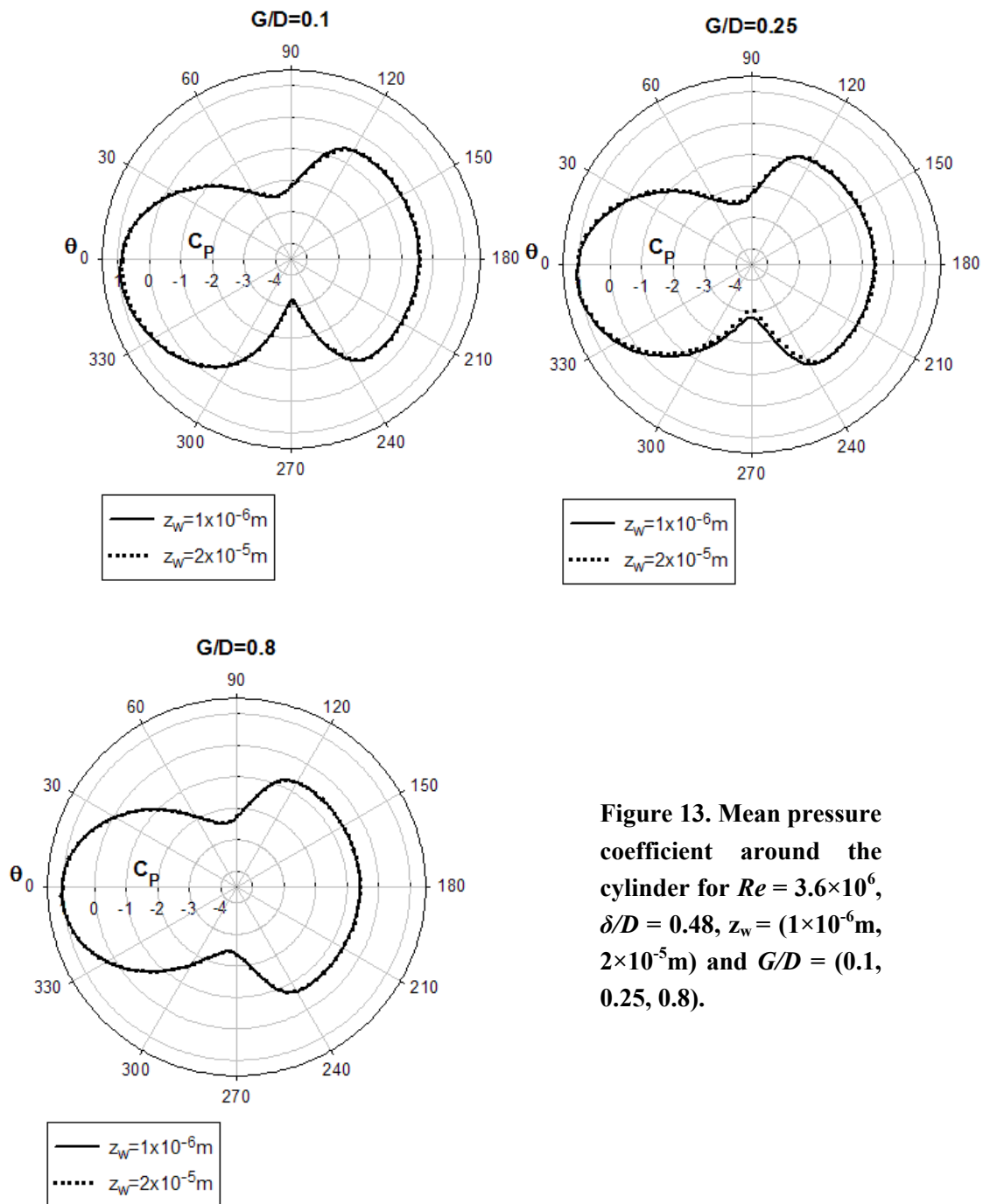

Figure 13. Mean pressure coefficient around the cylinder for $Re = 3.6\times10^6$, $\delta/D = 0.48$, $z_w = (1\times10^{-6}$m, 2×10^{-5}m) and $G/D = (0.1, 0.25, 0.8)$.

3.2 Vortex shedding and suppression

Figure 14 shows C_{Lrms} versus G/D for $\delta/D = 0.48$ and the beds with $z_w = 1\times10^{-6}$m and 2×10^{-5}m. It appears that C_{Lrms} versus G/D has the same qualitative behaviour for both cases, but C_{Lrms} is generally lower for $z_w = 2\times10^{-5}$m (rougher bed) than for $z_w = 1\times10^{-6}$m for $0.15 < G/D < 0.8$. The critical value for onset of vortex shedding, G/D_c (i.e. where the curve will intersect the horizontal axis), is between 0.1 and 0.15 in both cases, but it has not been calculated exactly here. Figure 15 shows C_{Lrms} versus G/D for the lower Reynolds number regime (Re ~ $O(10^4)$) for various δ/D. By comparing Fig. 15 (the lower Reynolds number results) with Fig. 14 (the high Reynolds number results), it is observed that G/D_c decreases when Re increases. This indicates that the initiation of the vortex shedding occurs earlier when Re is larger. Lei et al. (2000) found a similar relation between G/D_c and Re for their simulations at $Re = 80$ - 1000. In Fig. 14, $C_{Lrms} = 0$ at $G/D = 0.1$, suggesting no vortex shedding. For $G/D > G/D_c$, the magnitude of C_{Lrms} exhibits a rapid initial increase as G/D increases. Figure 14 also shows that there is a transitional trough of C_{Lrms} for $0.2 < G/D < 0.4$. This might be caused by the transition of vortex shedding development which cannot be captured correctly by the present turbulence model. For $G/D > 0.4$, C_{Lrms} decreases smoothly as G/D increases, suggesting that the behaviour of the vortex shedding is rather stable.
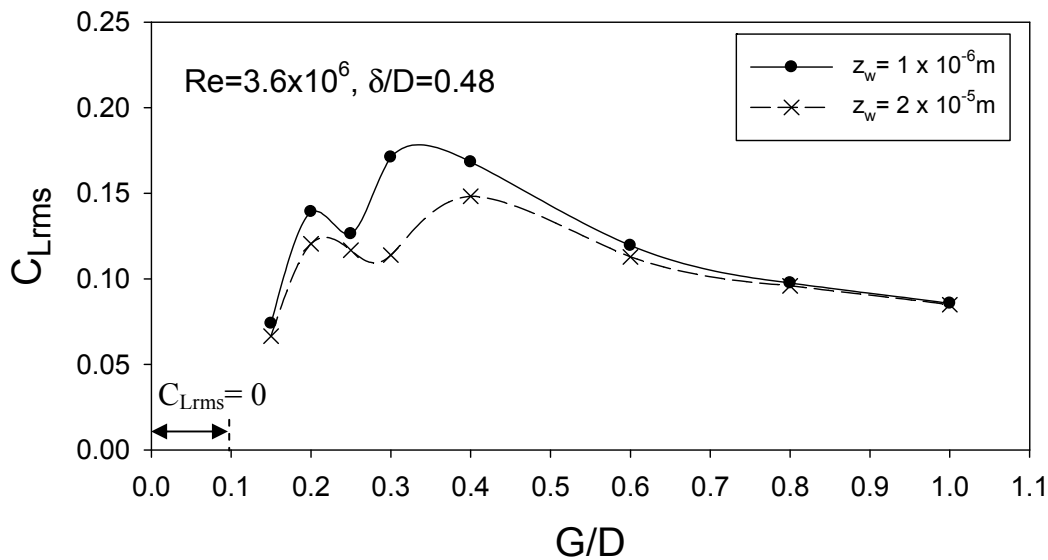

Figure 14. RMS value of the fluctuating lift coefficient versus gap to diameter ratio for the given values of *Re*, *δ/D* and *z_w*.
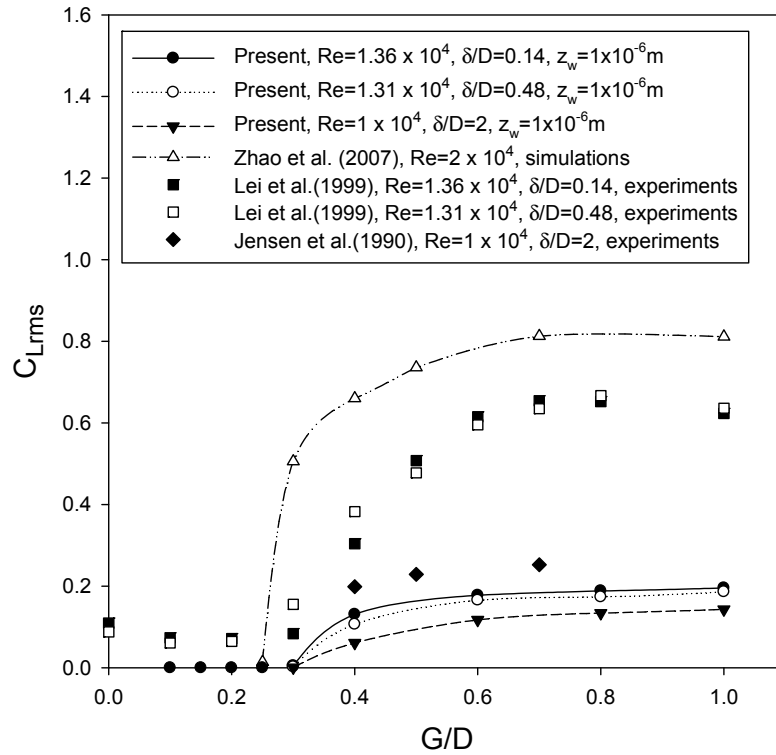
Figure 15. RMS value of the fluctuating lift coefficient versus gap to diameter ratio for *Re* ~ O(10⁴).

Figure 16 shows the instantaneous non-dimensional vorticity ($\omega D/U_\infty$) contour plots for flows at $Re = 3.6 \times 10^6$ with $\delta/D = 0.48$ and $G/D = (0.1, 0.15, 0.3, 0.8)$ near a bed with $z_w = 1 \times 10^{-6}$m at the non-dimensional time of $200D/U_\infty$. Here ω is the vorticity. The solid contour lines indicate the positive vorticity (counter-clockwise) and the dashed lines indicate the negative vorticity (clockwise). There are three shear layers; two in the vicinity of the cylinder and one at the bed. The suppression and formation of the vortex shedding are also influenced by the interaction between these three shear layers.

It appears that there is no mutual interaction between the two shear layers from the cylinder to form any Kármán-like vortex shedding for $G/D = 0.1$ (Fig. 16a). Both shear layers continue to grow and advect downstream without forming any vortices in the near wake of the cylinder. The flow pattern remains steady. For $G/D = 0.15$ (Fig. 16b), the two shear layers have begun to interact with each other and form Kármán-like vortices in the near wake of the cylinder. The bottom shear layer with positive vorticity interacts with the shear layer (negative vorticity) from the flat bed. A counter-clockwise vortex shed from the lower side of the cylinder clearly destabilizes the wall boundary layer, and it is accompanied by a clockwise vortex in the near-flat-bed region. For $G/D = 0.3$ (Fig. 16c), the vortex shedding behind the cylinder continues to develop. The vortex with negative vorticity (clockwise) shed

from the upper shear layer, interacts with the clockwise vortex formed by the shear layer from the bed. These two groups of vortices interact and form a larger vortex. The evolvement of the vortex shedding during one vortex-shedding period will be shown in Fig. 18 and discussed in the following paragraph with greater details. For $G/D = 1.0$ (Fig. 16d), the vortices shed from the cylinder are not influenced by the shear layer at the bed. The vortex shedding is similar to the case for flow around an isolated circular cylinder (see Ong et al. (2009), Fig. 6). Figure 17 shows that the development of the vortex shedding for the lower Reynolds number flow regime ($Re = 1.31 \times 10^4$) is qualitatively similar to that for the high Reynolds number flow regime ($Re = 3.6 \times 10^6$), except that the dependency of G/D_c is different. Wang and Tan (2008) and Lei et al. (2000) have observed a similar development of vortex shedding in both their experimental and numerical results at lower Reynolds numbers (i.e. $Re < 10^5$).

Figure 18 shows the non-dimensional vorticity ($\omega D/U_\infty$) contour plots at eight time instants within one cycle of vortex shedding for the case of $Re = 3.6 \times 10^6$, $\delta/D = 0.48$, $G/D = 0.3$ and $z_w = 1 \times 10^{-6}$m (i.e. for the same conditions as shown in Fig. 16). The vortex shedding period T is computed to be 6.552s based on $St = 0.3052$ (see Table 1). Figure 18(a) shows that the upper shear layer from the cylinder interacts with the lower shear layer from the cylinder. At time = $T/8$, it is clearly seen that the lower shear layer is going to be shed as a counter-clockwise discrete vortex (C2) .The clockwise vortex with negative vorticity (B) contributed from the flat bed is interacting with the clockwise vortex shed from the upper shear layer of the cylinder (C1), and they are forming an agglomerated clockwise vortex (M) (see also Fig. 18b at time = $7T/8$ and T). At time = $3T/8$, the counter-clockwise vortex (C2) is fully shed from the lower shear layer. This vortex is advecting and pushing the agglomerated vortex (M) downstream. These two vortices do not mix due to different signs of vorticity. The vortex C2 is moving downstream and suppressing the development of the agglomerated vortex M. The energy carried by the vortices diminishes as they are travelling downstream. Due to the continuous interference with the vortex C2, the vortex M is eventually separated into two vortices at time = $4T/8$. They are then transported downstream individually. The whole process of this vortex shedding will repeat itself in the next vortex shedding period, see Fig. 18b.

3.3   Mean pressure coefficient and friction force along the flat seabed

This section discusses the flow mechanisms and hydrodynamic quantities along the flat seabed. For the flows in the upper-transition flow regime (i.e. $Re = 3.6 \times 10^6$ in the present study), to our knowledge, no such results have been published in the open literature. These results have been compared with numerical and experimental results for lower Reynolds numbers ($Re \sim O(10^4)$).

(a) G/D=0.1
Vortex-shedding suppressed
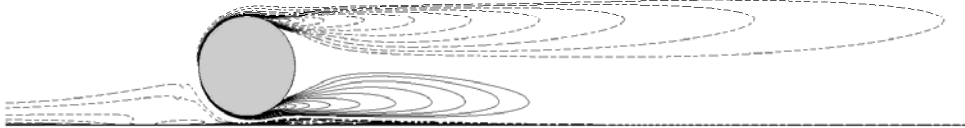
(b) G/D=0.15
Vortex shedding formed and starts the interaction with the flat bed
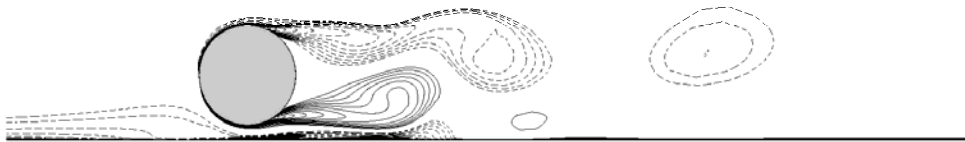
(c) G/D=0.3
Vortex shedding formed and interacting with the flat bed

(d) G/D=1
Vortex shedding developed and interacting less with the flat bed
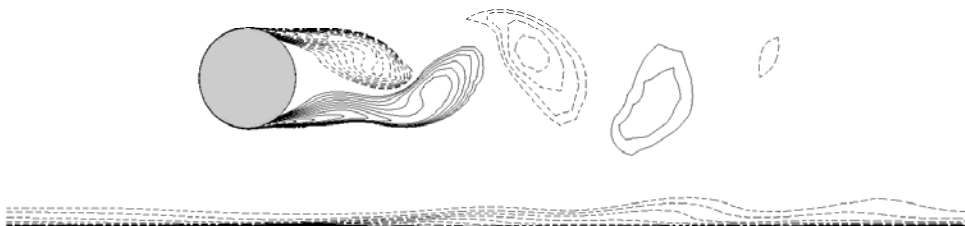
Figure 16. The development of vortex shedding shown by instantaneous non-dimensional vorticity contour plots for $Re = 3.6 \times 10^6$, $\delta/D = 0.48$ and $z_w = 1 \times 10^{-6}$m at the non-dimensional time of $200D/U_\infty$. 46 contour levels of $\omega D/U_\infty$ from -540 to 540 are plotted.

(a) G/D=0.1
Vortex shedding suppressed
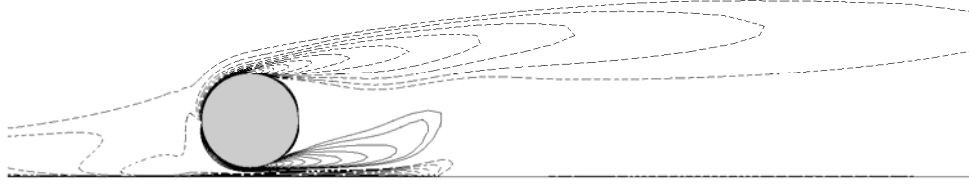
(b) G/D=0.3
Initiation of vortex shedding
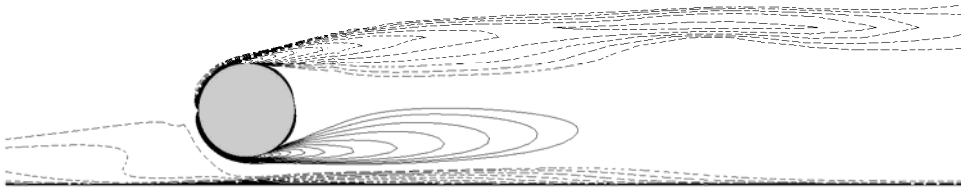
(c) G/D=0.4
Vortex shedding formed and interacting with the flat bed
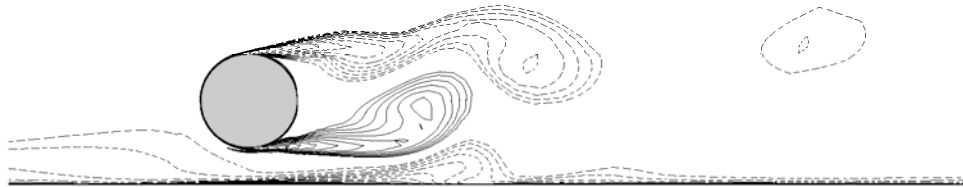
(d) G/D=1
Vortex shedding developed and interacting less with the flat bed
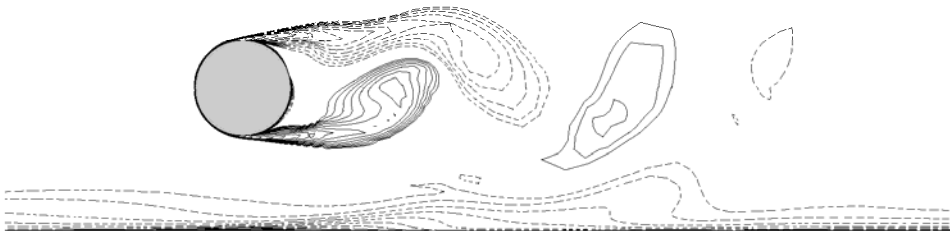
Figure 17. Instantaneous non-dimensional vorticity contours of flow around a smooth circular cylinder for $Re = 1.31 \times 10^4$ and $\delta/D = 0.48$ at the dimensionless time of 200 D/U_∞. 40 contour levels of $\omega D/U_\infty$ from -240 to 240 are plotted.
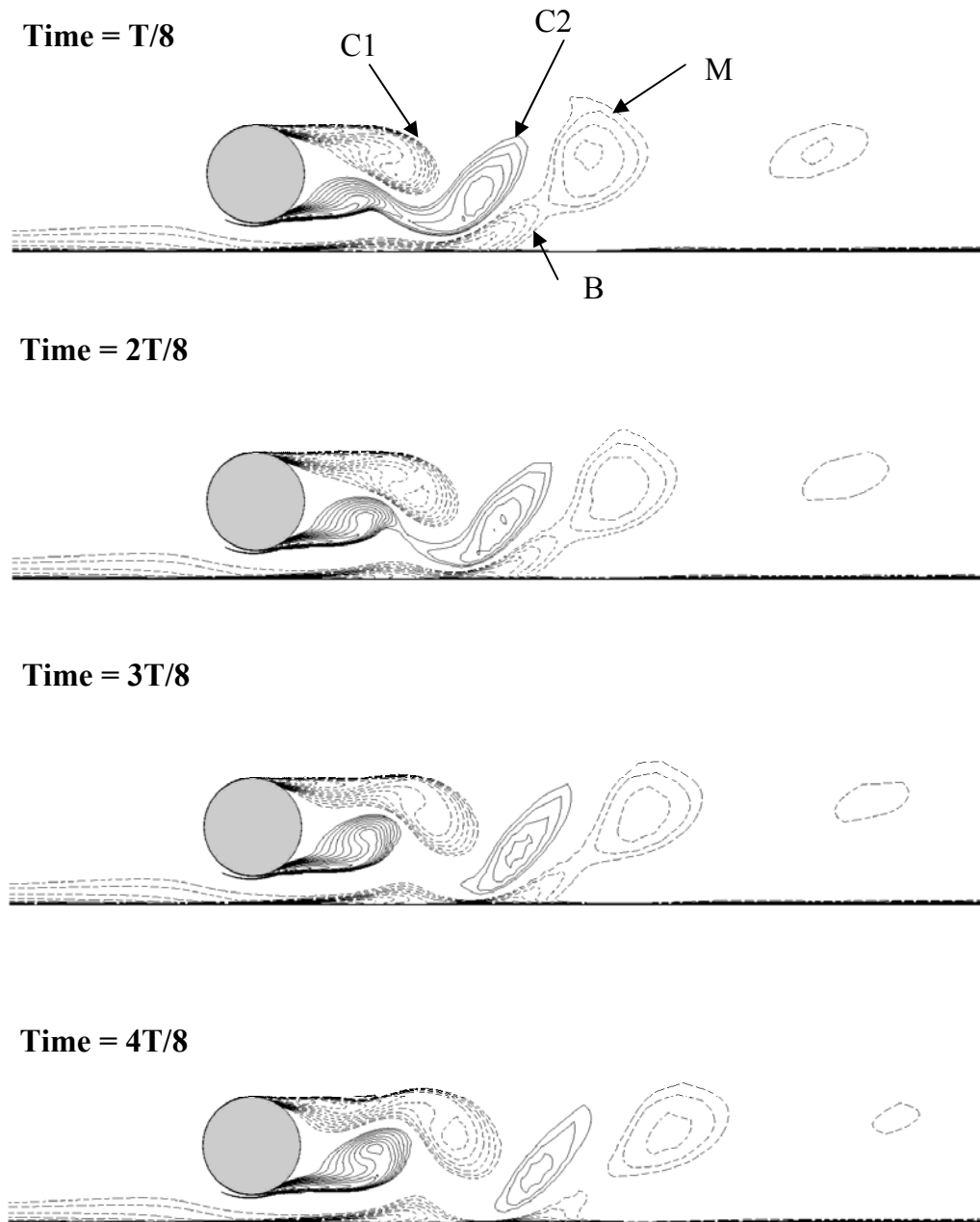
Figure 18a. Time-history of non-dimensional vorticity contour plots for *Re* =3.6×10⁶, *δ/D* = 0.48, z_w = 1×10⁻⁶m and *G/D* = 0.3 from time = *T*/8 to time = *T*/2. 46 contour levels of *ωD*/U_∞ from -540 to 540 are plotted.

Time = 5T/8

C1

C2

B

Time = 6T/8

Time = 7T/8
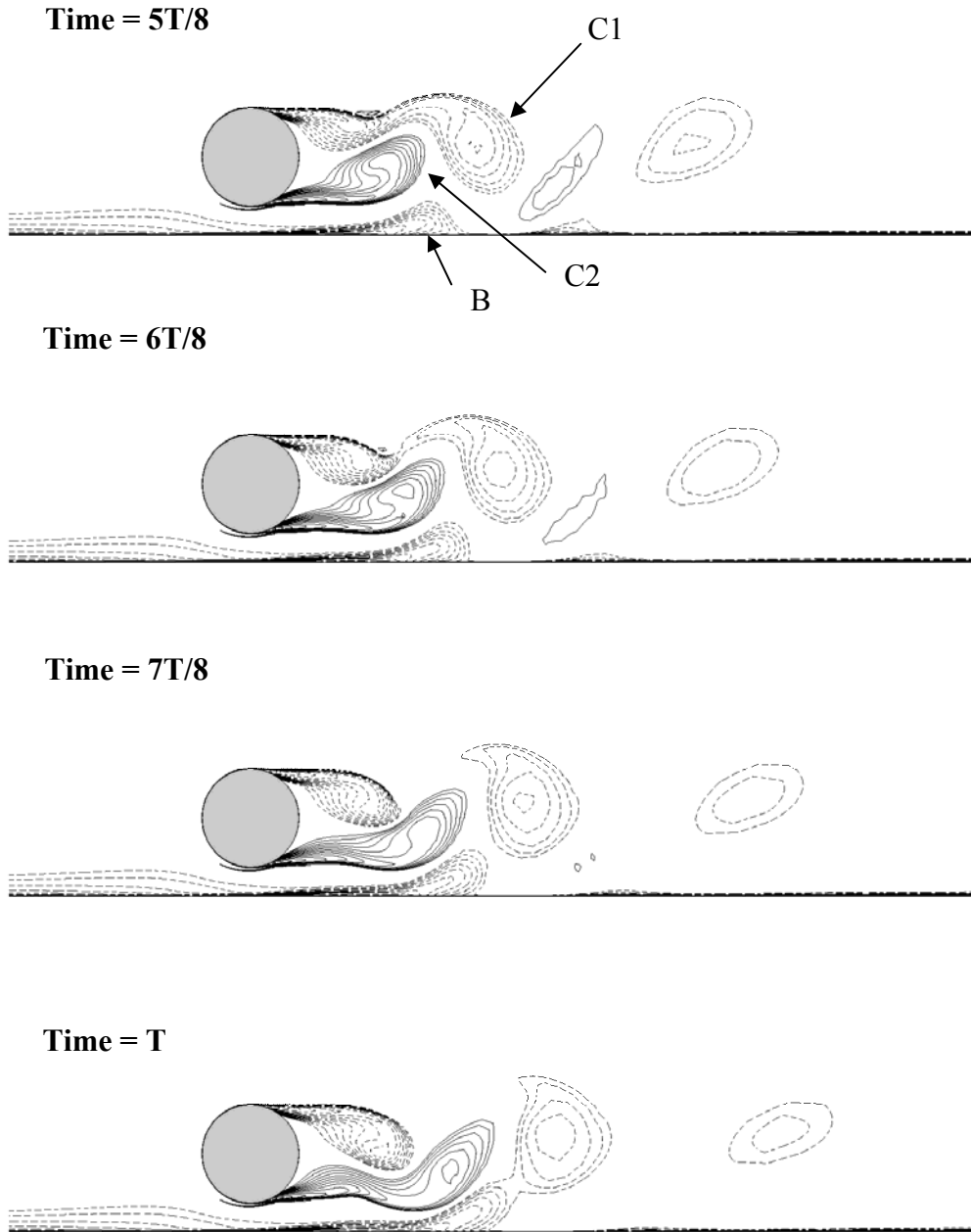
Time = T

Figure 18b. Time-history of non-dimensional vorticity contour plots for Re =3.6×10^6, δ/D = 0.48, z_w = 1×10^{-6}m and G/D = 0.3 from time = 5T/8 to time = T. 46 contour levels of $\omega D/U_\infty$ from -540 to 540 are plotted.

Figure 19 shows the mean pressure coefficient along the bed ($C_{pw} = [p_w-p_\infty]/[0.5\rho U_\infty^2]$) for Re = 3.6×10^6, $\delta/D = 0.48$, $z_w = 1 \times 10^{-6}$m and $G/D = (0.1, 0.4, 0.8)$. Here p_w is the pressure along the bed. C_{pw} is substantially influenced by the existence of the cylinder. For a small gap, i.e. $G/D = 0.1$, it appears that the pressure suction is large compared with those for $G/D = 0.4$ and 0.8. This is mainly due to the higher magnitude of the velocity at the gap. Figure 20 shows that the predicted C_{pw} along the bed for low Reynolds numbers is in good agreement with the experimental data reported by Bearman and Zdravkovich (1978) for $G/D = (0.1, 0.4, 0.8)$ at $Re = 4.8 \times 10^4$ and $\delta/D = 0.8$. It should be noted that C_{pw} exhibits a quantitatively similar behavior for low and high Reynolds numbers. Figure 21 shows that the effect of the bed roughness (with $z_w = 2 \times 10^{-5}$m) on C_{pw} is insignificant as compared with the results of $z_w = 1 \times 10^{-6}$m.

By comparing Figs. 19 and 20, the magnitude of the negative C_{pw} at the gap for $Re = 3.6 \times 10^6$ is much larger than that for $Re = 4.8 \times 10^4$. Figure 22 shows comparisons of C_p around the cylinder for high and low Reynolds numbers (i.e. $Re = 3.6 \times 10^6$ and 1.31×10^4), $\delta/D = 0.48$, $z_w = 1 \times 10^{-6}$m and $G/D = (0.1, 0.8)$. It is observed that the values of C_p around the cylinder at $\theta = 270^\circ$ for both $Re = 1.31 \times 10^4$ and $Re = 3.6 \times 10^6$ show that the magnitude of the negative C_p increases as Re increases. These two observations suggest that the higher Reynolds number flow leads to the stronger suction at the gap.
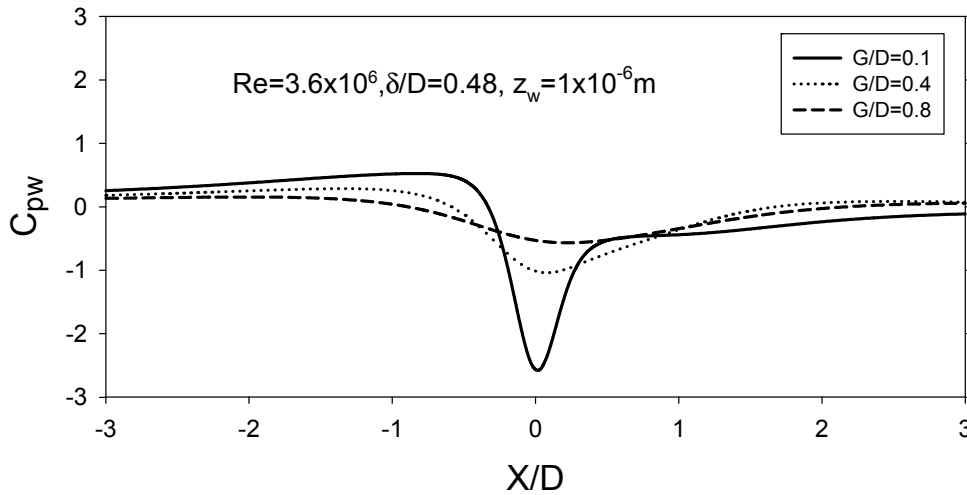
Figure 19. Mean pressure coefficient along the flat bed for the given values of *Re*, *δ/D* and *G/D*.

Figure 20. Mean pressure coefficient along the flat bed for *Re* = 4.8×10⁴, *δ/D* = 0.8 and *G/D* = (0.1, 0.4, 0.8).
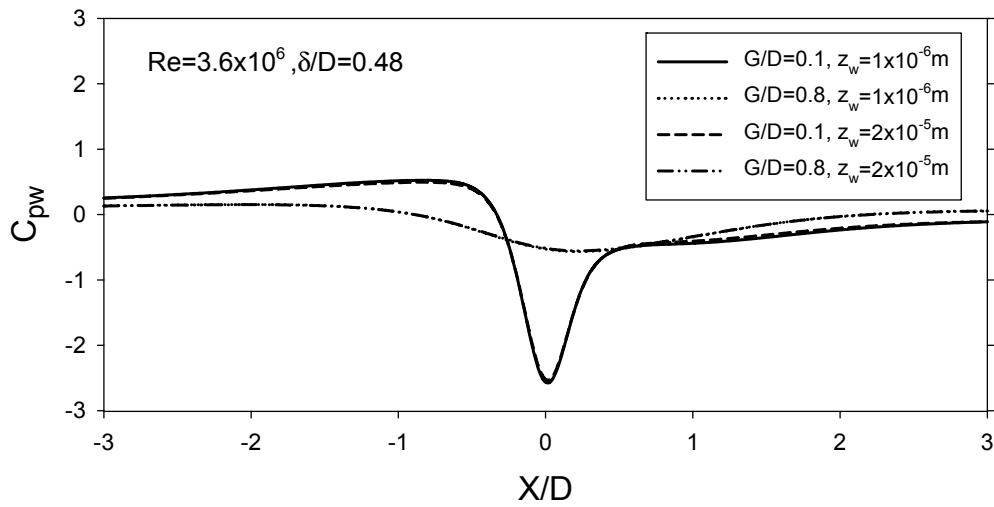
Figure 21. Mean pressure coefficient along the flat bed for the given values of *Re, δ/D, zₗ* and *G/D*.
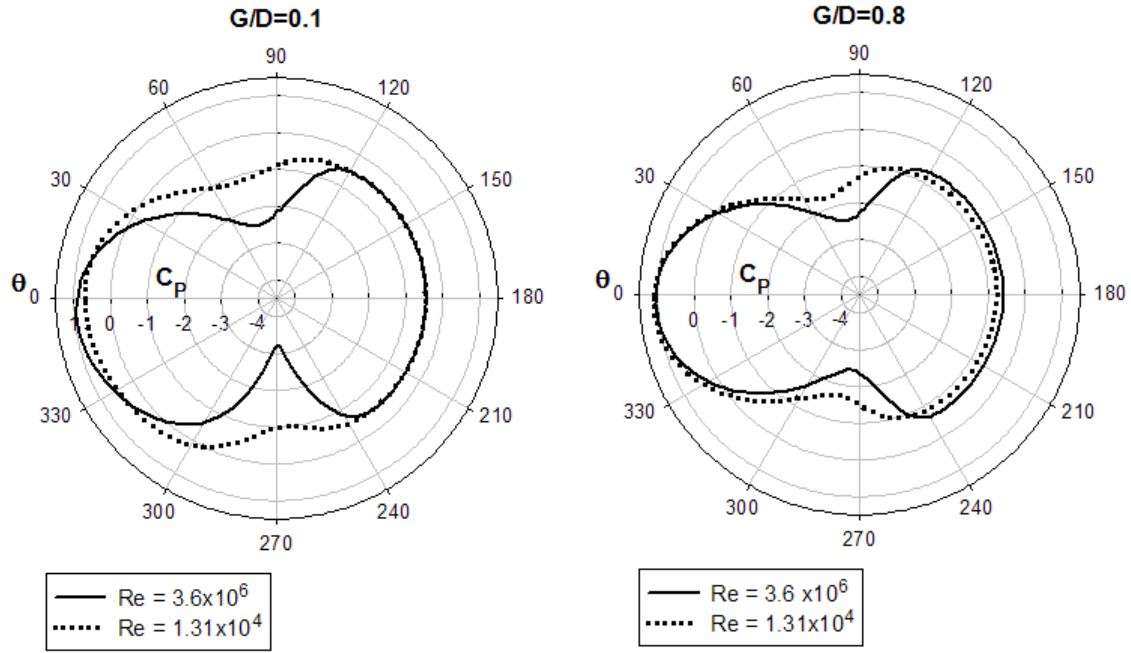
Figure 22. Mean pressure coefficient around the cylinder for high and low Reynolds numbers ($Re = 3.6\times10^6$ and 1.31×10^4), $\delta/D = 0.48$, $z_w = 1\times10^{-6}$m and $G/D = (0.1, 0.8)$.

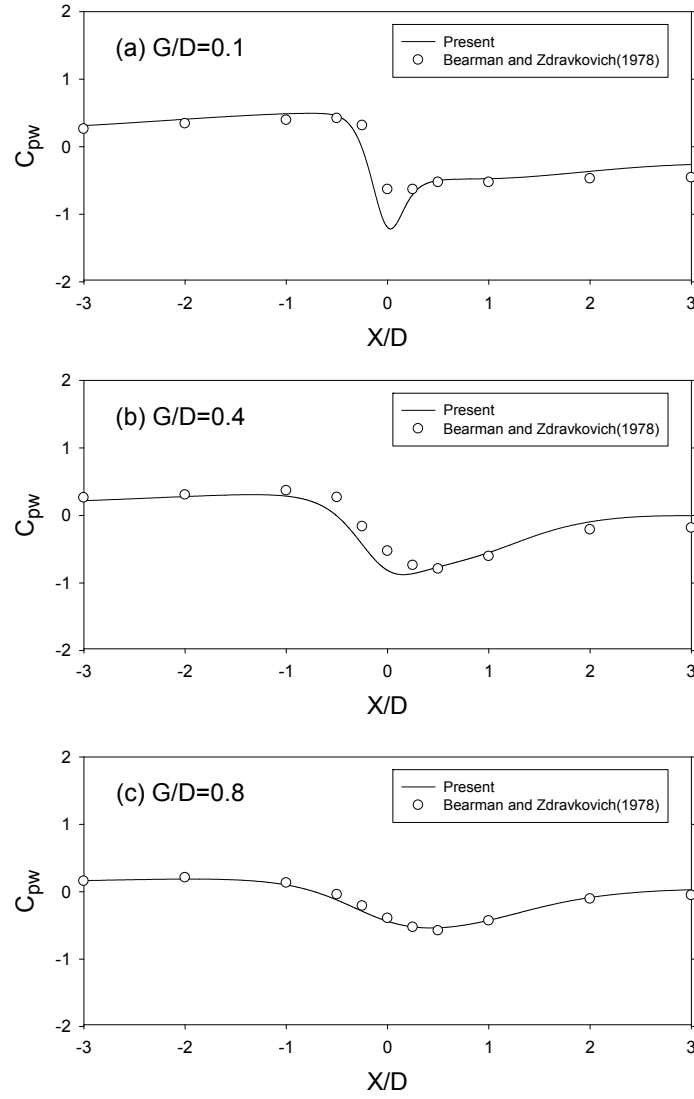Figure 23 shows the instantaneous friction velocity along the flat bed (u_{*w}) at four time instants within one cycle of vortex shedding for $Re = 3.6\times10^6$, $\delta/D=0.48$, $z_w = 1\times10^{-6}$m and $G/D = (0.1, 0.4, 0.8)$. It is observed that there is no variation of u_{*w} along the flat bed with time for $G/D = 0.1$ (Fig. 23a). This is reasonable because there is no periodic vortex shedding in the near wake of the cylinder. Hence, the effect of the cylinder on the flat bed is steady. For $G/D = 0.4$ (Fig. 23b), the existence of the vortex shedding causes u_{*w} to vary with time. For $0 < X/D < 5$, the temporal variation of u_{*w} is substantial (here X is the horizontal coordinate along the flat bed where $X = 0$ is located at the center of the gap; see Fig. 1). It appears that the temporal variation of u_{*w} becomes weaker as G/D increases. This is physically sound because the effect of the cylinder is reduced when the cylinder is farther away from the bed. Figure 24 shows the mean friction velocity (u_{*wm}) for $Re = 3.6\times10^6$, $\delta/D = 0.48$, $G/D = (0.1, 0.8)$ and $z_w = (1\times10^{-6}$m, 2×10^{-5}m). It is observed that u_{*wm} is higher for the rougher bed ($z_w = 2\times10^{-5}$m) than that for the less rough bed ($z_w = 1\times10^{-6}$m), as expected. Figure 25 shows u_{*wm} for $Re = 1\times10^4$- 4.8×10^4, $\delta/D = 0.14 - 2$, $z_w = 1\times10^{-6}$m and $G/D = (0.1, 0.4, 0.6, 0.8)$ together with Brørs' (1999) numerical results for $Re = 1.5\times10^4$, $\delta/D = 1$, $z_w = 1.7\times10^{-5}$m and $G/D = 0.6$. It is observed in Fig. 25c that Brørs' (1999) results, in which a higher bed roughness was used ($z_w = 1.7\times10^{-5}$m), generally show higher value of u_{*wm} along the bed compared with the present results ($z_w = 1\times10^{-6}$m). This is physically sound, given the results in Fig. 24. Figure 24 also shows that u_{*wm} at the gap is much higher for $G/D = 0.1$ than that for $G/D = 0.8$. This is mainly due to the higher velocity at the gap when G/D is small as

shown in Fig. 26 (which shows the velocity profile at the center of the gap for $G/D = 0.1$, 0.4 and 0.8). The same feature is also observed in Fig. 25 for $Re \sim O(10^4)$.
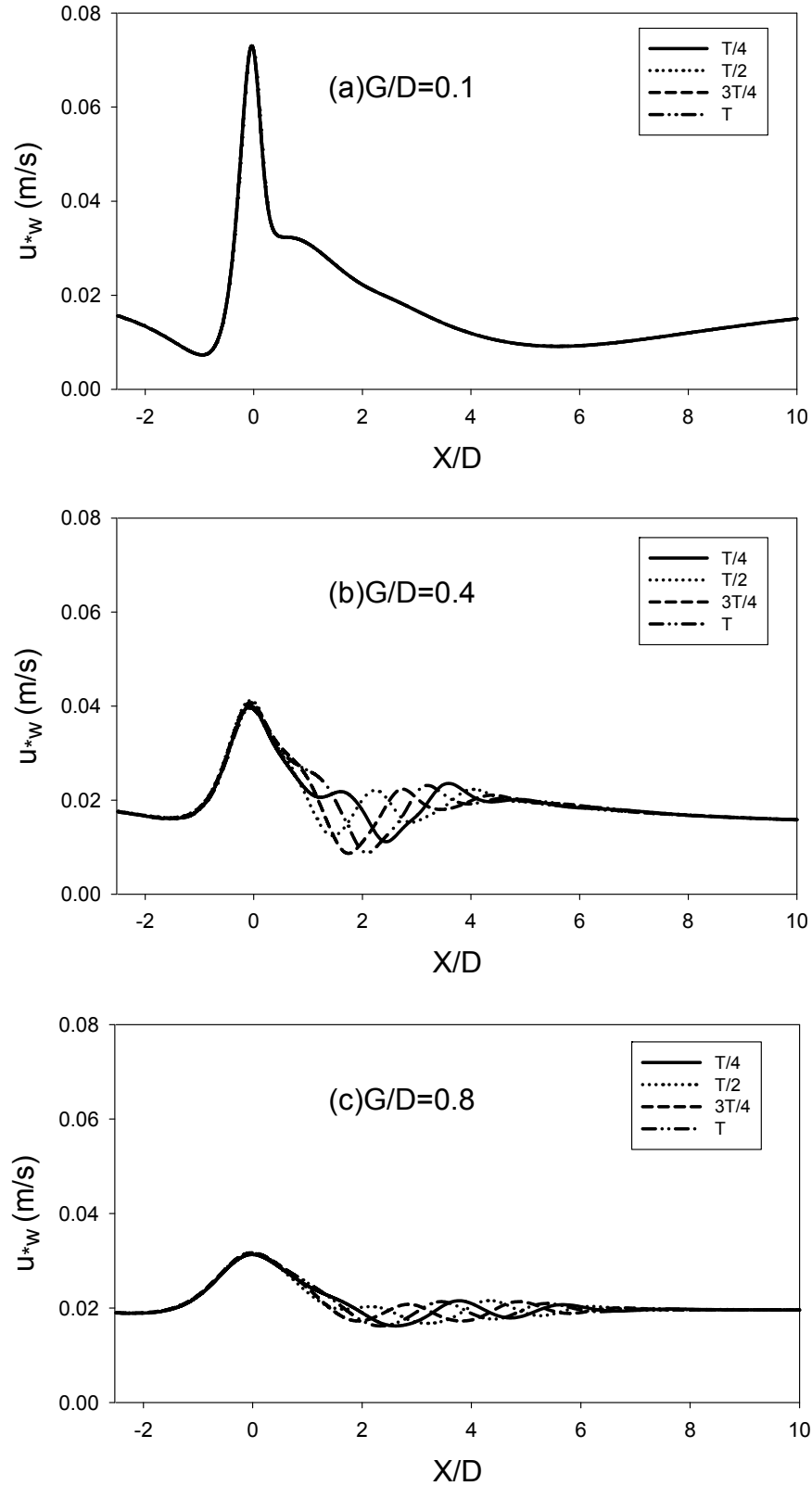
Figure 23. Effect of the vortex shedding on the instantaneous friction velocity along the bed for $Re = 3.6 \times 10^6$, $\delta/D = 0.48$, $z_w = 1 \times 10^{-6}$m and $G/D = (0.1, 0.4, 0.8)$.
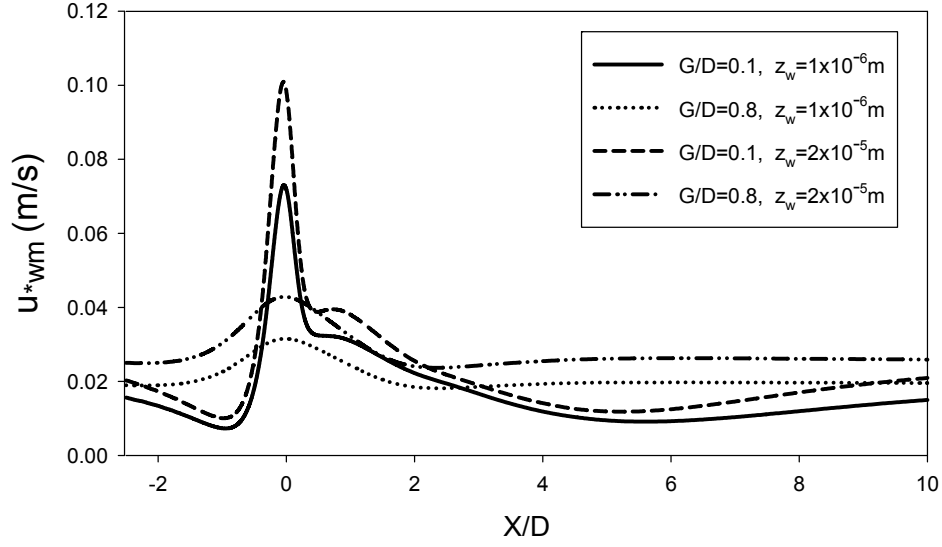
Figure 24. Mean friction velocity along the bed for $Re = 3.6 \times 10^6$, $\delta/D = 0.48$, $z_w = (1 \times 10^{-6}\text{m},$
$2 \times 10^{-5}\text{m})$ **and** $G/D = (0.1, 0.8)$.
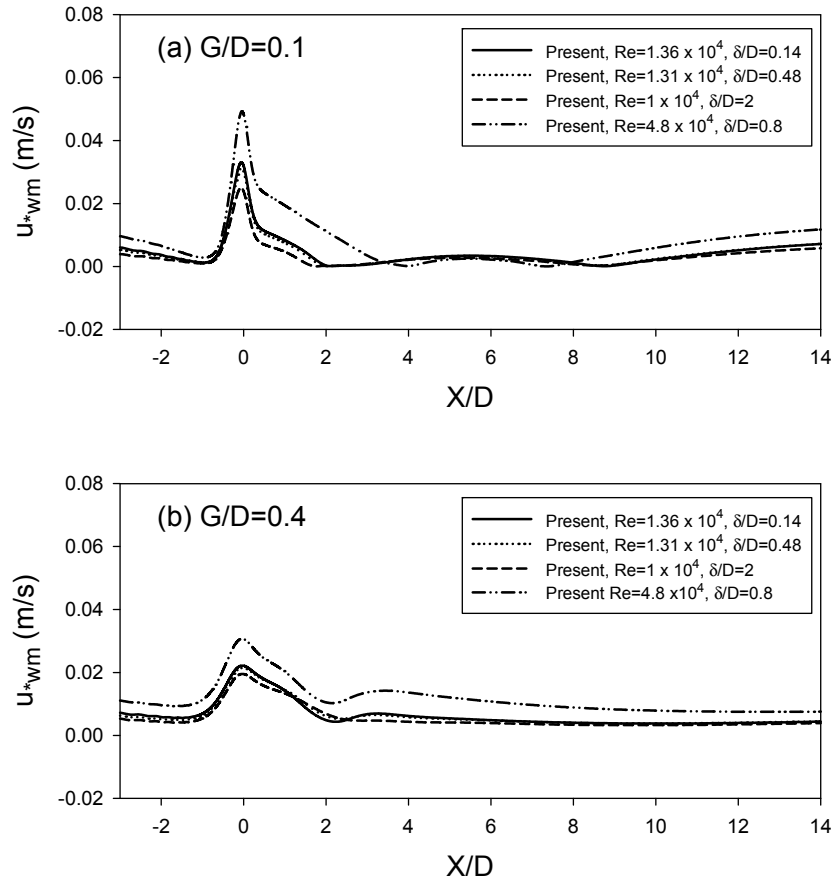
Figure 25. Mean friction velocity distribution along the flat bed for $Re = 1 \times 10^4 - 4.8 \times 10^4$, $\delta/D =$
$0.14 - 0.8$ **and** $G/D = (0.1, 0.4, 0.6, 0.8)$.
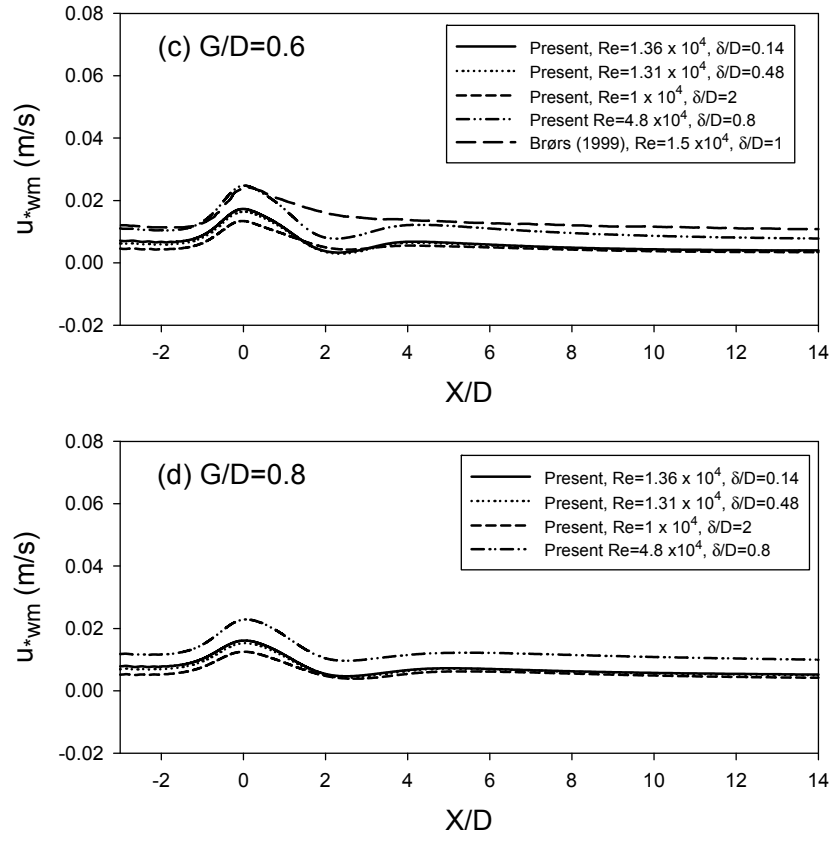
Figure 25. Continued.
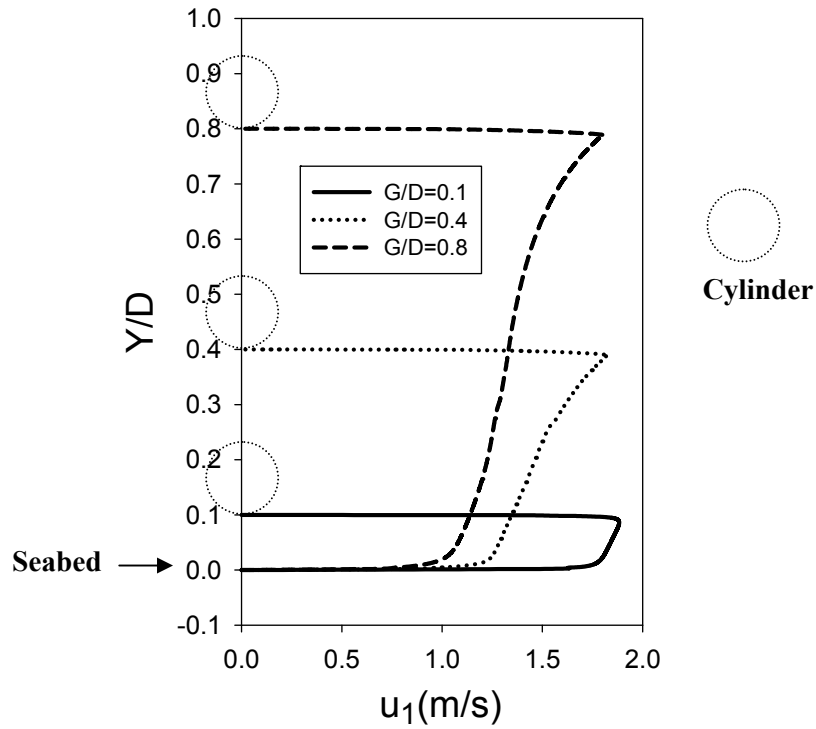
Figure 26. Instantaneous horizontal velocity profile in the gap for $Re = 3.6 \times 10^6$, $\delta/D = 0.48$, $z_w = 1 \times 10^{-6}$m **and** $G/D = (0.1, 0.4, 0.8)$ **at the non-dimensional time of** $200D/U_\infty$.

3.2.4. An Example of Bedload Sediment Transport Calculation

The calculation of the bedload sediment transport along the flat bed is demonstrated in this section. The instantaneous non-dimension bedload sediment transport Φ is a function of the instantaneous non-dimensional seabed shear stress (Shields parameter) θ_s and is given by (Nielsen, 1992)

$$\Phi = 12 |\theta_s|^{1/2} (\theta_s - \theta_{sc}) \frac{\theta_s}{|\theta_s|} \qquad (13)$$

where

$$\Phi = \frac{q_b}{\left(g(s-1)d_{50}^3 \right)^{1/2}} \qquad (14)$$

$$\theta_s = \frac{u_{*w}^2}{g(s-1)d_{50}} \qquad (15)$$

Here q_b is the instantaneous dimensional bedload sediment transport, $g = 9.81\text{m/s}^2$ is the gravitational acceleration and $s = 2.65$ is the density ratio between the bottom sediments and the water (taken as for quartz sand). The critical Shields parameter $\theta_{sc} = 0.05$ must be exceeded for bedload transport to occur.

Figures 27 shows θ_s along the flat bed for $Re = 3.6 \times 10^6$, $\delta/D = 0.48$, $z_w = 2 \times 10^{-5}\text{m}$ (i.e. $d_{50} = 12z_w = 0.24\text{mm}$, fine sand) and $G/D = 0.1$. The locations where the sediment transport takes place for $\theta_s > \theta_{sc}$ can be determined from the figure. Figure 28 shows Φ_m (the mean non-dimensional bedload transport) along the bed for $Re = 3.6 \times 10^6$, $\delta/D = 0.48$, $z_w = 2 \times 10^{-5}\text{m}$ and $G/D = (0.1, 0.4, 0.8)$. It is observed that the bedload sediment transport is significantly amplified at the location of the gap ($X/D = 0$) for $G/D = 0.1$ compared with those for $G/D = 0.4$ and 0.8. If the flat bed is movable, scouring around the cylinder will take place. The scouring process will not be investigated here. Detailed explanations of the flow mechanisms and the development of the scour can be found in Sumer and Fredsøe (2002).
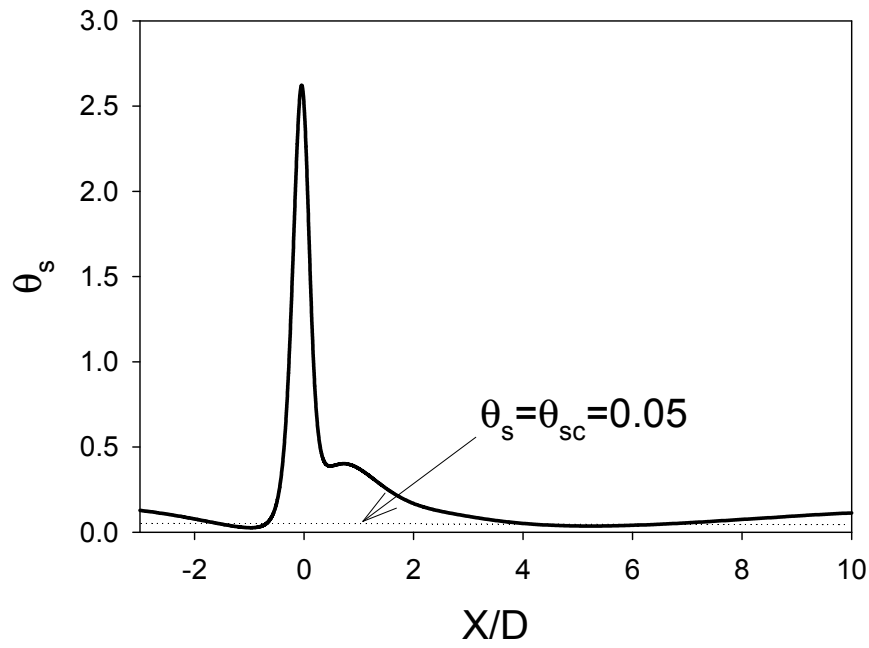
Figure 27. Instantaneous Shields parameter along the bed for $Re = 3.6\times10^6$, $\delta/D = 0.48$, $z_w = 2\times10^{-5}$m and $G/D = 0.1$.
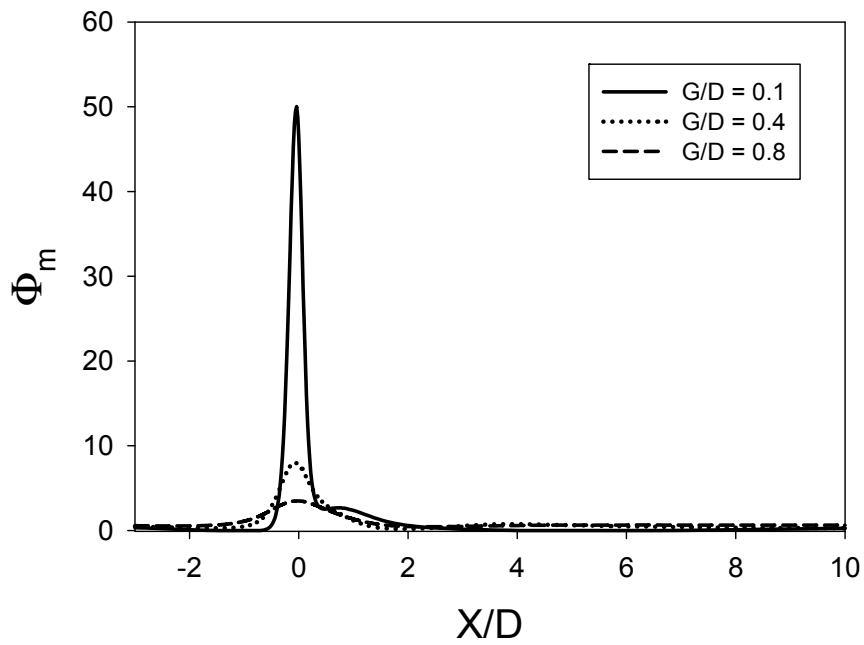
Figure 28. Mean non-dimensional bedload sediment transport along the bed for $Re = 3.6\times10^6$, $\delta/D = 0.48$, $z_w = 2\times10^{-5}$m and $G/D = (0.1, 0.4, 0.8)$.

4. Conclusions

High Reynolds number flows around a circular cylinder close to a flat seabed have been computed using a two-dimensional standard high Reynolds number k-ε model. The effects of gap to diameter ratio, Reynolds number, flat seabed roughness for a given boundary layer thickness of the inlet flow upstream of the cylinder have been investigated. Hydrodynamic quantities and the resulting bedload transport have been predicted, and the vortex shedding mechanisms have been investigated. Predictions of hydrodynamic quantities around a cylinder located far away from the bed (so that the effect of the bed is negligible) are in satisfactory agreement with published experimental data and numerical results obtained for the flow around an isolated cylinder. Results for lower Reynolds number flows have also been computed for comparison with the high Reynolds number flow results. The main results are summarized as follows:

1. The time-averaged drag coefficient (C_D) of the cylinder increases as the gap to diameter ratio (G/D) increases for small G/D. This is qualitatively the same behaviour as for lower Reynolds numbers. C_D reaches a maximum value when the gap is substantially large. Then, it decreases approaching a constant. The higher bed roughness reduces C_D for the same Reynolds number and boundary layer thickness of the inlet flow.

2. For a small gap ($G/D = 0.1$, without vortex shedding), the mean pressure coefficient (C_p) around the cylinder is asymmetric about the horizontal centerline of the cylinder. The positive zone of C_p is skewed upstream near the gap, and consequently a net upward lift force is exerted on the cylinder. For an intermediate gap ($G/D = 0.25$, with vortex shedding), the positive pressure zone becomes symmetric at the front of the cylinder, but the suction at the gap is large, and causes a negative mean lift force on the cylinder. For large gaps, C_p becomes symmetric, and the mean lift force approaches zero.

3. Suppression and formation of the vortex shedding are influenced by the interaction between three shear layers; two from the top and the bottom of the cylinder and one at the bed. The vortex shedding is suppressed when the gap is smaller than the critical gap (i.e. corresponding to the onset of vortex shedding). Beyond the critical gap, vortex shedding develops as the gap increases, and becomes fully developed as the influence of the bed diminishes.

4. For the same Reynolds number (Re), inlet boundary layer thickness (δ), bed roughness (z_w) and cylinder, the magnitude of negative pressure coefficient at the bed at the location of the gap increases as the gap (G) becomes smaller; and it increases as Re increases for the same δ, G and z_w.

5. There is no variation of the instantaneous friction velocity (u_{*w}) with time along the flat bed downstream of the gap for gaps smaller than the critical gap. The temporal variation of u_{*w} is substantial for the gap slightly larger than the critical gap; and it becomes weaker as the gap increases. The mean friction velocity at the gap (at the bed) is much larger for small gaps than for large gaps. This is due to the higher velocities within the gap when the gap is small. As a consequence, the bedload sediment transport is much larger for small gaps than for large gaps.

Overall it appears that the present approach is suitable for design purposes at high Reynolds numbers which are present near the seabed in the real ocean. However, experimental data are required in order to perform a more detailed validation study of the model.

Acknowledgements

References

Achenbach, E. (1968). Distribution of local pressure and skin friction around a circular cylinder in cross-flow up to Re $=5\times10^6$. *Journal of Fluid Mechanics,* 34 (4), 625-639.

Bearman, P.W. and Zdravkovich, M.M. (1978). Flow around a circular cylinder near a plane boundary. *Journal of Fluid Mechanics*, 89(1), 33-47.

Brørs, B. (1999). Numerical modeling of flow and scour at pipelines. *Journal of Hydraulic Engineering*, 125(5), 511-523.

Catalano, P., Wang, M., Iaccarino, G. and Moin, P. (2003). Numerical simulation of the flow around a circular cylinder at high Reynolds numbers. *International Journal of Heat and Fluid Flow*, 24, 463-469.

Gresho, P.M. and Sani, R.L. (1999). *Incompressible flow and the finite element method,* John Wiley & Sons Ltd, West Sussex, England.

Jensen, B.L., Sumer, B.M., Jensen, H.R. and Fredsøe, J. (1990). Flow around and forces on a pipeline near a scoured bed in steady current. *ASME Journal of Offshore Mechanics and Arctic Engineering*, 112, 206-213.

Lei, C., Cheng, L. and Kavanagh, K. (1999). Re-examination of the effect of a plane boundary on force and vortex shedding of a circular cylinder. *Journal of Wind Engineering and Industrial Aerodynamics*, 80(3), 263-286

Lei, C., Cheng, L., Armfield, S.W. and Kavanagh, K. (2000). Vortex shedding suppression for flow over a circular cylinder near a plane boundary. *Ocean Engineering*, 27, 1109-1127.

Launder, B.E. and Spalding, D.B. (1972). *Mathematical models of turbulence,* Academic Press, London.

Majumdar, S. and Rodi, W. (1985). Numerical calculation of turbulent flow past circular cylinder. *Proc. 7th Turbulent Shear Flow Symposium*, Stanford, USA, 3.13-3.25.

Mittal, R. and Balachandar, S. (1995). Effect of three-dimensionality on the lift and drag of nominally two-dimesional cylinders. *Phys. Fluids*, 7, 1841-1865.

Nielsen, P. (1992). *Coastal Bottom Boundary Layers and Sediment Transport.* World Scientific, Singapore.

Ong, M.C., Utnes, T., Holmedal, L.E., Myrhaug, D. and Pettersen, B. (2008). Numerical simulation of flow around a marine pipeline close to the seabed. *Proc. 31st Int. Conf. Coast. Eng.*, Hamburg, Germany. (In press).

Ong, M.C., Utnes, T., Holmedal, L.E., Myrhaug, D. and Pettersen, B. (2009). Numerical simulation of flow around a smooth circular cylinder at very high Reynolds numbers. *Marine Structures*, 22, 142-153.

Rodi, W. (1993). *Turbulence models and their application in hydraulics. A state-of-the-art review. IAHR Monograph Series, 3rd Ed.,* A.A. Balkema, Rotterdam, Netherlands.

Sumer, B.M. and Fredsøe, J. (2002). *The Mechanics of Scour in the Marine Environment: Advanced series on ocean engineering- Vol. 17*, World Scientific, Singapore.

Taniguchi, S. and Miyakoshi, K. (1990). Fluctuating fluid forces acting on a circular cylinder and interference with a plane wall. *Experiments in Fluids*, 9, 197-204.

Utnes, T. (1988). Two-equation (k, ε) turbulence computations by the use of a finite element model. *International Journal of Numerical Methods in Fluids*, 8, 965-975.

Utnes, T. (2008). A segregated implicit pressure projection method for incompressible flows. *Journal of Computational Physics*, 227, 2198-2211.

Wang, X. and Tan, S.K. (2008). Near-wake flow characteristics of a circular cylinder close to a wall. *Journal of Fluids and Structures*, 24(5), 605-627.

Zhao, M., Cheng, L. and Teng, B. (2007). Numerical modeling of flow and hydrodynamics forces around a piggyback pipeline near the seabed. *Journal of Waterway, Port, Coastal and Ocean Engineering*, 133(4), 286-295.

Zdravkovich, M.M. (1985). Forces on a circular cylinder near a plane wall. *Applied Ocean Research*, 7(4), 197-201.

Zdravkovich, M.M. (1997). *Flow around Circular Cylinders, Vol. 1: Fundamentals*, Oxford University Press, New York.

Chapter 9

Scour at Marine Structures and Stochastic Approach

9.1. Introduction

When a marine structure is placed in open sea environments, the flow field will be changed due to the presence of the structure. This may result in contraction of flow, formation of lee-wake vortices behind the structure, formation of a horseshoe vortex in front of the structure, generation of turbulence, occurrence of reflection and diffraction of waves, etc. (Sumer and Fredsøe, 2002). These changes will cause an increase of the local sediment transport rate and thus lead to scour. Scour is defined as the erosion of sediments caused by the presence of a structure (Coastal Engineering Manual, 2001).

Excessive scour gives threats to the stability of marine structures and may further lead to failure of the structures. The type of structures, where such local scour is involved, vary from simple structures, such as a pipeline, a pile or a trunk section of vertical-wall breakwater, to complex structures such as a group of piles, a sub-sea template, or an offshore platform. These structures are exposed to currents, waves and combined waves and currents. This causes high complexity of the flow mechanisms around the structures.

This chapter will describe the basic concepts of scour, such as amplification factor in the bed shear stress near a structure, equilibrium of scour and time scale of scour, difference between clear-water scour and live-bed scour, and difference between local scour and global scour.

Effects of random waves on the scour below marine pipelines and the scour at the trunk section of breakwaters will be discussed in Chapters 10 and 11, respectively. Hence, brief literature reviews on mechanisms of the scour below the pipelines (Section 9.3) and the scour around the breakwaters (Section 9.4) will be given.

Section 9.5 describes the stochastic approach proposed by Myrhaug and Rue (2003), which is used in the present analytical studies of random-wave induced scour.

9.2. Basic Concepts of Scour

The presence of the structure will change the flow in its neighborhood. This local change usually causes an increase of the bed shear stress and the degree of turbulence level close to the structure. It is well-known that the seabed shear stress is the governing parameter for the amount of sediment transport. Hence the change in the flow will lead to an increase in the local sediment transport rate.

The increase in the bed shear stress is expressed by the amplification factor β, defined by

$$\beta = \frac{\tau}{\tau_\infty} \qquad (9.1)$$

where τ is the bed shear stress and τ_∞ is the bed shear stress for the undisturbed flow. For $\beta > 1$, the sediment transport rate will increase as the bed load is proportional to $\tau^{3/2}$, and scour occurs. This process will continue until the scouring reaches a situation where $\beta = O(1)$ for the bed shear stress around the structure. When the scour process ceases, the stage is called the equilibrium stage.

Figure 9.1 shows a general time development of scour depth. It is observed that a substantial amount of scour needs a certain amount of time to develop. This time T is called the time scale of the scour process and defined as (Sumer and Fredsøe, 2002)

$$S_t = S\left(1 - \exp\left(\frac{t}{T}\right)\right) \qquad (9.2)$$

where S is the equilibrium scour depth, i.e. the scour depth corresponding to the equilibrium stage; S_t is the instantaneous scour depth; and t is the time.

The scour depth is an important parameter because it indicates the degree of scour potential. Hence engineers require this information essentially in designing foundations of marine structures and scour protections. Furthermore, scour often happens during storms. In order to check whether the storm lasts longer than the time needed for a substantial amount of scour to occur, the time scale becomes an essential parameter for this engineering assessment. The

time scale of the scour around marine structures may vary from hours to years (Smith and Foster, 2002).
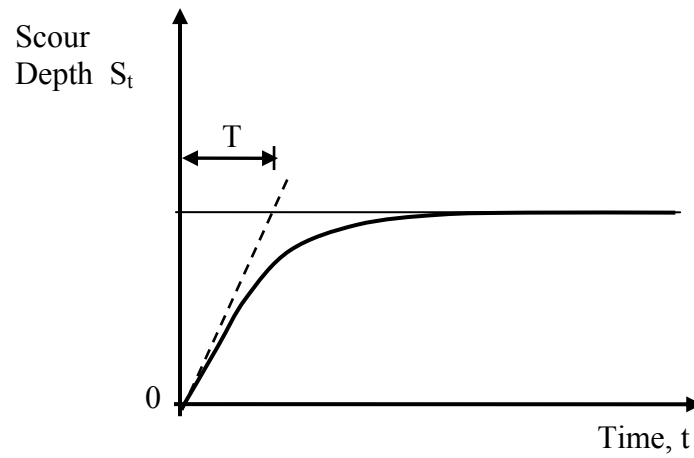
Figure 9.1. Time development of scour depth (reproduced from Sumer and Fredsøe (2002)).

Moreover, scour may be classified in two categories, which are clear-water scour and live-bed scour. The category can be determined by judging the Shields parameter, θ_s, defined as

$$\theta_s = \frac{\tau_\infty}{\rho g \left(s-1 \right) d_{50}} \tag{9.3}$$

where $s = \rho_s/\rho$ is the sediment density to fluid density ratio; ρ_s is the sediment density; d_{50} is the median grain size of the sediments; g is the gravitational acceleration. Note that τ_∞ should be replaced by the maximum value of undisturbed shear stress, $\tau_{\infty,max}$, in the case of waves. The incipient motion of sediments on the seabed will occur when θ_s is larger than a critical value, θ_{scr}, of the inception of sediment motion. More details on the basic concepts of sediment transport are given in Fredsøe and Deigaard (1992, Ch. 7).

In clear-water scour, no sediment motion take places far from the structure ($\theta_s < \theta_{scr}$), whereas the sediment transport prevails over the entire bed in live-bed scour ($\theta_s > \theta_{scr}$) (Sumer and Fredsøe, 2002).

Scour can appear as both local scour and global scour. Figure 9.2 shows these two kinds of scour at a piled steel platform when exposed to a flow action (Angus and Moore, 1982). The local scour holes are seen around the individual supporting piles, and the global scour hole is observed beneath and around the structure in the form of a saucer-shaped depression (Sumer and Fredsøe, 2002). The global scour is generally caused by the combined action of all the flow effects generated by the individual structural elements.
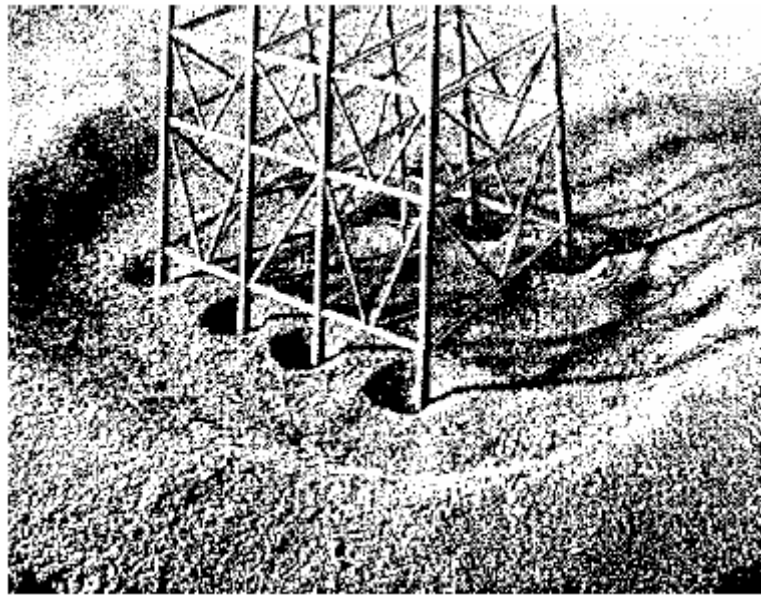
Figure 9.2. Scour around a piled steel platform. Angus and Moore (1982)

9.3. Scour below Marine Pipelines

Marine pipelines are installed in open sea environments for transportation of crude oil and gas from offshore platforms or disposals of industrial and municipal wastewater. Typically, the size of the pipeline varies from 0.3m to more than 1.0m in diameter, and the length may be up to a few hundred kilometers. Normally the pipeline is laid on the seabed or buried in the seabed. However, scour may lead to a free span with a gap (G) between the pipeline and the seabed usually in the range $0.1D$ to $1D$. Here the process of scour and the two-dimensional (2D) scour under the effects of currents, waves, waves plus current and shoaling conditions are described.

9.3.1 Process of scour

A whole scour process can usually be divided into four stages which are onset of scour, followed by tunnel erosion, lee-wake erosion, and finally the equilibrium state.

9.3.1.1 Onset of scour

The onset of scour is related to the seepage flow in the sand beneath the pipeline, which is driven by the pressure difference between the upstream and downstream sides of the pipeline (Fig. 9.3 and Fig. 9.4) when it is subject to a current (Sumer and Fredsøe, 2002). When the current velocity is increased, a critical point is reached where the discharge of the seepage flow will be increased more rapidly than the driving pressure difference. At location A (Fig. 9.4), the surface of the sand will rise, and then a mixture of sand and water will break through the space beneath the pipeline. This process is called piping (Sumer and Fredsøe, 2002).
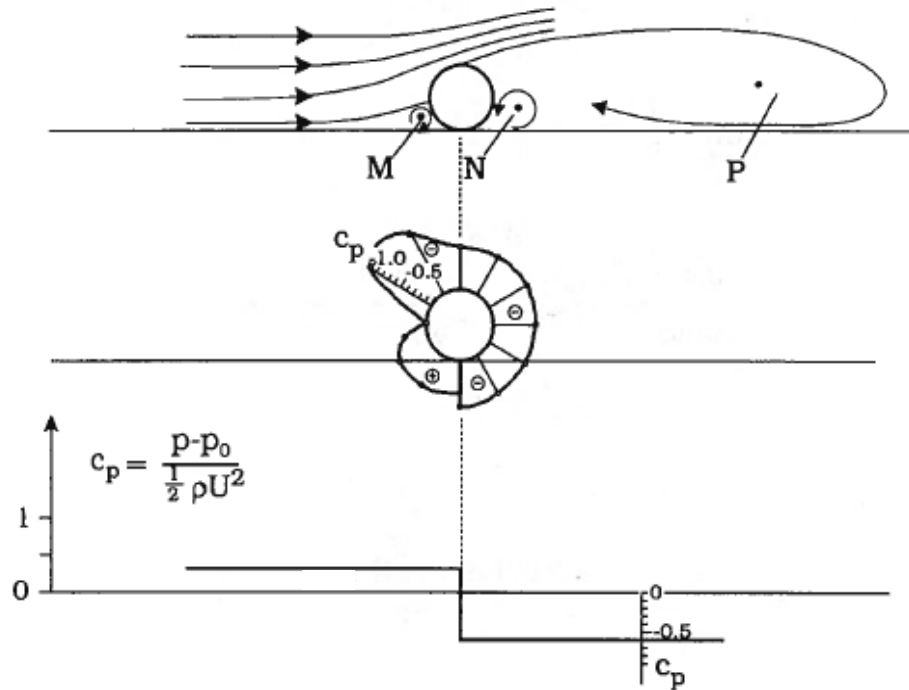
Figure 9.3. Pressure distributions for bottom-seated pipe (from Sumer and Fredsøe (2002)).
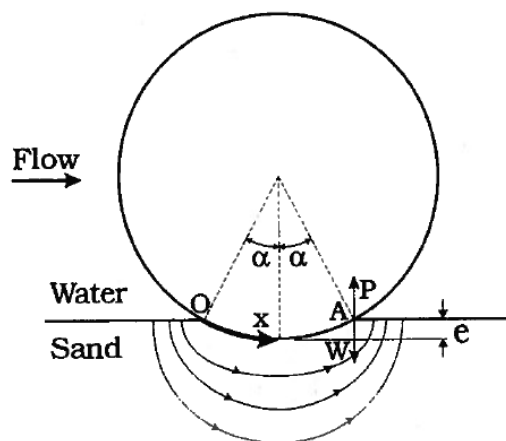
Figure 9.4. Seepage flow underneath the pipe. Here *W* is the submerged weight of the sand. *e* is the burial depth (from Sumer and Fredsøe (2002)).

Cevik and Yüksel (1999) described the undisturbed flow around the pipeline by three vortices (A, B and C) in the neighbourhood of the pipeline in Fig. 9.5. Vortex A is at the upstream side of the pipeline; Vortex C is at the downstream side of the pipeline; and there is one larger vortex, Vortex B, behind Vortex C. Vortex A and C move sediments away from the footing in opposite directions. Vortex B moves sediments towards the pipe. The scour process in close vicinity downstream of the pipeline (i.e. close to A in Fig. 9.4) is enhanced by the pressure difference driven seepage flow beneath the pipeline. The seepage flow reduces the submerged weight of sediments at the immediate downstream side of the pipeline and causes the sediments to be more easily entrained by Vortex C. Eventually a small gap will be formed beneath the pipeline and the scour process has reached the next stage, tunnel erosion.
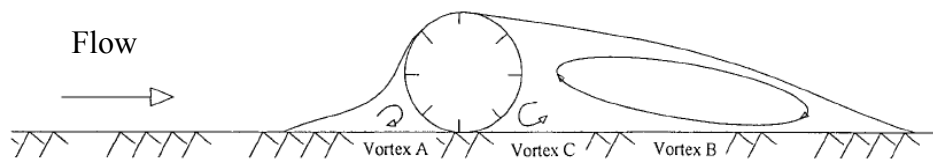
Figure 9.5. Sketch of the three vortices (reproduced from Cevik and Yüksel (1999)).

It should also be noted that visual observations made by Sumer et al. (2001) showed that vortices generated downstream and upstream sides of the pipeline (corresponding to vortices C and A, respectively, in Fig. 9.5) did not undermine the pipeline prior to the onset of scour. This is contrary to the generally accepted view by Mao (1986), Chiew (1990), Sumer and Fredsøe (1991) and Cevik and Yuksel (1999).

Sumer and Fredsøe (2002) studied the onset of scour in both current and waves. Breakthrough at the critical condition and piping occurs in both current and waves. However, the exposure time of the critical pressure gradient in the two cases is different and therefore it gives different breakthrough processes. In the case of current, the onset of scour and the piping are the same as described earlier. In the case of waves, the varying wave height affects the breakthrough process. According to Sumer and Fredsøe (2002), the onset of scour takes place in a crest-half period, while the trough-half periods do not have large enough pressure difference to onset the scour. A detailed explanation on this phenomenon is given in Sumer and Fredsøe (2002).

9.3.1.2. Tunnel erosion

After the onset of scour has occurred and the piping has started, the next stage in the scour process is tunnel erosion. In this stage the gap between the pipeline and the bed, G, remain

small, i.e. G<<D. As shown in Fig. 9.6, a substantial amount of water is diverted through the gap, leading to very large velocities in the gap. This results in very large shear stresses on the bed just below the pipeline. Similar flow phenomenon is observed in the present numerical work – flow around a circular cylinder close to a flat bed, as shown in Chapters 7 and 8.
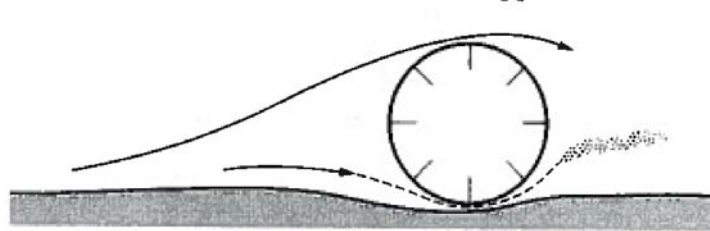
Figure 9.6. Tunnel erosion below a pipeline (from Sumer and Fredsøe (2002)).

The large increase in the bed shear stress below the pipeline results in a significant increase in the sediment transport. For example, by considering $q_b \sim \tau^{3/2}$ in which q_b is the sediment transport rate , a factor of 4 increase in the bed shear stress causes a factor of 8 increase in the sediment transport. Hence, the scour below the pipeline occurs violently, and a mixture of sand and water flows as a violent "jet" (Mao (1986), Sumer and Fredsøe (2002)). As the gap becomes larger due to the scour, the flow velocity in the gap decreases. The scour process moves to the next stage, lee wake erosion.

9.3.1.3. Lee-wake erosion

This stage of the scour process is governed by the vortex-shedding behind the pipeline. Vortex shedding will occur when the gap between the pipeline and the bed reaches a critical value due to scour (Sumer et al., 1988). This flow mechanism has also been discussed in Chapters 7 and 8. The vortices shed from the downstream side of the pipeline sweep the bed, as they are transported downstream (Fig. 9.7). According to Sumer et al. (2003), bed shear stress measurements show that the Shields parameter can easily be increased up to O(4) times during the vortex shedding period. This will result in significant increase of sediment transport at the lee side of the pipeline.
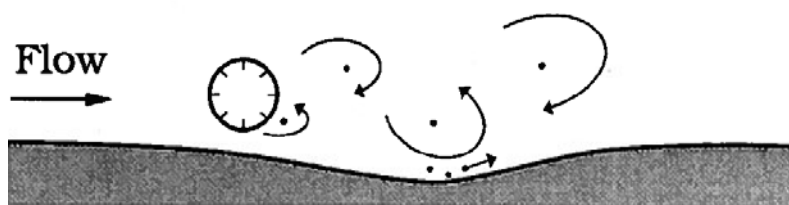
Figure 9.7. Sediment motion caused by vortex shedding (from Sumer et al. (1988)).

9.3.1.4. Equilibrium stage

Beyond the lee-wake erosion, the scour process finally reaches a steady state, called the equilibrium stage. The equilibrium stage is reached when the bed shear stress along the bed underneath the pipeline becomes constant and equal to its undisturbed value, $\tau = \tau_\infty$. The sediment transport is the same over the reach of the scour hole. It means that the amount of sediment which enters the scour hole is identical to that leaving the scour hole in this stage.

9.3.2. Two-dimensional scour depth

The scour process can be considered as a two-dimensional (2D) process or a three-dimensional (3D) process. The scour development at the cross-section of the pipeline is considered for a 2D process. For a 3D process, the scour development along the length of the pipeline is also taken into consideration. In this thesis only 2D scour is considered. The scour depth corresponding to the fully developed stage is called the equilibrium scour depth. This section focuses on the equilibrium scour depth.

The scour depth in steady current has been studied extensively by e.g. Chao and Hennessy (1972), Kjeldsen et al. (1973), Bijker and Leeuwenstein (1984), Lucassen (1984), Herbich (1985), Mao (1986), and Kristiansen and Tørum (1989). An illustration of this scour process is shown in Fig. 9.7. The non-dimensional scour depth *S/D* is found to depend on the following parameters:

$$\frac{S}{D} = f\left(\frac{K_N}{D}, \text{Re}, \theta_s\right) \tag{9.4}$$

The influence of Reynolds number (*Re*) and relative roughness (K_N /D) appears through their effects on the downstream flow of the pipe. If the pipe is hydraulically rough, the wake flow is almost unaffected by *Re*, but for a hydraulically smooth pipe, the influence of Re is expected in the downstream of vortex shedding pattern (Sumer and Fredsøe, 2002). Regarding the influence of the Shields parameter (θ_s), clear-water scour ($\theta_s < \theta_{scr}$) and live-bed scour ($\theta_s > \theta_{scr}$) should be considered. In the clear-water case, the variation in scour depth with θ_s is more pronounced than that in the live-bed case. As the variation of scour depth with θ_s in the case of live bed is very small, this weak variation is often neglected (Sumer and Fredsøe, 2002). Details of the scour depth formulas are given in Sumer and Fredsøe (2002).

In the ocean, the pipe is also exposed to the flow from both sides due to the near-bed oscillatory flow induced by waves. The main difference between the wave case and the steady current case is that the downstream wake system now occurs on the both sides of the

pipe. Figure 9.9 shows the scour process in waves. In this case the flow is governed by the Keulegan-Carpenter number (KC) defined as (Sumer and Fredsøe, 2002)

$$KC = \frac{U_m T_w}{D}$$ (9.5)

where T_w is the wave period.
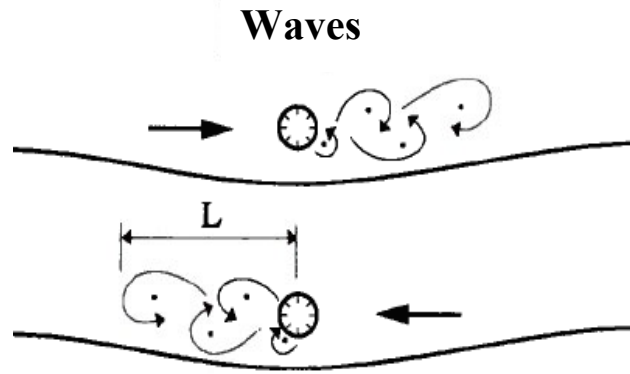
Waves

Figure 9.9. The scour process in waves (from Sumer and Fredsøe (2002)).

In the case of random waves, Sumer and Fredsøe (1996) determined the properties of the random variables wave height H and wave period T_w to be used to represent the scour depth below pipelines. By trial and error they found that the use of the root-mean-square (rms) wave height, H_{rms}, and the peak period of wave spectrum, T_p, in an otherwise deterministic approach gave the best agreement with data. Hence the scour depth in the case of random waves can be predicted using the regular wave expression provided that KC is calculated by

$$KC_{SF} = \frac{\sqrt{2}\sigma_U T_P}{D}$$ (9.6)

where σ_u is the rms value of the orbital velocity at the bed.

The scour depth in combined waves and current has been studied by Lucassen (1984), Hansen (1992) and Sumer and Fredsøe (1996). Sumer and Fredsøe (1996) presented their experimental data under combined irregular waves and current with KC_{SF} ranging from 5 to about 50 and the full range of $U_c/(U_c+U_m)$ (from 0 to 1) in live-bed conditions. Their experimental data shows that the scour depth may increase or decrease depending on the values of KC and $U_c/(U_c+U_m)$. Sumer and Fredsøe (1996) also found that their empirical formula for the scour depth for regular waves (Sumer and Fredsøe (1990)) can be used for random waves provided that the governing parameter, such as KC, in the regular wave

equations are represented by H_{rms} and T_p. Details of the scour depth formulas are given in Sumer and Fredsøe (1996, 2002).

Cevik and Yüksel (1999) studied the effect of shoaling conditions on the scour depth below pipelines beneath non-breaking and breaking regular waves using three kinds of bottom slopes, which are the horizontal bottom, and two beach profiles with slopes 1/5 and 1/10. They found that the scour depth in the case of the shoaling condition is always larger than that in the case of the horizontal bottom under the same incident wave conditions. This is important to consider in engineering design, i.e. scour protection measures should be assessed in areas where shoaling conditions prevails. Chapter 10 presents the study of random wave-induced scour below marine pipelines in shoaling conditions by using a stochastic approach (see Section 9.5).

Sumer and Fredsøe (1990, 1996) measured the scour width for the cases of waves alone and combined waves plus current. The net effect of a current on waves is to make the scour width at the downstream side of the pipe larger than that at the upstream side due to the effect of the lee-wake (Sumer and Fredsøe, 1996). The scour width formulas are given in Sumer and Fredsøe (1990, 1996, 2002).

9.4. Scour around Breakwaters

A shore area, a harbour, or a basin is vulnerable to wave action. Breakwaters are needed to protect these areas from damages created by waves. However, scour is one of the failure modes of breakwaters. According to Fredsøe and Sumer (1997) it is not unusual to observe scour holes with depths larger than 10m at the head of a breakwater at an exposed location. Oumeraci (1994) reported vertical-wall breakwater failures due to scour. Lillycrop and Hughes (1993) gave many examples of scour hole formations at the toe and along the sides of rubble-mound breakwaters and jetties, and the resulting failures monitored. According to them, the repair cost is usually at the level of $2-10 million. Günbak et al. (1990) reported damage to the "bend" section of the main rubble-mound breakwater of Samandag Fishing Port near Iskenderm, Turkey, due to a scour depth of 4-5m at the toe. Silvester and Hsu (1997) presented field evidences of scour from Europe, Japan, United States and Africa.

A definition sketch of a breakwater is illustrated in Fig. 9.10. There are two kinds of scour processes for the breakwater. One is the scour process around the head of the breakwater (A, in Fig. 9.10) and the other is that in front of the structure along the length of the trunk section (B, in Fig. 9.10). When the waves attack at normal incidence angle to the breakwater, the scour in front of the trunk section is 2D, and that at the head is 3D.
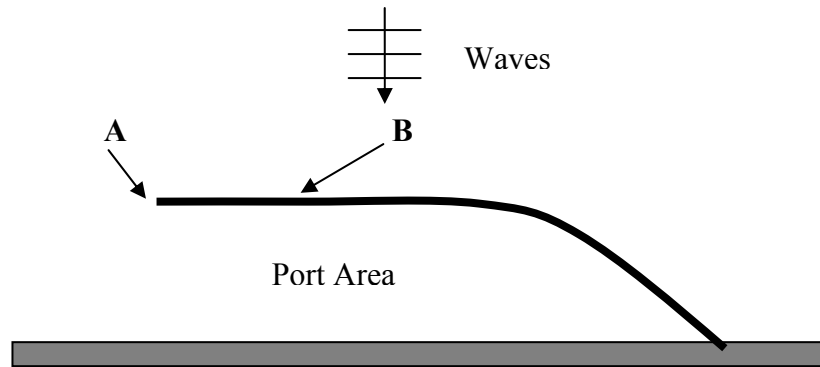
Figure 9.10. Definition sketch of a breakwater. A: Head. B: Trunk section (reproduced from Sumer and Fredsøe (2002)).

Sumer and Fredsøe (1997) and Fredsøe and Sumer (1997) performed experimental studies on scour around the heads of a vertical-wall breakwater and a rubble-mound breakwater, respectively. In the case of scour at the head of a vertical-wall breakwater where the waves are propagating in the direction perpendicular to the breakwater, separation vortices form at the lee side during each half period of the waves. Sumer and Fredsøe (1997) commented that these lee-wake vortices mainly cause the scour occur. In the case of scour around the round head of a rubble-mound breakwater, two key mechanisms have been identified in the study of Fredsøe and Sumer (1997): (1) the wave-induced steady streaming around the head; and (2) the plunging breaker occurring locally at the head. A detailed summary of these scour mechanisms is given in Sumer and Fredsøe (2002). Moreover, the empirical formulas for the scour depth and the protection layer width are given in Sumer and Fredsøe (1997), Fredsøe and Sumer (1997) and Sumer and Fredsøe (2002).

Myrhaug et al. (2004) proposed a stochastic approach by which the scour depth and protection layer width around the head of a vertical breakwater in random waves can be derived. The formulas for scour depth and protection layer width by Sumer and Fredsøe (1997) and Fredsøe and Sumer (1997) are used together with describing the waves as a stationary Gaussian narrow-band random process to derive the formulas for scour depth and protection layer width in random waves. They suggested that the scour variable formulas for regular waves can be applied for random waves if the random waves are represented by the mean of the $1/n$'th highest waves. The value of n should be chosen based on the real wave conditions at the location where the breakwater will be located.

Chapter 10 will present scour depth predictions at the trunk section of breakwaters for random waves. Hence, descriptions of the scour mechanisms at the trunk section of vertical-wall breakwaters and rubble-mound breakwaters are given in the following subsections, respectively.

9.4.1. Scour mechanism at the trunk section of a vertical-wall breakwater

When a vertical, rigid wall (Fig. 9.11) is subject to a incident progressive wave, a reflected wave will move in the offshore direction. This results in a superposition of these two waves and leads to occurrence of a standing wave. The height of the standing wave is twice the wave height (H) of each of the two progressive waves forming the standing wave (see Dean and Dalrymple (1984)).

The standing wave generates a field of steady streaming, i.e. a system of recirculating cells consisting of bottom and top cells (Sumer and Fredsøe (2002), Carter et al.(1973)). If the sediment grain size is relatively small, the sediments will be stirred up by the wave-induced flow and brought up into the suspension. They will be carried to a higher elevation, mostly to the top cells. Figure 9.12a shows the corresponding scour and deposition pattern as demonstrated experimentally by Xie (1981). If the sediment grain size is relatively coarse, the sediments will be transported in no-suspension mode. Sediment transport activity will mainly remain in the bottom cells. The scour and deposition pattern are shown in Fig. 9.12b.
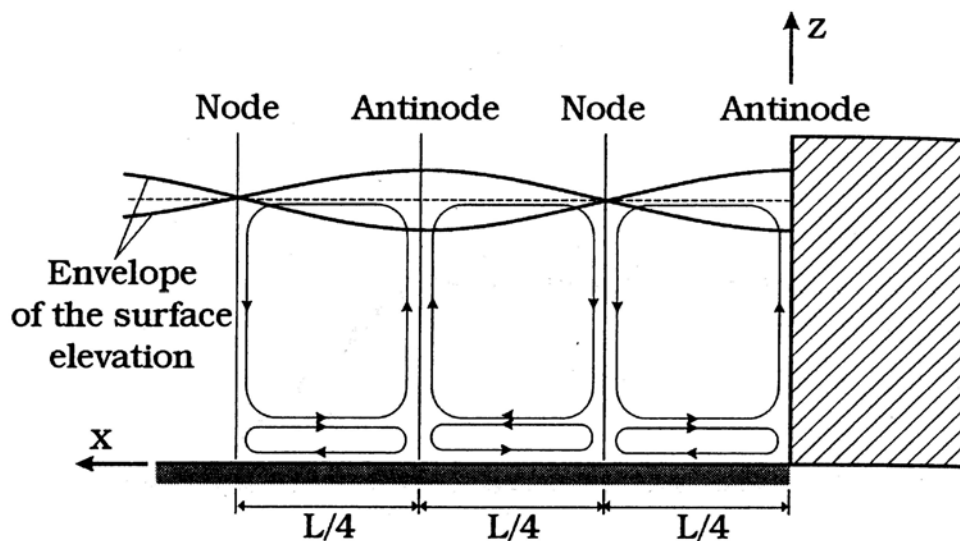
Figure 9.11. Steady streaming in the vertical plane in front of a breakwater. Here L_w is the wave length (from Sumer and Fredsøe (2002)).
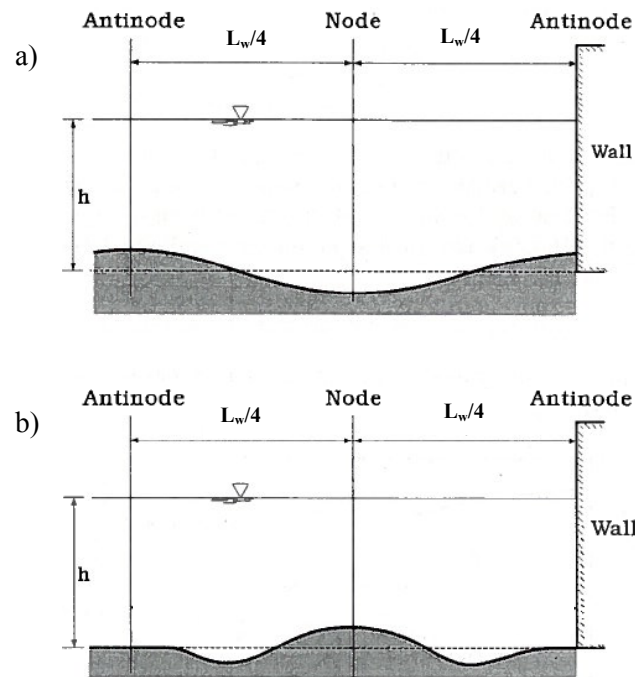
Figure 9.12. Scour/deposition pattern at the trunk section of a vertical-wall breakwater. (a) Suspension mode (b) No-suspension mode (from Xie (1981)). Here *h* is the water depth.

9.4.2. Scour mechanism at the trunk section of a rubble-mound breakwater

A rubble-mound breakwater has two differences in structural aspect as compared with a vertical-wall breakwater. Firstly the breakwater is made of rubble; and secondly it has a sloping wall, usually in the range 1:1.3 to 1:2. These differences will cause the reduction of reflection coefficient and affect the steady streaming. Consequently, the scour processes will be different (Sumer and Fredsøe, 2002).

In order to study the differences in the two scour processes clearly, Sumer and Fredsøe (2000) made 2D breakwater models with three slopes, i.e. 1:1.75, 1:1.2 and one with a vertical-wall. The sand transport in their tests was in the no-suspension mode.

Figure 9.13 shows the scour/deposition profiles from the Sumer and Fredsøe (2000) study for two breakwater slopes; the vertical-wall (Fig. 9.13a) and the slope 1:1.2 (Fig. 9.13b). They observed that the scour/deposition of the rubble-mound breakwater occurs mostly in the same way as in the case of the vertical-wall breakwater, but there are several differences between these two cases:

i) The scour at the toe of the rubble-mound breakwater has a non-zero value (Fig. 9.13b) while it is zero in the vertical-wall breakwater case (Fig. 9.13a). This is because the

steady streaming at the toe of the rubble-mound breakwater is significant, while it is practically nonexistent in the vertical-wall breakwater case. This is evidently related to the sloping surface of the breakwater. It should be noted that there may be a flow from inside the rubble-mound breakwater towards the sand layer, and it will enhance the scour at the toe.

ii) A substantial amount of scour occurs below the antinode point in the case of the rubble-mound breakwater, but no signicant scour is observed at the same location for the vertical-wall breakwater. Sumer and Fredsøe (2000) commented that no clear explanation has been found for this behaviour.

iii) Due to the smaller reflection, the streaming in the case of the rubble-mound breakwater is weaker than that for the vertical-wall breakwater. It therefore results in smaller scour for the rubble-mound breakwater than that for the vertical-wall breakwater.
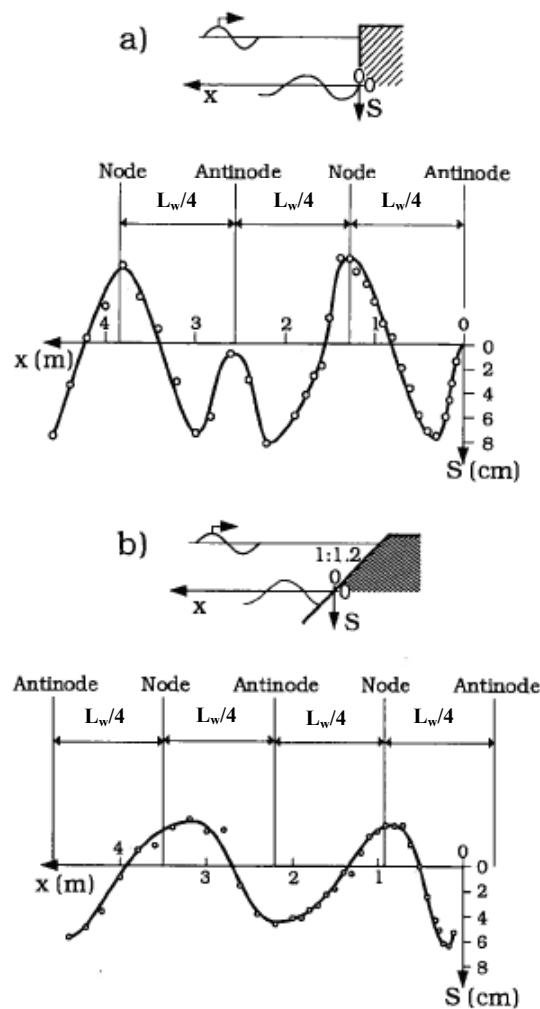
Figure 9.13. Scour/deposition in front of (a) a vertical-wall breakwater and (b) a rubble-mound breakwater (from Sumer and Fredsøe (2000)).

iv) It is observed that the precise location of the maximum deposition for the rubble-mound breakwater appears to be shifted slightly in the onshore direction (Figs. 9.13a and 9.13b). This shift may be caused by the phase shift on the reflected waves in the case of a sloping structure (Hughes and Fowler, 1995). This will lead to a change in the locations of nodes and antinodes as seen in Figs. 9.13a and 9.13b.

9.5. Outline of Stochastic Approach

For scour below pipelines and around vertical piles in random waves Sumer and Fredsøe (1996, 2001) determined the characteristics of the random variables wave height and wave period to be used to represent the scour depth and width below pipelines and scour depth around slender vertical piles. By trial and error they found that use of H_{rms} and T_p in an otherwise deterministic approach gave the best agreement with data. Here a stochastic approach is outlined. The highest among random waves in a stationary narrow-band sea state are considered, as it is reasonable to assume that it is mainly the highest waves which are responsible for the scour response. It is also assumed that the sea state has lasted long enough to develop the equilibrium scour depth. Let x represent A, U_m or H. The highest waves considered here are those which cause the random variable x to be exceeded by the probability $1/n$, $x_{1/n}$. The quantity of interest here is the expected (mean) scour response caused by the highest waves, which is given as

$$E\left[S(x)\,|\,x > x_{1/n}\right] = n \int_{x_{1/n}}^{\infty} S(x)\,p(x)\,dx \qquad (9.7)$$

where $p(x)$ is the probability density function (*pdf*). More specifically, the present method is based on the following assumptions: (1) the free surface elevation $\zeta(t)$ is a stationary Gaussian narrow-band random process with zero expectation described by the single-sided spectral density $S_{\zeta\zeta}(\omega)$, and (2) the scour depth formulas for regular waves are valid for irregular waves as well. These assumptions are essentially the same as those given in Myrhaug and Rue (2003, 2005), Myrhaug et al. (2004, 2007) and Myrhaug and Ong (2009), where further details are found.

Based on the present assumptions, the time-dependent near-bed orbital displacement $a(t)$ and the velocity $u(t)$ are both stationary Gaussian narrow-band processes with zero expectations and with single-sided spectral densities

$$S_{aa}(\omega) = \frac{S_{\zeta\zeta}(\omega)}{\sinh^2 kh} \tag{9.8}$$

$$S_{uu}(\omega) = \omega^2 S_{aa}(\omega) = \frac{\omega^2 S_{\zeta\zeta}(\omega)}{\sinh^2 kh} \tag{9.9}$$

It follows from the narrow-band assumption that the near-bed orbital displacement amplitude, A, the near-bed orbital velocity amplitude, U_m, and the linear wave height, H, are Rayleigh-distributed with the cumulative distribution function (*cdf*) given by

$$P(\hat{x}) = 1 - \exp(-\hat{x}^2) \quad ; \quad \hat{x} = x/x_{rms} \geq 0 \tag{9.10}$$

where x represents A, U or H, and x_{rms} is the *rms*-value of x representing A_{rms}, U_{rms} or H_{rms}.

Now A_{rms}, U_{rms} and H_{rms} are related to the zeroth moments of the amplitude, velocity and free surface elevation spectra m_{0aa}, m_{0uu} and $m_{0\zeta\zeta}$, respectively, given by

$$A_{rms}^2 = 2m_{0aa} = 2\sigma_{aa}^2 = 2\int_0^\infty S_{aa}(\omega)\,d\omega \tag{9.11}$$

$$U_{rms}^2 = 2m_{0uu} = 2\sigma_{uu}^2 = 2\int_0^\infty S_{uu}(\omega)\,d\omega \tag{9.12}$$

$$H_{rms}^2 = 8m_{0\zeta\zeta} = 8\sigma_{\zeta\zeta}^2 = 8\int_0^\infty S_{\zeta\zeta}(\omega)\,d\omega \tag{9.13}$$

From Eqs. (9.11) and (9.12), it also appears that $m_{0uu} = m_{2aa}$, where m_{2aa} is the second moment of the amplitude spectrum. The wave frequency ω is taken as the mean zero-crossing frequency for the near-bed orbital displacement, ω_z, which is obtained from the spectral moments of $a(t)$, giving

$$\omega = \omega_z = \left(\frac{m_{2aa}}{m_{0aa}}\right)^{1/2} = \left(\frac{m_{0uu}}{m_{0aa}}\right)^{1/2} = \frac{U_{rms}}{A_{rms}} \tag{9.14}$$

where Eqs. (9.11) and (9.12) have been used. This result is valid for a stationary Gaussian random process.

This stochastic approach is used in the study of scour below marine pipelines in shoaling conditions for random waves (Chapter 10) and the study of random wave-induced scour at the trunk section of a breakwater (Chapter 11). This approach has also been applied on scour around marine structures, e.g. Myrhaug and Rue (2003, 2005), Myrhaug et al. (2004, 2007) and Myrhaug and Ong (2009). These publications commented that more experimental data are required before a conclusion regarding the validity of this approach can be given. In the meantime, the method should be useful as an engineering tool for design purpose beneath random wave conditions.

134

References

Angus, N.M. and Moore, R.L. (1982). Scour repair methods in the Southern North Sea. *Proc. 14th Annual Offshore Tech. Conf.*, Houston, Texas, Paper No. 4410, pp. 385-399.

Bijker, E.W. and Leeuwenstein, N. (1984). Interaction between pipelines and the seabed under the influence of waves and currents. In: *Seabed Mechanics*, B. Denness, ed., Graham and Trotman, Gettysburg, Md., 235-242.

Carter, T.G., Liu, L.F.P. and Mei, C.C. (1973). Mass transport by waves and offshore sand bedforms. *J. Waterways, Harbors and Coastal Eng.*, ASCE, 99(WW2), 165-184.

Cevik, E. and Yüksel, Y., (1999). Scour under submarine pipelines in waves in shoaling conditions. *J. Waterway, Port, Coastal and Ocean Eng.,* ASCE, 125 (1), 9-19.

Chao, J.L. and Hennessy, P.V. (1972). Local scour under ocean outfall pipelines. *J. Water Pollution Control Fed.*, 44(7), 1443-1447.

Chiew, Y.M. (1990). Mechanics of local scour around submarine pipelines. *J. Hydr. Eng.*, ASCE, 116(4), 515-529.

Coastal Engineering Manual (2001). *Scour and Scour Protection. Chapter VI-5-6, Engineering Manual EM 1110-2-1100*, Headquarters, U.S. Army Corps of Engineers, Washington, D.C.

Dean, R. and Dalrymple, R.A. (1984). *Water Wave Mechanics for Engineers and Scientists*. Prentice-Hall, Inc., xi + 353p.

Fredsøe, J. and Deigaard, R. (1992). *Mechanics of Coastal Sediment Transport*. World Scientific, Singapore.

Fredsøe, J. and Sumer, B.M. (1997). Scour at the round head of a rubble-mound breakwater. *Coast. Eng.*, 29, 231-262.

Günbak, A.R., Gökçe, T. and Güler, I. (1990). Erosion and protection of Samandag Breakwater. *J. Coast. Res., Proc. of Skagen Symposium*, 2-5, vol. 2, 753-771.

Hansen, E.A. (1992). Scour below pipelines and cables: A simple model. *Proc 11th Offshore Mech. and Arctic Eng.*, ASME, Calgary, Canada, vol. V-A, Pipeline Technology, 133-138.

Herbich, J.B. (1985). Hydromechanics of submarine pipelines: Design problems. *Can. J. Civil Eng.*, 12(4), 863-887.

Hughes, S.A. and Fowler, J.E. (1995). Estimating wave-induced kinematics at sloping structures. *J. Waterway, Port, Coastal and Ocean Eng.*, ASCE, 121(4), 209-215.

Kjeldsen, S.P., Gjörsvik, O., Bringaker, K.G. and Jacobsen, J. (1973). Local scour near offshore pipelines. *2ⁿᵈ Int. Port and Ocean Eng. Under Artic Conditions*, Conf. Reykjavik, pp. 308-331.

Kristiansen, Ø. and Tørum, A. (1989). Interaction between current induced vibrations and scour of pipelines on a sandy bottom. *Proc. 8ᵗʰ Int. Conf. Offshore Mech. and Arctic Eng. ASME*, The Hague, The Netherlands, vol. V, pp. 167-174.

Lillycrop, W.J. and Hughes, S.A. (1993). Scour hole problems experienced by the Corps of Engineers; Data presentation and summary. Miscellaneous papers. CERC-93-2, US Army Engineer Waterways Experiment Station, Coast. Eng. Res. Center, Vicksburg, MS.

Lucassen, R.J. (1984). Scour underneath submarine pipelines. Report No. PL-4 2A, Netherlands Marine Tech. Res., Netherland Industrial Council for Oceanology, Delft University of Technology, Delft, The Netherlands.

Oumeraci, H. (1994). Review and analysis of vertical breakwater failures- lessons learned. *Coast. Eng.*, Special Issue on Vertical Breakwaters, vol. 22, 3-29.

Mao, Y. (1986). The Interaction Between a Pipeline and an Erodible Bed. Series Paper 39, Tech. Univ. of Denmark, ISVA, in partial fulfilllment of the requirement for the degree of Ph.D.

Myrhaug, D., Føien, H. and Rue, H. (2007). Tentative engineering approach to scour around spherical bodies in random waves. *Applied Ocean Research*, 29, 80-85.

Myrhaug, D. and Ong, M.C. (2009). Burial and scour of short cylinders under combined random waves and currents including effects of second order wave asymmetry. *Coast. Eng.*, 56(1), 73-81.

Myrhaug, D. and Rue, H. (2003). Scour below pipelines and around vertical piles in random waves. *Coast. Eng.*, 48, 227-242.

Myrhaug, D. and Rue, H. (2005). Scour around groups of slender vertical piles in random waves. *Applied Ocean Research*, 27, 56-63

Myrhaug, D., Rue, H. and Tørum, A. (2004). Tentative engineering approach to scour around breakwaters in random waves. *Coast. Eng.*, 51, 1051-1065.

Silvester, R. and Hsu, J.R.C. (1997). *Coastal Stabilization*. World Scientific, xvi + 578p.

Smith, H.D. and Foster, D.L. (2002). Modelling of flow and scour around a pipeline. *Proc. 28th Int. Conf. Coast. Eng.*, Cardiff, Wales, pp. 1722-1732.

Sumer, B.M., Chua, L.H.C., Cheng, N.S. and Fredsøe, J. (2003). Influence of turbulence on bed load sediment transport. *J. Hydr. Eng.,* ASCE, 129(8), 585-596.

Sumer, B.M. and Fredsøe, J. (1990). Scour below pipelines in waves. *J. Waterway, Port, Coastal and Ocean Eng.*, ASCE, 116(3), 307-323.

Sumer, B.M. and Fredsøe, J. (1991). Onset of scour below a pipeline exposed to waves. *Int. J. Offshore and Polar Eng.*, 1(3), 189-194.

Sumer, B.M. and Fredsøe, J. (1996). Scour around pipelines in combined waves and current. *Proc. 7th Int. Conf. Offshore Mech. and Arctic Eng.,* ASME, Florence, Italy, vol. V, Pipeline Technology, pp. 595-602.

Sumer, B.M. and Fredsøe, J. (1997). Scour at the head of a vertical-wall breakwater. *Coast. Eng.*, 29, 201-230.

Sumer, B.M. and Fredsøe, J., (2000). Experimental study of 2D scour and its protection at a rubble-mound breakwater. *Coast. Eng.*, 40, 59-87.

Sumer, B.M. and Fredsøe, J. (2001). Scour around pile in combined waves and current. *J. Hydr. Eng.*, ASCE, 127 (5), 403-411.

Sumer B.M. and Fredsøe J. (2002). *The Mechanics of Scour in the Marine Environment: Advanced series on ocean engineering- Vol. 17*, World Scientific, Singapore.

Sumer, B.M., Jensen, R., Mao, Y. and Fredsøe, J. (1988). The effect of lee-wake on scour below pipelines in current. *J. Waterway, Port, Coastal and Ocean Eng.* ASCE, 114(5), 599-614.

Xie, S.L. (1981). Scouring patterns in front of vertical breakwaters and their influence on the stability of the foundations of the breakwaters. Report, Department of Civil Eng., Delft University of Technology, Delft, The Netherlands, September, 61p.

Chapter 10

Scour Below Marine Pipelines in Shoaling Conditions for Random Waves

Dag Myrhaug, Muk Chen Ong and Cecilie Gjengedal

Department of Marine Technology,
Norwegian University of Science and Technology, NO-7491 Trondheim, Norway.

Abstract[#]

This paper provides an approach by which the scour depth below pipelines in shoaling conditions beneath non-breaking and breaking random waves can be derived. Here the scour depth formula in shoaling conditions for regular non-breaking and breaking waves with normal incidence to the pipeline presented by Cevik and Yüksel (1999) combined with the wave height distribution including shoaling and breaking waves presented by Mendez et al. (2004) are used. Moreover, the approach is based on describing the wave motion as a stationary Gaussian narrow-band random process. An example of calculation is also presented.

Keywords: Scour depth; Pipeline; Shear stress; Shoaling; Breaking; Random waves; Stochastic approach.

1.   Introduction

Pipelines on sandy seabeds in the coastal zone are exposed to random waves under shoaling and breaking conditions, and consequently the pipelines are exposed to scour. The assessment

---

of scour below pipelines is essential in design of marine pipelines and in scour protection work.

A pipeline originally installed on a plane bed consisting of fine sand may experience a range of seabed conditions, i.e., the bed may be flat or rippled; the pipeline may be partly or fully buried or in free spans. This is caused by the complicated flow generated by the interaction between the incoming flow, the pipeline and the seabed. The result will depend on the incoming flow velocity (e.g., the relative magnitude between waves and current), the geometry of the bed and the bed material, as well as the ratio between the near-bed oscillatory fluid particle excursion amplitude and the diameter of the pipeline. The flow is in the rough turbulent regime; therefore, an essential part of the flow modelling even in the simplest case of, e.g., a pipeline resting on a flat seabed exposed to steady flow is the turbulence modelling. Furthermore, real waves are stochastic, and e.g., pipelines in free span will behave as a hydroelastic structure and thereby interact with the ambient flow, making the problem more complex. Further details on the background and complexity as well as reviews of the problem are given in, e.g., Whitehouse (1998), Sumer and Fredsøe (2002). Cevik and Yüksel (1999) presented results from a laboratory study on the effect of shoaling conditions on the scour depth below pipelines. The pipeline was exposed to non-breaking and breaking regular waves with normal incidence to the pipeline using three bed slopes, i.e. horizontal bed and two beaches with slopes 1/5 and 1/10. To our knowledge no studies are available in the open literature dealing with random wave scour under shoaling conditions.

The purpose of this paper is to provide a practical approach for estimating the scour depth below pipelines in shoaling conditions beneath non-breaking and breaking random waves with normal incidence to the pipeline. This is achieved by using the scour depth formula for non-breaking and breaking regular waves in shoaling conditions presented by Cevik and Yüksel (1999) combined with the wave height distribution including shoaling and breaking waves presented by Mendez et al. (2004), and the scour depth is derived. The wave motion is assumed to be a stationary Gaussian narrow-band random process. An example of calculation is also given to demonstrate the application of the method.

2. Scour in Regular Waves

The scour below pipelines in shoaling conditions for non-breaking and breaking regular waves was investigated in laboratory tests by Cevik and Yüksel (1999) for horizontal bed and for sloping beds with the two beach slopes 1/5 and 1/10. The experiments were carried out for spilling and plunging breakers, from intermediate water depth to the plunging point (Yüksel, 2008). They obtained the following empirical formula for the equilibrium scour

depth, S, below a pipeline with diameter D with normal incidence of waves to the pipeline (see Fig. 1)

$$\frac{S}{D} = a U_{RP}^{b} \qquad \text{for} \qquad 2 \,\char94\, U_{RP} \,\char94\, 3000 \qquad (1)$$

where a and b are coefficients given by the following values

$$(a,b) = (0.042, 0.41) \qquad (2)$$

The modified Ursell number is defined as

$$U_{RP} = \frac{H^3 \lambda^2}{h^3 D^2} \qquad (3)$$

where H is the wave height, $\lambda = 2\pi / k$ is the wave length, k is the wave number determined from the dispersion relationship $\omega^2 = gk \tanh kh$, $\omega = 2\pi / T$ is the angular wave frequency, T is the wave period, g is the acceleration of gravity, and h is the water depth. This modified Ursell number is the product of the Ursell number, $U_R = H\lambda^2 / h^3$, and $(H/D)^2$, as introduced by Cevik and Yüksel (1999). Equation (1) is valid for live-bed scour, for which $\theta > \theta_{cr}$, where θ is the undisturbed Shields parameter defined by

$$\theta = \frac{\tau_w}{\rho g (s-1) d_{50}} \qquad (4)$$
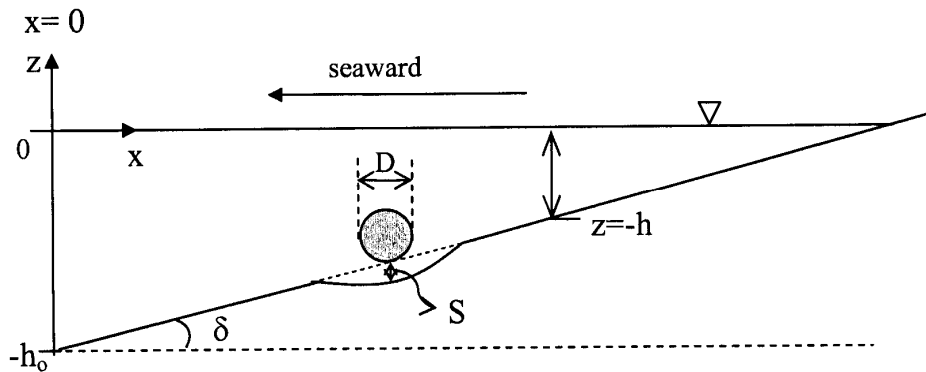
Fig. 1. Definition sketch of scour depth (*S*) below a pipeline in shoaling conditions.

Here τ_w is the maximum bottom shear stress under the waves, ρ is the density of the fluid, $s = \rho_s / \rho$ is the sediment grain density to the fluid density ratio, ρ_s is the sediment grain density, d_{50} is the median grain size diameter, and θ_{cr} is the critical value of the Shields parameter corresponding to the initiation of motion at the bed, i.e. $\theta_{cr} \approx 0.05$.

When the bed is sloping, the gravity gives a force component on the grain which may increase or decrease the threshold shear stress required from the flow. The threshold Shields parameter, $\theta_{\delta cr}$, for initiation of motion of the grains at a bed sloping at an angle δ to the horizontal in upsloping flows is related to the value θ_{cr} for the same grains on a horizontal bed by (see e.g. Soulsby (1997, Section 6.4))

$$\frac{\theta_{\delta cr}}{\theta_{cr}} = \cos\delta\left(1 + \frac{\tan\delta}{\tan\phi_i}\right) \qquad (5)$$

where ϕ_i is the angle of repose of the sediment.

One should note that the scour process attains its equilibrium stage through a transition period. Cevik and Yüksel (1999) considered a minimum of 1000 waves for the equilibrium scour depth, since they found no significant changes in the equilibrium scour depth with waves more than 1000. Thus the approach is valid when it is assumed that the storm has lasted longer than the time scale of the scour. More details on the time scale for scour below pipelines are given in Sumer and Fredsøe (2002).

It should also be noted that since Eq. (1) appears to be physically sound for $U_{RP} \geq 0$, i.e. S equals zero for $U_{RP} = 0$, the formula can be taken to be valid from $U_{RP} = 0$. This extension of Eq. (1) relies on the threshold of motion being exceeded, which for small values of the modified Ursell number may not be the case.

The main results found by Cevik and Yüksel (1999) were that the scour depth in shoaling conditions is always larger than that for a horizontal bed for the same incident wave conditions. Moreover, the maximum scour depth occurs at the offshore side of the breaking depth. More discussion is given in Section 4.

3.   Scour in Random Waves

3.1.   Stochastic method

For scour below pipelines and around vertical piles in random waves Sumer and Fredsøe (1996, 2001) determined the properties of the random variables wave height H and wave period T to be used to represent the scour depth and width below pipelines and scour depth around slender vertical piles. By trial and error they found that the use of H_{rms} (= root-mean-square (*rms*) wave height) and T_p (= peak period of wave spectrum) in an otherwise deterministic approach gave the best agreement with data. Here a tentative stochastic approach will be outlined. The highest among random waves in a stationary narrow-band sea state is considered, as it is reasonable to assume that it is mainly the highest waves which are responsible for the scour response. It is also assumed that the sea state has lasted long enough to develop the equilibrium scour depth. The highest waves considered here are those exceeding the probability $1/n$, $H_{1/n}$. The quantity of interest is the expected (mean) scour depth caused by the highest waves, which is given as

$$E\left[S(H) \mid H > H_{1/n}\right] = n \int_{H_{1/n}}^{\infty} S(H) p(H) dH \qquad (6)$$

where $p(H)$ is the probability density function (*pdf*) of H. More specifically, the present approach is based on the following assumptions: (1) the free surface elevation, $\zeta(t)$, is a stationary Gaussian narrow-band process with zero expectation, and (2) the scour depth formulas for regular waves given in the previous section (Eqs. (1) to (3)), are valid for irregular waves as well. These assumptions are essentially the same as those given in Myrhaug and Rue (2003, 2005) and Myrhaug et al. (2004, 2007), where further details are found.

Here the wave height distribution including shoaling and breaking on planar beaches given by Mendez et al. (2004) is adopted, given by the cumulative distribution function (*cdf*)

$$P(\hat{H}) = 1 - \exp\left[-\left(\frac{\phi(\kappa)\hat{H}}{1 - \kappa\hat{H}}\right)^2\right] \quad ; \quad 0 \le \hat{H} < \frac{1}{\kappa} \qquad (7)$$

where $\hat{H} = H / H_{rms}$ is the dimensionless wave height , and $\kappa = H_{rms} / H_{max}$ is a shape parameter where H_{max} is the maximum wave height; κ depends on the shoaling coefficient and a breaking-wave decay coefficient, and

$$\phi(\kappa) = \left(1 - \kappa^{0.944}\right)^{1.187} \quad ; \quad 0 \le \kappa \le 1 \qquad (8)$$

It should be noted that $\kappa = 0$ corresponds to the seaward conditions, i.e. before shoaling, where Eq. (7) reduces to the Rayleigh distribution. The waves are assumed to be narrow-banded in frequency seaward the breaking zone, which is consistent with the Rayleigh *pdf* for the wave height distribution. Moreover, for the asymptotic case of $\kappa = 1$, Eq. (7) reduces to the Dirac delta distribution. More details are given in Mendez et al. (2004).

It should also be noted that H_{rms} represents a local value, which in the Mendez et al. (2004) distribution is at a between the seaward value $H_{rms,0}$ at the location where initiation of breaking occurs, and the shoreline value. It is also assumed that the shallow water assumption applies at the seaward boundary. Mendez et al. (2004) give the following relationship between the local and seaward values

$$H_{rms} = \left(\frac{h_0}{h}\right)^{1/4} \phi(\kappa) H_{rms,0} \tag{9}$$

where $(h_0 / h)^{1/4}$ is the shoaling coefficient for shallow water waves, h_0 is the water depth at the seaward location, $h = h_0 - mx$, m is the bed slope, and x is the horizontal coordinate with $x = 0$ at the seaward location and positive towards the shoreline. Thus, if $\kappa = 0$ (and consequently that $\phi(\kappa) = 1$) between the seaward location and the shoreline, it means that κ only depends on the shoaling coefficient, and that wave breaking is neglected. It should be noted that there are restrictions on κ for a given water depth; a tentative relationship based on wave parameters within a limited range is given in Mendez et al. (2004, Section 4.1).

For a narrow-band process $\omega = \omega_z$ where ω_z is the mean zero-crossing wave frequency, and Eq. (1) can be re-arranged to

$$\hat{S} \equiv \frac{S/D}{aU_{RP\,rms}^b} = \hat{H}^{3b} \tag{10}$$

where

$$U_{RP\,rms} = \frac{H_{rms}^3 \bar{\lambda}^2}{h^3 D^2} \;\; ; \;\; 2 \lesssim U_{RP\,rms} \lesssim 3000 \tag{11}$$

Here $\bar{\lambda} = 2\pi / \bar{k}$ is the wave length based on the wave number corresponding to ω_z, determined from $\omega_z^2 = g\bar{k} \tanh \bar{k}h$.

Now the mean scour depth caused by the $1/n$'th highest waves follows from Eq. (6) as

$$E\left[\hat{S}(\hat{H})\big|\hat{H} > \hat{H}_{1/n}\right] = n\int_{\hat{H}_{1/n}}^{1/\kappa} \hat{H}^{3b} p(\hat{H})d\hat{H} \tag{12}$$

where $p(\hat{H}) = dP(\hat{H})/d\hat{H}$ with $P(\hat{H})$ as given in Eq. (7), and $\hat{H}_{1/n}$ is given in Mendez et al. (2004) as

$$\hat{H}_{1/n} = \frac{\sqrt{\ln n}}{\phi(\kappa) + \kappa\sqrt{\ln n}} \tag{13}$$

For $\kappa = 0$, i.e. at the seaward location, the result of Eq. (12) is

$$E\left[\hat{S}(\hat{H})\,|\,\hat{H} > \hat{H}_{1/n}\right] = n\Gamma\left(1 + \frac{3}{2}b, \ln n\right)$$
$$= (1.54, 2.07)\ ;\ n = (3,10),\ b = 0.41 \tag{14}$$

where $\Gamma(\text{gg})$ is the incomplete gamma function, and with $\hat{H}_{1/n} = \sqrt{\ln n}$ from Eq. (13).

The local value of $U_{RP\,rms}$ in Eq. (11) can also be expressed in terms of the seaward value $U_{RP\,rms,0}$, as elaborated in the following. In shallow water $\tanh \overline{k}h \approx \overline{k}h$; thus $\omega_z^2 = g\overline{k}^2h$. Since ω_z is constant, it follows that $\overline{\lambda}^2 = \overline{\lambda}_0^2 h/h_0$ where $\overline{\lambda}_0$ refers to the seaward location. By using this together with Eq. (9), Eq. (11) can be re-arranged to

$$U_{RP\,rms} = \left(\frac{h_0}{h}\right)^{11/4} \phi^3(\kappa)U_{RP\,rms,0} \tag{15}$$

where

$$U_{RP\,rms,0} = \frac{H_{rms,0}^3\,\overline{\lambda}_0^2}{h_0^3\,D^2} \tag{16}$$

3.2. Alternative view of scour process. Approximate method

An alternative pragmatic view of the scour process below pipelines and around a single vertical pile under random waves is that of Sumer and Fredsøe (1996, 2001) referred to in Section 3.1. They looked for which parameters of the random waves to represent the scour variable, finding by trial and error that the use of H_{rms} and T_p in an otherwise deterministic approach gave the best agreement with data.

This alternative view of the scour process will now be considered using the results of the present stochastic method. The question is how well the mean scour depth caused by the $1/n$ 'th highest waves, $E[S(H)|H > H_{1/n}]$ (see Eq. (6)), can be represented by using the mean of the $1/n$ 'th highest waves in the scour depth formula for regular waves, i.e. $S(E[H_{1/n}])$.

An alternative modified Ursell number for random waves is defined as

$$U_{RP1/n} = \frac{\left(E[H_{1/n}]\right)^3 \bar{\lambda}^2}{h^3 D^2} \tag{17}$$

which can be re-arranged to

$$U_{RP1/n} = U_{RPrms}\left(E\left[\hat{H}_{1/n}\right]\right)^3 \tag{18}$$

where U_{RPrms} is given in Eq. (11) and

$$E\left[\hat{H}_{1/n}\right] = n \int_{\hat{H}_{1/n}}^{1/\kappa} \hat{H} p\left(\hat{H}\right) d\hat{H} \tag{19}$$

Now the results of the alternative view of the scour process are obtained by replacing U_{RP} with $U_{RP1/n}$ in the regular wave formula in Eq. (1), giving

$$\frac{S}{D} = a U_{RPrms}^b \left(E\left[\hat{H}_{1/n}\right]\right)^{3b} \tag{20}$$

The following polynomial functions for $E\left[\hat{H}_{1/n}\right]$ for $n = (3,10)$ are given by Mendez et al. (2004, Table 1)

$$E\left[\hat{H}_{1/n}\right] = \begin{pmatrix} 1.416 \\ 1.800 \end{pmatrix} - \begin{pmatrix} 0.140 \\ 0.830 \end{pmatrix}\kappa - \begin{pmatrix} 0.749 \\ 0.477 \end{pmatrix}\kappa^2 + \begin{pmatrix} 0.887 \\ 0.985 \end{pmatrix}\kappa^3 - \begin{pmatrix} 0.413 \\ 0.478 \end{pmatrix}\kappa^4 \quad ; n = \begin{pmatrix} 3 \\ 10 \end{pmatrix}$$

$$\tag{21}$$

For $\kappa = 0$ (at the seaward location $x = 0$), Eq. (20) gives (as a consequence of Eqs. (15) and (19))

$$\frac{S}{D} = a U_{RPrms,0}^b \left(E\left[\hat{H}_{1/n,0}\right]\right)^{3b} \tag{22}$$

where $E\left[\hat{H}_{1/n,0}\right]$ is based on the results for the Rayleigh distribution given in Eq. (21) with $\kappa = 0$ for $n = (3,10)$.

3.3. Shields parameter

Following Myrhaug (1995) it can be shown that the bottom shear stress maxima for individual narrow-band random waves are Weibull distributed with the *cdf*

$$P(\hat{\tau}) = 1 - \exp\left(-\hat{\tau}^{\beta}\right) \quad ; \quad \hat{\tau} \geq 0, \beta = 1.35 \tag{23}$$

where $\hat{\tau} = \tau_w / \overline{\tau}_{wrms}$ is the non-dimensional shear stress, and, by definition

$$\frac{\overline{\tau}_{wrms}}{\rho} = \frac{1}{2} 1.39 \left(\frac{A_{rms}}{z_0}\right)^{-0.52} U_{rms}^2 \tag{24}$$

Here $z_0 = d_{50}/12$ is the bed roughness, A_{rms} is the *rms* value of the near-bed orbital displacement amplitude related to H_{rms} by

$$A_{rms} = \frac{H_{rms}}{2\sinh \overline{k}h} \tag{25}$$

and $U_{rms} = \omega_z A_{rms}$ is the *rms* value of the near-bed orbital velocity amplitude. By taking $\hat{\theta} = \theta / \overline{\theta}_{rms}$ and defining a Shields parameter, where the wave-related quantities are replaced by their *rms*-values in Eq. (4), i.e.

$$\overline{\theta}_{rms} = \frac{\overline{\tau}_{wrms}/\rho}{g(s-1)d_{50}} \tag{26}$$

it follows that $\hat{\theta} = \hat{\tau}$, and thus $\hat{\theta}$ is distributed as $\hat{\tau}$, i.e. with the *cdf*

$$P(\hat{\theta}) = 1 - \exp\left(-\hat{\theta}^{\beta}\right) \quad ; \quad \hat{\theta} \geq 0, \beta = 1.35 \tag{27}$$

For random waves it is not obvious which value of the Shields parameter to use to determine the conditions corresponding to live-bed scour. However, it seems to be consistent to use corresponding statistical values of the scour depth and the Shields parameter, e.g. $E\left[\hat{\theta}_{1/n}\right]$, which for the *cdf* in Eq. (27) is given by

$$E\left[\hat{\theta}_{1/n}\right] = n\Gamma\left(1 + \frac{1}{\beta}, \ln n\right) = n\Gamma(1.74, \ln n) = (1.70, 2.40) \quad \text{for} \quad n = (3,10) \tag{28}$$

Moreover

$$\hat{\theta}_{rms} = \left[\Gamma\left(1+\frac{2}{\beta}\right) \right]^{1/2} = 1.14 \qquad (29)$$

$$\hat{\theta}_{1/n} = \left(\ln n\right)^{1/\beta} = \left(\ln n\right)^{0.74} = \left(1.07, 1.85\right) \quad \text{for} \quad n = \left(3, 10\right) \qquad (30)$$

This is used in conjunction with Eq. (5) when the bed is sloping.

4. Results and Discussion

For the scour depth below pipelines in shoaling conditions no data exist for random waves in the open literature. Therefore the results in this section should be taken as tentative, and data for comparisons are required before any conclusion can be made regarding the validity of the approach. However, in the meantime the method should be useful as an engineering approach; an example is given to demonstrate the use of the method.

4.1. Main results

Figure 2 shows S/D versus U_{RPrms} for values of κ in the range 0 to 0.8 according to the stochastic method in Eq. (12) exemplified by $n = 3$ and $n = 10$. It should be noted that the effect of shoaling including breaking increases as κ increases. From Fig. 2 it appears that: S/D increases as U_{RPrms} increases for a given value of κ, i.e. S/D increases as the wave activity increases at a given location at the sloping bed; and S/D decreases as κ increases for a given value of U_{RPrms}, i.e. which overall means that S/D decreases as the effect of shoaling including breaking increases. Both these effects are physically sound. It should be noted that $U_{RPrms} = \left(\dfrac{h_0}{h}\right)^{11/4} U_{RPrms,0}$ for $\kappa = 0$ (see Eq. (15)), i.e. in this case shoaling does not include breaking.

Figure 3 shows the ratio between the approximate and the stochastic method versus κ for $n = 3$ and $n = 10$, i.e.

$$R = \frac{\left(E\left[\hat{H}_{1/n}\right]\right)^{3b}}{E\left[\hat{S}\left(\hat{H}\right) | \hat{H} > \hat{H}_{1/n}\right]} \qquad (31)$$
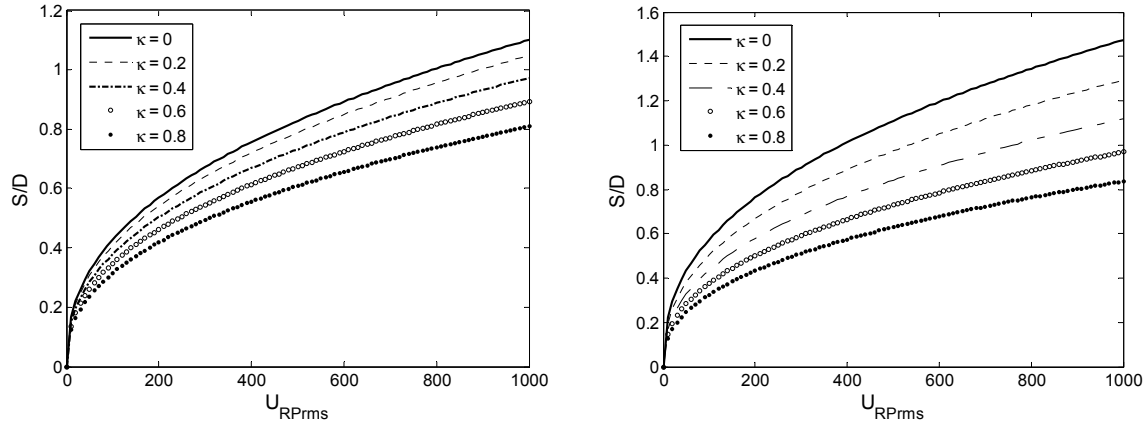
Fig. 2. Scour depth in shoaling conditions versus U_{RPrms} and κ; here S/D represents $E\left[(S/D)\,|\,\hat{H} > \hat{H}_{1/n}\right]$ for $n = 3$ (left figure) and $n = 10$ (right figure), respectively.
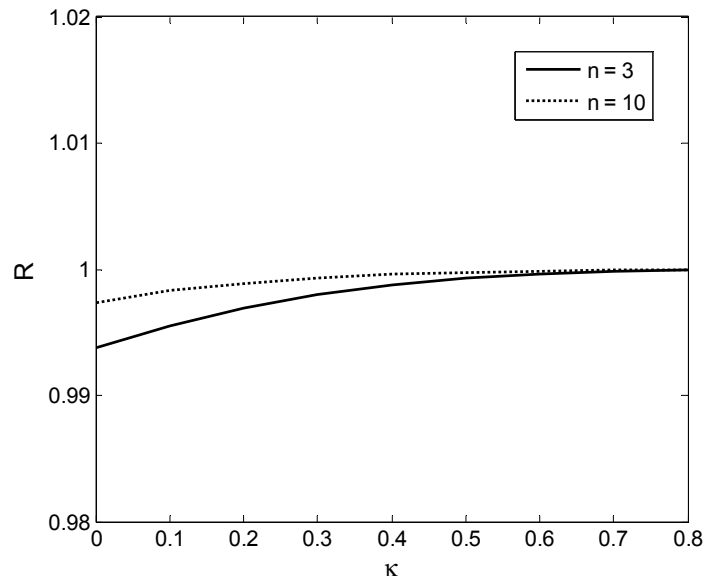
Fig. 3. Ratio between approximate method and stochastic method according to Eq. (31) versus κ for $n = 3$ and $n = 10$.

It appears that this ratio is very close to 1 for all κ values, suggesting that the scour depth formula for regular waves can be applied for random waves if the random waves are represented by the mean of the $1/n$'th highest waves; exemplified here for $n = 3$ and $n = 10$. Thus this justifies that the approximate method can replace the stochastic method in engineering applications.

However, the most appropriate statistical value of the scour depth to use is not conclusive; it will depend on the problem considered, and it is subject to the designer's judgment.

4.2. Example of calculation

This example is included to demonstrate the application of the approach. The given flow conditions are:

Water depth at seaward location, $h_0 = 3$ m

Local water depth, $h = 1.5$ m

Significant wave height at seaward location, $H_{s,0} = 0.28$ m

Mean wave period, $T_z = 9.1$ s, corresponding to $\omega_z = 0.690$ rad/s

Median grain diameter (very fine sand according to Soulsby, 1997, Fig. 4), $d_{50} = 0.1$ mm

Pipe diameter, $D = 0.2$ m

Bed slope, $m = 1/10$; corresponding to $\delta = 5.7$ degrees

Angle of repose of sediment (Soulsby, 1997, Section 2.3), $\phi_i = 32$ degrees

Shape parameter, $\kappa = 0.4$

$s = 2.65$ (as for quartz sand)

Critical Shields parameter of sloping bed for $\theta_{cr} = 0.05$ (Eq. (5)), $\theta_{\delta cr} = 0.058$

The calculated quantities are given in Table 1. Here the *rms* wave height at the seaward location is given according to the Rayleigh distribution of the seaward wave height, i.e. $H_{rms,0} = H_{s,0}/\sqrt{2}$; $\bar{k}_0$ is the wave number determined from the shallow water dispersion relationship $\omega_z^2 = g\bar{k}_0^2 h_0$ (which is a good approximation for the value $\bar{k}_0' = 0.130$ rad/m determined from $\omega_z^2 = g\bar{k}_0' \tanh \bar{k}_0' h_0$). The Ursell number $U_{R\,rms,0}$ is calculated to check if linear wave theory is applicable; for regular waves it is required that $U_R \lesssim 15$ (Skovgaard et al., 1974); here the value is 18 which is only slightly larger than 15; therefore linear wave theory is assumed to be applicable. $A_{rms,0}$ is determined from Eq. (25) for shallow water, i.e. $A_{rms,0} = H_{rms,0}/2\bar{k}_0 h_0$; $E\left[\theta_{1/n,0}\right] = \bar{\theta}_{rms,0} E\left[\hat{\theta}_{1/n}\right]$ by using Eq. (28), noticing that the values for $n = (3,10)$ exceed the critical Shields parameter $\theta_{\delta cr} = 0.058$.

As shown in Fig. 3, Eq. (20) can be used to calculate the scour depth for $n = 3$ and $n = 10$. The results in Table 1 are obtained by substituting $E\left[\hat{H}_{1/n}\right]$ for $n = (3,10)$ and $\kappa = 0$ from Eq. (21) in Eq. (20). Thus, it appears that the scour depth at the seaward location is given by 4.2 cm and 5.6 cm for the random waves represented by $E\left[H_{1/3}\right]$ and $E\left[H_{1/10}\right]$, respectively.

First, consider $\kappa = 0.4$, meaning that shoaling includes breaking. At the local water depth it appears that the Ursell number is significantly larger than 15 (i.e. $U_{Rrms} = 44$), suggesting that linear wave theory is not applicable, and that an appropriate wave theory should be used. However, in the present example linear wave theory is used to serve the purpose of demonstrating the use of the method. It is noted that $E[\theta_{1/n}]$ for $n = (3,10)$ exceed $\theta_{\delta cr} = 0.058$. The scour depth results in Table 1 are obtained by substituting $E[\hat{H}_{1/n}]$ for $n = (3,10)$ and $\kappa = 0.4$ from Eq. (21) in Eq. (20). It appears that the scour depth at the local water depth is given by 3.6 cm and 4.0 cm based on using $E[H_{1/3}]$ or $E[H_{1/10}]$, respectively, i.e. giving the reasonable result that both values are smaller than the corresponding values at the seaward location.

Table 1. Example of calculation at the seaward location and at a local water depth

At the seaward location ; $h_0 = 3$ m, $\kappa = 0$	
$H_{rms,0}$ (m)	0.20
$\bar{k}_0$ (rad/m)	0.127
$\bar{\lambda}_0$ (m)	49.5
$U_{Rrms,0} = H_{rms,0} \bar{\lambda}_0^2 / h_0^3$	18
$A_{rms,0}$ (m)	0.26
$U_{rms,0}$ (m/s)	0.18
$A_{rms,0} / z_0$	31 200
$\bar{\theta}_{rms,0}$, Eqs. (24) and (26)	0.064
$E[\theta_{1/n,0}]$, $n = (3,10)$	0.11, 0.15
$U_{RPrms,0}$, Eq. (16)	18
S (m), $n = (3,10)$, Eq. (20)	0.042, 0.056

	Local water depth; $h = 1.5\,\text{m},\ \kappa = 0.4$ (i.e. shoaling including breaking)	Local water depth; $h = 1.5\,\text{m},\ \kappa = 0$ (i.e. shoaling without breaking)
H_{rms} (m), Eqs. (8) and (9)	0.12	0.24
$\bar{\lambda}(\text{m}) = \bar{\lambda}_0 (h/h_0)^{1/2}$	35	35
$U_{Rrms} = H_{rms}\lambda^2/h^3$	44	88
A_{rms} (m)	0.22	0.44
U_{rms} (m/s)	0.15	0.30
A_{rms}/z_0	26 400	52800
$\bar{\theta}_{rms}$, Eqs. (24) and (26)	0.049	0.135
$E[\theta_{1/n}]$, $n = (3,10)$	0.083, 0.11	0.23, 0.32
U_{RPrms}, Eq. (11)	16	125
$S(m), n = (3,10)$, Eq. (20)	0.036, 0.040	0.093, 0.125

Second, consider $\kappa = 0$, meaning that the waves are shoaling without breaking. At the local water depth it appears that the Ursell number is even larger than in the first case with $\kappa = 0.4$, but linear wave theory is still used to demonstrate the use of the method. It appears that the scour depth at the local water depth is given by 9.3 cm and 12.5 cm based on the two statistical values considered, i.e. giving the reasonable results that both values are larger than the corresponding values at the seaward location.

Thus this example demonstrates the features shown in Fig. 2. That is; first, for shoaling including breaking the scour depth is reduced compared with that at the seaward location; and second, for shoaling without breaking the scour depth increases compared with that at the seaward location.

5. Summary

1. A practical approach for estimating the scour depth below a pipeline exposed to random waves with normal incidence to the pipeline in shoaling conditions is provided. The approach is valid for non-breaking and breaking waves. Moreover, it is valid for

$2 \lesssim U_{RP\,rms} \lesssim 3000$, provided that the threshold of motion of sand grains is exceeded.

2.   The present results suggest that the scour depth formula for regular waves can be applied for random waves if the random waves are represented by the mean of the $1/n$'th highest waves; exemplified here for $n = 3$ and $n = 10$.

Although simple, the present approach should be useful as a first approximation to represent the stochastic properties of the scour depth below pipelines in shoaling conditions under non-breaking and breaking random waves. However, comparisons with data are required before a conclusion regarding the validity of this approach can be given. In the meantime the method should be useful as an engineering tool for the assessment of scour and in scour protection work.

References

Cevik, E. and Yüksel, Y. (1999). Scour under submarine pipelines in waves in shoaling conditions. *J. Waterway, Port, Coastal and Ocean Engineering*, ASCE, 125 (1), 9-19.

Mendez, F.J., Losada, I.J. and Medina, R. (2004). Transformation model of wave height distribution on planar beaches. *Coast. Eng.*, 50 (3), 97-115.

Myrhaug, D., Føien, H. and Rue, H. (2007). Tentative engineering approach to scour around spherical bodies in random waves. *Applied Ocean Research*, 29, 80-85.

Myrhaug, D. (1995). Bottom friction beneath random waves. *Coast. Eng.*, 24, 259-273.

Myrhaug, D. and Rue, H. (2003). Scour below pipelines and around vertical piles in random waves. *Coast. Eng.*, 48, 227-242.

Myrhaug, D. and Rue, H. (2005). Scour around groups of slender vertical piles in random waves. *Applied Ocean Research*, 27, 56-63.

Myrhaug, D., Rue, H. and Tørum, A. (2004). Tentative engineering approach to scour around breakwaters in random waves. *Coast. Eng.*, 51, 1051-1065.

Skovgaard, O., Svendsen, I.A., Jonsson, I.G. and Brink-Kjær, O. (1974). Sinusoidal and cnoidal gravity waves formulae and tables. Institute of Hydrodynamics and Hydraulic Engineering (ISVA), Technical University of Denmark, Lyngby, Denmark.

Soulsby R.L. (1997). *Dynamics of Marine Sands. A Manual for Practical Applications*. Thomas Telford, London, UK.

Sumer, B.M. and Fredsøe, J. (1996). Scour below pipelines in combined waves and current. *Proc. 15th OMAE Conf.*, Florence, Italy, Vol. 5, pp. 595-602.

Sumer, B.M. and Fredsøe, J., (2001). Scour around pile in combined waves and current, *ASCE J. Hydraul. Eng.*, 127 (5), 403-411.

Sumer, B.M. and Fredsøe, J. (2002). *The Mechanics of Scour in the Marine Environment*. World Scientific, Singapore.

Whitehouse, R.J.S. (1998). *Scour at Marine Structures. A Manual for Practical Applications*. Thomas Telford, London, UK.

Yüksel, Y. (2008). Private Communication.

Chapter 11

Random Wave-Induced Scour at the Trunk Section of a Breakwater

Dag Myrhaug and Muk Chen Ong

Department of Marine Technology,
Norwegian University of Science and Technology, NO-7491 Trondheim, Norway.

Abstract[#]

This paper provides a stochastic method by which the random wave-induced scour depth at the trunk section of vertical-wall and rubble-mound breakwaters can be derived. Here the formulas for regular wave-induced scour depth provided by Xie (1981) for vertical-wall breakwater and Sumer and Fredsøe (2000) for rubble-mound breakwater are used. These formulas are combined with describing the waves as a stationary Gaussian narrow-band random process to derive the random wave-induced scour depth. Comparisons are made between the present method and the Sumer and Fredsøe (2000) random wave scour data for rubble-mound breakwater, as well as the Hughes and Fowler (1991) random wave scour data and formula for vertical-wall breakwater. A tentative approach to random wave-induced scour at a vertical impermeable submerged breakwater is also suggested.

Keywords: Breakwater; Rubble-mound; Vertical-wall; Vertical impermeable submerged breakwater; Scour depth; Random waves; Stochastic method

1.   Introduction

The occurrence of scour around breakwaters is one of the major failure modes of these structures (see e.g. Sumer and Fredsøe (2002)). During the lifetime of a breakwater, it may experience a range of seabed conditions, i.e. the bed may be flat or rippled; the structure may be surrounded by scour holes. This is caused by the complicated flow generated by the interaction between the incoming flow, the structure and the seabed. The results will depend on the incoming flow velocity (e.g. the relative magnitude between waves and current), the geometry of the seabed and the bed material, as well as the ratio between the oscillatory fluid particle excursion amplitude and a characteristic length of the structure. Furthermore, real waves are stochastic, making the problem more complex. Further details on the background and complexity as well as reviews of the problem are given in e.g. Whitehouse (1998) as well as Sumer and Fredsøe (2002).

The purpose of the present paper is to provide a tentative engineering approach by which the random wave-induced scour depth at the trunk section of a breakwater can be derived. Both vertical-wall and rubble-mound breakwaters are considered. Here the formulas for regular wave-induced scour depth given by Xie (1981) for vertical-wall breakwaters and by Sumer and Fredsøe (2000) for rubble-mound breakwaters are used. The wave motion is assumed to be a stationary Gaussian narrow-band random process, and the random wave-induced scour depth is derived. Comparisons are made between the present approach predictions and the Sumer and Fredsøe (2000) random wave-induced scour data for rubble-mound breakwater, as well as the Hughes and Fowler (1991) random wave-induced scour data and formula for vertical-wall breakwater. A similar approach was applied by Myrhaug et al. (2004), where the scour depth and protection layer width around the head of vertical-wall breakwaters, the scour and deposition depths as well as the protection layer widths at the round head of rubble-mound breakwaters in random waves were derived. The results in Hughes and Fowler (1991) and Sumer and Fredsøe (2000) show that the maximum scour depth for random waves is generally reduced compared with that for regular waves; it is typically reduced by a factor 2. A tentative approach to random wave-induced scour at a vertical impermeable submerged breakwater based on a formula for regular waves presented by Lee and Mizutani (2008) is also suggested.

2.   Scour in Regular Waves

The maximum scour depth at the trunk section of a vertical-wall breakwater exposed to normally incident regular waves was investigated in laboratory tests by Xie (1981). Data were obtained for suspension mode transport of fine sediments with the median grain size diameter $d_{50} = 0.106$ mm (and one test with $d_{50} = 0.20$ mm). The following empirical formula

for the maximum scour depth S for regular waves with incident wave height H and wave length L at a water depth h (see Fig. 1) was obtained

$$\frac{S}{H} = \frac{0.4}{(\sinh kh)^{1.35}} \tag{1}$$

Here $k = 2\pi / L$ is the wave number determined from the dispersion relationship $\omega^2 = gk \tanh kh$, where $\omega = 2\pi / T$ is the angular wave frequency, and T is the wave period.

Sumer and Fredsøe (2000) found a similar empirical formula for the maximum scour depth at the trunk section of a vertical-wall breakwater corresponding to no-suspension mode transport of coarse sand with $d_{50} = 0.20$ mm:

$$\frac{S}{H} = \frac{0.3}{(\sinh kh)^{1.35}} \tag{2}$$

Sumer and Fredsøe (2000) also investigated the maximum scour depth at the trunk section of a rubble-mound breakwater under regular and irregular waves. Data were obtained for no-suspension mode transport of coarse sand with $d_{50} = 0.20$ mm for breakwater slopes $\alpha = 30^\circ$ and 40° for regular waves and $\alpha = 40^\circ$ for irregular waves. For regular waves they found that the data can be represented by the empirical formula (see Fig. 2)

$$\frac{S}{H} = \frac{f(\alpha)}{(\sinh kh)^{1.35}} \tag{3}$$

where

$$f(\alpha) = 0.3 - 1.77 \exp\left(-\frac{\alpha}{15}\right) \; ; \quad 30^\circ \lesssim \alpha \lesssim 90^\circ \tag{4}$$

Thus Eqs. (1) to (4) can be represented by Eq. (3) with

$$f(\alpha) = c - 1.77 \exp\left(-\frac{\alpha}{15}\right) \tag{5}$$

where

$$c = 0.3 \; ; \; 30^\circ \lesssim \alpha \lesssim 90^\circ \text{ for coarse sand} \tag{6}$$

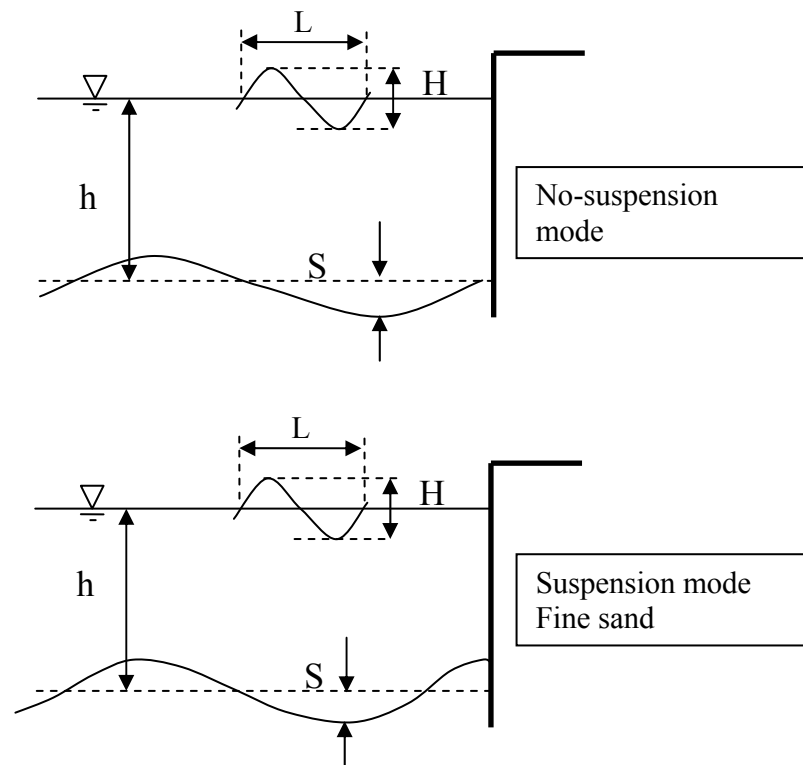$$c = 0.4 \; ; \; \alpha = 90^\circ \text{ for fine sand} \tag{7}$$

Figure 1. Definition sketch of scour depth (*S*) at the trunk section of a vertical-wall breakwater, where *H* is the incident wave height and *L* is the incident wave length.
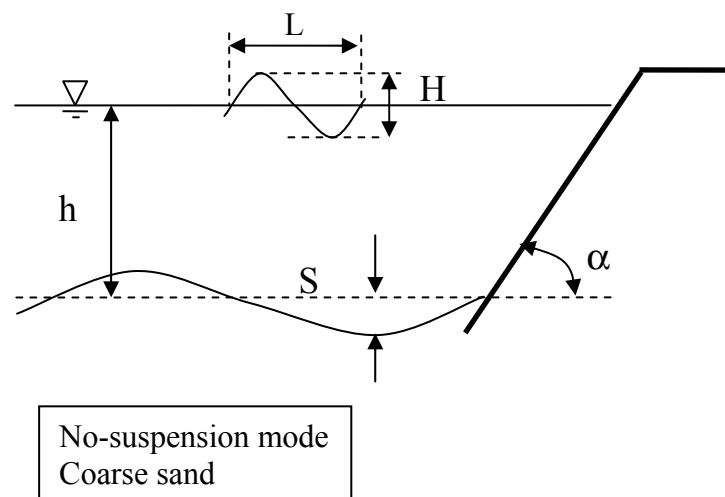

Figure 2. Definition sketch of scour depth (*S*) at the trunk section of a rubble-mound breakwater, where *H* is the incident wave height and *L* is the incident wave length.

All these equations are valid for live-bed scour, for which $\theta > \theta_{cr}$, and θ is the undisturbed Shields parameter defined by

$$\theta = \frac{\tau_w}{\rho g(s-1)d_{50}} \tag{8}$$

where τ_w is the maximum bottom shear stress under waves, ρ is the density of the fluid, g is the acceleration of gravity, $s = \rho_s / \rho$ is the sediment grain density to fluid density ratio, ρ_s is the sediment grain density, and θ_{cr} is the critical value of motion at the bed, i.e. $\theta_{cr} \approx 0.05$. In addition to θ, the mode of sand transport is governed by the fall velocity parameter w/u_* where w is the fall velocity of sand grains, and $u_* = (\tau_w / \rho)^{1/2}$ is the friction velocity. The sand transport will be in the suspension mode if $\theta > \theta_s$ and $w/u_* < 1$; otherwise the sand transport is in the no-suspension mode. Here θ_s is the critical value for initiation of suspension from the bed, depending on the grain Reynolds number $u_* d_{50}/v$ where v is the kinematic viscosity of the fluid. According to Sumer and Fredsøe (2002, Eq. (7.7)) θ_s is given by

$$\theta_s = \left(\frac{u_* d_{50}}{v}\right)^{-0.05} \left[0.7 \exp\left(-0.04 \frac{u_* d_{50}}{v}\right)\right] + 0.26\left[1 - \exp\left(-0.025 \frac{u_* d_{50}}{v}\right)\right] \tag{9}$$

It should be noted that this relationship is strictly only valid for the initiation of suspension from the bed in the case of steady currents, but to a first approximation it can be used for waves (see Sumer and Fredsøe (2002) for more details).

One should note that the scour process attains its equilibrium stage through a transition period. Thus the approach is valid when it is assumed that the storm has lasted longer than the time scale of the scour.

A vertical-wall breakwater exposed to normally incident regular waves will cause the waves to be reflected, and the superposition of these waves results in a standing wave. The standing wave generates a steady streaming field, i.e. a system of bottom and top recirculating cells. The bottom cells are related to the bottom boundary layer flow, which cause the sediments to respond; the response depends on the Shields parameter and the fall velocity parameter. Thus the scour process is a consequence of this response. For a rubble-mound breakwater there are two changes; the breakwater is made of rubble, and it has a sloping wall meaning that the reflection coefficient is reduced. However, the standing wave-induced steady streaming is also the main mechanism causing the scour at the trunk of a rubble-mound breakwater. More

details on the time scale of the scour process as well as the mechanisms of the scour are given in Sumer and Fredsøe (2000, 2002).

In the following it is assumed that the bottom shear stresses can be calculated from the progressive wave boundary layer rather than from the standing wave boundary layer. Thus the maximum bottom shear stress within a wave cycle is taken as

$$\frac{\tau_w}{\rho} = \frac{1}{2} f_w U^2 \tag{10}$$

where U is the near-bed orbital velocity amplitude, and f_w is the wave friction factor, which here is taken as (Soulsby, 1997, Eq. (62a))

$$f_w = 1.39 \left(\frac{A}{z_0} \right)^{-0.52} \tag{11}$$

Here $A = U / \omega$ is the near-bed orbital displacement amplitude, and $z_0 = d_{50} / 12$ is the bed roughness. Eq. (11) is valid for rough turbulent flow under sinusoidal waves and is obtained as best fit to data in the range $10 \lesssim A / z_0 \lesssim 10^5$. Moreover, A is related to the linear wave height by

$$A = \frac{H}{2 \sinh kh} \tag{12}$$

3. Scour in Random Waves

3.1. Stochastic method

For scour below pipelines and around vertical piles in random waves Sumer and Fredsøe (1996, 2001) determined the properties of the random variables wave height H and wave period T to be used to represent the scour depth and width below pipelines and scour depth around slender vertical piles. By trial and error they found that the use of H_{rms} (= root-mean-square (rms) wave height) and T_p (= spectral peak period) in an otherwise deterministic approach gave the best agreement with data. Here a tentative stochastic approach is outlined. The highest among random waves in a stationary narrow-band sea state are considered, as it is reasonable to assume that it is mainly the highest waves which are responsible for the scour response. It is also assumed that the sea state has lasted long enough to develop the

equilibrium scour depth S. The highest incident waves considered here are those with the random wave heights H exceeding the probability $1/n$, $H_{1/n}$. The quantity of interest here is the expected (mean) scour depth caused by the highest waves, which is given as

$$E\left[S(H)\,|\,H > H_{1/n}\right] = n \int_{H_{1/n}}^{\infty} S(H)\,p(H)\,dH \qquad (13)$$

where $p(H)$ is the probability density function (*pdf*). More specifically, the present approach is based on the following assumptions: (1) the free surface elevation $\zeta(t)$ of the incident waves is a stationary Gaussian narrow-band random process with zero expectation described by the single-sided spectral density $S_{\zeta\zeta}(\omega)$, and (2) the scour depth formulas for regular waves given in the previous section (Eqs. (1) to (7)), are valid for irregular waves as well. These assumptions are essentially the same as those given in Myrhaug et al. (2004), where further details are found.

Based on the present assumptions, the time-dependent near-bed orbital displacement $a(t)$ and the velocity $u(t)$ are both stationary Gaussian narrow-band processes with zero expectations and with single-sided spectral densities

$$S_{aa}(\omega) = \frac{S_{\zeta\zeta}(\omega)}{\sinh^2 kh} \qquad (14)$$

$$S_{uu}(\omega) = \omega^2 S_{aa}(\omega) = \frac{\omega^2 S_{\zeta\zeta}(\omega)}{\sinh^2 kh} \qquad (15)$$

It follows from the narrow-band assumption that the near-bed orbital displacement amplitude, A, the near-bed orbital velocity amplitude, U, and the linear wave height, H, are Rayleigh-distributed with the cumulative distribution function (*cdf*) given by

$$P(\hat{x}) = 1 - \exp\left(-\hat{x}^2\right) \;\; ; \;\; \hat{x} = x/x_{rms} \geq 0 \qquad (16)$$

where x represents *A, U* or *H*, and x_{rms} is the *rms*-value of *x* representing A_{rms}, U_{rms} or H_{rms}.

Now A_{rms}, U_{rms} and H_{rms} are related to the zeroth moments of the amplitude, velocity and free surface elevation spectra m_{0aa}, m_{0uu} and $m_{0\zeta\zeta}$, respectively, given by

$$A_{rms}^2 = 2m_{0aa} = 2\sigma_{aa}^2 = 2\int_0^\infty S_{aa}(\omega)\,d\omega \tag{17}$$

$$U_{rms}^2 = 2m_{0uu} = 2\sigma_{uu}^2 = 2\int_0^\infty S_{uu}(\omega)\,d\omega \tag{18}$$

$$H_{rms}^2 = 8m_{0\zeta\zeta} = 8\sigma_{\zeta\zeta}^2 = 8\int_0^\infty S_{\zeta\zeta}(\omega)\,d\omega \tag{19}$$

From Eqs. (17) and (18), it also appears that $m_{0uu} = m_{2aa}$, where m_{2aa} is the second moment of the amplitude spectrum. The wave frequency ω is taken as the mean zero-crossing frequency for near-bed orbital displacement, ω_z, which is obtained from the spectral moments of $a(t)$, giving

$$\omega = \omega_z = \left(\frac{m_{2aa}}{m_{0aa}}\right)^{1/2} = \left(\frac{m_{0uu}}{m_{0aa}}\right)^{1/2} = \frac{U_{rms}}{A_{rms}} \tag{20}$$

where Eqs. (17) and (18) have been used. This result is valid for a stationary Gaussian random process.

For a narrow-band process $T = T_z$ where $T_z = 2\pi/\omega_z = 2\pi A_{rms}/U_{rms}$ is the mean zero-crossing wave period, and where Eq. (20) has been used. Eq. (3) can be re-arranged to

$$s \equiv \frac{S/H_{rms}}{f(\alpha)/(\sinh \overline{k}h)^{1.35}} = \hat{H} \tag{21}$$

where $\hat{H} = H/H_{rms}$, and $\overline{k}$ is the wave number corresponding to ω_z from $\omega_z^2 = g\overline{k}\tanh \overline{k}h$. Since s is distributed as $\hat{H}$, i.e. given by the Rayleigh cdf in Eq. (16), it follows from Eq. (13) that

$$E\left[s_{1/n}\right] \equiv E\left[s\left(\hat{H}\right) \mid \hat{H} > \hat{H}_{1/n}\right] = E\left[\hat{H} \mid \hat{H} > \hat{H}_{1/n}\right] \equiv E\left[\hat{H}_{1/n}\right]$$
$$= n\Gamma(1.5, \ln n) = (1.42, 1.80) \text{ for } n = (3, 10) \tag{22}$$

where $\Gamma(\cdot, \cdot)$ is the incomplete gamma function, and by using that $\hat{H}_{1/n} = \sqrt{\ln n}$. Moreover,

$$s_{rms} = \hat{H}_{rms} = 1 \tag{23}$$

Thus it follows that the random wave-induced scour depth is obtained by using the regular wave-induced scour depth formula if the random waves is represented by $T = T_z$ and H by a characteristic statistical value, i.e. $E[H_{1/n}]$ or H_{rms}.

3.2.   Scour prediction at vertical walls by Hughes and Fowler (1991)

The maximum scour depth at the foot of a vertical wall exposed to normally incident irregular waves was investigated in laboratory tests by Hughes and Fowler (1991). Data were obtained for fine sand with $d_{50} = 0.13$ mm, and the following empirical formula for the maximum scour depth S_m:

$$\frac{S_m}{(U_{rms})_m T_p} = \frac{0.05}{(\sinh k_p h)^{0.35}} \qquad (24)$$

Here k_p is the wave number determined from the dispersion relationship $\omega_p^2 = gk_p \tanh k_p h$, where $\omega_p = 2\pi / T_p$ is the spectral peak frequency, and $(U_{rms})_m$ is given by the empirical formula

$$\frac{(U_{rms})_m}{gk_p T_p H_{m0}} = \frac{\sqrt{2}}{4\pi \cosh k_p h} \left[0.54 \cosh \left(\frac{1.5 - k_p h}{2.8} \right) \right] \qquad (25)$$

Eq. (25) is valid in the range $0.05 < k_p h < 3.0$, and H_{m0} is the significant wave height of the incident waves, which is related to H_{rms} by $H_{m0} = \sqrt{2} H_{rms}$ when H is Rayleigh-distributed. Moreover, there is also a relationship between T_p and T_z, i.e. $T_p = bT_z$ where b is a coefficient, which will be further discussed in Section 4.

In order to compare the results of the predictions in this section and in Section 4.1, a relationship between k_p and $\bar{k}$ is required, which is obtained from

$$b^2 k_p h \tanh k_p h = \bar{k} h \tanh \bar{k} h \qquad (26)$$

This determines $k_p h$ for given $\bar{k} h$, or vice versa.

3.3. Shields parameter, fall velocity parameter and grain Reynolds number

Following Myrhaug (1995), it can be shown that the bottom shear stress maxima for individual narrow-band progressive random waves are Weibull-distributed with the *cdf*

$$P(\hat{\tau}) = 1 - \exp(-\hat{\tau}^{\beta}) \; ; \; \hat{\tau} \geq 0, \beta = 1.35 \qquad (27)$$

where $\hat{\tau} = \tau_w / \overline{\tau}_{wrms}$ is the non-dimensional shear stress and by definition

$$\frac{\overline{\tau}_{wrms}}{\rho} = \frac{1}{2} 1.39 \left(\frac{A_{rms}}{z_0} \right)^{-0.52} U_{rms}^2 \qquad (28)$$

By taking $\hat{\theta} = \theta / \overline{\theta}_{rms}$ and defining a Shields parameter where the wave-related quantities are replaced by their rms-values in Eq. (8), i.e.

$$\overline{\theta}_{rms} = \frac{\overline{\tau}_{wrms} / \rho}{g(s-1)d_{50}} \qquad (29)$$

it follows that $\hat{\theta} = \hat{\tau}$, and thus $\hat{\theta}$ is distributed as $\hat{\tau}$, i.e. with the *cdf*

$$P(\hat{\theta}) = 1 - \exp(-\hat{\theta}^{\beta}) \; ; \; \hat{\theta} \geq 0, \beta = 1.35 \qquad (30)$$

Moreover, the fall velocity parameter w/u_* and the grain Reynolds number $u_* d_{50}/\nu$ are obtained by using that

$$u_*^2 = \hat{\theta} \frac{\overline{\tau}_{wrms}}{\rho} \qquad (31)$$

4. Results and Discussion

Comparisons will now be made between predictions and measurements for rubble-mound breakwater (Sumer and Fredsøe, 2000) and for a vertical wall (Hughes and Fowler, 1991),

representing random wave conditions. Finally, the Shields parameter, the fall velocity parameter and the grain Reynolds number are discussed.

4.1.   Rubble-mound breakwater

As referred to in Section 2, Sumer and Fredsøe (2000) made tests with irregular waves, and it should be noted that these waves were generated using the same procedure as for the irregular wave tests for scour below pipeline (Sumer and Fredsøe, 1996) and around vertical circular pile (Sumer and Fredsøe, 2001). Based on the results presented in Sumer and Fredsøe (1996, Table 1 and Fig. 3), it is found that the ratio between the peak period and the mean zero-crossing period is about $T_p / T_z = 1.5$. Thus Eq. (26) with $b = 1.5$ is used to compare the Sumer and Fredsøe (2000) data with the present stochastic method predictions. In this paper the irregular wave data for the scour depth given in Sumer and Fredsøe (2000, Table 1) (i.e. the five data sets referred to as Run 15 to 19) are used for comparison. The slope of the breakwater is $\alpha = 40^\circ$, and the data represent coarse sand conditions ($d_{50} = 0.20$ mm).

Figure 3 shows comparison between prediction and measured data of S / H_{rms} versus $h / \overline{L}$, where $\overline{L} = 2\pi / \overline{k}$ is the wave length corresponding to the wave number $\overline{k}$ (i.e. related to the mean zero-crossing wave period). The predictions correspond to using Eq. (5) with $c = 0.3$ (coarse sand) and represented by the values $E[s_{1/3}]$, $E[s_{1/10}]$ and s_{rms} given in Eqs. (21) to (23). Overall, although the data basis used for comparison is limited, the results in Fig. 3 suggest that the present stochastic method represented by s_{rms} can be taken to represent an upper value of the data, and that this value can be used for design purposes. However, comparison with more data is required to support this.

4.2.   Vertical-wall breakwater

Figure 4 shows comparison between predictions and measured data of S / H_{rms} versus $h / \overline{L}$. The data used here represent the vertical wall data for fine sand ($d_{50} = 0.13$ mm) presented by Hughes and Fowler (1991, Fig. 6). The Hughes and Fowler (1991) model given in Eqs. (24) and (25) is shown together with the present stochastic method predictions with $c = 0.4$ (fine sand) and $\alpha = 90^\circ$ in Eq. (5). It should be noted that Eq. (26) with $b = 1.5$ is used to compare the present stochastic method predictions with the data as well as the predictions by the Hughes and Fowler model. This value of b is used because the relationship between T_p and T_z is not available in Hughes and Fowler (1991). From Fig. 4 it appears that the Hughes and

Fowler model gives the best representation of the data. Moreover, the present stochastic method represented by s_{rms} gives larger values than the data and the Hughes and Fowler model for lower values of $h/\overline{L}$, while it agrees well with the data and the Hughes and Fowler model for higher values of $h/\overline{L}$. The other model predictions representing $E[s_{1/3}]$ and $E[s_{1/10}]$ give larger values than those represented by s_{rms}. Overall, although the data basis used for comparison is limited, this suggests that the present stochastic method represented by s_{rms} can be taken to represent an upper value of the data, and that it can be used for design purposes. However, comparison with more data is required to support this.
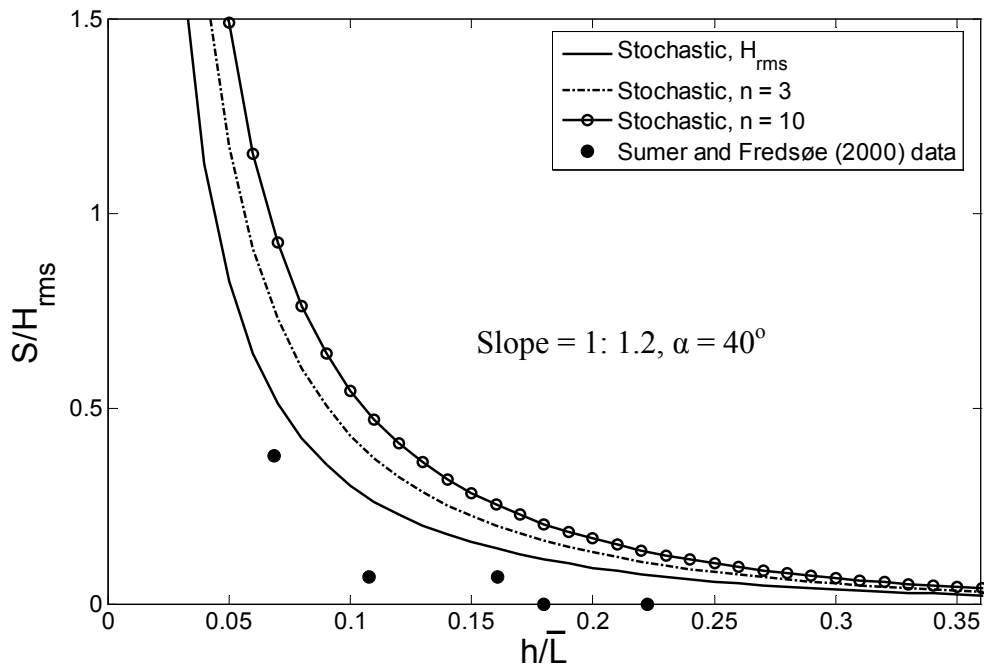
Figure 3. Maximum scour depth $\left(S/H_{rms}\right)$ **at the trunk section of a rubble-mound breakwater with slope** $\alpha = 40^{\circ}$ **versus** $h/\overline{L}$. **The results represent the present stochastic method by** s_{rms} **and** $E[s_{1/n}]$ **for** $n = 3$ **and** $n = 10$; **the Sumer and Fredsøe (2000) data.**
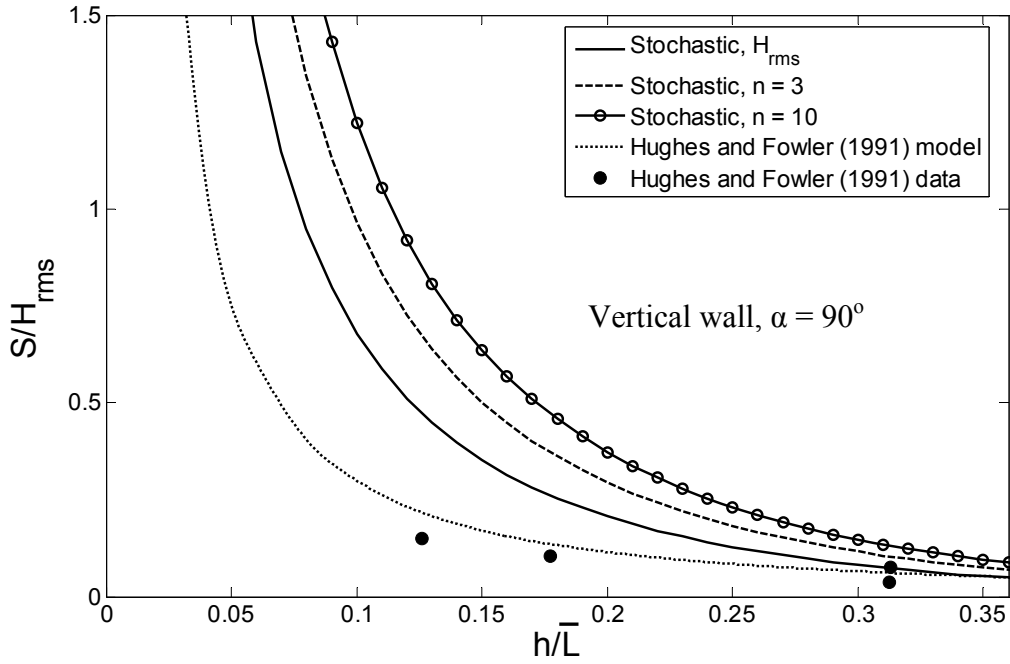
Figure 4. Maximum scour depth $\left(S / H_{rms} \right)$ **at the trunk section of a vertical-wall breakwater versus** $h / \overline{L}$. **The results represent the present stochastic method by** s_{rms} **and** $E\left[s_{1/n} \right]$ **for** $n = 3$ **and** $n = 10$; **the Hughes and Fowler (1991) data and empirical model.**

4.3. Shields parameter, fall velocity parameter and grain Reynolds number

For random waves it is not obvious which value of the Shields parameter, the fall velocity parameter and the grain Reynolds number to use to determine the conditions corresponding to live-bed scour. However, it seems to be most consistent to use corresponding statistical values of the scour depth, the Shields parameter, the fall velocity parameter and the grain Reynolds number. That is, consistent with the results in Sections 4.1 and 4.2 where the present stochastic method is compared with data, it appears that $\hat{\theta}_{rms}$ is the most appropriate value to use related to the random wave-induced scour depth. Consequently, w / u_{*rms} and $u_{*rms} d_{50} / v$ are the corresponding fall velocity parameter and the grain Reynolds number, respectively, where it follows from Eq. (31) that $u_{*rms}^2 = \hat{\theta}_{rms} \overline{\tau}_{wrms} / \rho$. For the *cdf* in Eq. (30) it follows that (see e.g. Bury (1975))

$$\hat{\theta}_{rms} = \left[\Gamma \left(1 + \frac{2}{\beta} \right) \right]^{1/2} = 1.14 \quad \text{for} \quad \beta = 1.35 \tag{32}$$

where Γ is the gamma function.

4.4. Tentative approach to random wave-induced scour at a vertical impermeable submerged breakwater

The maximum scour depth in the front of a vertical impermeable submerged breakwater exposed to normally incident waves was recently investigated in laboratory tests by Lee and Mizutani (2008). Data were obtained for bedload transport (i.e. no-suspension mode) of coarse sand with $d_{50} = 0.2$ mm. The following empirical formula for the maximum scour depth S for regular waves with incident wave height H (see Fig. 5) was obtained

$$\frac{S}{H} = \frac{0.06}{(1-C_r)(\sinh kh)^{2.04}} \qquad \text{for} \qquad C_r < 1 \qquad (33)$$

Here C_r is the reflection coefficient, which in these experiments ranged from 0.28 to 0.68, and Eq. (33) is valid for live-bed scour. It was found that the scour depth of the submerged breakwater was clearly smaller than in the case of the vertical-wall breakwater. The reason is that the incident waves are partly reflected and partly transmitted in the case of a submerged breakwater. More details are given in Lee and Mizutani (2008).

For narrow-band random incident waves Eq. (33) can be re-arranged to

$$s \equiv \frac{S/H_{rms}}{0.06 \Big/ \left[(1-C_r)(\sinh \overline{k} h)^{2.04} \right]} = \hat{H} \qquad (34)$$

Thus all the results given for the scour depth in random incident waves given in Section 3.1 can be used in this case as well, i.e. $E[s_{1/n}]$ and s_{rms} are given in Eqs. (22) and (23), respectively. No experimental data exist for scour in random waves in this case.
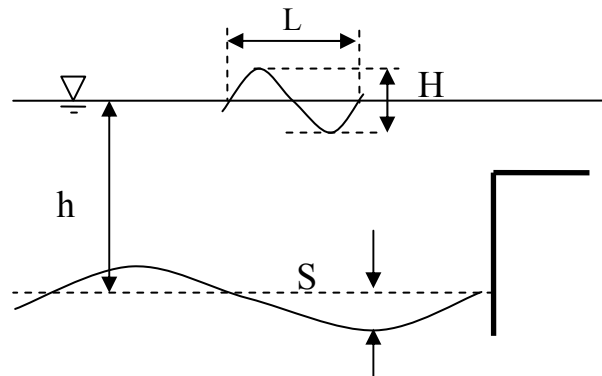

Figure 5. Definition sketch of the scour depth (*S*) at a vertical impermeable submerged breakwater, where *H* is the incident wave height and *L* is the incident wave length.

5.   Conclusions

1. The paper provides a stochastic method by which the random wave-induced scour depth at the trunk section of vertical-wall and rubble-mound breakwaters can be derived.

2. The random wave-induced scour depth is obtained by using the regular wave-induced scour depth formulas if the incident random waves are represented by the mean zero-crossing wave period T_z and a characteristic statistical value of the wave height, i. e. H_{rms} or $E[H_{1/n}]$.

3. It is recommended to use H_{rms} to represent the wave height of the incident random waves in the regular wave-induced scour depth formulas. This is based on comparisons with the Sumer and Fredsøe (2000) random wave-induced scour depth data for rubble-mound breakwater, as well as the Hughes and Fowler (1991) random wave-induced scour data and empirical formula for vertical-wall breakwater.

4. This suggests that T_z and H_{rms} can be used to represent incident random waves for design purposes, although the data basis used for comparison is limited. The results should be taken as tentative as comparison with more data is required to support this.

5. A tentative approach to random wave-induced scour at a vertical impermeable submerged breakwater based on a formula for regular waves presented by Lee and Mizutani (2008) is also suggested.

References

Bury, K.V. (1975). *Statistical Models in Applied Science*. John Wiley & Sons, New York.

Hughes, S.A. and Fowler, J.A. (1991). Wave-induced scour predictions at vertical walls. *ASCE Proc. Conf. Coastal Sediments 91*, 1886-1899.

Lee, K.-H. and Mizutani, N. (2008). Experimental study on scour occurring at a vertical impermeable submerged breakwater. *Applied Ocean Research*, 30 (2), 92-99.

Myrhaug, D. (1995). Bottom friction beneath random waves. *Coast. Eng.*, 24, 259-273.

Myrhaug, D., Rue, H. and Tørum, A. (2004). Tentative engineering approach to scour around breakwaters in random waves. *Coast. Eng.*, 51, 1051-1065.

Soulsby, R.L. (1997). *Dynamics of Marine Sands, A Manual for Practical Applications*. Thomas Telford, London, UK.

Sumer, B.M. and Fredsøe, J. (1996). Scour below pipelines in combined waves and current. *Proc. 15th OMAE Conf.*, Florence, Italy, Vol. 5, 595-602.

Sumer, B.M. and Fredsøe, J. (2000). Experimental study of 2D scour and its protection at a rubble-mound breakwater. *Coast. Eng.*, 40, 59-87.

Sumer, B.M. and Fredsøe, J. (2001). Scour around pile in combined waves and current. *J. Hydraul. Eng.*, ASCE, 127 (5), 403-411.

Sumer, B.M. and Fredsøe, J. (2002). *The Mechanics of Scour in the Marine Environment*. World Scientific, Singapore.

Whitehouse, R.J.S. (1998). *Scour at Marine Structures. A Manual for Practical Applications*. Thomas Telford, London, UK.

Xie, S.L. (1981). Scouring patterns in front of vertical breakwaters and their influence on the stability of the foundations of the breakwaters. Report. Department of Civil Engineering, Delft University of Technology, Delft, The Netherlands, September, 61 p.

Recommendations for Future Work

In this thesis, the following two topics are covered: 1) Applications of the standard high Reynolds number k-ε model in coastal, marine and offshore engineering, and 2) A stochastic scour prediction model for marine structures. In general, satisfactory results and conclusions have been obtained based on both numerical and analytical research work discussed in Chapters 5, 6, 7, 8, 10 and 11.

At the end of this thesis, it is feasible to point out some possible areas of future research, and they are listed as follows:

- Some marine structures have a square or a rectangular shape. Thus, it is of interesting to study the flow mechanisms around a 2D square/rectangular cylinder at high Reynolds numbers by using the present CFD codes.

- Chapters 5 - 8 show detailed numerical studies of rough turbulent oscillatory boundary layer flows with suspended sediments and flows around a circular cylinder at high Reynolds numbers. Based on these results, the present CFD codes can be extended to perform numerical simulations of scour around a marine pipeline for current and waves.

- There are not many published numerical work of LES on the rough turbulent oscillatory boundary layer flows. Although the near-bed conditions and the bed roughness are difficult to model numerically, LES might be a useful tool for gaining more physical insight on this topic.

- Based on Chapters 10 and 11, it appears that the proposed stochastic approach gives reasonable results for random wave-induced scour predictions for marine structures. However, more experimental data are required for comparisons before a conclusion regarding the validity of this approach can be given. Moreover, CFD work on the random wave-induced scour around these marine structures can be carried out to cross-validate the results obtained from the stochastic approach.

UR-79-01 Brigt Hatlestad, MK: The finite element method used in a fatigue evaluation of fixed offshore platforms. (Dr.Ing. Thesis)

UR-79-02 Erik Pettersen, MK: Analysis and design of cellular structures. (Dr.Ing. Thesis)

UR-79-03 Sverre Valsgård, MK: Finite difference and finite element methods applied to nonlinear analysis of plated structures. (Dr.Ing. Thesis)

UR-79-04 Nils T. Nordsve, MK: Finite element collapse analysis of structural members considering imperfections and stresses due to fabrication. (Dr.Ing. Thesis)

UR-79-05 Ivar J. Fylling, MK: Analysis of towline forces in ocean towing systems. (Dr.Ing. Thesis)

UR-80-06 Nils Sandsmark, MM: Analysis of Stationary and Transient Heat Conduction by the Use of the Finite Element Method. (Dr.Ing. Thesis)

UR-80-09 Sverre Haver, MK: Analysis of uncertainties related to the stochastic modelling of ocean waves. (Dr.Ing. Thesis)

UR-85-46 Alf G. Engseth, MK: Finite element collapse analysis of tubular steel offshore structures. (Dr.Ing. Thesis)

UR-86-47 Dengody Sheshappa, MP: A Computer Design Model for Optimizing Fishing Vessel Designs Based on Techno-Economic Analysis. (Dr.Ing. Thesis)

UR-86-48 Vidar Aanesland, MH: A Theoretical and Numerical Study of Ship Wave Resistance. (Dr.Ing. Thesis)

UR-86-49 Heinz-Joachim Wessel, MK: Fracture Mechanics Analysis of Crack Growth in Plate Girders. (Dr.Ing. Thesis)

UR-86-50 Jon Taby, MK: Ultimate and Post-ultimate Strength of Dented Tubular Members. (Dr.Ing. Thesis)

UR-86-51 Walter Lian, MH: A Numerical Study of Two-Dimensional Separated Flow Past Bluff Bodies at Moderate KC-Numbers. (Dr.Ing. Thesis)

UR-86-52 Bjørn Sortland, MH: Force Measurements in Oscillating Flow on Ship Sections and Circular Cylinders in a U-Tube Water Tank. (Dr.Ing. Thesis)

UR-86-53 Kurt Strand, MM: A System Dynamic Approach to One-dimensional Fluid Flow. (Dr.Ing. Thesis)

UR-86-54 Arne Edvin Løken, MH: Three Dimensional Second Order Hydrodynamic Effects on Ocean Structures in Waves. (Dr.Ing. Thesis)

UR-86-55 Sigurd Falch, MH: A Numerical Study of Slamming of Two-Dimensional Bodies. (Dr.Ing. Thesis)

UR-87-56 Arne Braathen, MH: Application of a Vortex Tracking Method to the Prediction of Roll Damping of a Two-Dimension Floating Body. (Dr.Ing. Thesis)

UR-87-57 Bernt Leira, MR: Gaussian Vector Processes for Reliability Analysis involving Wave-Induced Load Effects. (Dr.Ing. Thesis)

UR-87-58 Magnus Småvik, MM: Thermal Load and Process Characteristics in a Two-Stroke Diesel Engine with Thermal Barriers (in Norwegian). (Dr.Ing. Thesis)

MTA-88-59 Bernt Arild Bremdal, MP: An Investigation of Marine Installation Processes - A Knowledge - Based Planning Approach. (Dr.Ing. Thesis)

MTA-88-60 Xu Jun, MK: Non-linear Dynamic Analysis of Space-framed Offshore Structures. (Dr.Ing. Thesis)

MTA-89-61 Gang Miao, MH: Hydrodynamic Forces and Dynamic Responses of Circular Cylinders in Wave Zones. (Dr.Ing. Thesis)

MTA-89-62 Martin Greenhow, MH: Linear and Non-Linear Studies of Waves and Floating Bodies. Part I and Part II. (Dr.Techn. Thesis)

MTA-89-63 Chang Li, MH: Force Coefficients of Spheres and Cubes in Oscillatory Flow with and without Current. (Dr.Ing. Thesis)

MTA-89-64 Hu Ying, MP: A Study of Marketing and Design in Development of Marine Transport Systems.

(Dr.Ing. Thesis)

MTA-89-65 <u>Arild Jæger</u>, MH: Seakeeping, Dynamic Stability and Performance of a Wedge Shaped Planing Hull. (Dr.Ing. Thesis)

MTA-89-66 <u>Chan Siu Hung</u>, MM: The dynamic characteristics of tilting-pad bearings.

MTA-89-67 <u>Kim Wikstrøm</u>, MP: Analysis av projekteringen for ett offshore projekt. (Licenciat-avhandling)

MTA-89-68 <u>Jiao Guoyang</u>, MR: Reliability Analysis of Crack Growth under Random Loading, considering Model Updating. (Dr.Ing. Thesis)

MTA-89-69 <u>Arnt Olufsen</u>, MK: Uncertainty and Reliability Analysis of Fixed Offshore Structures. (Dr.Ing. Thesis)

MTA-89-70 <u>Wu Yu-Lin</u>, MR: System Reliability Analyses of Offshore Structures using improved Truss and Beam Models. (Dr.Ing. Thesis)

MTA-90-71 <u>Jan Roger Hoff</u>, MH: Three-dimensional Green function of a vessel with forward speed in waves. (Dr.Ing. Thesis)

MTA-90-72 <u>Rong Zhao</u>, MH: Slow-Drift Motions of a Moored Two-Dimensional Body in Irregular Waves. (Dr.Ing. Thesis)

MTA-90-73 <u>Atle Minsaas</u>, MP: Economical Risk Analysis. (Dr.Ing. Thesis)

MTA-90-74 <u>Knut-Aril Farnes</u>, MK: Long-term Statistics of Response in Non-linear Marine Structures. (Dr.Ing. Thesis)

MTA-90-75 <u>Torbjørn Sotberg</u>, MK: Application of Reliability Methods for Safety Assessment of Submarine Pipelines. (Dr.Ing. Thesis)

MTA-90-76 <u>Zeuthen, Steffen</u>, MP: SEAMAID. A computational model of the design process in a constraint-based logic programming environment. An example from the offshore domain. (Dr.Ing. Thesis)

MTA-91-77 <u>Haagensen, Sven</u>, MM: Fuel Dependant Cyclic Variability in a Spark Ignition Engine - An Optical Approach. (Dr.Ing. Thesis)

MTA-91-78 <u>Løland, Geir</u>, MH: Current forces on and flow through fish farms. (Dr.Ing. Thesis)

MTA-91-79 <u>Hoen, Christopher</u>, MK: System Identification of Structures Excited by Stochastic Load Processes. (Dr.Ing. Thesis)

MTA-91-80 <u>Haugen, Stein</u>, MK: Probabilistic Evaluation of Frequency of Collision between Ships and Offshore Platforms. (Dr.Ing. Thesis)

MTA-91-81 <u>Sødahl, Nils</u>, MK: Methods for Design and Analysis of Flexible Risers. (Dr.Ing. Thesis)

MTA-91-82 <u>Ormberg, Harald</u>, MK: Non-linear Response Analysis of Floating Fish Farm Systems. (Dr.Ing. Thesis)

MTA-91-83 <u>Marley, Mark J.</u>, MK: Time Variant Reliability under Fatigue Degradation. (Dr.Ing. Thesis)

MTA-91-84 <u>Krokstad, Jørgen R.</u>, MH: Second-order Loads in Multidirectional Seas. (Dr.Ing. Thesis)

MTA-91-85 <u>Molteberg, Gunnar A.</u>, MM: The Application of System Identification Techniques to Performance Monitoring of Four Stroke Turbocharged Diesel Engines. (Dr.Ing. Thesis)

MTA-92-86 <u>Mørch, Hans Jørgen Bjelke</u>, MH: Aspects of Hydrofoil Design: with Emphasis on Hydrofoil Interaction in Calm Water. (Dr.Ing. Thesis)

MTA-92-87 <u>Chan Siu Hung</u>, MM: Nonlinear Analysis of Rotordynamic Instabilities in High-speed Turbomachinery. (Dr.Ing. Thesis)

MTA-92-88 <u>Bessason, Bjarni</u>, MK: Assessment of Earthquake Loading and Response of Seismically Isolated Bridges. (Dr.Ing. Thesis)

MTA-92-89 <u>Langli, Geir</u>, MP: Improving Operational Safety through exploitation of Design Knowledge - an investigation of offshore platform safety. (Dr.Ing. Thesis)

MTA-92-90 <u>Sævik, Svein</u>, MK: On Stresses and Fatigue in Flexible Pipes. (Dr.Ing. Thesis)

MTA-92-91 <u>Ask, Tor Ø.</u>, MM: Ignition and Flame Growth in Lean Gas-Air Mixtures. An Experimental Study with a Schlieren System. (Dr.Ing. Thesis)

MTA-86-92 <u>Hessen, Gunnar</u>, MK: Fracture Mechanics Analysis of Stiffened Tubular Members. (Dr.Ing. Thesis)

MTA-93-93 <u>Steinebach, Christian</u>, MM: Knowledge Based Systems for Diagnosis of Rotating Machinery. (Dr.Ing. Thesis)

MTA-93-94 Dalane, Jan Inge, MK: System Reliability in Design and Maintenance of Fixed Offshore Structures. (Dr.Ing. Thesis)

MTA-93-95 Steen, Sverre, MH: Cobblestone Effect on SES. (Dr.Ing. Thesis)

MTA-93-96 Karunakaran, Daniel, MK: Nonlinear Dynamic Response and Reliability Analysis of Drag-dominated Offshore Platforms. (Dr.Ing. Thesis)

MTA-93-97 Hagen, Arnulf, MP: The Framework of a Design Process Language. (Dr.Ing. Thesis)

MTA-93-98 Nordrik, Rune, MM: Investigation of Spark Ignition and Autoignition in Methane and Air Using Computational Fluid Dynamics and Chemical Reaction Kinetics. A Numerical Study of Ignition Processes in Internal Combustion Engines. (Dr.Ing. Thesis)

MTA-94-99 Passano, Elizabeth, MK: Efficient Analysis of Nonlinear Slender Marine Structures. (Dr.Ing. Thesis)

MTA-94-100 Kvålsvold, Jan, MH: Hydroelastic Modelling of Wetdeck Slamming on Multihull Vessels. (Dr.Ing. Thesis)

MTA-94-102 Bech, Sidsel M., MK: Experimental and Numerical Determination of Stiffness and Strength of GRP/PVC Sandwich Structures. (Dr.Ing. Thesis)

MTA-95-103 Paulsen, Hallvard, MM: A Study of Transient Jet and Spray using a Schlieren Method and Digital Image Processing. (Dr.Ing. Thesis)

MTA-95-104 Hovde, Geir Olav, MK: Fatigue and Overload Reliability of Offshore Structural Systems, Considering the Effect of Inspection and Repair. (Dr.Ing. Thesis)

MTA-95-105 Wang, Xiaozhi, MK: Reliability Analysis of Production Ships with Emphasis on Load Combination and Ultimate Strength. (Dr.Ing. Thesis)

MTA-95-106 Ulstein, Tore, MH: Nonlinear Effects of a Flexible Stern Seal Bag on Cobblestone Oscillations of an SES. (Dr.Ing. Thesis)

MTA-95-107 Solaas, Frøydis, MH: Analytical and Numerical Studies of Sloshing in Tanks. (Dr.Ing. Thesis)

MTA-95-108 Hellan, øyvind, MK: Nonlinear Pushover and Cyclic Analyses in Ultimate Limit State Design and Reassessment of Tubular Steel Offshore Structures. (Dr.Ing. Thesis)

MTA-95-109 Hermundstad, Ole A., MK: Theoretical and Experimental Hydroelastic Analysis of High Speed Vessels. (Dr.Ing. Thesis)

MTA-96-110 Bratland, Anne K., MH: Wave-Current Interaction Effects on Large-Volume Bodies in Water of Finite Depth. (Dr.Ing. Thesis)

MTA-96-111 Herfjord, Kjell, MH: A Study of Two-dimensional Separated Flow by a Combination of the Finite Element Method and Navier-Stokes Equations. (Dr.Ing. Thesis)

MTA-96-112 Æsøy, Vilmar, MM: Hot Surface Assisted Compression Ignition in a Direct Injection Natural Gas Engine. (Dr.Ing. Thesis)

MTA-96-113 Eknes, Monika L., MK: Escalation Scenarios Initiated by Gas Explosions on Offshore Installations. (Dr.Ing. Thesis)

MTA-96-114 Erikstad, Stein O., MP: A Decision Support Model for Preliminary Ship Design. (Dr.Ing. Thesis)

MTA-96-115 Pedersen, Egil, MH: A Nautical Study of Towed Marine Seismic Streamer Cable Configurations. (Dr.Ing. Thesis)

MTA-97-116 Moksnes, Paul O., MM: Modelling Two-Phase Thermo-Fluid Systems Using Bond Graphs. (Dr.Ing. Thesis)

MTA-97-117 Halse, Karl H., MK: On Vortex Shedding and Prediction of Vortex-Induced Vibrations of Circular Cylinders. (Dr.Ing. Thesis)

MTA-97-118 Igland, Ragnar T., MK: Reliability Analysis of Pipelines during Laying, considering Ultimate Strength under Combined Loads. (Dr.Ing. Thesis)

MTA-97-119 Pedersen, Hans-P., MP: Levendefiskteknologi for fiskefartøy. (Dr.Ing. Thesis)

MTA-98-120 Vikestad, Kyrre, MK: Multi-Frequency Response of a Cylinder Subjected to Vortex Shedding and Support Motions. (Dr.Ing. Thesis)

MTA-98-121 Azadi, Mohammad R. E., MK: Analysis of Static and Dynamic Pile-Soil-Jacket Behaviour. (Dr.Ing. Thesis)

MTA-98-122 Ulltang, Terje, MP: A Communication Model for Product Information. (Dr.Ing. Thesis)

MTA-98-123 Torbergsen, Erik, MM: Impeller/Diffuser Interaction Forces in Centrifugal Pumps. (Dr.Ing. Thesis)

MTA-98-124 Hansen, Edmond, MH: A Discrete Element Model to Study Marginal Ice Zone Dynamics and the Behaviour of Vessels Moored in Broken Ice. (Dr.Ing. Thesis)

MTA-98-125 Videiro, Paulo M., MK: Reliability Based Design of Marine Structures. (Dr.Ing. Thesis)

MTA-99-126 Mainçon, Philippe, MK: Fatigue Reliability of Long Welds Application to Titanium Risers. (Dr.Ing. Thesis)

MTA-99-127 Haugen, Elin M., MH: Hydroelastic Analysis of Slamming on Stiffened Plates with Application to Catamaran Wetdecks. (Dr.Ing. Thesis)

MTA-99-128 Langhelle, Nina K., MK: Experimental Validation and Calibration of Nonlinear Finite Element Models for Use in Design of Aluminium Structures Exposed to Fire. (Dr.Ing. Thesis)

MTA-99-129 Berstad, Are J., MK: Calculation of Fatigue Damage in Ship Structures. (Dr.Ing. Thesis)

MTA-99-130 Andersen, Trond M., MM: Short Term Maintenance Planning. (Dr.Ing. Thesis)

MTA-99-131 Tveiten, Bård Wathne, MK: Fatigue Assessment of Welded Aluminium Ship Details. (Dr.Ing. Thesis)

MTA-99-132 Søreide, Fredrik, MP: Applications of underwater technology in deep water archaeology. Principles and practice. (Dr.Ing. Thesis)

MTA-99-133 Tønnessen, Rune, MH: A Finite Element Method Applied to Unsteady Viscous Flow Around 2D Blunt Bodies With Sharp Corners. (Dr.Ing. Thesis)

MTA-99-134 Elvekrok, Dag R., MP: Engineering Integration in Field Development Projects in the Norwegian Oil and Gas Industry. The Supplier Management of Norne. (Dr.Ing. Thesis)

MTA-99-135 Fagerholt, Kjetil, MP: Optimeringsbaserte Metoder for Ruteplanlegging innen skipsfart. (Dr.Ing. Thesis)

MTA-99-136 Bysveen, Marie, MM: Visualization in Two Directions on a Dynamic Combustion Rig for Studies of Fuel Quality. (Dr.Ing. Thesis)

MTA-2000-137 Storteig, Eskild, MM: Dynamic characteristics and leakage performance of liquid annular seals in centrifugal pumps. (Dr.Ing. Thesis)

MTA-2000-138 Sagli, Gro, MK: Model uncertainty and simplified estimates of long term extremes of hull girder loads in ships. (Dr.Ing. Thesis)

MTA-2000-139 Tronstad, Harald, MK: Nonlinear analysis and design of cable net structures like fishing gear based on the finite element method. (Dr.Ing. Thesis)

MTA-2000-140 Kroneberg, André, MP: Innovation in shipping by using scenarios. (Dr.Ing. Thesis)

MTA-2000-141 Haslum, Herbjørn Alf, MH: Simplified methods applied to nonlinear motion of spar platforms. (Dr.Ing. Thesis)

MTA-2001-142 Samdal, Ole Johan, MM: Modelling of Degradation Mechanisms and Stressor Interaction on Static Mechanical Equipment Residual Lifetime. (Dr.Ing. Thesis)

MTA-2001-143 Baarholm, Rolf Jarle, MH: Theoretical and experimental studies of wave impact underneath decks of offshore platforms. (Dr.Ing. Thesis)

MTA-2001-144 Wang, Lihua, MK: Probabilistic Analysis of Nonlinear Wave-induced Loads on Ships. (Dr.Ing. Thesis)

MTA-2001-145 Kristensen, Odd H. Holt, MK: Ultimate Capacity of Aluminium Plates under Multiple Loads, Considering HAZ Properties. (Dr.Ing. Thesis)

MTA-2001-146 Greco, Marilena, MH: A Two-Dimensional Study of Green-Water Loading. (Dr.Ing. Thesis)

MTA-2001-147 Heggelund, Svein E., MK: Calculation of Global Design Loads and Load Effects in Large High Speed Catamarans. (Dr.Ing. Thesis)

MTA-2001-148 Babalola, Olusegun T., MK: Fatigue Strength of Titanium Risers - Defect Sensitivity. (Dr.Ing. Thesis)

MTA-2001-149 Mohammed, Abuu K., MK: Nonlinear Shell Finite Elements for Ultimate Strength and Collapse Analysis of Ship Structures. (Dr.Ing. Thesis)

MTA-2002-150 Holmedal, Lars E., MH: Wave-current interactions in the vicinity of the sea bed. (Dr.Ing. Thesis)

MTA-2002-151 Rognebakke, Olav F., MH: Sloshing in rectangular tanks and interaction with ship motions. (Dr.Ing. Thesis)

MTA-2002-152 Lader, Pål Furset, MH: Geometry and Kinematics of Breaking Waves. (Dr.Ing. Thesis)

MTA-2002-153 Yang, Qinzheng, MH: Wash and wave resistance of ships in finite water depth. (Dr.Ing. Thesis)

MTA-2002-154 Melhus, Øyvin, MM: Utilization of VOC in Diesel Engines. Ignition and combustion of VOC released by crude oil tankers. (Dr.Ing. Thesis)

MTA-2002-155 Ronæss, Marit, MH: Wave Induced Motions of Two Ships Advancing on Parallel Course. (Dr.Ing. Thesis)

MTA-2002-156 Økland, Ole D., MK: Numerical and experimental investigation of whipping in twin hull vessels exposed to severe wet deck slamming. (Dr.Ing. Thesis)

MTA-2002-157 Ge, Chunhua, MK: Global Hydroelastic Response of Catamarans due to Wet Deck Slamming. (Dr.Ing. Thesis)

MTA-2002-158 Byklum, Eirik, MK: Nonlinear Shell Finite Elements for Ultimate Strength and Collapse Analysis of Ship Structures. (Dr.Ing. Thesis)

IMT-2003-1 Chen, Haibo, MK: Probabilistic Evaluation of FPSO-Tanker Collision in Tandem Offloading Operation. (Dr.Ing. Thesis)

IMT-2003-2 Skaugset, Kjetil Bjørn, MK: On the Suppression of Vortex Induced Vibrations of Circular Cylinders by Radial Water Jets. (Dr.Ing. Thesis)

IMT-2003-3 Chezhian, Muthu   Three-Dimensional Analysis of Slamming. (Dr.Ing. Thesis)

IMT-2003-4 Buhaug, Øyvind   Deposit Formation on Cylinder Liner Surfaces in Medium Speed Engines. (Dr.Ing. Thesis)

IMT-2003-5 Tregde, Vidar   Aspects of Ship Design: Optimization of Aft Hull with Inverse Geometry Design. (Dr.Ing. Thesis)

IMT-2003-6 Wist, Hanne Therese   Statistical Properties of Successive Ocean Wave Parameters. (Dr.Ing. Thesis)

IMT-2004-7 Ransau, Samuel   Numerical Methods for Flows with Evolving Interfaces. (Dr.Ing. Thesis)

IMT-2004-8 Soma, Torkel   Blue-Chip or Sub-Standard. A data interrogation approach of identity safety characteristics of shipping organization. (Dr.Ing. Thesis)

IMT-2004-9 Ersdal, Svein   An experimental study of hydrodynamic forces on cylinders and cables in near axial flow. (Dr.Ing. Thesis)

IMT-2005-10 Brodtkorb, Per Andreas   The Probability of Occurrence of Dangerous Wave Situations at Sea. (Dr.Ing. Thesis)

IMT-2005-11 Yttervik, Rune   Ocean current variability in relation to offshore engineering. (Dr.Ing. Thesis)

IMT-2005-12 Fredheim, Arne   Current Forces on Net-Structures. (Dr.Ing. Thesis)

IMT-2005-13 Heggernes, Kjetil   Flow around marine structures. (Dr.Ing. Thesis)

IMT-2005-14 Fouques, Sebastien   Lagrangian Modelling of Ocean Surface Waves and Synthetic Aperture Radar Wave Measurements. (Dr.Ing. Thesis)

IMT-2006-15 Holm, Håvard   Numerical calculation of viscous free surface flow around marine structures. (Dr.Ing. Thesis)

IMT-2006-16 Bjørheim, Lars G.   Failure Assessment of Long Through Thickness Fatigue Cracks in Ship Hulls. (Dr.Ing. Thesis)

IMT-2006-17 Hansson, Lisbeth   Safety Management for Prevention of Occupational Accidents. (Dr.Ing. Thesis)

IMT-2006-18 Zhu, Xinying   Application of the CIP Method to Strongly Nonlinear Wave-Body Interaction Problems. (Dr.Ing. Thesis)

IMT-2006-19 Reite, Karl Johan   Modelling and Control of Trawl Systems. (Dr.Ing. Thesis)

IMT-2006-20 Smogeli, Øyvind Notland   Control of Marine Propellers. From Normal to Extreme Conditions. (Dr.Ing. Thesis)

IMT-2007-21 Storhaug, Gaute   Experimental Investigation of Wave Induced Vibrations and Their Effect on the Fatigue Loading of Ships. (Dr.Ing. Thesis)

IMT-2007-22 Sun, Hui   A Boundary Element Method Applied to Strongly Nonlinear Wave-Body Interaction Problems. (PhD Thesis, CeSOS)

IMT-2007-23 Rustad, Anne Marthine   Modelling and Control of Top Tensioned Risers. (PhD Thesis, CeSOS)

IMT-2007-24 Johansen, Vegar

Modelling flexible slender system for real-time simulations and control applications.

IMT-2007-25 Wroldsen, Anders Sunde

Modelling and control of tensegrity structures. (PhD Thesis, CeSOS)

IMT-2007-26 Aronsen, Kristoffer Høye

An experimental investigation of in-line and combined in-line and cross flow vortex induced vibrations. (Dr.avhandling, IMT)

IMT-2007-27 Zhen, Gao

Stochastic response analysis of mooring systems with emphasis on frequency-domain analysis of fatgue due to wide-band processes. (PhD-thesis, CeSOS).

IMT-2007-28 Thorstensen, Tom Anders

Lifetime Profit Modelling of Ageing Systems Utilizing Information about Technical Condition.
Dr.ing. thesis, IMT.

IMT-2008-29 Berntsen, Per Ivar B.

Structural Reliability Based Position Mooring.
PhD-Thesis, IMT.

IMT-2008-30 Ye, Naiquan

Fatigues Assessment of Aluminium Welded Box-stiffener Joints in ships.
Dr.ing. thesis, IMT.

IMT-2008-31 Radan, Damir

Integrated Control of Marine Electrical Power
Systems. PhD-Thesis, IMT.

IMT-2008-32 Norum, Viggo L.

Analysis of Ignituin and Combustion in Otto Lean-Burn Engines with Prechambers.
Dr.ing. thesis, IMT.

IMT-2008-33 Pákozdi, Csaba

A Smoothed Particle Hydrodynamics Study of Two-dimensional Nonlinear Sloshing in Rectangular Tanks.
Dr.ing.thesis, IMT.

IMT-2008-34 Grytøyr, Guttorm

A Higher-Order Boundary Element Method and Applications to Marine hydrodynamics.
Dr.ing. thesis, IMT.

IMT-2008-35 Drummen, Ingo

Experimental and Numerical Investigation of Nonlinear Wave-Induced Load effects in Containerships Considering Hydroelasticity.
PhD-Thesis. CeSOS.

IMT-2008-36 Skejic, Renato

Maneuvering and Seakeeping of a Singel Ship and of Two Ships in Interaction.
PhD-Thesis. CeSOS.

IMT-2008-37 Harlem, Alf

An Age-Based Replacement Model for Repairable Systems with Attention to High-Speed Marine Diesel Engines.
PhD-Thesis, IMT.

IMT-2008-38 Alsos, Hagbart S.

Ship Grounding. Analysis of Ductile Fracture, Bottom Damage and Hull Girder Response.
PhD-thesis, IMT.

IMT-2008-39 Graczyk, Mateusz

Experimental Investigation of Sloshing Loading and Load Effects in Membrane LNG Tanks Subjected to Random Excitation.
PhD-thesis, CeSOS.

IMT-2008-40 Taghipour, Reza

Efficient Prediction of Dynamic Response for Flexible amd Multi-body Marine Structures.
PhD-thesis, CeSOS.

IMT-2008-41 Ruth, Eivind

Propulsion Control and Thrust Allocation on Marine Vessels.
PhD-thesis, CeSOS.

IMT-2008-42 Nystad, Bent Helge

Technical Condition Indexes and Remaining Useful Life of Aggregated Systems.
PhD-thesis, IMT.

IMT-2008-43 Soni, Prashant Kumer

Hydroyynamic Coefficients for Vortex Induced Vibrations of Flexible Beams,
PhD-thesis, CeSOS.

IMT-2009-44 Amlashi, Hadi K.K.

Ultimate Strength and Reliability Analysis of Ship Hulls with Emphasis on Combined Global and Local Loads.
PhD-thesis, IMT.